Georgia State University
ScholarWorks @ Georgia State University

Physics and Astronomy Dissertations | Department of Physics and Astronomy

Fall 12-15-2016

Optoelectronic and Structural Properties of Group III-Nitride Semiconductors Grown by High Pressure MOCVD and Migration Enhanced Plasma Assisted MOCVD

Indika Matara Kankanamge
Georgia State University

Follow this and additional works at: https://scholarworks.gsu.edu/phy_astr_diss

Recommended Citation

Matara Kankanamge, Indika, "Optoelectronic and Structural Properties of Group III-Nitride Semiconductors Grown by High Pressure MOCVD and Migration Enhanced Plasma Assisted MOCVD." Dissertation, Georgia State University, 2016.
https://scholarworks.gsu.edu/phy_astr_diss/89

This Dissertation is brought to you for free and open access by the Department of Physics and Astronomy at ScholarWorks @ Georgia State University. It has been accepted for inclusion in Physics and Astronomy Dissertations by an authorized administrator of ScholarWorks @ Georgia State University. For more information, please contact scholarworks@gsu.edu.

OPTOELECTONIC AND STRUCTURAL PROPERTIES OF GROUP III- NITRIDE SEMICONDUCTORS GROWN BY HIGH PRESSURE MOCVD AND MIGRATION ENHANCED PLASMA ASSISTED MOCVD

by

INDIKA S MATARA KANKANAMGE

Under the Direction of Prof. Nikolaus Dietz

ABSTRACT

The objective of this dissertation is to understand the structural and optoelectronic properties of group III-nitride materials grown by High-Pressure Metal Organic Chemical Vapor Deposition (HP-MOCVD) and Migration Enhanced Plasma Assisted MOCVD by FTIR reflectance spectroscopy, Raman spectroscopy, X-ray diffraction, and Atomic Force Microscopy.

The influence of the substrates/templates (Sapphire, AlN, Ga-polar GaN, N-polar GaN, n-GaN, and p-GaN) on the free carrier concentration, carrier mobility, short-range crystalline ordering, and surface morphology of the InN layers grown on HP-MOCVD were investigated using those techniques. The lowest carrier concentration of 7.1×10^{18} cm^{-3} with mobility of 660 $cm^2V^{-1}s^{-1}$ was found in the InN film on AlN template, by FTIR reflectance spectra analysis. Furthermore, in addition to the bulk layer, an intermediate InN layers with different optoelectronic properties were identified in these samples. The best local crystalline order was observed in the InN/AlN/Sapphire by the Raman E_2 high analysis. The smoothest InN surface was observed on the InN film on p-GaN template.

The influence of reactor pressures (2.5–18.5 bar) on the long-range crystalline order, in plane structural quality, local crystalline order, free carrier concentration, and carrier mobility of the InN epi-layers deposited on GaN/sapphire by HP-MOCVD has also been studied using those methods. Within the studied process parameter space, the best material properties were achieved at a reactor pressure of 12.5 bar and a group-V/III ratio of 2500 with a free carrier concentration of 1.5×10^{18} cm^{-3}, a mobility in the bulk InN layer of 270 cm^2 $V^{-1}s^{-1}$ and the Raman (E_2 high) FWHM of 10.3 cm^{-1}. The crystalline properties, probed by XRD 2θ–ω scans have shown an improvement with the increasing reactor pressure.

The effect of an AlN buffer layer on the free carrier concentration, carrier mobility, local crystalline order, and surface morphology of InN layers grown by Migration-Enhanced Plasma Assisted MOCVD were also investigated. Here, the AlN nucleation layer was varied to assess the physical properties of the InN layers. This study was focused on optimization of the AlN nucleation layer (e.g. temporal precursor exposure, nitrogen plasma exposure, and plasma power) and its effect on the InN layer properties.

INDEX WORDS: Aluminum Nitride (AlN), Gallium Nitride (GaN), Indium Nitride (InN), Group III-nitrides, InGaN, Raman Spectroscopy, FTIR Reflectance Spectroscopy, Dielectric Function, X-ray Diffraction, AFM, Free Carrier Concentration, Mobility, High frequency dielectric constant, High Pressure MOCVD, Migration Enhanced Plasma Assisted MOCVD

OPTOELECTRONIC AND STRUCTURAL PROPERTIES OF GROUP III-NITRIDE SEMICONDUCTORS GROWN BY HIGH PRESSURE MOCVD AND MIGRATION ENHANCED PLASMA ASSISTED MOCVD

by

INDIKA MATARA KANKANAMGE

A Dissertation Submitted in Partial Fulfillment of the Requirements for the Degree of

Doctor of Philosophy

in the College of Arts and Sciences

Georgia State University

2016

Copyright by
Indika Senevirathna Matara Kankanamge
2016

OPTOELECTRONIC AND STRUCTURAL PROPERTIES OF GROUP III-NITRIDE SEMICONDUCTORS GROWN BY HIGH PRESSURE MOCVD AND MIGRATION ENHANCED PLASMA ASSISTAED MOCVD

by

INDIKA S. MATARA KANKANAMGE

Committee Chair: Nikolaus Dietz

Committee: Vadym Apalkov

Michael Williams

Yohannes Abate

Electronic Version Approved:

Office of Graduate Studies

College of Arts and Sciences

Georgia State University

December 2016

DEDICATION

This dissertation is dedicated to my loving husband, father,

and

all my teachers

who inspired, encouraged, supported and guided me in this journey.

ACKNOWLEDGEMENTS

First, I would like to express my deepest gratitude to my supervisor Prof. Nikolaus Dietz for his patient guidance, and encouragement throughout this study. His endless enthusiasm, support, and invaluable suggestions made this work successful. Deepest gratitude is also due to the members of my dissertation committee: Prof. Vadym Apalkov, Prof. Michael D. Williams, and Prof. Yohannes Abate for the fruitful discussions, technical assistance, and effort in reading and providing me with valuable comments on this dissertation. I would also be thankful to Prof. A. G.U. Perera, Prof. Vadym Apalkov, and Prof. Douglas Gies who served in my MS committee.

In addition, I wish to thank Prof. Perera and his group for allowing me to access the FTIR spectrometer for this study and Dr. Abate and Mr. Alireza for the AFM data. I would like to convey special acknowledgment to former group members and colleagues Dr. Ramazan Atalay, Dr. Max Bugler, and Mr. S. Gamage for valuable discussions and support in this work. I am also thankful for the present colleagues in the group: Mr. Daniel Seidlitz, Mr. Mark Vernon, and Mr. Ernesto Potdevin for their support and discussion in the successful completion of this work.

My thanks also goes to Mr. Peter Walker and the workshop staff, who were there to aid whenever we need to make a mechanical part or a repair is needed on any laboratory instruments. Furthermore, I wish to thank department chair Prof. Michael Crenshaw, graduate director Prof. Xiaochum He and all the individuals of the Department of Physics and Astronomy, and friends for their contribution and help.

I also acknowledge funding agencies as; this material is based upon work supported by, or in part by, Air Force Office of Scientific Research (AFOSR) and GSU-PRE.

Last but not the least, I would like to express my profound gratitude to my beloved husband, Duleepa Pitigala, my dear parents, parents in law, and my elder sister, for their infinite support and patience throughout my endeavor.

TABLE OF CONTENTS

ACKNOWLEDGEMENTS .... **v**

LIST OF TABLES .... **xi**

LIST OF FIGURES .... **xiii**

1 CHAPTER 1: INTRODUCTION **1**

1.1 Properties of Group III-Nitride Semiconductors **2**

1.1.1 Crystal Structure ***2***

1.1.2 Polarity and Polarization ***5***

1.1.3 Crystal defects ***7***

1.1.4 Lattice Strains ***12***

1.1.5 Band Structure and Bandgap ***15***

1.1.6 Effective Mass ***19***

1.1.7 Phonon Structure ***20***

1.2 History of InN and their Alloys **23**

1.3 Scope of the Thesis **34**

1.4 References **35**

2 CHAPTER 2: THIN FILM GROWTH TECHNIQUES UTILIZED FOR GROUP III-NITRIDES **45**

2.1 Epitaxy and Growth Related Issues **45**

2.1.1 Substrates ***46***

2.1.2 Solutions for Lattice-mismatched Sapphire Substrates ***47***

2.2 Hydride Vapor Phase Epitaxy (HVPE) **48**

2.3 Molecular Beam Epitaxy (MBE) **49**

2.4 Atomic Layer Deposition (ALD) **50**

2.5 Metalorganic Chemical Vapor Deposition (MOCVD) **51**

2.6 High Pressure Metalorganic Chemical Vapor Deposition (HP-MOCVD or HPCVD) **55**

2.7 Migration Enhanced Plasma Assisted Metalorganic Chemical Vapor Deposition (MEPA-MOCVD) **58**

2.8 References **60**

3 CHAPTER 3: CHARACTERIZATION TECHNIQUES **63**

3.1 Atomic Force Microscopy (AFM) **63**

3.2 X-Ray Diffraction (XRD) **66**

3.3 Photoluminescence Spectroscopy (PL) **74**

3.3.1 Experimental setup for PL Spectroscopy ***77***

3.4 Raman Spectroscopy **79**

3.4.1 Kinematical limitation in Raman Scattering ***81***

3.4.2 Raman Scattering Selection Rules ***82***

3.4.3 Raman and IR Allowed Phonons for Hexagonal Structure ***85***

3.4.4 Experimental Setup ***89***

3.4.5 Raman Scattering Geometry ***90***

3.5 Infrared (IR) Spectroscopy **91**

3.5.1 Fourier Transform Infrared (FTIR) Spectroscopy ***92***

3.5.2 FTIR Reflection Spectroscopy Measurements ***95***

3.6 References **96**

4 **CHAPTER 4: ANALYSIS OF GROUP III-NITRIDES PROPERTIES USING MULTILAYER STACK MODELLING OF FTIR REFLECTANCE SPECTRA** **98**

4.1 **Electromagnetic Wave and Maxwell's Equations** **98**

4.2 **Electromagnetic Waves at Dielectric Interfaces** **100**

4.2.1 S- and P- Polarization *100*

4.2.2 Boundary Conditions at Interfaces *101*

4.3 **Wave propagation in Isotropic and Anisotropic media** **102**

4.3.1 Reflection and Transmission Coefficients at a Single Interface *102*

4.3.2 Modelling Reflectance and Transmittance for Isotropic three layer Structures *105*

4.3.3 Modelling Isotropic Multilayer Structures *108*

4.3.4 Modeling Surface Roughness *114*

4.4 **Reflectance of Anisotropic Multilayer Structure** **114**

4.4.1 Modelling Anisotropic Multilayer Structures *115*

4.5 **Model of Dielectric Function of Semiconductors** **116**

4.6 **Flow Chart of Fitting Program** **120**

4.7 **References** **122**

5 **CHAPTER 5: INFLEUNCE OF SUBSTRATE POLARITY AND DOPING ON THE STRUCTURAL AND OPTOELECTRONIC PROPERITIES OF InN LAYERS GROWN BY HP-MOCVD** **123**

5.1 **Introduction** **123**

5.2 **Experimental** **125**

5.2.1 Growth of InN Films *125*

5.2.1 Infrared Reflection Measurements *126*

5.2.2 Raman Measurements *127*

5.3 Results and Discussion 127

5.3.1 Analysis of IR reflectance Spectra for Sapphire *127*

5.3.1 Analysis of IR reflectance Spectra for Templates *131*

5.3.2 Analysis of IR reflectance Spectra for InN films *147*

5.3.1 AFM Analysis *162*

5.3.2 Analysis of Raman Spectra *167*

5.4 Conclusion 172

5.5 References 172

6 CHAPTER 6: EFFECT OF REACTOR PRESSURE ON THE ELECTRICAL AND STRUCTURAL PROPERTIES OF InN EPILAYERS GROWN BY HP-MOCVD 175

6.1 Introduction 175

6.2 Experimental 176

6.3 Results and Discussion 178

6.4 Conclusion 188

6.5 References 188

7 CHAPTER 7: INITIAL GROWTH AND CHARACTERIZATION RESULTS OF InN-AlN-SAPPHIRE GROWN BY MIGRATION-ENHANCED PLASMA ASSISTED MOCVD 191

7.1 Introduction 191

7.2 Experimental 192

7.3 Results and Discussion ... 193

7.4 Conclusion ... 205

7.5 References ... 205

8 CHAPTER 8: SUMMARY ... 211

APPENDICES ... 213

Appendix A ... 213

Appendix A.1 Geometry configuration and Raman active modes for wurtzite structure ... 213

Appendix A.2 The Operating Window for PL ... 213

Appendix B ... 214

Appendix B.1 MATLAB code for the simulation program ... 214

LIST OF TABLES

Table 1.1 Experimental and calculated (FT-LMTO: full potential linear muffin-tin orbital) lattice parameters for wurtzite AlN, GaN and InN materials. 4

Table 1.2 Summary of the phonon type, their motion and phase in a solids with more than one types of atoms in the unit cell. 22

Table 2.1 Lattice mismatch with different substrates. 47

Table 3.1 Various structural parameters used in defining materials. 68

Table 3.2 Available scan type on HR diffractometers. 73

Table 3.3 The x-ray techniques and the type of the sample information that can be extracted from the certain technique. 74

Table 3.4 Character table and the symmetry operation for C_{6v} point group symmetry. 85

Table 3.5 The number of phonon modes accompanied with a unit cell with N atoms in the basis. 87

Table 5.1 The best parameters (isotropic and anisotropic) of sapphire. 130

Table 5.2 Best fitted isotropic and anisotropic high frequency dielectric constant, plasma frequencies, and their damping values for AlN and GaN layers. 145

Table 5.3 Best fit isotropic and anisotropic phonon frequencies, and their broadening values for AlN and GaN layers. 145

Table 5.4 Best fit isotropic and anisotropic layer thicknesses, free carrier concentration, mobility of the carriers, and surface roughness values for AlN and GaN layers. 146

Table 5.5 Best fitted isotropic and anisotropic high frequency dielectric constant, plasma frequencies, and their damping values for InN layers. 160

Table 5.6 Best fit isotropic and anisotropic phonon frequencies, and their broadening values for InN layers. 161

Table 5.7 Best fit isotropic and anisotropic layer thicknesses, free carrier concentration, mobility of the carriers, and surface roughness values for InN layers. 162

Table 5.8 The RMS surface roughness values obtained from AFM analysis and FTR analysis (in parentheses) for templates and InN films on corresponding templates. 166

Table 5.9 Raman E_2 high and A_1LO position and their FWHM values different templates. (532 nm of excitation wavelength). 169

Table 5.10 Raman E_2 high and A_1LO position and their FWHM values for InN layers grown on different templates (532 nm of excitation wavelength). 171

Table 6.1 InN layer parameters obtained from the best fits of FTIR reflectance spectra for InN epilayers grown are various reactor pressures. 184

Table 7.1 The best fit InN layer parameters, thickness (d), high frequency dielectric constant (ε_∞), free carrier concentration, and mobility obtained from the FTIR reflectance simulation. 203

LIST OF FIGURES

Figure 1.1 The crystal structure of group III-nitrides in ball and stick representation. (a) Zincblende structure in hexagonal cell and its stacking sequence; (b) Wurtzite structure and its stacking sequence; (c) Rock salt structure. 3

Figure 1.2 Illustration of high-symmetry crystal planes of wurtzite structure for group III-nitrides........ 4

Figure 1.3 Wurtzite structure of III-nitride: (a) III-polar III-nitride and (b) N-polar III-nitride. 6

Figure 1.4 Illustration of common type of point defects. 8

Figure 1.5 Schematic representation of (a) perfect crystal (b) edge dislocation. 9

Figure 1.6 Schematic representation of (a) screw dislocation (b) mixed dislocation. 10

Figure 1.7 Schematic of the changes of crystal orientation across grain boundary. 11

Figure 1.8 Schematic representation of a twin boundary and adjacent atom arrangements. 12

Figure 1.9 A schematic of strain induced in a film due to lattice mismatch between sapphire and film: (a) compressive strain in the plane of film, when lattice constants $a_f > a_s$; (b) tensile strain in the plane of film, when $a_f < a_s$ 14

Figure 1.10 First Brillouin zones and the symmetry points of the wurtzite structure. 15

Figure 1.11 Schematic of energy band structure at Γ point for GaN. 16

Figure 1.12 Bandgaps versus lattice constant (a) for III-nitrides wurtzite and zincblende structure. 17

Figure 1.13 (a) In group III and V elements, atomic orbital energies. (b) Conduction and valance band minimum of the III-V materials relative to the E_{FS}. 18

Figure 1.14 Schematic showing the Burstein-Moss effect in InN. 19

Figure 1.15 Schematic of phonon propagation in diatomic chain. (a) Longitudinal acoustic phonon, (b) Longitudinal optical phonon, (c) Transverse acoustic phonon, and (d) Transverse optical phonon. 22

Figure 2.1 A schematic representation of the five most frequently occurring growth modes on a flat surface substrate. (a) layer-by-layer or Frank-van der Merwe (FM-mode), (b) layer plus island or Stanski-Krastanov (SK-mode), and (c) island or Volmer-Weber (VW-mode). 46

Figure 2.2 Schematic of a vertical HVPE reactor. 48

Figure 2.3 A schematic representation of PAMBE. 50

Figure 2.4 A schematic of a general ALD process. (a) Functionalized substrate surface (naturally or unnaturally). (b) Precursor A is pulsed and reacts with surface. (c) Remove the excess precursor and by-products by purging with inert carrier gas. (d) Precursor B is pulsed and reacts with surface. (e) Remove the excess precursor and by-products by purging with inert carrier gas. (f) Repeat the first-five steps until preferred thickness is reached. 51

Figure 2.5 Basic transport and reaction steps for GaN growth in MOCVD reactor 52

Figure 2.6 Thermal regimes of growth rate in MOCVD. 53

Figure 2.7 A schematic of a typical MOCVD. 54

Figure 2.8 (a) A view of upper and lower halves of the inner reactor and (b) A schematic of heating configuration of inner reactor for HP-MOCVD reactor. 56

Figure 2.9 A schematic of cross-sectional view of the HP-MOCVD reactor with the optical access ports. 57

Figure 2.10 A schematic of a MO and N* plasma precursor injection modulation in MEPA-MOCVD system 60

Figure 3.1 A schematic of a typical AFM. 64

Figure 3.2 The typical force-distance curve and different modes and regimes of the tip-surface interaction in an AFM. 66

Figure 3.3 The main macroscopic parameters that characterize a layered structure. 69

Figure 3.4 The main microscopic parameters that characterize a layered structure. 69

Figure 3.5 Schematic representation of x-ray diffraction; (a) conditions required for Bragg's diffraction to be occurred and (b) an illustration showing the relationship of the incident (k_0), diffracted (k_h), and scattering (S) vectors with respect the crystal. 70

Figure 3.6 (a) The example geometries for the HR diffraction and (b) Sample reference frame with axes of rotation. 71

Figure 3.7 Possible recombination process in a semiconductor in real space. 76

Figure 3.8 Designed experimental setup for PL measurements by the author. 77

Figure 3.9 Jablonski diagram for Rayleigh and Raman (Stokes and anti-Stokes) scattering. 80

Figure 3.10 Optical phonon modes of wurtzite structure. In our case, the blue (big) and yellow (small) sphere represent the group III and nitride atoms, respectively. 89

Figure 3.11 Designed experiment setup for the Raman measurements by the author. 90

Figure 3.12 A schematic of the basic component of an FTIR spectrometer. 93

Figure 3.13 (a) Schematic of simplest form of the Michelson interferometer. At x=0, path difference between two beams is zero. (b) The source and interferogram I(x) plot is given. 94

Figure 3.14 Reflection at (a) near-normal incidence and (b) grazing angle incidence. 95

Figure 4.1 An electromagnetic wave incident on an interface between two dielectric media. 100

Figure 4.2 Schematic representation showing the transmission and reflection of an electromagnetic wave at interface. (a) s-polarization and (b) p-polarization. 102

Figure 4.3 Schematic showing the partial waves of a single film on substrate. 106

Figure 4.4 Schematic showing a multilayer stack (ambient/film_1 to film_k/substrate) and their reflection contributions. 109

Figure 4.5 Schematic for illustration of mth layer showing the e-field components. 109

Figure 4.6 Flow chart of analysis reflectance spectra based on the Multilayer stack model and model of IR dielectric function. 121

Figure 4.7 Showing the layer configuration of InN on GaN/Sapphire. 121

Figure 5.1 Schematic showing the temperature and precursor profiles of the InN growth. 126

Figure 5.2 Experimental (solid) and the best fitted (dash) reflectance spectra for sapphire. (a) at near normal incidence, (b) for oblique incidence of 25° (un-polarized light), (c) S-polarized at 25° incidence, and (d) P-polarized at 25° incidence. 129

Figure 5.3 The real (a) and imaginary (b) dielectric function of sapphire at normal incidence (solid), at 25° incidence angle E-field perpendicular to the c-axis (dash), and at 25° incidence angle E-filed parallel to the c-axis (short-dash). 131

Figure 5.4 (a) Experimental spectra for AlN/Sapphire at near normal (solid) and 25° unpolarized incidence light (dash), (b) experimental spectra for sapphire (solid) and AlN/Sapphire at 25° unpolarized incidence, (c) and (d) experimental and best fitted spectra of sapphire at normal (solid) and 25° unpolarized incidence for AlN/Sapphire. 133

Figure 5.5 The real (a) and imaginary (b) dielectric function of AlN/sapphire at normal incidence (solid), at 25° incidence angle E filed perpendicular to the c-axis (dash), and at 25° incidence angle E filed parallel to the c-axis (short dashed). 134

Figure 5.6 (a) Experimental spectra at normal incidence (solid), at 25° incidence for unpolarized (dash-dot), P-polarized (dash), and S-polarized (short-dash) light, (b) and (c) experimental and best fitted spectra at normal and 25°-unpolarized incidence light, respectively, and (d) experimental and best fitted spectra for 25°unpolarized incidence light, showing range of 300-6500 cm^{-1}, for Ga-polar GaN/AlN/Sapphire. 135

Figure 5.7 Experimental reflectance spectra for Sapphire, AlN/Sapphire, and Ga-polar GaN/AlN/Sapphire. 136

Figure 5.8 The real (a) and imaginary (b) dielectric function of Ga polar GaN/AlN/sapphire at normal incidence (solid), at 25° incidence angle E filed perpendicular to the c-axis (dash), and at 25° incidence angle E filed parallel to the c-axis (dash-dotted). 137

Figure 5.9 (a) Experimental spectra at normal incidence (solid), at 25° incidence for unpolarized, P-polarized, and S-polarized (dash), (b) and (c) experimental and best fitted spectra at normal and

25°-unpolarized incidence light, respectively, and (d) experimental and best fitted spectra with surface roughness for 25° unpolarized incidence light for N-polar GaN/Sapphire. 139

Figure 5.10 Model layer structures used in N-polar GaN/sapphire simulation. 139

Figure 5.11 Experimental and best fitted spectra obtained using (a) three layer, (b) four layer, and (c) five layer models for N polar GaN/sapphire template. 140

Figure 5.12 The real (a) and imaginary (b) dielectric function of N polar GaN layers (L1 and L2) at normal incidence, at 25° incidence angle E filed perpendicular to the c-axis, and at 25° incidence angle E filed parallel to the c-axis... 140

Figure 5.13 (a) Experimental spectra at normal incidence (solid), at 25° incidence for unpolarized, P-polarized, and S-polarized (dash), (b) and (c) experimental and best fitted spectra at normal and 25°-unpolarized incidence light, respectively, and (d) experimental and best fitted spectra with surface roughness for 25° unpolarized incidence light for n-GaN/i-GaN/AlN/Sapphire. 141

Figure 5.14 The real (a) and imaginary (b) dielectric function of n-GaN layers (L1 and L2) at normal incidence, at 25° incidence angle E filed perpendicular to the c-axis, and at 25° incidence angle E filed parallel to the c-axis.. 142

Figure 5.15 (a) Experimental spectra at normal incidence (solid), at 25° incidence for unpolarized, P-polarized, and S-polarized (dash), (b) and (c) experimental and best fitted spectra at normal and 25°-unpolarized incidence light, respectively, and (d) experimental and best fitted spectra with surface roughness for 25° unpolarized incidence light for p-GaN/i-GaN/AlN/Sapphire. 143

Figure 5.16 The real (a) and imaginary (b) dielectric function of p-GaN layers (L1 and L2) at normal incidence, at 25° incidence angle E filed perpendicular to the c-axis, and at 25° incidence angle E filed parallel to the c-axis.. 144

Figure 5.17 Experimental spectra at normal incidence, at 25° incidence for unpolarized, P-polarized, and S-polarized, (b) and (c) experimental (solid) and best fitted (dash) spectra at normal and 25°-unpolarized incidence light, respectively, and (d) experimental and best fitted spectra with surface roughness for 25° unpolarized incidence light for InN/Sapphire.. 148

Figure 5.18 The real (a) and imaginary (b) dielectric function of InN layers (L1 and L2) grown on sapphire at normal incidence, at 25° incidence angle E filed perpendicular to the c-axis, and at 25° incidence angle E filed parallel to the c-axis. 149

Figure 5.19 Experimental spectra at normal incidence (solid), at 25° (unpolarized) incidence (dash), (b) and (c) experimental (solid) and best fitted (dash) spectra at normal and 25°-unpolarized incidence light, respectively, and (d) experimental and best fitted spectra with surface roughness for 25° unpolarized incidence light for InN/AlN/Sapphire. 150

Figure 5.20 The real (a) and imaginary (b) dielectric function of InN layers (L1, L2 and L3) grown on AlN/sapphire at normal incidence, at 25° incidence angle E filed perpendicular to the c-axis, and at 25° incidence angle E filed parallel to the c-axis. 151

Figure 5.21 Experimental spectra at normal incidence (solid), at 25° (unpolarized) incidence (dash), (b) and (c) experimental (solid) and best fitted (dash) spectra at normal and 25°-unpolarized incidence light, respectively, and (d) experimental and best fitted spectra for 25° unpolarized incidence light, in the range of 300-2500 cm^{-1} for InN/Ga polar GaN/AlN/Sapphire. 152

Figure 5.22 The real (a) and imaginary (b) dielectric function of InN layers (L1, L2 and L3) grown on Ga polar GaN/AlN/sapphire at normal incidence, at 25° incidence angle E filed perpendicular to the c-axis, and at 25° incidence angle E filed parallel to the c-axis. 153

Figure 5.23 Experimental spectra at normal incidence (solid), at 25° (unpolarized) incidence (dash), (b) and (c) experimental (solid) and best fitted (dash) spectra at normal and 25°-unpolarized incidence light, respectively, and (d) experimental and best fitted spectra with surface roughness for 25° unpolarized incidence light for InN/N polar GaN/Sapphire. 154

Figure 5.24 The real (a) and imaginary (b) dielectric function of InN layers (L1 and L2) grown on N polar GaN/sapphire at normal incidence, at 25° incidence angle E filed perpendicular to the c-axis, and at 25° incidence angle E filed parallel to the c-axis. 155

Figure 5.25 Experimental spectra at normal incidence (solid), at 25° (unpolarized) incidence (dash), (b) and (c) experimental (solid) and best fitted (dash) spectra at normal and 25°-unpolarized

incidence light, respectively, and (d) experimental and best fitted spectra with surface roughness for 25° unpolarized incidence light for InN/n-GaN/AlN/Sapphire. 156

Figure 5.26 The real (a) and imaginary (b) dielectric function of InN layers (L1, L2 and L3) grown on n-GaN/AlN/sapphire at normal incidence, at 25° incidence angle E filed perpendicular to the c-axis, and at 25° incidence angle E filed parallel to the c-axis. 157

Figure 5.27 Experimental spectra at normal incidence (solid), at 25° (unpolarized) incidence (dash), (b) and (c) experimental (solid) and best fitted (dash) spectra at normal and 25°-unpolarized incidence light, respectively, and (d) experimental and best fitted spectra with surface roughness for 25° unpolarized incidence light for InN/p-GaN/AlN/Sapphire. 158

Figure 5.28 The real (a) and imaginary (b) dielectric function of InN layers (L1 and L2) grown on p-GaN/AlN/sapphire at normal incidence, at 25° incidence angle E filed perpendicular to the c-axis, and at 25° incidence angle E filed parallel to the c-axis. 159

Figure 5.29 2D-AFM and 3D-AFM surface images with the profile of change in the height along distance, and corresponding s-SNOM images for (a) sapphire and (b) InN/sapphire. 163

Figure 5.30 2D-AFM and 3D-AFM surface images with the profile of change in the height along distance, and corresponding s-SNOM images for (a) Ga polar GaN template and (b) InN on Ga polar GaN. 164

Figure 5.31 2D-AFM and 3D-AFM surface images with the profile of change in the height along distance, and corresponding s-SNOM images for (a) N polar GaN template and (b) InN on N polar GaN. 164

Figure 5.32 2D-AFM and 3D-AFM surface images with the profile of change in the height along distance, and corresponding s-SNOM images for (a) n-GaN template and (b) InN on n-GaN. .. 165

Figure 5.33 2D-AFM and 3D-AFM surface images with the profile of change in the height along distance, and corresponding s-SNOM images for (a) p-GaN template and (b) InN on p-GaN. .. 165

Figure 5.34 Raman spectra of sapphire (a), AlN/sapphire (b), Ga-polar GaN/AlN/sapphire (c), N-polar-GaN/sapphire (d), n-type GaN/i-GaN/AlN/sapphire (e), p-type GaN/i-GaN/AlN/sapphire (f). . 168

Figure 5.35 Raman spectra of InN films grown on sapphire (a), AlN/sapphire (b), Ga-polar GaN/AlN/sapphire (c), N-polar-GaN/sapphire (d), n-type GaN/AlN/sapphire (e), p-type GaN/AlN/sapphire (f). 170

Figure 6.1 Schematic illustration of the temperature precursor profiles for the growth process. 177

Figure 6.2 Schematic illustration for precursor pulse timing. 177

Figure 6.3 XRD FWHM (2θ –ω) scan in triple crystal geometry) of InN peak ((0002) Bragg reflex at about 31.33°) as function of the reactor pressure 179

Figure 6.4 XRD FWHM (2θ-ω scan in triple crystal geometry) values of off-axis InN (2-102) of the InN epilayers as a function of reactor pressure. 180

Figure 6.5 The FWHM of the Raman E_2 (high) of the InN epilayers grown on GaN templates vs. reactor pressure. 180

Figure 6.6 Experimental (solid line) and best fit (dotted line) IR reflectance spectra for an InN /GaN/ Sapphire film grown at 800°C and 10 bar reactor pressure. 181

Figure 6.7 Dependence of free carrier concentration of InN- bulk layer on the reactor pressure. 185

Figure 6.8 Dependence of free carrier concentration of InN- nucleation layer on the reactor pressure. 185

Figure 6.9 Mobility of the carriers of the InN bulk layer as function of reactor pressure. 187

Figure 6.10 Growth rate as a function of reactor pressure. 188

Figure 7.1 2D-AFM surface topography (scale bar = 200 nm) of sapphire (a) and AlN buffer layers grown with 4 s (b), 8 s (c), and 12 s (d) plasma exposure per pulse 194

Figure 7.2 2D-AFM surface topography (scale bar = 200 nm) within a 0.5×0.5 μm^2 scan area and corresponding profile of change in the height along distance for AlN-NL grown at (a) 300 W, (b) 400 W, and (c) 500 W plasma power 195

Figure 7.3 2D-AFM surface topography (scale bar = 200 nm) of (a) as- grown AlN-NL and annealing temperature of AlN -NL layers at (b) 800 °C, (c) 825 °C, (d) 850 °C and (e) 875 °C. 196

Figure 7.4 RMS surface roughness vs annealing temperature 197

Figure 7.5 Raman spectra for the AlN buffer grown on sapphire by varying post-annealing temperature, (long-dashed)) 800 °C, (dotted) 825 °C, (dashed-long dashed) 850 °C, (dashed) 875 °C, and (solid) sapphire. 198

Figure 7.6 (a) 2D-AFM surface image (scale bar = 200 nm) with the corresponding profile of change in the height along position, (b) 3D-AFM surface topography for the InN/sapphire 199

Figure 7.7 2D-AFM surface image (scale bar = 200 nm) with the profile of change in the height along distance, and (b) 3D-AFM surface topography for the InN/AlN/sapphire 199

Figure 7.8 (a) 2D-AFM surface image (scale bar = 200 nm) with the profile of change in the height along distance, and (b) 3D-AFM surface topography for the InN/AlN-annealed at 850 °C/sapphire... 200

Figure 7.9 The Raman spectra for the InN/sapphire (solid), InN/AlN/sapphire (dashed), and InN grown on AlN annealed at 850°C /sapphire (dotted-dashed), and sapphire (dotted). 201

Figure 7.10 The experimental reflectance spectra for InN/sapphire (dotted line), InN/AlN/sapphire (solid line), and InN/AlN annealed at 850 °C/sapphire (dashed line) 202

Figure 7.11 Experimental (solid line) and best fit (dashed line) IR reflectance spectra for InN/AlN/sapphire. 203

1 CHAPTER 1: INTRODUCTION

In the last few decades, the group III-nitride semiconductor materials have been shown remarkable progress in the development and design of optical and electronic devices, such as photovoltaic cells, light emitting diodes (LED), laser diodes, detectors, high electron mobility transistors, piezoelectric filters, fiber optical devices, biosensors, gas sensors, due to their properties such as high thermal and chemical stability, large break-down voltage, polarization, piezoelectricity. As comparing with the other group III- nitride materials (AlN and GaN), InN owes a higher peak-drift velocity, higher peak overshoot velocity, a narrow band gap, which leads to a smaller electron effective mass and higher electron mobility. Due to these properties, InN is an auspicious material in developing electronic and optoelectronic devices. However, much less effort has been devoted to the growth of InN and indium-rich InGaN in the scientific community until discovering the new band gap value 0.7 eV [1, 2] of wurtzite InN, compared to the long time established value of 1.9 eV [3]. However, the growth of high quality InN is a challenge, due to the lattice and thermal coefficients mismatch between the substrate and sample, and the high partial pressure of nitrogen at optimum growth temperatures above the growth surface. Therefore, under the growth temperature which is required for the decomposition of ammonia which is one of the main nitrogen source used in chemical vapor deposition, decomposition of InN occurs.

At present, low indium-content $In_{1-x}Ga_xN$ ($x \leq 0.25$) based LEDs are commercially available in traffic displays, automobile headlights, general lighting, etc., but the fabrication of indium-rich InGaN layer is still a challenge due to phase segregations, control of surface chemistry, vastly different partial pressures, and the differences in growth temperatures between their binaries, which requires the adjustment of the growth conditions for each composition between the binaries InN and GaN. The different surface chemistry in the incorporation of the group III metals is often observed as In-/Ga-rich lateral surface segregations and/or metallic indium on the growth surface.

This chapter provides an overview of the group III- nitride semiconductors properties. The wurtzite structure and properties of these materials are described, including polarity and polarization, crystal

defects, lattice strains, band structure and band gap, effective mass, and phonon structure. The latter section present a brief history of InN research and development. The scope of this research work and thesis layout are presented at the end of the chapter.

1.1 Properties of Group III-Nitride Semiconductors

1.1.1 Crystal Structure

Group III-nitride (AlN, GaN, InN) crystalline structures can be formed wurtzite (hexagonal/ α-phase) which is thermodynamically stable under ambient conditions, zincblende (cubic/β -phase) which is only metastable, and rock salt structure which forms phase transition from the wurtzite structure at hydrostatic pressure of 16.6 GPa (AlN), 51.8 GPa (GaN), and 21.6 GPa (InN) [4, 5], and each structure has different properties. Wurtzite structure is associated with space group P63mc in the Hermann-Mauguin notation (C_{6v}^4 in the Schoenflies notation). The space grouping for the zincblende and rock salt structures are $F\bar{4}3m$ (T_d^2) and Fm3m (O_h^5) respectively [4, 6]. The wurtzite and the cubic structures are the stable forms, and in the both case, each group III atom is bound by four N atoms and vice versa. The difference between the wurtzite and zincblende structure is the stacking sequence of the close-packed diatomic plane. The wurtzite structure consists of ABAB stacking sequence of (001) close-packed plane. The zincblende structure belongs to ABCABC stacking sequence of (111) close-packed plane. Here, A, B, and C, are Al/Ga/In-N bonds. The wurtzite, zincblende, and rock salt structure of group III-nitride are shown in Fig. 1.1 (a), (b), and (c).

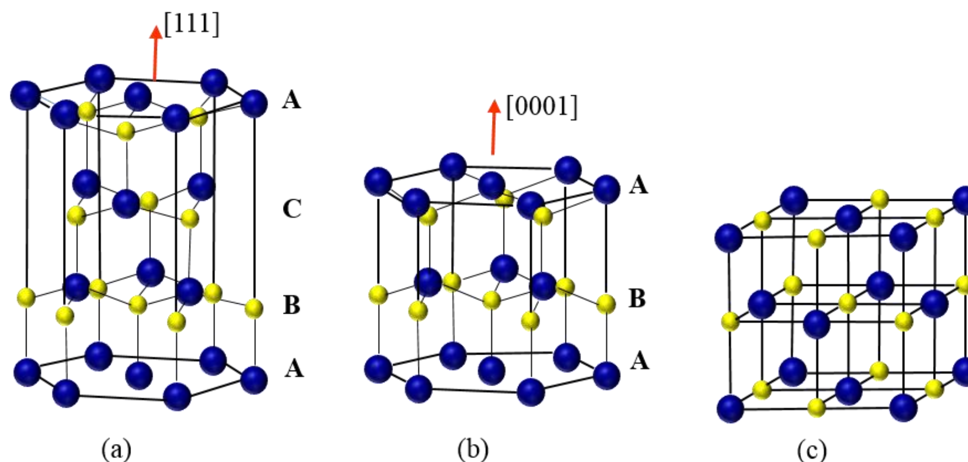

Figure 1.1 The crystal structure of group III-nitrides in ball and stick representation. (a) Zincblende structure in hexagonal cell and its stacking sequence; (b) Wurtzite structure and its stacking sequence; (c) Rock salt structure.
The figure is after Ref. [7].

This study focuses the wurtzite structure of AlN, GaN, InN, and their alloys. Wurtzite structure has two interpenetrating hexagonal close-packed lattices shifted along the [0001] direction (c-axis). The crystal axes and the crystal planes of wurtzite structure are shown in Fig. 1.2. The lattice parameter (lattice constant) 'a' is the edge length of the basal hexagon along a-axis, and 'c' is the height of the hexagonal prism along c-axis as shown in Fig. 1.2. Group III-nitrides have different lattice parameters due to different cations and ionic radii [8]. Structural properties of the material can be predicted by the lattice parameters since the lattice parameters will be different or deviated from their intrinsic values due to impurities, inhomogeneity, residual strain (for example, induced by the substrate) and stress, dislocations etc.. As an example, Table 1.1 presents the comparison of the measured and the calculated lattice parameter values for the wurtzite AlN, GaN, and InN structures.

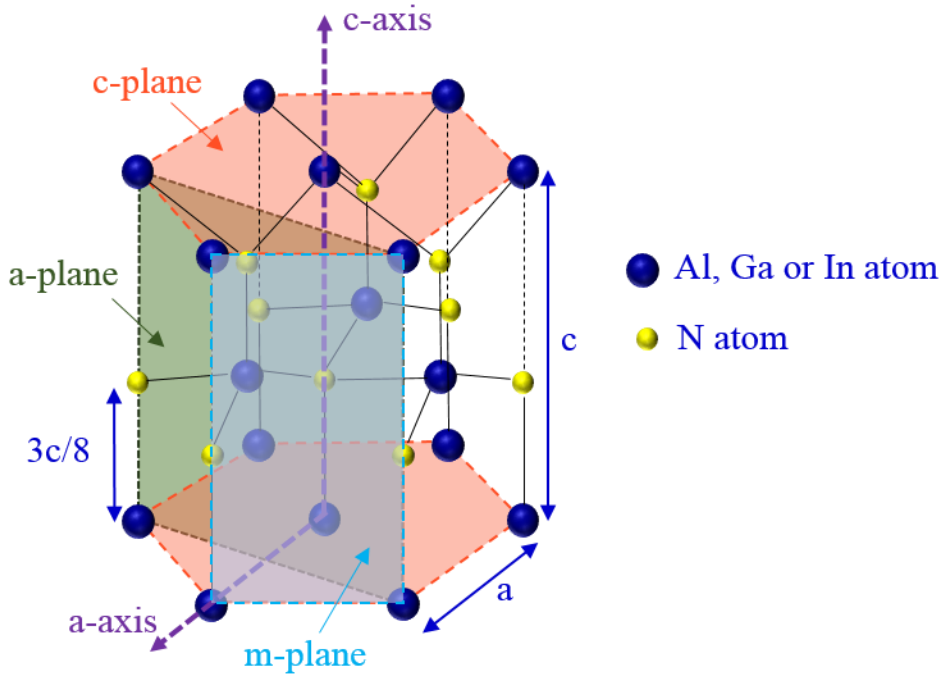

Figure 1.2 Illustration of high-symmetry crystal planes of wurtzite structure for group III-nitrides. The figure is after Ref. [9].

Table 1.1 Experimental and calculated (FT-LMTO: full potential linear muffin-tin orbital) lattice parameters for wurtzite AlN, GaN and InN materials.
Data is taken from Ref. [10-14].

	AlN		GaN		InN	
	Cal.	Exp.	Cal.	Exp.	Cal.	Exp.
a (Å)	3.084	3.110	3.17	3.1892	3.53	3.538
c (Å)	4.948	4.980	5.13	5.1850	5.54	5.703

The lattice parameters ‘a’ and ‘c’ of $In_xGa_{1-x}N$ can be determined from Vegard’s law given in Eq. (1.1) and (1.2) for known indium composition (x) and lattice parameters of InN and GaN.

$$c(In_xGa_{1-x}N) = x.c(InN) + (1-x).c(GaN) \quad 1.1$$

$$a(In_xGa_{1-x}N) = x.a(InN) + (1-x).a(GaN) \quad 1.2$$

The composition values $In_xGa_{1-x}N$ can be determined by Rutherford backscattering spectrometry (RBS), sputtered ion mass spectroscopy (SIMS), and electron probe microanalysis (EPMA). The most common method used in obtaining lattice parameter is X-ray diffraction measurements. From the lattice parameter, information on the residual strain and stress, doping levels, composition, and thermal expansion coefficients of the layers can be obtained [10]. Apart from lattice parameter X-ray diffraction provides information about other structural properties such as defect type and densities, crystallite size and microstrain, wafer bowing, residual stress, alloy ordering, phase separation, composition, and non-uniformities.

1.1.2 Polarity and Polarization

Wurtzite crystal structure of group III-nitrides has a non-centrosymmetric structure which is the lack of inversion symmetry. The most general growth direction of III-nitrides is along the c-axis (the polar axis), normal to the basal plane. On this plane, atoms placed in bilayers which consist of two closely spaced hexagonal close-packed layers. One has the cations, and the other has the anions. The polarity orientation is determined by these bilayers, and it is said that the film has III-polarity (+c III-nitride), if the basal surface is III-faced or the III-N bond orientation is along the c-direction from III atom to nitrogen atoms. The film has N-polarity (-c III-nitride), if the basal surface is N-faced or the III-N bond orientation along c-direction from nitrogen atom to III atom. One should not confuse here the III-faced (or N-faced) with the III-termination (or N-termination). The termination refers to the surface property. If the III-faced surface is covered with N-atoms, it can be N-terminated. However, it is to be N-faced, the crystal should be flipped [8]. Figure 1.3 presents the two polarity orientations of III-nitrides. The polarity of the film depends on the growth modes.

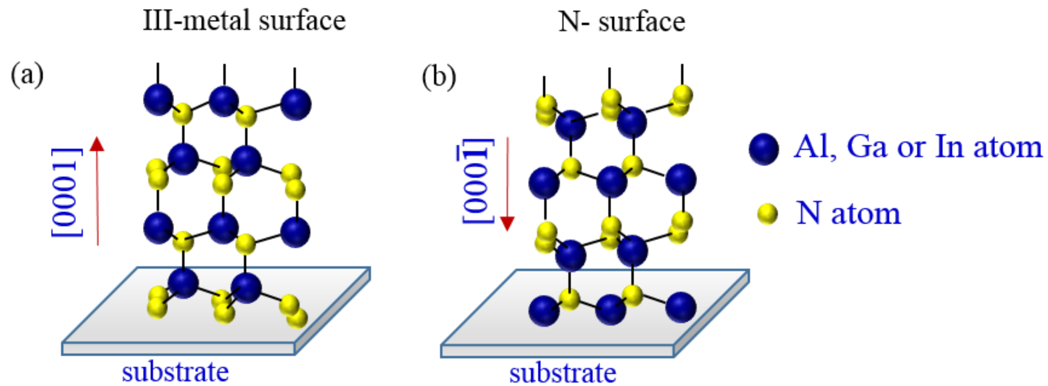

Figure 1.3 Wurtzite structure of III-nitride: (a) III-polar III-nitride and (b) N-polar III-nitride. The figure is after Ref. [15].

As mentioned before, typically, the wurtzite structure of group III-nitride materials are grown in [0001] direction. In the strained materials, there exist a piezoelectric polarization field associated with electrostatic charge densities [16]. The direction of the piezoelectric polarization (P_{PZ}) depends on the polarity of the materials [8]. Mechanical stress also results in piezoelectric polarization. Therefore, it also depends on the compressive and tensile strain. In general, P_{PZ} is negative for tensile stress and positive for compressive stress. In addition to piezoelectric polarization, group III-nitride materials also possess a large spontaneous polarization (P_{SP}). The crystalline cell size in the epitaxial films can differ from the ideal crystalline size and which causes the positive and negative charges of the centers to locate at different places, the cell itself is creating an electric dipole [17]. The phenomenon is called spontaneous polarization (which is independent of strain), and it is along c-axis and depends on the polarity of the materials, lattice constants a, c, c/a ratio and the internal parameter u [16, 18]. The spontaneous polarization has a negative sign, and it increases from GaN over InN to AlN [19] due to the increasing nonideality of the crystal structure. The piezoelectric polarization also increases with the strain in the same order under the same strain. When defining the orientation of the both polarization, it is assumed that positive direction is the direction from the metal to the nearest nitrogen atom on the c-axis. Thus, in general, if the strain is tensile, the orientation of the both polarizations is parallel, and it is antiparallel in the case compressive strain. In a particular case of both polarization in the same direction, the total polarization (P) is $P = P_{SP} +$

P_{PZ} [20]. Spontaneous and piezoelectric polarization can influence the optical and electrical properties of the group III-nitride layers.

1.1.3 Crystal defects

Optical, electrical, and structural properties of a semiconductor can be categorized as intrinsic properties that depend on the perfect crystalline nature of it, and extrinsic properties that depend on the impurities or defects. If the atomic arrangement of a crystal structure has deviated from its perfect arrangement (periodic arrangement), it is said that the crystal contains imperfections or defects. Defects are formed during the growth, and they can be classified as (1) point defects (zero-dimensional defects), (2) line defects (one-dimensional defects), (3) planar defects (two-dimensional defects), and (4) volume defects (three-dimensional defects).

(1) Point defects can be distinguished as intrinsic defects, which come from the crystal itself, and extrinsic defects, which caused by foreign atoms (impurity or solute). Interstitials, vacancies, and substitutional atoms are the main three types of point defects, and there are few other types as well. Vacancies and self-interstitial, and antisite fall into the category of intrinsic defects, while interstitial impurity and substitutional impurity fall into extrinsic defects.

When an atom is missing the place where it should be, it creates an empty place, and it is called a vacancy. Migration of atoms in the crystal lattice (solid state diffusion) can only occur because of vacancies. As temperature increases, the number of vacancies increases as follows,

$$N_v = N_A \exp(-\frac{Q_v}{kT}) \qquad 1.3$$

Where N_A, Q_v, k, and T are the total number of atoms in the solid, the energy required to form a vacancy, Boltzmann constant, and the temperature in Kelvin, respectively [21, 22].

If an extra atom is positioned between the atomic sites (interstitial sites, a small void space), a self-interstitial is formed. To develop the self-interstitial defects in a crystal, it must have enough space between the host atoms. When a foreign atom occupies a site between regular atoms, instead of a regular crystal site, it is an interstitial impurity defect. The impurity atom must have enough low energy to stay at

the interstitial site. If one atom in the crystal is replaced by a different atom, a substitutional defect is occurred. If a foreign atom occupies a crystal sites, it is called substitutional impurity. Substitutional impurity can be produced in the crystal intentionally by doping which is used to control the type (n- or p-type) of the semiconductor, or it can be presented in the crystal unintentionally as contaminants. Sometimes, the substitution can occur in a crystal itself, and it does not need a foreign atom. In binary systems (group III-nitride semiconductors), the first atom can occupy a regular site of the second atom and the second atom can occupy in the first site [23]. This kind of defects does not fall into either a vacancy, impurity, or an interstitial and it is called an antisite defect. Furthermore, the lattice is under tension when the substitutional atom is smaller than the original atom; it is in compression when the substitutional atom is larger than the original atom. Figure 1.4 illustrates the common three type of point defects.

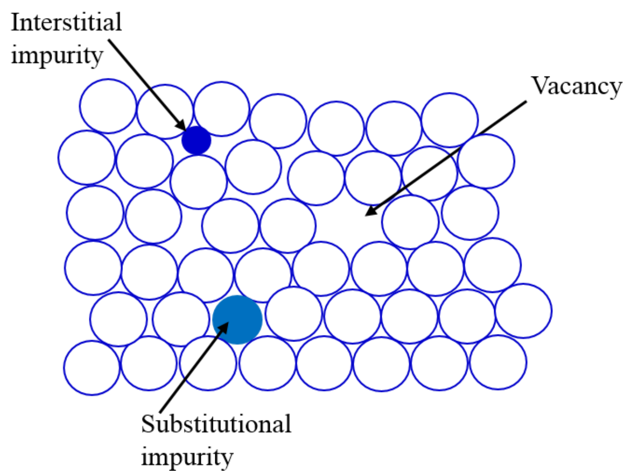

Figure 1.4 Illustration of common type of point defects.
The figure is after Ref. [23].

(2) Line defects or dislocations are sudden changes in the regular ordering of atoms (generally, due to misalignment of atoms or existence of vacancies) along a line (dislocation line). There are three main types of dislocations, known as edge dislocations, screw dislocations, and mixed dislocations which include of both the edge and the screw dislocations.

Dislocations are characterized by the Burgers vector, **b**. The Burgers vector defines the magnitude and direction of the lattice distortion, and it is measured as a distance along the close loop directions in the lattice [24].

Edge dislocations take place when an extra plane of atoms inserted into a part of the crystal lattice which results in one part of the lattice to contain extra atoms while the other part is containing the correct number of atoms. Due to this, the lattice part with the extra atoms may be under compressive stresses, while the other part may be under tensile stresses [23]. The Burgers vector, b is perpendicular to the dislocation line which is at the end of the plane, in the edge dislocation (see Figure 1.5 (a) and (b)).

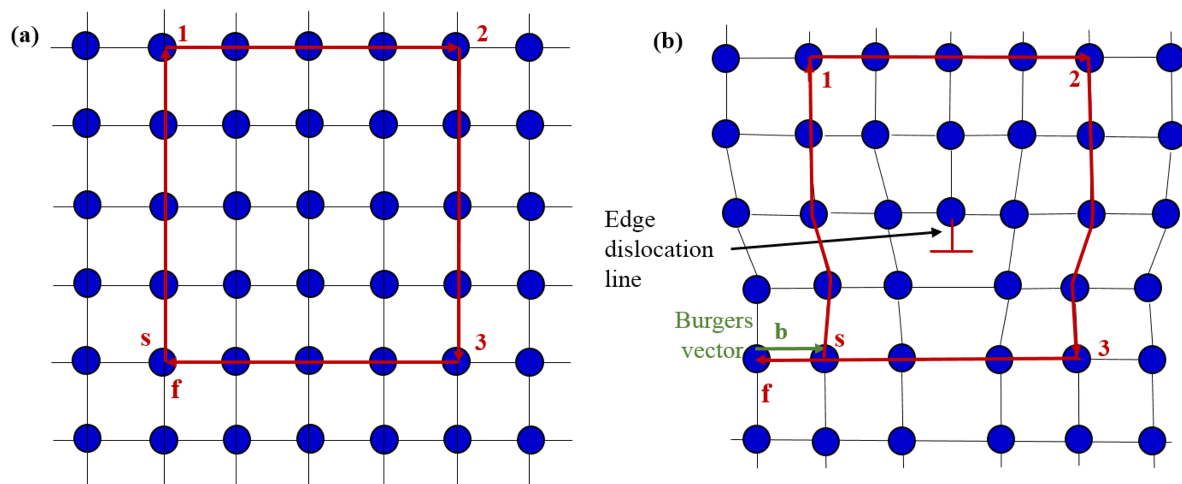

Figure 1.5 Schematic representation of (a) perfect crystal (b) edge dislocation.

The second type of dislocation is screw dislocation which results when planes are displaced relative to each other through shear stress, and the Burger vector is parallel to the dislocation line. Visualization of the screw dislocation in a crystal is difficult. As shown in Fig. 1.6 (a), due to the shear stress, the right region of the crystal is shifted/slipped one atomic distance to the down relative about the left region.

In real crystals, most dislocations are neither purely edge nor purely screw, and they usually exhibit a combination of the two and named as mixed dislocations. Figure 1.6 (b) illustrate the schematic representation of mixed dislocations in a crystal. The Burgers vector is nor perpendicular or parallel to the

dislocation line, in this case, however, there a fixed orientation in space. The dislocations in crystals can be observed using transmission electron microscopy, field ion microscopy or using atom probe techniques.

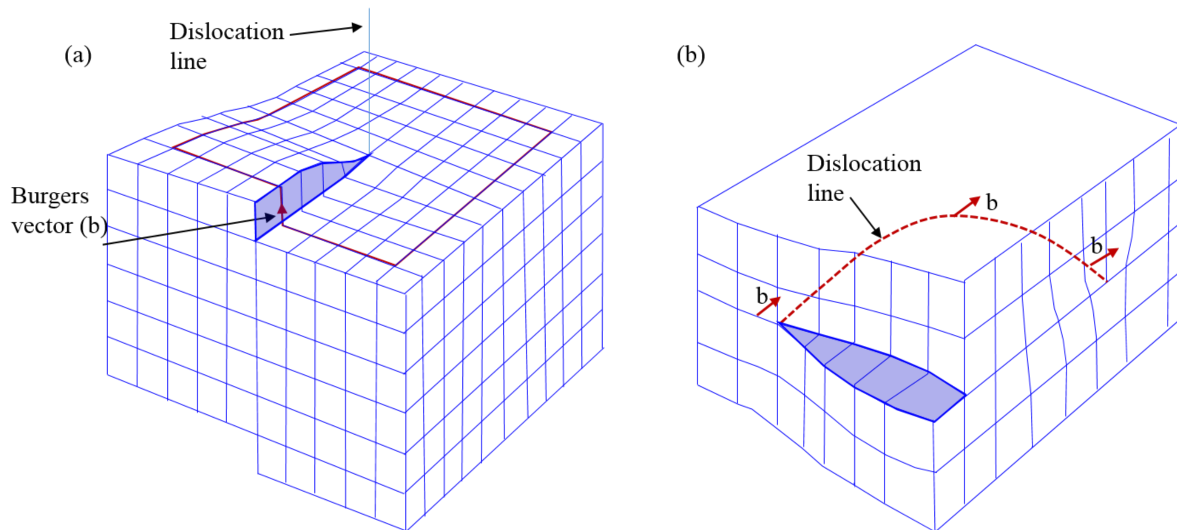

Figure 1.6 Schematic representation of (a) screw dislocation (b) mixed dislocation.
The figure is after Ref. [25].

(3) Planar defects are the discontinuity of the ideal crystal structure across a 2D plane. The stacking fault, grain boundaries, and twin boundaries are planar defects. Change or interruption the regular sequence in the stacking of lattice planes, over a few atomic spacing produces a stacking fault. As an example, in the hcp structure, the regular stacking sequence is ABABABAB, and this can arrange itself as ABABABCABAB, which produces a stacking fault in the crystal.

Polycrystalline materials consist of many small crystals or grains which have different crystallographic orientation. The region, where exist atomic mismatch in a transition from the crystalline orientation of one grain to the adjacent one, is called grain boundary and which is probably a few atomic diameter wide. If the crystallographic misalignment of atomic planes between the adjacent grains is on order of a few degrees, it is called low-angle grain boundary, and if the misorientation angle is larger than 15°, it is

called high-angle grain boundary. The changes of the orientation of the crystal across the grain boundaries are shown in Fig. 1.7.

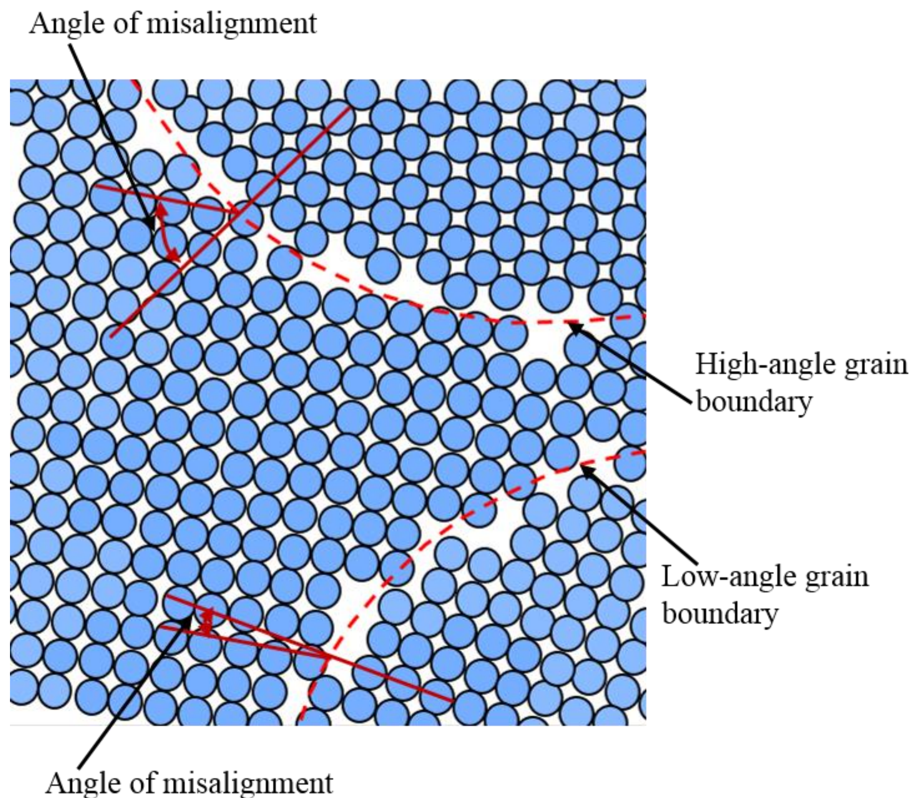

Figure 1.7 Schematic of the changes of crystal orientation across grain boundary.
The figure is after Ref. [26].

The low-angle boundaries can be described in terms of the orientation of their dislocation arrays. One of the simple forms is referred as tilt boundary which is explained by an array of edge dislocations when misorientation angle is perpendicular to the grain boundary. The other type is called twist boundary which can be described by an array of screw dislocations that are parallel to the misorientation angle. Grain boundaries are more reactive than grains themselves, and impurities tend to segregate along the boundaries due to their higher energy state. Since the total interfacial energy is greater in fine-grained materials than large-grained materials, the grains tend to grow larger grains in order to minimize the energy [26]. This phenomenon occurs at high temperatures by diffusion. The cooling rate can control grains size,

and rapid and slow cooling rate produce smaller and larger grains in the materials, respectively. Smaller grain size will increase the strength of the materials.

Twin boundary separates two crystalline regions that have a mirror image of one side on the other side. Twin boundary is formed by annealing and mechanical deformation. Figure 1.8 shows a schematic representation of twin boundary and the adjacent atom arrangements.

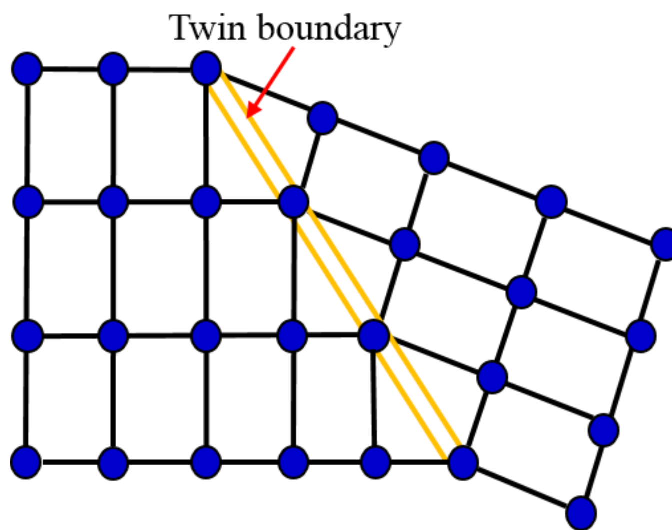

Figure 1.8 Schematic representation of a twin boundary and adjacent atom arrangements.
The figure is after Ref. [26].

(4) Volume defects or bulk defects: If any three-dimensional regions in the semiconductor are altered from the rest of the crystal (which can be in structure, orientation, composition, etc.), they are called volume defects [27]. They include pores, voids/cracks, clusters/precipitation, foreign inclusions, and other phases. Volume defects form during the semiconductor processing and fabrication steps and they can affect the mechanical, thermal, electrical, and optical properties of the semiconductor.

1.1.4 Lattice Strains

Typically, III-nitride semiconductors are grown on different materials (substrates), which is called heteroepitaxy. Thus, in group III- nitride semiconductors, strains are formed due to lattice mis-

match and thermal mismatch between the epitaxial film and the substrate. These strains cause crystal defects. When the epitaxial layer is sufficiently small, the deposited first atomic layers will be strained, and consequently, the interface will be coherent [28]. If the stored strain energy in the epilayer exceeds a certain threshold, the system relaxes and the strain support to misfit dislocations [28, 29]. The strain caused by the mismatch of lattice or thermal is known as biaxial strain.

When the sample is cooled down to room temperature after growth, the thermal expansion coefficients mismatch between the substrate and the film may cause residual internal strain to form (A degree of strain depend on the cool down procedure) [23].

The type of strain in the film due to lattice mismatch will depend on the lattice constants of film and substrate. The film is in compressive strain when the lattice constant of the film is greater than the lattice constant of the substrate, and the film is in tensile strain when the film lattice constant is less than the substrate one. Lattice mismatch or strain (ε) of the film can be given by following Eq. 1.4 [30].

$$\varepsilon = \frac{a_f - a_s}{a_s} \qquad 1.4$$

Where, a_f and a_s are unstrained lattice constants of the film and the substrate, respectively. A schematic of strain induced in a film is shown in Fig. 1.9. Here, the substrate also experiences in strain, and it is negligible due to the larger thickness of substrate compare to that of the film.

The presence of the strain in the film cause to change the physical properties of the film. As an example, strain in the film during the growth will change the Ga- ad-atoms mobility of the surface, which influence on the surface morphology [23]. Additionally, due to strain, the lattice constant of the crystal will increase (tensile strain) or decrease (compressive strain) relative about its unstrained value. Moreover, the strain field will change the interatomic distance, and consequently, the band gap energy of the material will be altered. Phonon frequencies of the crystal will also upshift (compressive strain) or downshift (tensile strain) due to strain [23].

X-ray diffraction (XRD), Raman spectroscopy, high-resolution transmission electron microscopy can be used for strain measurements [30].

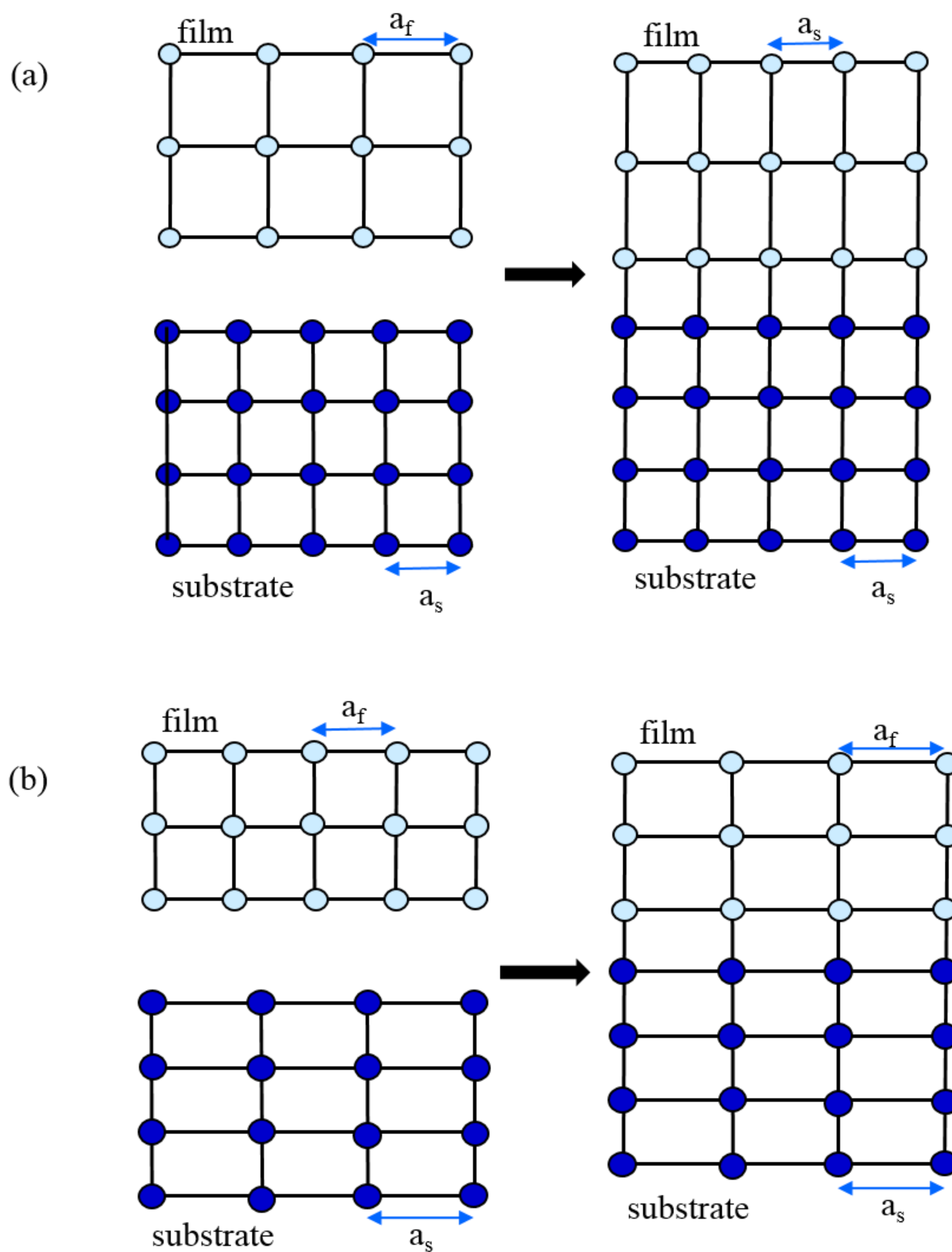

Figure 1.9 A schematic of strain induced in a film due to lattice mismatch between sapphire and film: (a) compressive strain in the plane of film, when lattice constants $a_f > a_s$; (b) tensile strain in the plane of film, when $a_f < a_s$.
The figure is after Ref. [23].

1.1.5 Band Structure and Bandgap

Optical and electronic properties of a semiconductor material will be decided by the basic quantities, bandgap and refractive index (or dielectric function) which are closely related to the electronic band structure of the material and the band structure is related to the crystal symmetry of it. Optoelectronic properties of semiconductors based on the refractive index (dielectric function) will be discussed in Chapter 4. Figure 1.10 depicts the first Brillouin zones of the group III-nitride wurtzite structure with the symmetry points. Γ point located at the zone-center (wave vector k=0) has the highest symmetry in the Brillouin space.

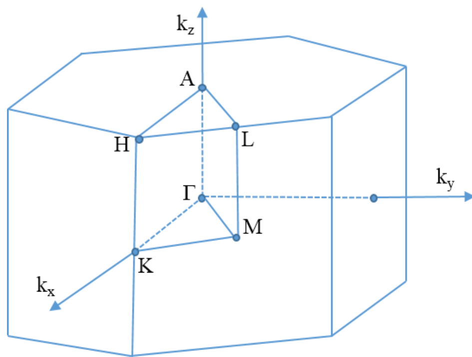

Figure 1.10 First Brillouin zones and the symmetry points of the wurtzite structure.

Group III-nitrides and their alloys are direct bandgap semiconductors, where conduction band minima and the valence band maxima are at the same position in the k-space (k-vector). Although the conduction band minimum (CBM) of the GaN and AlN can be calculated by a parabolic approximation, the non-parabolic approximation has to be used in the case of InN due to its narrow band gap. In the wurtzite group III-nitride materials valence band structure is affected by the spin-orbit splitting and crystal field splitting. Several methods such as GW (Green's function and the screened Coulomb interaction) quasiparticle approach with exact-exchange optimized effective potential (OEPx) and local density approximation (LDA) [31, 32], have been used to calculate the valence band structure of the III-nitrides at the Γ point. In the valence band (VB) of the III-nitride wurtzite crystal, the crystal field and spin-orbit coupling result in three doubly degenerate bands are called heavy-holes (HH) band, light holes (LH)

band, and crystal field split-off (CH) band [33, 34]. These three bands and CBM for GaN are shown in Fig. 1.11. The wave vector k, along the c-axis, is k_z and in the plane is k_x.

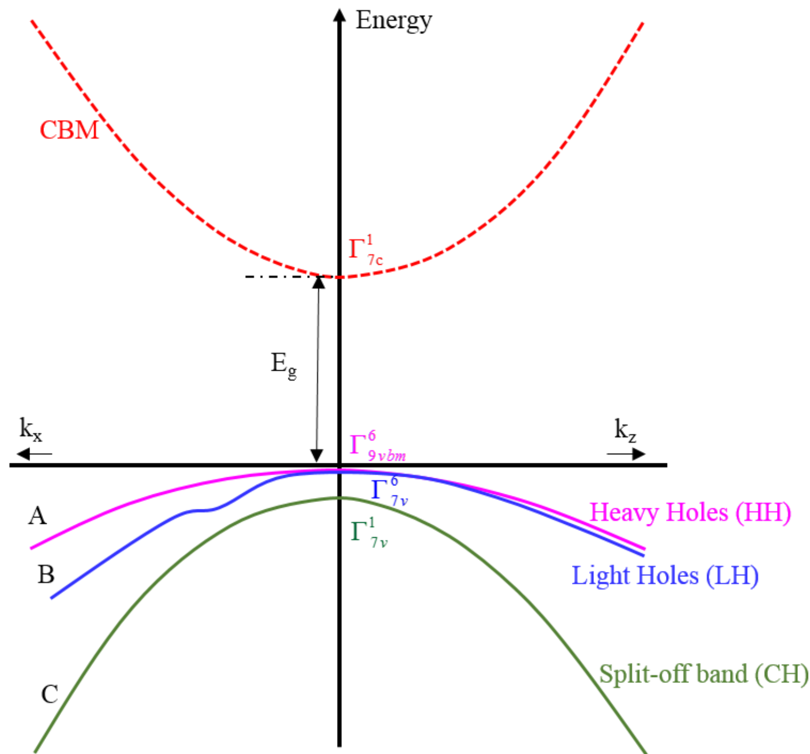

Figure 1.11 Schematic of energy band structure at Γ point for GaN.
It is noted that bands are not drawn to a scale. The calculated valance bands of AlN, GaN, and InN with and without spin-orbit coupling can be found in elsewhere [31].

The valance bands in GaN crystal are given in the order of increasing their transition energies: Γ^6_{9vbm} (A), Γ^6_{7v} (B), Γ^1_{7v} (C). The ordering is same for the InN, although the energies are different. However, this order changes for AlN as Γ^1_{7vbm} (C), Γ^6_{9v} (A), Γ^6_{7v} (B) hence; AlN has a negative crystal field splitting while GaN has a positive value for it. In AlN, the top band Γ^1_{7vbm} (which is in GaN : Γ^6_{9vbm}) determine the fundamental optical transition near the Γ point and transport properties of the free holes [35]. Due to the negative crystal field splitting, AlN can have different optical properties from GaN and InN [35]. It is known that the crystal field splitting is sensitive to the lattice deformations, such as changes in internal parameter (u), the c_0/a_0.

AlN, GaN, and InN have the bandgap values, the energy difference between the valence band maximum and conduction band minimum, of 6.2 eV, 3.39 eV, and 0.7eV, respectively [1, 34]. Since the band structure is influenced by the crystal symmetry, the bandgap depends on the lattice parameters of the crystal. Figure 1.12 shows the bandgap vs. lattice constant (a) for group III-nitride wurtzite and zincblende structure.

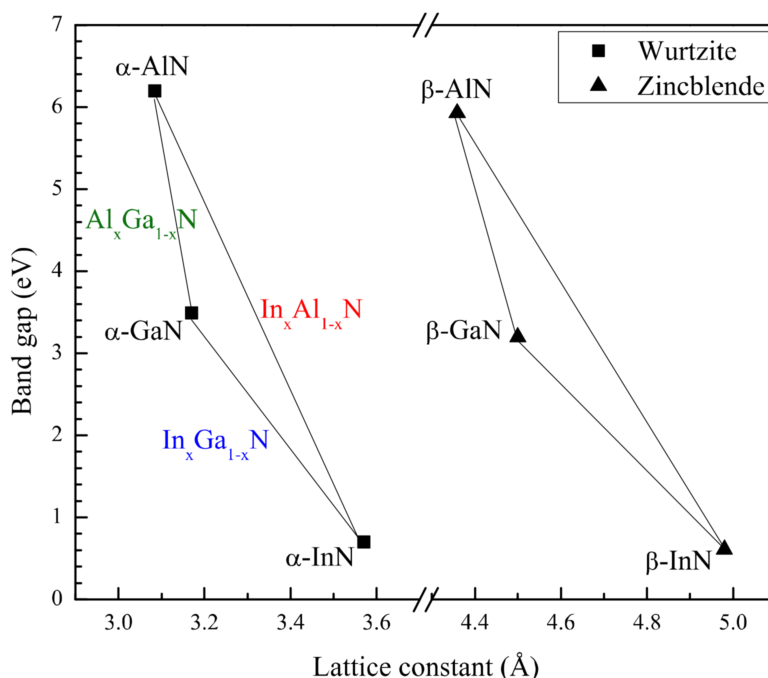

Figure 1.12 Bandgaps versus lattice constant (a) for III-nitrides wurtzite and zincblende structure.

Among III-nitrides (i.e. AlN, GaN, and InN), InN is owing to the smallest bandgap. The recently obtained bandgap value of InN (0.7 eV) breaks the common-cation (common-anion) rule which says, as decreases in atomic number, the direct gap at the Γ point increases. This rule does not apply for InN and InP. According to the rule, band gap value of InN (0.7 eV) should be larger than that of InP (1.344 eV) and which is not. According to the tight-binding model, the valence band minimum derives from bonding anion and cation *p* orbitals and the conduction band minimum originates from the anti-bonding state of anion and cation *s* orbitals [4, 36]. Figure 1.13 shows these orbitals energies for III-V elements [4, 37, 38].

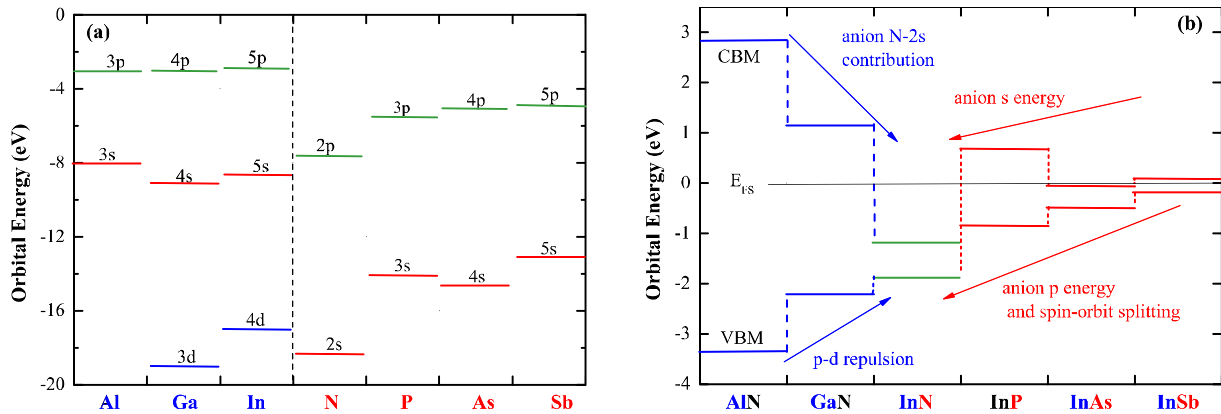

Figure 1.13 (a) In group III and V elements, atomic orbital energies. (b) Conduction and valance band minimum of the III-V materials relative to the E_{FS}.
Figure is after Ref. [4].

N-2*s* orbital energy is lower than the other elements *s* orbital energies shown in Fig. 13(a) when compared with that of P. Therefore, CBM of InN is lower than that of InP and not follow the common-cation rule. There is not much *s* energy difference among Al, Ga, and In. Thus, the energy of the N-2*s* and its weight in the CBM determines the CBM. As the ionicity increases from AlN to GaN, and to InN, the contribution of N-2*s* state increases, which results to have lowest CBM among III-V semiconductors (see Figure 1.13(b)). Similarly, the VBM is determined by the interaction between the cation N-2*p* and *d* orbitals. Because the In 4*d* level is the highest among AlN, GaN, and InN, the VBM of InN is moved more up by this *p-d* repulsion. However, the atomic size and volume effect also is significant when determining the bandgap [4].

The other reason for the narrow bandgap of InN is non-parabolicity of the CBM, as a results of the ***k.p*** interaction across the narrow gap between VB and CB [39].

Several explanations has been proposed to clarify the origin of the discrepancy between previously reported bandgap value and recently reported bandgap value. One explanation is, InN film grown by sputtering formed an indium oxynitride, which has a large bandgap. Another one is, bandgap could increase due to the quantum-size effects in InN nanocrystals. A phenomenon known as Burstein-Moss ef-

fect (see Fig. 1.14) is another reason. In degenerate doping semiconductors, optical absorption is forbidden for transitions below the Fermi level (E_F). Thus, the onset of the optical absorption could overestimate the intrinsic bandgap [4, 40, 41].

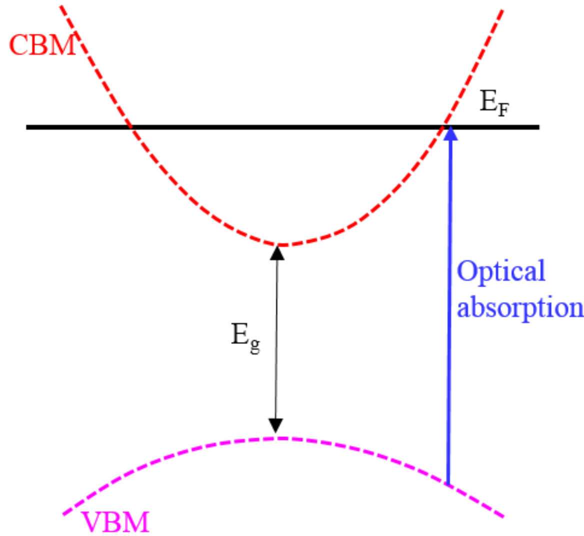

Figure 1.14 Schematic showing the Burstein-Moss effect in InN.

As mentioned before, this narrow bandgap of InN allows extending the energy gap range of III-nitride alloys from deep ultraviolet to near infrared spectral range [42]. The bandgap of $In_xGa_{1-x}N$ alloys can be varied between the 0.7 eV and 3.4 eV by changing the indium composition. For $In_xAl_{1-x}N$, it can be varied between 0.7 eV and 6.2 eV (see Fig. 1.12). For III-nitride alloys $A_xB_{1-x}N$ (A and B can be Al, Ga, or In), the bandgap can be given by Eq. 1.5.

$$E_g^{A_xB_{1-x}N} = xE_g^{AN} + (1-x)E_g^{BN} - bx(1-x) \quad 1.5$$

Where, x and b are the composition of A ($0 \le x \le 1$) and the bowing parameter of the alloys.

1.1.6 Effective Mass

It is known as that the mass of an electron in a solid is the same as the mass of a free electron. However, mass of the electron determined by experimentally shows larger (for some solids) or smaller (for other solids) values than the free electron mass [43]. Typically, the electron mass determined by experimentally is called the effective mass (m*). Due to the interactions between drifting electrons and the atoms in a

crystal, the effective mass (m^*) can be deviated from the free electron mass (m_0), and the deviation can be given as ratio m^*/m_0, which could be slightly smaller or larger than 1. As an example, when an electron is accelerating in an electric field, which could be slightly slow down due to collisions with some atoms. Then, the ratio is larger than 1. Electric field can be enhanced as the electron wave in another crystal have just the right phase, and then the ratio m^*/m_0 is smaller than 1.

The effective mass can be expressed by Eq. 1.6 [43].

$$m^* = \hbar^2 \left(\frac{d^2 E}{dk^2} \right)^{-1} \tag{1.6}$$

The effective mass is inversely proportional to the curvature of an electron band. The effective mass is small, when the curvature of $E = f(k)$ at a given point in k-space is large, and vice versa. The bottom of the CB is concave (see Fig. 1.11), and therefore effective mass is positive. The top of the VB is convex, hence effective mass is negative. A negative effective mass means that the particle will be accelerated to the opposite direction to an applied electric force. An electron with a negative mass is called an electron hole. However, it is commonly ascribed to a hole effective mass and a positive charge. Semiconductors have different properties in different direction, therefore, effective mass also differ in each direction. In such a case effective mass is a tensor.

1.1.7 Phonon Structure

The atoms in a solid are constantly periodically vibrating about fixed positions. The amplitude of these vibrations increase, if the material takes energy from heat or a photon. The vibrational waves are quantized. A phonon is quasiparticle which is a quantized lattice vibration wave. Phonon modes are the quantized vibrational modes of a crystal structure, therefore, phonon modes are determined by the crystal structure of the material [44].

Two types of phonons includes in a solid with a more than one type of atoms in the unit cell. They are acoustic phonons which are coherent movements of atoms of the lattice out of their equilibrium

positions, and optical phonons are caused by out of phase movements of the atoms in the lattice. The phonons in the lattice can be divided into two types: longitudinal and transverse, according to the direction of the atoms motion and wave propagation. For longitudinal phonons, motion of the atoms is in the direction of the wave propagation and for transverse phonons, atoms are moving perpendicular to the direction of wave propagation. The corresponding acoustic and optical phonons are abbreviated as LA (Longitudinal Acoustic), TA (Transverse Acoustic), LO (longitudinal Optical), and TO (Transverse Optical). Following Table 1.3 presents the summary of these phonons and Fig. 1.15 shows a schematic of each phonons in a diatomic chain.

Phonon spectrum plays an important role in determining the thermodynamic properties, optical properties, and kinetic properties of carriers in semiconductors. It can be known the specific features of the crystal structure and interatomic interactions which provides the details about the dynamical properties of the crystal, by studying the behavior of the phonon dispersion branches [45]. Another important aspect in phonons is their interaction with free carriers. Typically, these interactions is negatively affect in device performance though, the recent studies have shown that these interactions can be used in certain laser device engineering. The lifetimes of the phones are significant in these interactions and Raman spectroscopy is one way to measure the phonon lifetimes. The phonon lifetimes and the factors influence on them can be determined by analyzing the Raman linewidth [46]. In addition to this, Raman linewidth can be used to analyze the crystalline quality of the semiconductor. Further details in phonons and related properties of group III-nitrides are discussed in Chapter 3 under Raman spectroscopy.

Table 1.2 Summary of the phonon type, their motion and phase in a solids with more than one types of atoms in the unit cell.

Phonon Type	Motion of the atoms	Phase
LA	in the plane of the wave propagation	different atom types move in the same direction and in phase
TA	Perpendicular to the wave propagation	different atom types move in the same direction and in phase
LO	in the plane of the wave propagation	different atom types move in opposite direction and out of phase
TO	Perpendicular to the wave propagation	different atom types move in opposite direction and out of phase

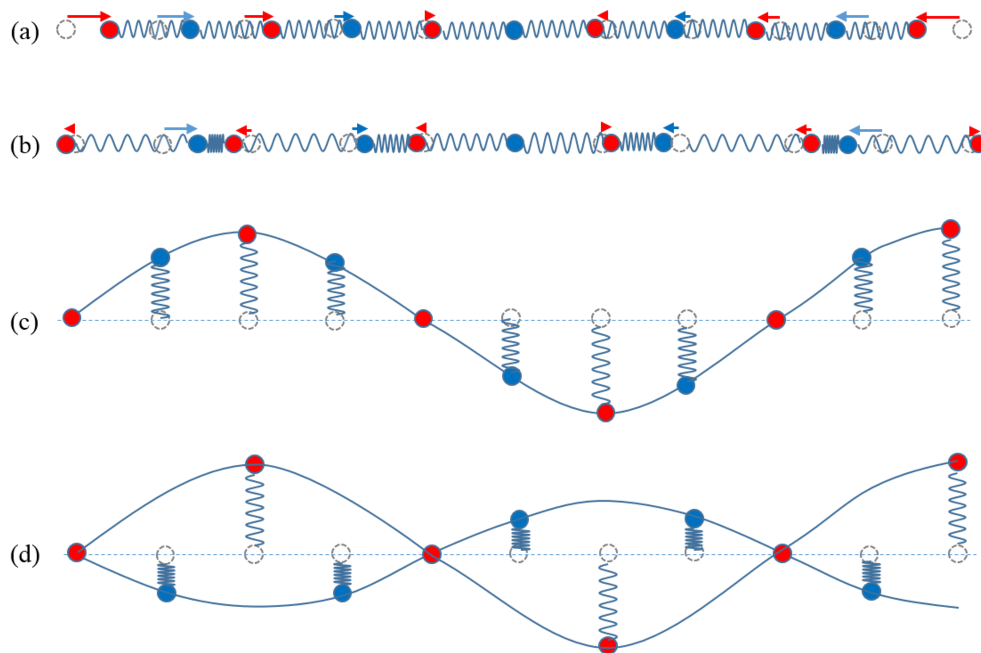

Figure 1.15 Schematic of phonon propagation in diatomic chain. (a) Longitudinal acoustic phonon, (b) Longitudinal optical phonon, (c) Transverse acoustic phonon, and (d) Transverse optical phonon. The figure is after Ref. [47]

1.2 History of InN and their Alloys

This section briefly discusses the history and development of InN and alloys. Which include the crystal growth techniques and physical properties (structural, optical, and electrical) of InN and alloys extracted from different studies.

The earliest report of InN was in 1938 by Juza and Hahn [48]. In this study, InN powder was synthesized by decomposition of $(NH_4)_3InF_6$ in a stream of NH_3. In which the first reported the crystal structure of wurtzite lattice parameters values: a = 3.53 Å and c = 5.69 Å by analysis of powder XRD. Only a few reports of InN are found in between 1940 and 1960 [49-51]. Those time, grown InN was in powder form or small crystal form. Most of the InN growth methods were In compounds interactions with ammonia or thermal decompositions of complex compounds which include direct bonding of In and N [52]. In 1963, Pastrnak et al. [53] grew InN by using CVD process in which $InCl_3$ react with N_2. It was understood that InN does not occur by direct interaction of In metal with nitrogen in an inactivated form even at high temperature [54]. In 1970, MacChesney et al. [55] suggested a possible method for single crystal growth by obtaining pressure-temperature phase relation of InN prepared in polycrystalline form by a modification of the procedure explained by Juza et al. [49]. This study suggested that the equilibrium dissociation temperature for InN was at ~ 527 °C, the pressure was ~ 1 atm, and that is at 600 °C, the pressure is higher than 20 atm. Therefore, the growth of InN is required low growth temperature due to the low dissociation temperature of InN and high equilibrium N_2 vapor pressure over InN.

The growth of InN by using plasma techniques started after 1970 and apparently Hovel et al. [56] were the first who grew InN by reactively RF sputtering using In target and pure N_2. The films were deposited on sapphire and Si substrate in the range of 25-600 °C, and they were dark red polycrystalline and n-type. Carrier concentration and Hall mobility of the layers were (5-8) × 10^{18} cm^{-3} and 250 ± 50 $cm^2V^{-1}s^{-1}$, respectively. The bandgap of these films was 1.9 eV. The high carrier concentration of the films was ascribed to a high density of native defects. In 1972 and 1975, Osamura et al. [57, 58] grew InN and its alloys with GaN by using reactive cathode evaporation technique. In the latter study [58] reported the

composition dependence of the transverse optical phonon frequency of $Ga_{1-x}In_xN$ by analyzing the reflectance spectra using Kramers-Kronig dispersion formula and found a linear behavior between the longitudinal and transverse phonon frequency. InN transverse phonon mode was calculated as 478 cm^{-1} by extrapolating the straight line to x = 1. As well as, the longitudinal phonon frequency was determined to be 694 cm^{-1}. In 1974, Trainor et al. grew InN using electron beam evaporation of In onto heated substrates in an atomic nitrogen environment and then only ground state species, provided from a continuous flow pulsed nitrogen plasma that was expanded into evaporation system directed into the substrates [59]. The bandgap, carrier concentration, and Hall mobility of the film were ~1.7 eV, (3-6) $\times 10^{20}$ cm^{-3} and 20 $cm^2V^{-1}s^{-1}$, respectively. Trainor et al. stated that the higher carrier concentration and lower mobility of these InN films compared with Hovel et al. [56] reported values could be due to the higher impurity density of indium metal and lack of the crystallinity of the films. Most of the InN films grown by RF sputtering were polycrystalline or amorphous. However, high Hall mobility of 2700 $cm^2V^{-1}s^{-1}$and low background carrier concentration of 5.3×10^{16} cm^{-3} were measured at room temperature by Tansley et al. [60] for polycrystalline InN films grown on Si or glass substrate by reactive RF sputtering from a nitride metallic target in a nitrogen ambient. The maximum Hall mobility measured at 150 K was 5000 $cm^2V^{-1}s^{-1}$. The bandgap of these films was 1.89 eV [3]. After reporting the high Hall mobility and low carrier concentration of InN films, although several groups attempted to reproduce these values using sputtering technique with different approach such as different substrate, different substrate temperature, they were not success [61-73].

In 1977, Marasina et al. [74] used chemical vapor deposition (CVD) method to grow mosaic crystalline epitaxial InN layers on sapphire (0001) substrate by the reaction between ammonia and $InCl_3$ (synthesized from In and Cl_2). The layers are n-type, and the electron concentration and mobility of the layers are in the range of 8×10^{21}-2×10^{20} cm^{-3} and 35-50 $cm^2V^{-1}s^{-1}$, respectively.

InN received little attention compared to GaN and AlN between the 1940s and 1970s because it was difficult to grow single crystalline InN. Various growth approach has been used to achieve the growth of InN at a low temperature which inhibits escaping N atoms from the surface which can affect

the quality of the films. In 1989, Wakahara et al. reported the epitaxial growth of InN on sapphire for the first time by microwave-excited metalorganic vapor phase epitaxy (MOVPE) in the temperature range of 400-600 °C. The crystal structure and composition of the layers were confirmed by XRD, RHEED (reflection high-energy electron diffraction) and ESCA (electron spectroscopy for chemical analysis) analysis.[75] Apparently, for the first time, InN heteroepitaxial growth on a GaAs substrate ((111)A and (100) oriented) were reported by Yuichi et al. in the same year [76]. The lattice mismatch between InN and GaAs (11.5%) was estimated to be less than that of between InN and sapphire (28.8%). The crystallinity of these samples grown by rf-excited reactive evaporation method was confirmed fairly good film by the value (17 s) of full width at half-maximum (FWHM) of an X-ray rocking curve (XRC). However, satisfactory epitaxial growth was not obtained for the (100) substrate. Nagatomo et al. have been studied the lattice constant and bandgap (varied from 3.20 eV to 2.01 eV) of $Ga_{1-x}In_xN$ as a function of composition (up to x=0.42) grown by MOVPE on sapphire at 500 °C in 1989 [77]. In 1990, single-crystal InN and $In_xGa_{1-x}N$ alloys grown by MOVPE on sapphire at 500 °C were reported by Matasuoka et al. [78]. Carrier concentration and Hall mobility of the InN films were in the range of 10^{18} cm^{-3} and 300-400 $cm^2V^{-1}s^{-1}$, respectively. Also, it was observed that a surface morphology depends on the V/III ratio. InN film on sapphire (0001) by MOVPE with a carrier concentration of ~5×10^{19} cm^{-3} and a Hall mobility of ~300 $cm^2V^{-1}s^{-1}$ were reproducibly obtained by Yamamoto et al. in 1998 [79].

In 1991, Davis published an overview of development in III-V nitrides including InN [80] After that, in 1992, Strite et al. published a review article which presented a comprehensive history of the development of III-nitrides, GaN, AlN, InN, and their alloys through the end of the 1991 calendar year, including growth process, chemical, structural, optical and electrical properties of them [81].

At the beginning of the 1990s, the evolution of the epitaxial single-crystal InN films and the discovery of the true bandgap value of 0.9 eV [82] in 2001and later 0.7 eV [1, 2] lead to an another transition in InN research. However, the different growth approaches exhibited a large variation in carrier concentration and mobility of the carriers even today. The values reported by Tansley et al. [60] were the highest that ever achieved. In 1988, Sullivan et al. [61] deposited InN films onto fused quartz, Corning 7059

glass, and carbon planchette substrates busing dc planar magnetron sputtering system. These films were transparent with reddish-brown color and n-type. The carrier concentration and mobility were ranged from 3 to 6× 10^{20} cm^{-3} and 35-50 $cm^2V^{-1}s^{-1}$, respectively. In this, Sullivan et al. [61] reported the first measurements of the dielectric function of InN in the spectral region 2.5-5.5 eV.

Usually, as-grown InN films were n-type and unintentionally doped p-type films were rare. Jenkins et al. studied the electronic structure and doping of InN, $In_xGa_{1-x}N$, and $In_xAl_{1-x}N$ in 1989 [83]. In this study, it was found (i) that the native defect responsible for naturally occurring n-type InN is a nitrogen vacancy, not N_{In} (N on an In site), (ii) that by introducing column II impurities on In sites, p-type doping should be feasible, and (iii) that n-type conductivity should be a consequence of oxygen atoms on N sites. For the first time, Feiler et al. [84] reported the unintentionally doped InN films grown on sapphire (0001) by pulsed laser deposition (PLD) in high vacuum and 5 mTorr of N_2. Crystalline orientations of the investigated InN films were InN(0001)||sapphire(0001) and InN[$11\bar{1}00$]||sapphire[$10\bar{1}0$] for high vacuum and N_2 ambient films respectively. The corresponding carrier concentration of the films were 6.5× 10^{20} cm^{-3} and 4.7× 10^{19} cm^{-3}, and mobility of the film were 30 $cm^2V^{-1}s^{-1}$ and 240 $cm^2V^{-1}s^{-1}$, respectively. Tansley et al. suggested that the high carrier concentration in the InN is due to the nitrogen vacancies [85, 86]. In 2004, Butcher et al. showed that the high n-type carrier concentration for RF sputtered InN is not due to nitrogen vacancies, and the excess nitrogen is possibly the source of the background n-type doping [70].

In 1993, the influence of the AlN buffer on sapphire (0001) on the structural and electrical properties of InN film grown by reactive sputtering studied by Kistenmacher et al. [63]. These results revealed that the carrier concentration is nearly constant up to 300 °C of InN growth temperature and the carrier concentration decreased by a factor of 5 with increasing growth temperature. The mobility of the InN films grown on AlN buffer/sapphire increased by a factor of two for the growth temperature beyond 400 °C. However, the mobility of the InN films on AlN buffer were in the range of ~20-60 $cm^2V^{-1}s^{-1}$ and greater than that of on sapphire. The carrier concentration of those films was in the range of ~1-4.5× 10^{20} cm^{-3} [63].

Several groups have predicted the theoretical values for mobility of InN. However, those values were far from the experimental values. Chin et al. predicted that the maximum mobility of the InN to be 4400 $cm^2V^{-1}s^{-1}$ and 33000 $cm^2V^{-1}s^{-1}$ at room temperature (300 K) and 77 K, respectively.[87] Nag et al. predicted that the highest value of mobility of InN is about 4000 $cm^2V^{-1}s^{-1}$ at room temperature [88]. Fareed et al. reported the highest predicted mobility value for InN as high as 5000 $cm^2V^{-1}s^{-1}$ at room temperature [89].

Fareed et al. [89] also studied the influence of the electrical properties of InN films grown on GaN/AlN buffer/sapphire template by migration enhance metalorganic chemical vapor deposition (MEMOCVD). The results revealed that the mobility of the InN layers increases from 12 $cm^2V^{-1}s^{-1}$ to 846 $cm^2V^{-1}s^{-1}$, with increasing the layer thickness from 75 nm to 900 nm. As well as, carrier concentration decreases from 5.5×10^{19} cm^{-3} to 4.1×10^{18} cm^{-3}, with increasing the InN film thickness from 75 nm to 900 nm [89]. In order to reduce the concentration of nitrogen vacancy and the corresponding carrier concentration, InN films were grown varying growth rates from 0.23 μm/h to 0.05 μm/h using reactive evaporation method by Sato et al. [90]. It was found that both, the carrier concentration from 3.2×10^{20} cm^{-3} to 4.3×10^{18} cm^{-3} and the mobility of the films from 34.7 $cm^2V^{-1}s^{-1}$ to 0.6 $cm^2V^{-1}s^{-1}$ decreased, with decreasing the growth rate. Additionally, Sato et al. examined the effect of the InN film damage by the plasma. The study revealed that carrier concentration increased from 4.3×10^{18} cm^{-3} to 1.6×10^{20} cm^{-3} as plasma power decreased from 80 W to 5 W [90].

Typical MOCVD growth temperatures for Al and Ga based nitride materials were required high growth temperatures (between 900 °C and 1200 °C). On the other hand, because of the relatively weak bond strength between In and N, In based nitrides requires low growth temperatures. As a solution to this problem, atomic layer epitaxy (ALE) has been suggested [91, 92]. Carrier concentration and mobility of the n-type InN films deposited on (0001) sapphire at 480 °C using ALE by McIntosh were ~ 10^{19} cm^{-3} and ~10 $cm^2V^{-1}s^{-1}$, respectively [93]. The single crystal InN films grown on (0001) sapphire at 440 using UV-assisted ALE by Inushima et al. exhibited the carrier concentration ~3×10^{20} cm^{-3} and mobility 60 $cm^2V^{-1}s^{-1}$ [94].

In 1997, Sato et al. found that it was essential to lower the growth rate than increasing the N-radical flux to achieve the low carrier density [95]. In this study, Sato et al. deposited the InN epitaxial films on (0001) sapphire using plasma-assisted MOCVD by which large amounts of radicals can be supplied little damaging to the surface. A growth temperature of 600 °C was the highest temperature to grow InN without In droplets, promoted surface reaction to fill N-vacancies and reduced the carrier densities. The achieved carrier density was 4×10^{19} cm^{-3} [95]. In 1998, Guo et al. studied the dependence of the mobility and carrier concentration on the glass substrate temperature (100 °C-500 °C) by radio frequency magnetron sputtering [66]. The results revealed that the carrier concentration was almost independent of the substrate temperature and the order 10^{20} cm^{-3}. However, the Hall mobility increased from 18 $cm^2V^{-1}s^{-1}$ to 115 $cm^2V^{-1}s^{-1}$ with substrate temperature from 100 °C to 500 °C [66]. In the same year, a similar study was carried out by Ikuta et al. The InN films were deposited on (0001) sapphire and ZnO buffer/sapphire. The maximum Hall mobility of the film on the ZnO buffer/sapphire (60 $cm^2V^{-1}s^{-1}$) was greater than that of bare sapphire (30 $cm^2V^{-1}s^{-1}$) at the same growth temperature. The minimum carrier concentration (2×10^{20} cm^{-3}) was slightly lower than that of bare sapphire (3×10^{20} cm^{-3}) at the same temperature [65].

In 1999, Blant et al. grew intentionally doped InN using Mg as a p-type dopant by modified MBE [96] However, the layer exhibited the n-type with the carrier concentration of 5.3×10^{19} cm^{-3} and a mobility of 17.7 $cm^2V^{-1}s^{-1}$. On the other hand the undoped InN film had a higher mobility (190 $cm^2V^{-1}s^{-1}$) and lower carrier concentration (3×10^{19} cm^{-3}) [96].

In 1999, Yamaguchi et al. found first that InN can be grown on GaN. An electron Hall mobility of InN grown by MOVPE with the film thickness of 2400 Å has been observed of 700 $cm^2V^{-1}s^{-1}$ at an electron concentration of 5×10^{19} cm^{-3}, as high as that of GaAs at the same electron concentration [97]. In the same year, Mamutin et al. investigated the InN film properties as dependent on initial growth stages grown by MBE. The initial state involving high temperature (~800 to 900 °C) annealing of a 15 nm thick InN buffer grown at low temperature demonstrated the highest Hall mobility of 600 $cm^2V^{-1}s^{-1}$, in spite of the high electron concentration of 1×10^{20} cm^{-3} [98].

Low temperature InN growth in common III-nitride techniques such as MBE, and MOVPE, is characterized by a short surface migration length of the column III atoms. This will form high defect density films. To enhance the migration distance of III-atoms during the low temperature epitaxial growth, Migration Enhanced Epitaxy (MEE) which composes of an alternative supply of pure In atoms and nitrogen plasma, has been introduced [99]. Lu et al. studied the InN films prepared by MEE on sapphire by varying substrate temperature from 360 °C to 590 °C. The highest mobility of 542 $cm^2V^{-1}s^{-1}$ and lowest electron carrier concentration of 3×10^{18} cm^{-3} at room temperature were found at ~500 °C growth temperature [99]. The results of this study argued against the common view that nitrogen vacancies are responsible for high background n-type doping. As well as, it has shown that AlN buffer layers improved the electrical properties of InN films. Further studies of the effect of the AlN buffer layer on the epitaxial growth of InN by MBE were carried out by Lu et al. in 2001 [100]. In this work, A Hall mobility of 805.3 $cm^2V^{-1}s^{-1}$ with a carrier concentration ~2.5×10^{18} cm^{-3} at room temperature was achieved on a 120 nm InN film on AlN buffer layer [100]. For the 300 nm thick InN layer, the Hall mobility, and carrier concentration were 911 $cm^2V^{-1}s^{-1}$ and 2.9×10^{18} cm^{-3} at room temperature, respectively. The measured the Hall mobility and carrier concentration for this sample at 77 K were 1147 $cm^2V^{-1}s^{-1}$. Lu et al. also showed that Hall mobility increases with InN film thickness. In 2003, Lu et al. found that increasing film thickness does not lead to an apparent improvement in electrical properties of the a-plane InN grown on r-plane sapphire. In these films, Hall mobility and carrier concentration fluctuated around 250 $cm^2V^{-1}s^{-1}$ and 6×10^{18} cm^{-3}, respectively in the thickness range of 0.5-3 μm [101]. In previously Lu. et al. described the enhancement of Hal mobility is due to the reduced defect density away from the lattice-mismatched buffer. For the c-plan film, Lu et al. also concluded that impurities from the growth environment are not responsible for the high background doping of InN. Instead of some structural defects or substrate/buffer impurities may be the major source and growing thicker films it can be reduced [101, 102]. However, for a-plane InN, a significant decrease of structural defects along the growth direction were not observed [101]. Higashiwaki et al. observed that there was an intermediate sharp increase in mobility up to a film thickness of 150 nm, beyond which it almost leveled out. The Hall mobility of the 200 nm thick InN film at room temperature

was 1180 $cm^2V^{-1}s^{-1}$ (1240 $cm^2V^{-1}s^{-1}$ at 77 K) with an electron concentration of 2.2×10^{18} cm^{-3}. The best electron concentration of 1.6×10^{18} cm^{-3} was achieved for the 300 and 350 nm thick InN films. The InN films were grown on the 10 nm thick LT-GaN intermediate and 10 nm thick LT-InN layer by PA-MBE [103]. Cimalla et al. found that both the interface and the surface of the InN layer influenced the electrical properties essentially [104].

In 2001, Inushima reported the mobility of 1700 $cm^2V^{-1}s^{-1}$ and the carrier concentration of 5×10^{19} cm^{-3} for the undoped InN grown on sapphire substrate with 15 nm InN buffer layer at 300°C by ECR-plasma assisted MBE [82]. The bandgap of this sample was 0.89 eV. In 2001, Yoshiki et al. was grown InN layers on sapphire (0001) with an intermediate buffer layer grown at 300 °C by RF-MBE. The best Hall mobility of 760 $cm^2V^{-1}s^{-1}$ and carrier concentration 3×10^{19} cm^{-3} of were found for the single-crystal InN films grown at 550 growth temperature and 240 W plasma power [105].

In 2002, Davydov et al. found the band gap value of InN as 0.9 eV, which was smaller than previously reported value of 1.89 eV. The single-crystalline InN epilayers were grown on (0001) sapphire either by plasma assisted MBE or MOMBE. Electron concentration ranged from 9×10^{18} cm^{-3} to 1.2×10^{19} cm^{-3} in the best samples, and their mobility was as high as ~1900 $cm^2V^{-1}s^{-1}$ [106]. Saito et al. reported the improvement of electrical properties of InN grown using buffer layer and intermediate layers by RF-MBE. Electron mobility (carrier concentration) of the InN film with and without intermediate layers were 830 $cm^2V^{-1}s^{-1}$ (1×10^{19} cm^{-3})and 150 $cm^2V^{-1}s^{-1}$ (4.2×10^{20} cm^{-3}), respectively [107].

With the rapid development and availability of characterization tools and development of InN based devices, researchers were interested in deep understanding of InN properties. Qian et al. has proposed InN as a good plasma filter material in thermophotovoltaic systems by studying IR reflection spectra of InN films grown on GaAs (111) by RF-sputtering. Carrier concentration and mobility of these films were in the range of $2\text{-}4\times10^{20}$ cm^{-3} and 30-40 $cm^2V^{-1}s^{-1}$, respectively [108]. In the same year, Qian et al. [109] reported the Raman spectra and IR reflectance spectra of InN films grown on GaAs (111) and sapphire (0001) substrates by RF magnetron sputtering and microwave-excited MOVPE. An evident of blue shift of the frequencies for the E_1(TO) and A_1(LO) phonon modes due to the residual compressive stress

was observed. From the Raman spectra, A_1(LO) modes at 598 cm^{-1} and E_2 (high) modes at 490 cm^{-1} were observed. From the IR spectra, phonon modes of A_1(TO) at 449 cm^{-1}, E_1(TO) at 488 cm^{-1}, free carrier concentration and mobility were extracted. The extracted carrier concentration and mobility were in the range of 2-3×10^{19} cm^{-3} and 69-325 $cm^2V^{-1}s^{-1}$, respectively. The mobility obtained from IR spectra was smaller (near half) than that from Hall measurements for the similar carrier concentration. Qian et al. stated that this effect is due to the increase of scattering for the carrier coupling with the incident phonons in the optical measurements [109]. Wu et al. found the effective mass of InN to be electron concentration dependent. The effective masses of the films were calculated using the plasma frequency obtained from the IR spectra and carrier concentrations obtained from the Hall measurements. The free carrier concentration and mobility were from 3.5×10^{17} cm^{-3} to 5.5×10^{18} cm^{-3} and 100 to 2050 $cm^2V^{-1}s^{-1}$, respectively for unintentionally doped samples [110]. The spectroscopic ellipsometry is one of other tool used in the analysis of optical and electrical properties of InN layers. Goldhahn et al. studied the anisotropic dielectric function of the a-plane InN film grown on r-plane sapphire with an AlN nucleation layer and a GaN buffer by spectroscopic ellipsometry [111]. Later, Kasic et al. studied the InN dielectric function from IR to ultraviolet range by spectroscopic ellipsometry and determined the film thickness, plasma frequency, and plasma damping for the samples with different free carrier concentrations (7.7×10^{17} cm^{-3}- 1.4×10^{19} cm^{-3}) [112].

For the first time, Yamamoto et al. reported that a MOVPE InN film with a carrier concentration in the order of 10^{18} cm^{-3} was grown with an electron mobility of 730 $cm^2V^{-1}s^{-1}$ by using atmospheric pressure growth. Yamamoto et al. also showed that improvement of morphology is needed to attain high electron mobility in InN films using AFM.[113] Yang et al. investigated the optical constants (refractive index and extinction coefficient) of InN films on GaAs (111) substrate by RF reactive magnetron sputtering as a function of energy with different growth conditions [68]. Further improvement in the electrical properties of the InN is one of the great challenges [114].

It has been found that quality of the InN layer is sensitive to the sapphire nitridation process [115]. Pan et al. found that the quality of the InN film was sensitive to the nitridation process, in particular

the nitridation temperature and nitridation duration. The results revealed that better InN film quality can be achieved with a nitridation temperature of 1000 °C for 40 minutes for InN growth temperature of 550 °C. The corresponding Hall mobility, carrier concentration, and Raman E_2 (high) FWHM values were 270 $cm^2V^{-1}s^{-1}$, 5×10^{19} cm^{-3}, and 4.5 cm^{-1}, respectively [116]. Nanishi et al. found that nitridation of sapphire prior to InN growth is effective for producing single crystals. As well as insertion of the low-temperature intermediate layer is effective in obtaining thick InN. XRC FWHM, $\omega-2\theta$ XRD FWHM, Raman E_2 high FWHM, carrier concentration, and mobility of this InN layer were 236.7 arcsec, 28.9 arcsec, 3.7 cm^{-1}, 4.9×10^{18} cm^{-3} and 1130 $cm^2V^{-1}s^{-1}$, respectively [117]. On the other hand, Maleyre et al. have shown that excessive temperature and time of nitridation is not beneficial for crystalline quality, morphology, optical and electrical properties of InN layer. The obtained root mean square roughness, mobility and electron concentration values for InN layer grown on lightly nitride sapphire were 0.60 nm, 800 $cm^2V^{-1}s^{-1}$, and 9×10^{18} cm^{-3}. According to Maleyre et al., these are the best results in low pressure MOCVD at that time [118]. Drago et al. found the optimum InN quality (electron concentration ~ 6×10^{18} cm^{-3} and electron mobility ~450 $cm^2V^{-1}s^{-1}$) for 45 s of sapphire nitridation with ammonia by MOVPE [119]. In 2014, Skuridina et al. observed the formation of crystalline AlN (where N-Al dominate) for nitridation of sapphire above 800 °C and found a smooth surface and single crystalline N-polar InN layer on top of this layer. Furthermore, a formation of amorphous AlN_xO_y (where N-O dominate) layer was found during the nitridation below 800 °C and In-polar InN layers with a rough surface, and a rough polycrystalline structure was grown on this layer [120]. The mechanism of sapphire nitridation has been studied with different growth techniques [121-124].

The effect of polarity on the InN films grown by MBE was studied by Xu et al. in 2003. It was found that FWHMs of N-polar InN (002) and In-polarity InN (002) were about 220 arcsec and 600 arcsec, respectively. Hall mobilities and electron concentration of the N-polar InN films were ranging from 500-1200 $cm^2V^{-1}s^{-1}$, and (1-5) $\times10^{18}$ cm^{-3}, respectively, while those for In-polar films were ranged from 300–900 $cm^2V^{-1}s^{-1}$ and (4-10)$\times10^{18}$ cm^{-3}, respectively [125].

In 2007, Lin et al. studied the properties of the InN layers grown on GaN/sapphire at different temperatures by MOCVD. The highest mobility of 1300 $cm^2V^{-1}s^{-1}$ and the lowest carrier concentration of 4.6×10^{18} cm^{-3} was achieved for the InN layer grown on GaN/sapphire at 625 °C [126]. The high mobility of InN layers grown with HT-GaN and LT-GaN buffer layer by MOCVD has been reported by Xie et al. in the same year. The mobility and electron concentration of this layer were 939 $cm^2V^{-1}s^{-1}$ and 3.9×10^{18} cm^{-3}, respectively [127]. Hall mobility of 1400 $cm^2V^{-1}s^{-1}$ with a carrier concentration of 7×10^{18} cm^{-3} was reported by Khan et al. for the InN layer deposited on AlN template. This result represented the highest electron mobility reported for MOCVD grown InN layers [128].

High electron mobility InN layers grown on sapphire by boundary temperature controlled epitaxy with MBE have been reported by Wang et al. The study revealed that the mobility of the InN layers increased, and electron concentration decreased with increasing the layer thicknesses. The highest mobility of 3280 $cm^2V^{-1}s^{-1}$ and lowest electron concentration of 1.47×10^{17} cm^{-3} found at 5 μm layer thickness. Wang et al. further reported that this increment of mobility and reduced of electron concentration was due to the reduction of threading dislocation [129]. In 2013, Sakaguchi et al. reported that dependence of InN layer thickness on the electrical properties and even 200 nm thick InN layer demonstrated relatively good mobility and electron concentration (1540 $cm^2V^{-1}s^{-1}$ and 2.1×10^{18} cm^{-3}). The InN layers were grown on GaN/sapphire template by PA-MBE [130].

This short history has shown that there still remains the controversy about the unintentional background electron concentration of InN layers. Impurities such as silicon, oxygen, and hydrogen acting as donors and dislocations could be a cause for the n-type conductivity in undoped InN [131]. Himmerlich et al. [132] studies have shown that electron concentration increases with carbon incorporation and dislocation densities independent of carbon incorporation. Control of carbon impurities incorporation is not difficult, and InN films can be doped with carbon by any growth method based on gas-phase epitaxy. It was found that edge dislocations influence on the electron concentrations and electron mobility of the InN [131, 133, 134].

1.3 Scope of the Thesis

The aim of this thesis is to understand and characterize the optoelectronic and structural properties of group III-nitrides epitaxial layers with different growth conditions, grown by High Pressure Metal Organic Chemical Vapor Deposition (HP-MOCVD) and Migration Enhanced Plasma Assisted Metal Organic Chemical Vapor Deposition (MEPA-MOCVD).

In this thesis, Chapter 2 discusses an overview of epitaxial growth methodologies and detailed description of growth technique employed for the samples studied in this thesis.

Chapter 3 describes characterization methods, which are used in this study, are briefly explained, including Atomic Force Microscopy, X-ray diffraction, Raman spectroscopy, and FTIR reflection spectroscopy.

Chapter 4 extensively describes theoretical models based on frequency dependent dielectric functions and Maxwell's equations for the interpretation of IR reflection spectra of multilayer structures. The theoretical model for isotropic media at normal incidence and angle incidence are explained. Next, IR dielectric functions for isotropic and anisotropic media are discussed. Furthermore, the model is extended for an anisotropic media and discuss here. The chapter then explains the determination layer thicknesses, optoelectronic properties, and structural properties by using these models.

Chapter 5 presents a detailed investigations of influence of substrate polarity and doping on the electrical and optical properties of Indium nitride layers by IR reflectance and Raman spectroscopy.

Chapter 6 presents the study of the effect of the reactor pressure on the electrical and structural properties of InN epilayers grown by HP-MOCVD using IR reflection spectroscopy and Raman spectroscopy.

Chapter 7 discusses the initial growth and characterization results of InN-AlN-sapphire grown by MEPA-MOCVD. Finally, Chapter 8 summarizes this research.

1.4 References

[1] J. Wu, W. Walukiewicz, K. M. Yu, J. W. A. III, E. E. Haller, H. Lu, W. J. Schaff, Y. Saito and Y. Nanishi, Applied Physics Letters **80** (21), 3967-3969 (2002).

[2] T. Matsuoka, H. Okamoto, M. Nakao, H. Harima and E. Kurimoto, Applied Physics Letters **81** (7), 1246-1248 (2002).

[3] T. L. Tansley and C. P. Foley, Journal of Applied Physics **59** (9), 3241-3244 (1986).

[4] J. Wu, Journal of Applied Physics **106** (1), 011101 (2009).

[5] N. E. Christensen and I. Gorczyca, Physical Review B **50** (7), 4397-4415 (1994).

[6] H. Harima, Journal of Physics: Condensed Matter **14** (38), R967 (2002).

[7] P. E. Faria Junior and G. M. Sipahi, Journal of Applied Physics **112** (10), - (2012).

[8] O. Ambacher, Journal of Physics D: Applied Physics **31** (20), 2653 (1998).

[9] Y. Taniyasu and M. Kasu, NTT Technical Review **8** (8) (2010).

[10] H. Morkoç, in *Handbook of Nitride Semiconductors and Devices* (Wiley-VCH Verlag GmbH & Co. KGaA, 2009), pp. 1-129.

[11] T. Deguchi, D. Ichiryu, K. Toshikawa, K. Sekiguchi, T. Sota, R. Matsuo, T. Azuhata, M. Yamaguchi, T. Yagi, S. Chichibu and S. Nakamura, Journal of Applied Physics **86** (4), 1860-1866 (1999).

[12] V. Darakchieva, B. Monemar and A. Usui, Applied Physics Letters **91** (3), 031911 (2007).

[13] E. Ruiz, S. Alvarez and P. Alemany, Physical Review B **49** (11), 7115-7123 (1994).

[14] B. Maleyre, S. Ruffenach, O. Briot and A. van der Lee, Superlattices and Microstructures **36** (4–6), 527-535 (2004).

[15] B. S. Kang, H.-T. Wang, L.-C. Tien, F. Ren, B. P. Gila, D. P. Norton, C. R. Abernathy, J. Lin and S. J. Pearton, Sensors (Basel, Switzerland) **6** (6), 643-666 (2006).

[16] E. T. Yu, X. Z. Dang, P. M. Asbeck, S. S. Lau and G. J. Sullivan, Journal of Vacuum Science & Technology B **17** (4), 1742-1749 (1999).

[17] W. K. TOMASZ PIASECKI, BOGDAN PASZKIEWICZ, Optica Applicata **XXXV** (3), 597-604 (2005).

[18] L. Semra, A. Telia, M. Kaddeche and A. Soltani, presented at the Engineering and Technology (ICET), 2012 International Conference on2012).

[19] F. Bernardini, V. Fiorentini and D. Vanderbilt, Physical Review B **56** (16), R10024-R10027 (1997).

[20] O. Ambacher, B. Foutz, J. Smart, J. R. Shealy, N. G. Weimann, K. Chu, M. Murphy, A. J. Sierakowski, W. J. Schaff, L. F. Eastman, R. Dimitrov, A. Mitchell and M. Stutzmann, Journal of Applied Physics **87** (1), 334-344 (2000).

[21] *Imperfections in Solids,* March 20, 2016, http://www.virginia.edu/bohr/mse209/chapter4.htm

[22] ENGR45 Materials Engineering, *Defects in the Crystalline Structure,* March 20, 2016, http://webpages.charter.net/ericbeaton/powerpt/chpt4.pdf

[23] F. K. Yam, L. L. Low, S. A. Oh and Z. Hassan, in *Optoelectronics - Materials and Techniques*, edited by P. P. Predeep (InTech, 2011), pp. 99-136.

[24] *Burgers Vector, b,* December 3, 2016, https://www.princeton.edu/~maelabs/mae324/glos324/burgersvector.htm

[25] Lindeke, *Crystal Defects and Noncrystalline Structure–Imperfection,* December 3, 2016, www.d.umn.edu/~rlindek1/ME2105/Crystal_Imperfection_CH%204.ppt

[26] J. William D. Callister, *Materials Sceience and Engineering: An Introduction*, Seventh ed. (John Wiley & Sons, Inc., 2007).

[27] B. G. Yacobi, *Semiconductor Materials: An Introduction to Basic Principles*. (Kliwer Academic Publishers, New York, 2003).

[28] R. People and J. C. Bean, Applied Physics Letters **47** (3), 322-324 (1985).

[29] S. M. Hu, Journal of Applied Physics **69** (11), 7901-7903 (1991).

[30] K. Wen, W. Lv and W. He, Journal of Materials Chemistry A **3** (40), 20031-20050 (2015).

[31] A. Punya and W. R. L. Lambrecht, Physical Review B **85** (19), 195147 (2012).

[32] P. Rinke, M. Winkelnkemper, A. Qteish, D. Bimberg, J. Neugebauer and M. Scheffler, Physical Review B **77** (7), 075202 (2008).

[33] G. B. Ren, Y. M. Liu and P. Blood, Applied Physics Letters **74** (8), 1117-1119 (1999).

[34] S. Yoshida, T. Ito, A. Hiraki, H. Saito, S. Fujita, Y. Ishitani, S.Sakai, T. Miyajima, Y. Yamada, Y. Kawakami, I. Suemune, K.Hiramatsu, H. Kawanishi, H.Amano, H. Okumura and T. Mizutani, in *Wide Bandgap Semiconductors: Fundamental Properties and Modern Photonic and Electronic Devices*, edited by K. Takahashi, A. Yoshikawa and A. Sandhu (Springer-Verlag Berlin Heidelberg, New York, 2007), pp. 38-39.

[35] J. Li, K. B. Nam, M. L. Nakarmi, J. Y. Lin, H. X. Jiang, P. Carrier and S.-H. Wei, Applied Physics Letters **83** (25), 5163-5165 (2003).

[36] P. Y. Yu and M. Cardona, *Fundamentals of Semiconductors: Physics and Materials Properties*. (Springer-Verlag Berlin Heidelberg, 2010).

[37] P. D. C. King, T. D. Veal, P. H. Jefferson, S. A. Hatfield, L. F. J. Piper, C. F. McConville, F. Fuchs, J. Furthmüller, F. Bechstedt, H. Lu and W. J. Schaff, Physical Review B **77** (4), 045316 (2008).

[38] C. Rauch, DISSERTATION, Aalto University, 2012.

[39] J. Wu and W. Walukiewicz, Superlattices and Microstructures **34** (1–2), 63-75 (2003).

[40] J. Wu, W. Walukiewicz, S. X. Li, R. Armitage, J. C. Ho, E. R. Weber, E. E. Haller, H. Lu, W. J. Schaff, A. Barcz and R. Jakiela, Applied Physics Letters **84** (15), 2805-2807 (2004).

[41] W. M. Linhart, University of Warwick, 2012.

[42] J. Wu, W. Walukiewicz, K. M. Yu, W. Shan, J. W. A. III, E. E. Haller, H. Lu, W. J. Schaff, W. K. Metzger and S. Kurtz, Journal of Applied Physics **94** (10), 6477-6482 (2003).

[43] R. E. Hummel, *Electronic Properties of Materials*. (Springer, New York, 2005).

[44] L. Sahonta, University of Cambridge, Deprtment of Materials Science and Metallurgy, *Natural Sciences Tripos Part III: MATERIALS SCIENCE: Introduction to Raman Spectroscopy,*

[45] V. Y. Davydov, Y. E. Kitaev, I. N. Goncharuk, A. N. Smirnov, J. Graul, O. Semchinova, D. Uffmann, M. B. Smirnov, A. P. Mirgorodsky and R. A. Evarestov, Physical Review B **58** (19), 12899-12907 (1998).

[46] L. Bergman, D. Alexson, P. L. Murphy, R. J. Nemanich, M. Dutta, M. A. Stroscio, C. Balkas, H. Shin and R. F. Davis, Physical Review B **59** (20), 12977-12982 (1999).

[47] *Lattice vibrations,*

[48] R. Juza and H. Hahn, Zeitschrift für anorganische und allgemeine Chemie **239** (3), 282-287 (1938).

[49] R. Juza and H. Hahn, Zeitschrift für anorganische und allgemeine Chemie **244** (2), 133-148 (1940).

[50] R. Juza and A. Rabenau, Zeitschrift für anorganische und allgemeine Chemie **285** (3-6), 212-220 (1956).

[51] T. Renner, Zeitschrift für anorganische und allgemeine Chemie **298** (1-2), 22-33 (1959).

[52] H. J. PARK, Dissertation, UNIVERSITY OF FLORIDA, 2006.

[53] J. Pastrňák and L. Součková, physica status solidi (b) **3** (2), K71-K74 (1963).

[54] N. A. Gorjunova, presented at the Slosnye Almazopodobnye Poluprovodniki, Moscow1964).

[55] J. B. MacChesney, P. M. Bridenbaugh and P. B. O'Connor, Materials Research Bulletin **5** (9), 783-791 (1970).

[56] H. J. Hovel and J. J. Cuomo, Applied Physics Letters **20** (2), 71-73 (1972).

[57] K. Osamura, K. Nakajima, Y. Murakami, P. H. Shingu and A. Ohtsuki, Solid State Communications **11** (5), 617-621 (1972).

[58] K. Osamura, S. Naka and Y. Murakami, Journal of Applied Physics **46** (8), 3432-3437 (1975).

[59] J. W. Trainor and K. Rose, Journal of Electronic Materials **3** (4), 821-828 (1974).

[60] T. L. Tansley and C. P. Foley, Electronics Letters **20** (25), 1066-1068 (1984).

[61] B. T. Sullivan, R. R. Parsons, K. L. Westra and M. J. Brett, Journal of Applied Physics **64** (8), 4144-4149 (1988).

[62] T. J. Kistenmacher and W. A. Bryden, Applied Physics Letters **59** (15), 1844-1846 (1991).

[63] T. J. Kistenmacher, S. A. Ecelberger and W. A. Bryden, Journal of Applied Physics **74** (3), 1684-1691 (1993).

[64] T. J. Kistenmacher and W. A. Bryden, Applied Physics Letters **62** (11), 1221-1223 (1993).

[65] K. Ikuta, Y. Inoue and O. Takai, Thin Solid Films **334** (1–2), 49-53 (1998).

[66] Q. Guo, N. Shingai, M. Nishio and H. Ogawa, Journal of Crystal Growth **189–190**, 466-470 (1998).

[67] N. Saito and Y. Igasaki, Applied Surface Science **169–170**, 349-352 (2001).

[68] H. F. Yang, W. Z. Shen, Z. G. Qian, Q. J. Pang, H. Ogawa and Q. X. Guo, Journal of Applied Physics **91** (12), 9803-9808 (2002).

[69] Motlan, E. M. Goldys and T. L. Tansley, Journal of Crystal Growth **241** (1–2), 165-170 (2002).

[70] K. S. A. Butcher, M. Wintrebert-Fouquet, P. P.-T. Chen, T. L. Tansley, H. Dou, S. K. Shrestha, H. Timmers, M. Kuball, K. E. Prince and J. E. Bradby, Journal of Applied Physics **95** (11), 6124-6128 (2004).

[71] Q. X. Guo, T. Tanaka, M. Nishio, H. Ogawa, X. D. Pu and W. Z. Shen, Applied Physics Letters **86** (23), 231913 (2005).

[72] X. D. Pu, W. Z. Shen, Z. Q. Zhang, H. Ogawa and Q. X. Guo, Applied Physics Letters **88** (15), 151904 (2006).

[73] S. Valdueza-Felip, J. Ibáñez, E. Monroy, M. González-Herráez, L. Artús and F. B. Naranjo, Thin Solid Films **520** (7), 2805-2809 (2012).

[74] L. A. Marasina, I. G. Pichugin and M. Tlaczala, Kristall und Technik **12** (6), 541-545 (1977).

[75] A. Wakahara and A. Yoshida, Applied Physics Letters **54** (8), 709-711 (1989).

[76] S. Yuichi and S. Susumu, Japanese Journal of Applied Physics **28** (9A), L1641 (1989).

[77] N. Takao, K. Takeshi, M. Hiroyuki and O. Osamu, Japanese Journal of Applied Physics **28** (8A), L1334 (1989).

[78] T. Matasuoka, H. Tanaka, T. Sasaki and K. Katsui, in *GaAs and Related Compounds 1989* (IOP Publishing Ltd, Karuizawa, Japan, 1990), pp. 141-146.

[79] A. Yamamoto, T. Shin-ya, T. Sugiura and A. Hashimoto, Journal of Crystal Growth **189–190**, 461-465 (1998).

[80] R. F. Davis, Proceedings of the IEEE **79** (5), 702-712 (1991).

[81] S. Striteb and H. Morkoc, Journal of Vacuum Science Technology B **10** (4), 1237-1266 (1992).

[82] T. Inushima, V. V. Mamutin, V. A. Vekshin, S. V. Ivanov, T. Sakon, M. Motokawa and S. Ohoya, Journal of Crystal Growth **227–228**, 481-485 (2001).

[83] D. W. Jenkins and J. D. Dow, Physical Review B **39** (5), 3317-3329 (1989).

[84] D. Feiler, R. S. Williams, A. A. Talin, H. Yoon and M. S. Goorsky, Journal of Crystal Growth **171** (1), 12-20 (1997).

[85] T. L. Tansley and R. J. Egan, Physical Review B **45** (19), 10942-10950 (1992).

[86] T. L. Tansley and R. J. Egan, Physica B: Condensed Matter **185** (1), 190-198 (1993).

[87] V. W. L. Chin, T. L. Tansley and T. Osotchan, Journal of Applied Physics **75** (11), 7365-7372 (1994).

[88] B. R. Nag, Journal of Crystal Growth **269** (1), 35-40 (2004).

[89] R. S. Q. Fareed, R. Jain, R. Gaska, M. S. Shur, J. Wu, W. Walukiewicz and M. A. Khan, Applied Physics Letters **84** (11), 1892-1894 (2004).

[90] Y. Sato and S. Sato, Journal of Crystal Growth **146** (1), 262-265 (1995).

[91] S. M. Bedair, M. A. Tischler, T. Katsuyama and N. A. El- Masry, Applied Physics Letters **47** (1), 51-53 (1985).

[92] B. T. McDermott, K. G. Reid, N. A. El- Masry, S. M. Bedair, W. M. Duncan, X. Yin and F. H. Pollak, Applied Physics Letters **56** (12), 1172-1174 (1990).

[93] F. G. McIntosh, E. L. Piner, J. C. Roberts, M. K. Behbehani, M. E. Aumer, N. A. El-Masry and S. M. Bedair, Applied Surface Science **112**, 98-101 (1997).

[94] T. Inushima, T. Shiraishi and V. Y. Davydov, Solid State Communications **110** (9), 491-495 (1999).

[95] S. Michio, Japanese Journal of Applied Physics **36** (6A), L658 (1997).

[96] A. V. Blant, T. S. Cheng, N. J. Jeffs, L. B. Flannery, I. Harrison, J. F. W. Mosselmans, A. D. Smith and C. T. Foxon, Materials Science and Engineering: B **59** (1–3), 218-221 (1999).

[97] S. Yamaguchi, M. Kariya, S. Nitta, T. Takeuchi, C. Wetzel, H. Amano and I. Akasaki, Journal of Applied Physics **85** (11), 7682-7688 (1999).

[98] V. V. Mamutin, V. A. Vekshin, V. Y. Davydov, V. V. Ratnikov, T. V. Shubina, S. V. Ivanov, P. S. Kopev, M. Karlsteen, U. Söderwall and M. Willander, physica status solidi (a) **176** (1), 247-252 (1999).

[99] H. Lu, W. J. Schaff, J. Hwang, H. Wu, W. Yeo, A. Pharkya and L. F. Eastman, Applied Physics Letters **77** (16), 2548-2550 (2000).

[100] H. Lu, W. J. Schaff, J. Hwang, H. Wu, G. Koley and L. F. Eastman, Applied Physics Letters **79** (10), 1489-1491 (2001).

[101] H. Lu, W. J. Schaff, L. F. Eastman, J. Wu, W. Walukiewicz, V. Cimalla and O. Ambacher, Applied Physics Letters **83** (6), 1136-1138 (2003).

[102] H. Lu, W. J. Schaff, L. F. Eastman, J. Wu, W. Walukiewicz, D. C. Look and R. J. Molnar, Mater. Res. Soc. Symp. Proc. **743**, L4.10 (2002).

[103] H. Masataka and M. Toshiaki, Japanese Journal of Applied Physics **41** (5B), L540 (2002).

[104] V. Cimalla, C. Förster, G. Kittler, I. Cimalla, R. Kosiba, G. Ecke, O. Ambacher, R. Goldhahn, S. Shokhovets, A. Georgakilas, H. Lu and W. Schaff, physica status solidi (c) **0** (7), 2818-2821 (2003).

[105] S. Yoshiki, T. Nobuaki, S. Akira, A. Tsutomu and N. Yasushi, Japanese Journal of Applied Physics **40** (2A), L91 (2001).

[106] V. Y. Davydov, A. A. Klochikhin, R. P. Seisyan, V. V. Emtsev, S. V. Ivanov, F. Bechstedt, J. Furthmüller, H. Harima, A. V. Mudryi, J. Aderhold, O. Semchinova and J. Graul, physica status solidi (b) **229** (3), r1-r3 (2002).

[107] Y. Saito, T. Yamaguchi, H. Kanazawa, K. Kano, T. Araki, Y. Nanishi, N. Teraguchi and A. Suzuki, Journal of Crystal Growth **237–239, Part 2**, 1017-1021 (2002).

[108] Z. G. Qian, W. Z. Shen, H. Ogawa and Q. X. Guo, Journal of Applied Physics **92** (7), 3683-3687 (2002).

[109] Z. G. Qian, G. Yu, W. Z. Shen, H. Ogawa and Q. X. Guo, Physica B: Condensed Matter **318** (2–3), 180-187 (2002).

[110] J. Wu, W. Walukiewicz, W. Shan, K. M. Yu, J. W. Ager, E. E. Haller, H. Lu and W. J. Schaff, Physical Review B **66** (20), 201403 (2002).

[111] R. Goldhahn, A. T. Winzer, V. Cimalla, O. Ambacher, C. Cobet, W. Richter, N. Esser, J. Furthmüller, F. Bechstedt, H. Lu and W. J. Schaff, Superlattices and Microstructures **36** (4–6), 591-597 (2004).

[112] A. Kasic, E. Valcheva, B. Monemar, H. Lu and W. J. Schaff, Physical Review B **70** (11), 115217 (2004).

[113] A. Yamamoto, T. Tanaka, K. Koide and A. Hashimoto, physica status solidi (a) **194** (2), 510-514 (2002).

[114] A. G. Bhuiyan, A. Hashimoto and A. Yamamoto, Journal of Applied Physics **94** (5), 2779-2808 (2003).

[115] A. Yamamoto, M. Tsujino, M. Ohkubo and A. Hashimoto, Journal of Crystal Growth **137** (3), 415-420 (1994).

[116] P. Yung-Chung, L. Wen-Hsiung, S. Chen-Ke, L. Heng-Ching, I. C. Chung, C. Horng, L. Deng-Sung, L. Ming-Chih and C. Wei-Kuo, Japanese Journal of Applied Physics **38** (2R), 645 (1999).

[117] Y. Nanishi, Y. Saito and T. Yamaguchi, Japanese Journal of Applied Physics **42** (5R), 2549 (2003).

[118] B. Maleyre, S. Ruffenach, O. Briot, B. Gil and A. van der Lee, physica status solidi (c) **2** (7), 2309-2315 (2005).

[119] M. Drago, C. Werner, M. Pristovsek, U. W. Pohl and W. Richter, physica status solidi (a) **203** (7), 1622-1625 (2006).

[120] D. Skuridina, D. V. Dinh, M. Pristovsek, B. Lacroix, M. P. Chauvat, P. Ruterana, M. Kneissl and P. Vogt, Applied Surface Science **307**, 461-467 (2014).

[121] C. Heinlein, J. K. Grepstad, S. Einfeldt, D. Hommel, T. Berge and A. P. Grande, Journal of Applied Physics **83** (11), 6023-6027 (1998).

[122] T. Hashimoto, Y. Terakoshi, M. Yuri, M. Ishida, O. Imafuji, T. Sugino and K. Itoh, Journal of Applied Physics **86** (7), 3670-3675 (1999).

[123] M. Losurdo, P. Capezzuto, G. Bruno, G. Namkoong, W. A. Doolittle and A. S. Brown, Journal of Applied Physics **91** (4), 2508-2518 (2002).

[124] F. Dwikusuma and T. F. Kuech, Journal of Applied Physics **94** (9), 5656-5664 (2003).

[125] K. Xu, W. Terashima, T. Hata, N. Hashimoto, M. Yoshitani, B. Cao, Y. Ishitani and A. Yoshikawa, physica status solidi (c) **0** (7), 2814-2817 (2003).

[126] J. C. Lin, Y. K. Su, S. J. Chang, W. H. Lan, W. R. Chen, Y. C. Cheng, W. J. Lin, Y. C. Tzeng, H. Y. Shin and C. M. Chang, Optical Materials **30** (4), 517-520 (2007).

[127] Z. L. Xie, R. Zhang, B. Liu, L. Li, C. X. Liu, X. Q. Xiu, H. Zhao, P. Han, S. L. Gu, Y. Shi and Y. D. Zheng, Journal of Crystal Growth **298**, 409-412 (2007).

[128] N. Khan, A. Sedhain, J. Li, J. Y. Lin and H. X. Jiang, Applied Physics Letters **92** (17), 172101 (2008).

[129] W. Xinqiang, L. Shitao, M. Nan, F. Li, C. Guang, X. Fujun, T. Ning, H. Sen, J. C. Kevin, Z. Shengqiang and S. Bo, Applied Physics Express **5** (1), 015502 (2012).

[130] S. Junichi, A. Tsutomu, F. Tatsuya, M. Elison, P. Tomás and N. Yasushi, Japanese Journal of Applied Physics **52** (8S), 08JD06 (2013).

[131] S. S. Khludkov, I. A. Prudaev and O. P. Tolbanov, Russian Physics Journal **56** (9), 997-1006 (2014).

[132] M. Himmerlich, A. Knübel, R. Aidam, L. Kirste, A. Eisenhardt, S. Krischok, J. Pezoldt, P. Schley, E. Sakalauskas, R. Goldhahn, R. Félix, J. M. Mánuel, F. M. Morales, D. Carvalho, T. Ben, R. García and G. Koblmüller, Journal of Applied Physics **113** (3), 033501 (2013).

[133] E. Baghani and S. K. O’Leary, Applied Physics Letters **99** (26), 262106 (2011).

[134] N. Miller, E. E. Haller, G. Koblmüller, C. Gallinat, J. S. Speck, W. J. Schaff, M. E. Hawkridge, K. M. Yu and J. W. Ager, Physical Review B **84** (7), 075315 (2011).

2 CHAPTER 2: THIN FILM GROWTH TECHNIQUES UTILIZED FOR GROUP III-NITRIDES

The objective of this chapter is to give a brief introduction to the epitaxial growth techniques used in group III-N thin film depositions and their growth-related issues and solutions. Although, there are several growth techniques, this will focus the high pressure metal organic chemical vapor deposition (HP-MOCVD) and migration-enhanced plasma-assisted meatal organic chemical vapor deposition (ME-PA-MOCVD), which were used in this study for the InN growth, while giving a brief overview of hydride vapor phase epitaxy (HVPE), molecular beam epitaxy (MBE), atomic layer deposition (ALD), as well as typical metal organic chemical vapor deposition (MOCVD) will be given.

2.1 Epitaxy and Growth Related Issues

Epitaxy is the process of the deposition of a crystalline over layer onto a crystalline substrate. Basically, there are two kinds of epitaxy, homoepitaxy, and heteroepitaxy. Homoepitaxy is the deposition of an epitaxial layer which is the same material (isochemical in composition) as the substrate. Heteroepitaxy is the deposition of an epitaxial layer which is a different material (heterochemical in composition) from the substrate. The advantages of homoepitaxy growth are lower defect density and doping control due to the lattice match, thermal match, and same surface chemistry between the two phases. These advantages result in higher quality films. However, heteroepitaxy is often required in optoelectronic structures and bandgap engineered devices.

The five possible epitaxial growth modes are layer-by-layer or Frank-van der Merwe (FM-mode), step flow (SF-mode), layer plus island or Stanski-Krastanov (SK-mode), island or Volmer-Weber (VW-mode), and columnar growth mode (C-mode). The occurrence of these growth modes depends on the lattice mismatch between the substrate and the film, the flux of the crystallizing phase, the growth temperature, and the adhesion energy [1]. A schematic representation of the three most frequently occurring growth modes on a flat surface substrate is shown in Fig. 2.1.

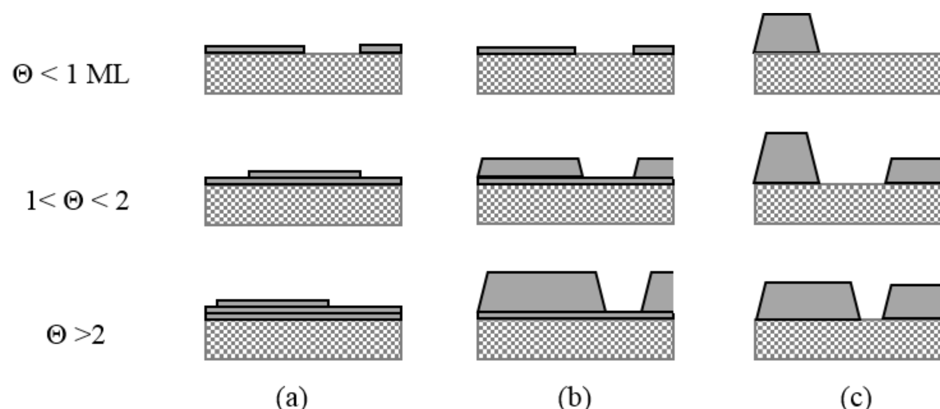

Figure 2.1 A schematic representation of the five most frequently occurring growth modes on a flat surface substrate. (a) layer-by-layer or Frank-van der Merwe (FM-mode), (b) layer plus island or Stanski-Krastanov (SK-mode), and (c) island or Volmer-Weber (VW-mode).
Θ is the monolayers coverage.

In the FM- mode (Fig. 2.1 (a)), atoms in the film are more likely to adhere to the substrate than to each other. Only after completing the bottom layer, is a new layer nucleated (2D growth). This type of growth mode can be observed in metal-metal systems and semiconductor growth on semiconductors. The VW-mode (3D growth) (Fig. 2.1 (c)) occurs when the atoms in the film are more likely to adhere to each other than to the substrate. Small clusters are nucleated on the substrate then new islands form on top of the clusters before filling the space between. This mode can be observed in metal growing on insulators and layer compounds such as mica. The SK- mode (Fig. 2.1 (b)) is an intermediate mode between the FK and VW modes. After the first few monolayers are formed, islands form on top of the intermediate layer. This mode occurs when the monotonic decrease in binding energy, characteristic for layer-by-layer growth, is disturbed [1].

2.1.1 Substrates

As mentioned in Chapter 1, structural and optoelectronic properties of the group III-nitride materials are influenced by the substrates and growth processes. Therefore, when choosing the substrate, the followings factors should be considered: the thermal mismatch, the lattice mismatch between the substrate and the overgrown layer, the availability on the market, and its cost. As mentioned in Chapter 1, several

substrates have been used and studied for InN epilayer growth. Lattice mismatch between the substrates and the group III-nitrides are tabulated in Table 2.1.

Table 2.1 Lattice mismatch with different substrates.

	Lattice mismatch (%)		
	GaN	AlN	InN
Sapphire (0001)	~16	~13	~25 [2]
Si (111)	17 [3]	19	~8
GaAs (111)		~ 20	~11.3
GaP (111)	17.2 [4]		~8
$MgAl_2O_4$ (111)	9.5 [5]		15
6H-SiC	3.4	~1	~14
Ge (111)	20 [6]		~ 11 [2]
AlN	~2.5	-	~13
GaN	-		~11

Even though, the lattice mismatch between sapphire substrates and the III-nitride films is higher than that of other substrates, sapphire (0001) is the most used substrate in group III-nitrides growth. Sapphire substrates are widely used due to the low cost, wide availability in different sizes, transparency, high temperature stability, as well as the high surface and crystal quality.

2.1.2 Solutions for Lattice-mismatched Sapphire Substrates

As discussed in chapter 1, several methods are being used to overcome the issues initiated by the lattice mismatch between the sapphire substrate and InN (or InGaN) films. Few of them are the substrate pretreatment and the insertion of the buffer layers and the intermediate layers between sapphire and III-nitride layer. In the InN growth, using an AlN or GaN layer in between the film and substrate can reduce the lattice mismatch from ~25% to 13% or 11%, respectively. The crystalline quality of the InN film can also be improved by through the nitridation of the sapphire substrate prior to the InN growth. This process changes the growth chemistry of the surface forming a thin nitrogen layer (AlN/ or AlN_xO_y) on top of the sapphire with N-species substituting the O-atoms [7].

2.2 Hydride Vapor Phase Epitaxy (HVPE)

HVPE is an attractive technique for growth of high quality, large diameter and high growth rate, which results in thick GaN layers (>200 μm). The thick GaN can be used as a free-standing substrate by separating the film from the sapphire substrate. In HVPE, a stream of HCl is passed through the III-metal (temperature around 860 °C) to form GaCl (or AlCl or InCl). These GaCl (or AlCl or InCl) are injected through a showerhead into the growth chamber and allowed to react with NH_3 at the substrate surface (growth temperature 950-1050 °C) to form III-nitride as in the Eq. 2.1 [8, 9].

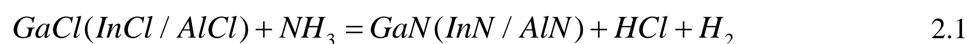

$$GaCl(InCl/AlCl) + NH_3 = GaN(InN/AlN) + HCl + H_2 \quad 2.1$$

A typical schematic of representation of a vertical reactor is shown in Fig. 2.2.

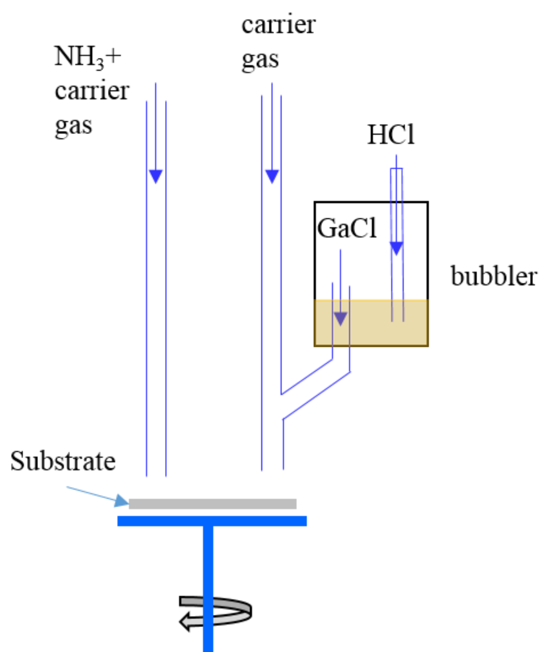

Figure 2.2 Schematic of a vertical HVPE reactor.
The figure is after Ref. [8].

There are several drawbacks in the use of HVPE techniques. One is the NH_3 dissociation which forms highly explosive NCl_3 by reacting with HCl. Another is associated with the use of HCl gas, which is corrosive, can quickly destroy the equipment in the reactor. Instead of HCl, some groups have been

used $GaCl_3$ to avoid this. P-type doping or AlGaN growth is difficult with HVPE, due to exchange reactions in magnesium-bearing or aluminum compounds with the hot quartz walls of the reactor [8].

2.3 Molecular Beam Epitaxy (MBE)

This is a versatile and precious technique for deposition thin semiconductors, metals or insulators. MBE uses nearly solid elements (in III-nitride growth, metal Al, Ga, or In); therefore, high temperature (above 100 °C) is required for elements vaporization. The elements are heated in separate Knudsen effusion or gas cells. In order to transport the vaporized materials, gas line temperature requires a higher temperature than the vaporization temperature. Thus, vaporized elements transport as beams of atoms or molecules in an ultrahigh vacuum environment, which minimizes the particle-particle interactions. However, in III-nitride growth, dissociation of a N_2 molecule into two reactive nitrogen atoms is difficult by thermal means since the triple bond between the two nitrogen atoms needs high energy. Therefore, III-nitrides are grown using plasma assisted (PA)-MBE where a plasma source (RF or electron cyclotron resonance plasma) is used to activate the N_2 [8]. In the PA-MBE process, III-metal or vapor beam from the effusion cells and plasma activated nitrogen are shot towards the heated substrate to form III-nitride. In order to improve the growth homogeneity, the substrate is rotated during the film growth. MBE requires ultra-high vacuum (UHV), typically around 10^{-6}-10^{-9} mbar growth, which is a relatively expensive growth method. Such high vacuums prevent the growth surface contamination from outgassing of O_2, CO_2, H_2O, and N_2 and therefore can produce high quality films. Additionally, MBE growth can control the growth thickness very precisely. Another advantage of MBE is the UHV allows the use in-situ characterization tools (RHEED, low energy electron diffraction, Auger electron spectroscopy, and modulated beam mass spectrometry) which is used to monitor the sample surface during growth. The abrupt interface and surface morphology, ability to grow complex heterostructures with many different layers and the low growth temperature are other advantages of MBE growth. MBE is seldom used in industry due to its low relative growth rate, high temperatures requirements, and its high cost. A schematic representation of a typical PA-MBE is depicted in Fig. 2.3.

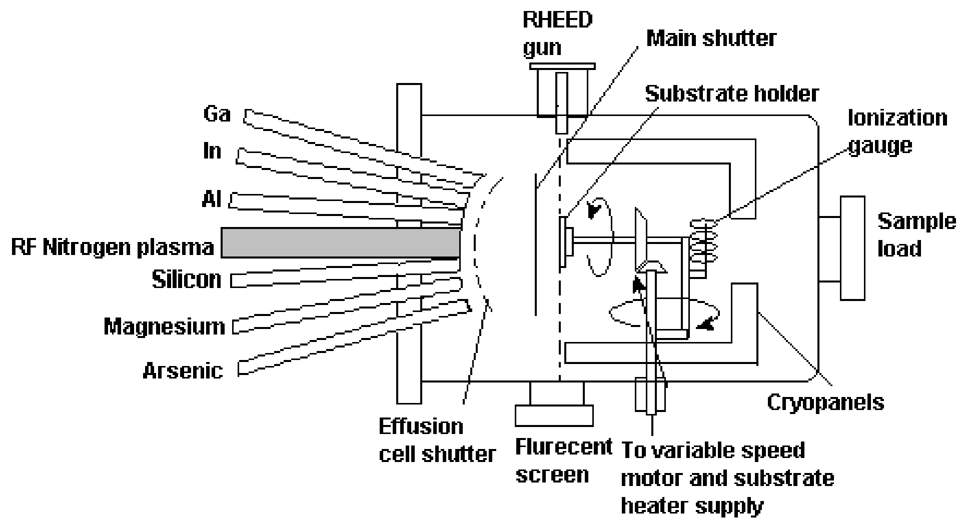

Figure 2.3 A schematic representation of PAMBE.
The figure is taken from Ref. [8].

2.4 Atomic Layer Deposition (ALD)

ALD was initially named as atomic layer epitaxy (ALE) and was introduced by the Suntola and Antson in 1977, depositing ZnS for flat panel displays [10, 11]. ALD, the more general name was adopted because this method was also developed to deposit non-epitaxial materials [12]. Due to its conformity and control over the material thickness and the composition originated from the cyclic, self-saturating nature of the process, the ALD has proven more advantageous than the other growth techniques. A schematic of a general ALD process is shown in Fig. 2.4, which is copied from Ref. [11].

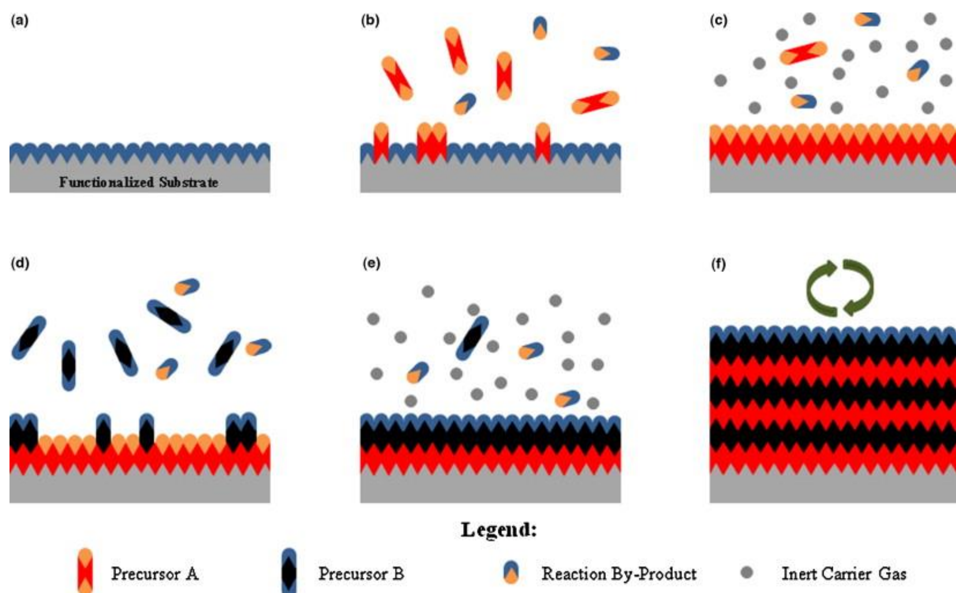

Figure 2.4 A schematic of a general ALD process. (a) Functionalized substrate surface (naturally or unnaturally). (b) Precursor A is pulsed and reacts with surface. (c) Remove the excess precursor and by-products by purging with inert carrier gas. (d) Precursor B is pulsed and reacts with surface. (e) Remove the excess precursor and by-products by purging with inert carrier gas. (f) Repeat the first-five steps until preferred thickness is reached.
The figure is copied from Ref. [11].

In the ALD process, the precursor is pulsed into the reactor under vacuum for a selected time duration, during each half-reaction. This allows precursor to completely react with the substrate surface through a self-limiting process and deposit an atomic layer (one monolayer) at the surface. Afterwards, to eliminate the unreacted precursor and by-products from the reaction, the reactor is purged with an inert gas. The, procedure is conducted for the counter-reactant precursor too. This whole process will cycle until desired film thickness is reached [11]. Since ALD growth is layer-by-layer process, the deposition rate is very slow. However, the layers are more uniform, as there is no reaction among the precursors and the reaction stops after all available sites occupied.

2.5 Metalorganic Chemical Vapor Deposition (MOCVD)

MOCVD is the most important manufacturing process for group III-V semiconductor growth. MOCVD is also known as OMCVD (organo-metallic chemical vapor deposition). Various kinds of MOCVD reactor designs are available. Commonly, there are two kinds of MOCVD reactors. One is based

on the horizontal laminar flow principle. In the other, chemicals are hosted into the reactor vertically through a showerhead. Usually, in MOCVD growth, Metal-organic compound and V-hydrides are used as group III and group V precursors, respectively. Typical group III precursors are TMAl (trimethylaluminum), TEAl (triethylaluminum), TMGa (trimethylgallium), TEGa (triethylgallium), TMIn (trimethylindium), and TEIn (triethylindium). In conventional MOCVD, NH_3 is used as the nitride precursor in III-nitride growth. MOCVD typically uses N_2, H_2 or a mixture of both as the carrier gas. In order to achieve high quality films, the use of high purity precursors and precise control of growth parameters, such as growth temperature and precursor ratios (V/III) are required.

The growth reactions occur at an open-tube system in the reactor. There are four main zones in the reactor that describe the growth mechanism: (i) precursor injection, (ii) mixing, (iii) boundary layer, and (iv) substrate surface. The MOCVD growth mechanism for GaN growth (with TMGa and NH_3 precursors) is illustrated in Fig. 2.5.

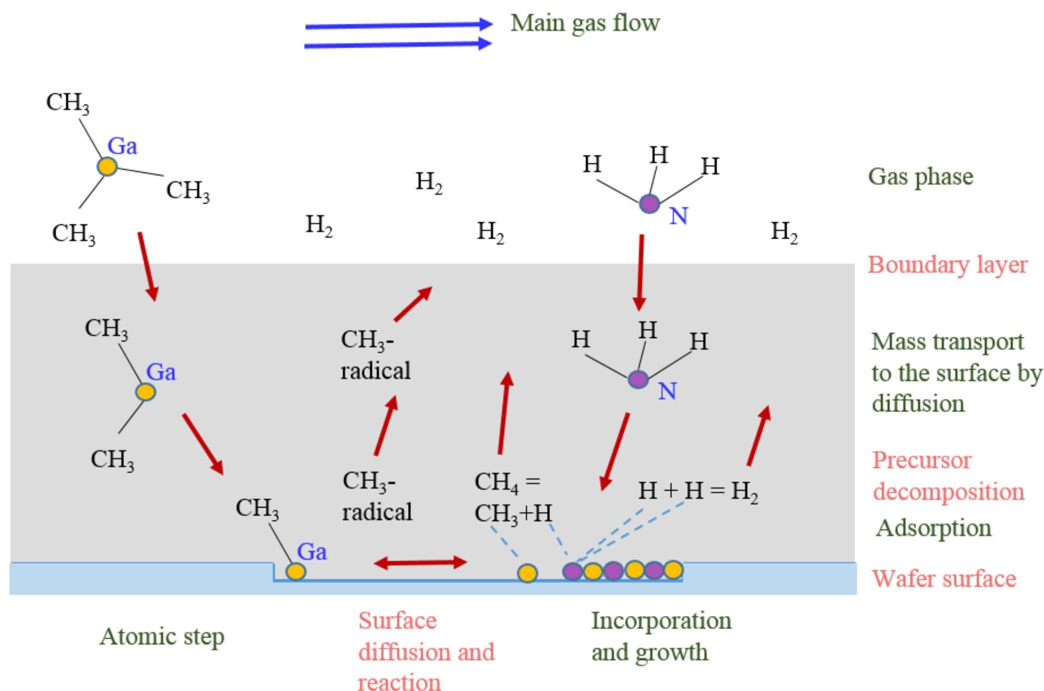

Figure 2.5 Basic transport and reaction steps for GaN growth in MOCVD reactor
The figure is after Ref. [13].

The growth rate depends on the growth temperature. Figure 2.6 illustrates the dependence of the growth rate on the growth temperature which is divided into three regions as described by Shaw [14].

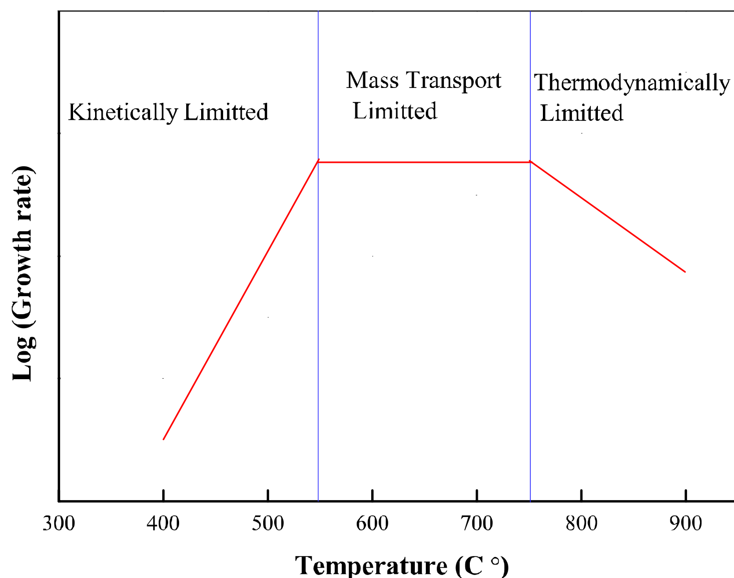

Figure 2.6 Thermal regimes of growth rate in MOCVD.

At low temperatures, (range about 400-550 °C), kinetics of chemical reactions that take place either on the surface of the substrate or in the gas-phase controls the growth rate. The mass transport of constituents through the boundary layer onto the substrate limits the growth rate under the intermediate temperature (range about 550-750 °C). The growth rate is constant in this region and only the boundary layer is dependent on temperature. In the third region, the decrease in growth rate with increasing temperature is thought to be the result of thermodynamic effects or reactant depletion due to upstream reactions [15, 16].

A typical MOCVD system can be grouped into four major components in term of their functions and gas flow streams: (i) precursor sources, (ii) gas delivery system for controlling precursor gasses or vapors into the reactor, (iii) reactor zone including a substrate holder and a heater, and (iv) exhaust system to remove waste [17]. A schematic of a typical MOCVD is depicted in Fig. 2.7 which is taken from Ref. [17] Chapter 6, Figure 6.8.

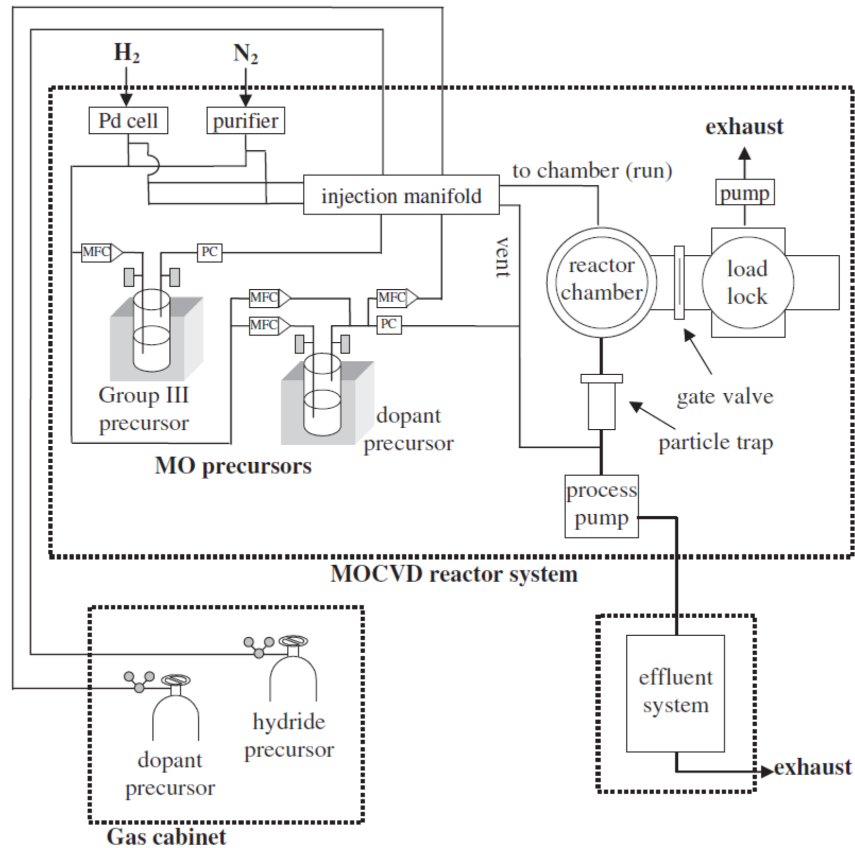

Figure 2.7 A schematic of a typical MOCVD.
The figure is taken from Ref.[17] Chapter 6, Figure 6.8.

The deposition rate of any MOCVD process can be controlled by the surface reaction rate or mass transport rate. Commercially, the deposition rate is controlled by the mass transport rate. In the shower-head reactor, which has become more common, the gasses are inserted from the showerhead flange through many small holes (~0.5 mm) toward the substrate. The showerhead uniformly distributes the re-actant gasses over the substrate yielding a uniform concentration field. Afterward, these gasses cross the boundary layer to the surface of the substrate via concentration diffusion. The close distance (~1cm) be-tween the showerhead and the substrate reduces the convection rolls and gas residence time (the time taken to remove mass by gas flow) [18]. In recent mathematical studies [18] of mass transport from a showerhead MOCVD reactor, it has been shown that the flow pattern is a stagnation flow and the vertical

velocity component, a point above the substrate which only depends on the vertical distance, is independent of the radial position. Also, the boundary layer thickness in stagnation flow is independent from the radial distance. Therefore, uniform velocity, concentration and temperature boundary layer can be built above the substrate. Furthermore, Hui [18] has shown that the there is an important effect of ceiling height of the reactor on the residence time and mass transport process. The small ceiling height leads to a short residence time, and diffusion plays an important role in axial transport, while both convection and diffusion are important in radial transport.

The advantages of this method are the large scale capability (multi-wafer achievable), ability to grow complex heterostructures, growth on patterned substrates and faster growth than MBE. Also, high purity materials and an abrupt interface between two materials can be obtained using this technique. However, since it is not possible to use RHEED in higher pressure, monitoring of exact growth rate is difficult in MOCVD. Additionally, the precursor materials used in this method are expensive.

2.6 High Pressure Metalorganic Chemical Vapor Deposition (HP-MOCVD or HPCVD)

When alloying ternary materials (InGaN, AlGaN, InAlN) using their binaries of InN, GaN, and AlN, in order to retain the same crystal structure, sufficient mixing of binaries is required. The deviation of the crystal structure from the ideal structure results in phase separation. The spinodal phase diagram calculations have shown a large unstable region at typical growth temperatures [19, 20]. For InGaN, the critical temperature has been found near 1250 ºC which exceeds the melting point of InN (1100 ºC). The calculated InN stability in GaN is less than 6% at the maximum growth temperature used for InGaN (800 ºC). These results indicated that InGaN alloys are unstable over most of the composition range at typical growth temperatures and the reported phase separation of InGaN could be a result of this [20]. However, there are many reports of InGaN growth over all of the composition range [19, 21, 22]. This disagreement could be explained by the reduction of the unstable region due to strain in the InGaN layer caused by the GaN substrate [19, 23].

The low pressure growth of InN and its alloys are limited due to the following issues. (i) The growth temperature window gap between InN and GaN or AlN requires the adjustment of the growth conditions for heterostructures and alloy growth and for each composition in alloys growth, (ii) low dissociation temperature of InN (~600 ºC), and the large partial pressure gap between trimethylindium and ammonia precursors. At low temperature, the cracking efficiency of ammonia is low hence high V/III ratio is required to avoid the metal droplets on the surface. There are two main advantages in using a higher growth temperature. One is, the mobility of the constituent can be increased, which may result in better quality films. The second is, the reduction of the growth temperature window gap between the binaries of InN and GaN (AlN), which may allow the stabilization of the InGaN alloy. The high pressure MOCVD approach is explored to utilize the growth process at elevated pressure in order to stabilize the surface of InN and InGaN at optimal growth temperatures [24].

A HP-MOCVD system is designed with a high-pressure horizontal narrow flow channel reactor for the III-nitrides and a real-time optical characterization system. Figure 2.8 (a) illustrates the view of the inner reactor, which consists of two halves. Each half is arranged symmetrically and include a substrate within a fused silica plate that is heated from the back side. This arrangement prevents a deposition on the opposite reactor wall and reduces heat induced turbulence above the substrate surface [24]. Figure 2.8 (b) shows a schematic of heating configuration.

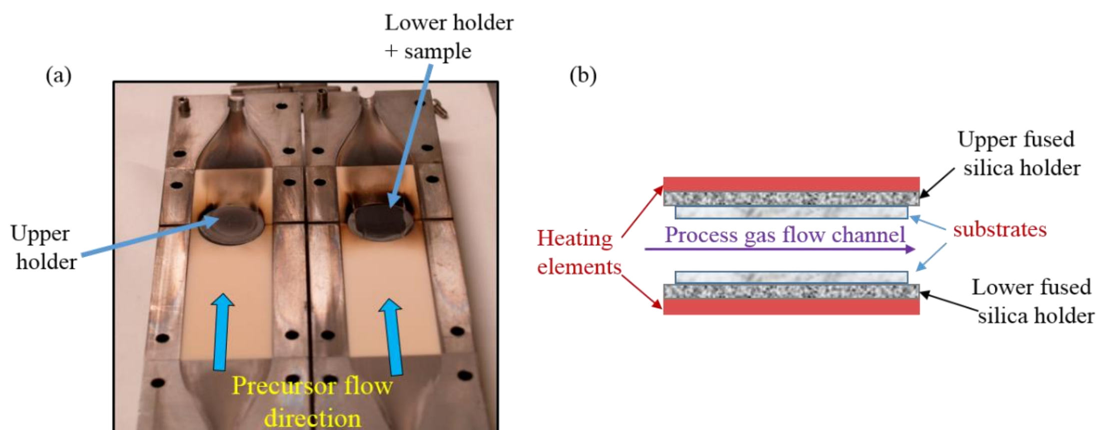

Figure 2.8 (a) A view of upper and lower halves of the inner reactor and (b) A schematic of heating configuration of inner reactor for HP-MOCVD reactor.

The height of the reactor channel is set as 1 mm in order to reduce the precursor length at elevated pressure and to optimize the use of gasses. Also, adjustment of the height of the reactor above the growth surface is required for optimum precursor utilization, because the thickness of the surface boundary layer has an inverse square-root of pressure relation. A constant cross section is upheld from gas inlet, throughout the reactor, to minimize flow induced turbulence in the reactor. The inner reactor cylinder is surrounded by an outer cylinder which can be pressurized up to 100 bar [24]. A pulsed precursor injection is utilized to attain compression of the precursors to the desired pressure, minimization of gas phase reactions, optimization of nucleation kinetics, and analysis of gas phase and surface decomposition dynamics in real-time [25].

In order to observe and understand the gas phase dynamics and surface chemistry, three real-time optical techniques are used in the HP-MOCVD system. As shown in Fig. 2.9 (The figure is adapted from Ref.[25, 26]), the optical access ports are integrated along the centerlines of the substrates, perpendicular to the flow direction, in the flow channel reactor, and are entered through the back side of the substrate.

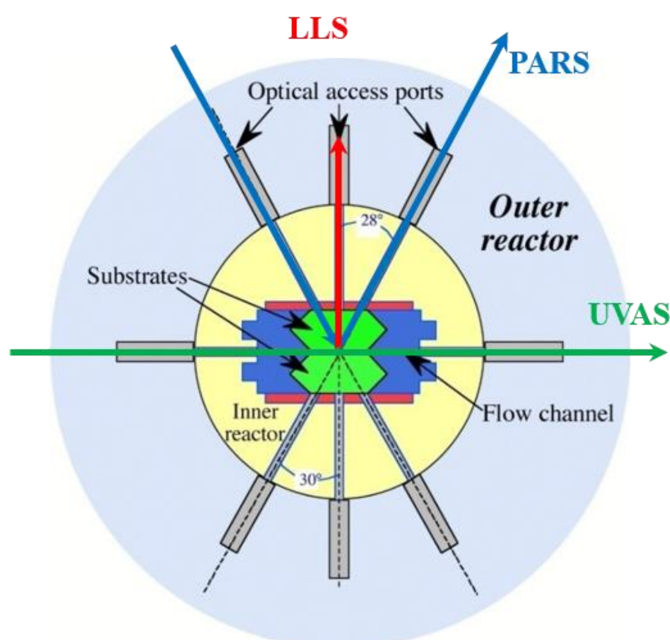

Figure 2.9 A schematic of cross-sectional view of the HP-MOCVD reactor with the optical access ports.

Precursor's arrival times and their decomposition are monitored by ultra-violet absorption spectroscopy (UVAS). Principal angle reflection spectroscopy (PARS) is utilized to monitor and determine the film thickness and change in dielectric constant of the film. Laser light scattering (LLS) is used to understand the surface roughness and crystalline quality of the grown layer.

2.7 Migration Enhanced Plasma Assisted Metalorganic Chemical Vapor Deposition (MEPA-MOCVD)

MEPA-MOCVD is another approach explored to overcome the growth issues discussed in section 2.1 and 2.6. This has been developed into the MOCVD system by integrating two approaches, migration enhanced (ME) and the plasma assisted (PA) techniques. The migration enhanced epitaxy which is a low temperature film growth technique was originally introduced to MBE system for the development of GaAs and AlAs films [27]. In 1997, it was applied to group III-nitride growth by Hooper et al. [28]. In this technique, the delivery of metal and nitrogen precursors are separated in time. Thus, the less volatile group III metal precursors are given extra time to migrate along the growth surface to energetically favorable sites via adatom diffusion. Then, the active nitrogen species are dosed to the growth front of the materials to form stationary molecules [28, 29]. This process is repeated for multiple cycles until sufficient film thickness is reached. However, until recently, for group III-nitrides, in order to prevent metal droplets from forming during metal-organic deposition, migration enhanced epitaxy has been limited to approximately a monolayer at a time (for each cycle, the deposition of metal layers is equal to the thickness of a metal wetting layer). Therefore, the growth rate was very low. However, recently, it has shown that a relatively high growth rate can be achieved even with the presence of meatal droplets by migration enhanced epitaxy MBE [30-32].

This technique has been further developed into the MEAglow MOCVD system for group III-nitride growth by Butcher et al. [29, 30]. The MEAglow system operates with a recently developed oxygen-free hollow cathode plasma source. The source can be operated at a RF frequency of 13.56 MHz with a maximum plasma power of 600 W and includes two hollow cathode arrays: ground plane and RF electrode. Due

to the self-biasing at the electrode, RF electrode is more cathodic than the ground plane, hence, higher plasma density at the RF electrode. However, plasma works as the anode for both electrodes [30]. The advantages of this plasma source are, it can achieve higher electron densities than the parallel plate capacitive type plasma sources, and it can be scaled into a large areas by increasing the number of holes (each hole that can independently operate).

At Georgia State University, a customized showerhead injection system with the recently developed MEAglow oxygen-free hollow cathode H_2/N_2 plasma source has been integrated into a traditional MOCVD system. In this system, precursors can be operated in a pulsed or continuous delivery mode. The growth pressure of the reactor can be operated in the range of 1-10 mbar. This system can narrow the growth temperature gap between III-N's binaries by kinetic means, using the kinetic energies of ionized nitrogen fragments in the afterglow plasma regime to stabilize the growth surface as well as group V-precursor fragments [33]. Thus, a significant relatively low growth temperature can be used compare to traditional MOCVD system. A schematic of a MO and N* plasma precursor injection modulation in MEPA-MOCVD system are illustrated in Fig. 2.10.

As shown in the Fig. 2.10, it is possible to have MO and N* plasma overlap or completely separate them. By tailoring the temporal interaction between MO precursors and N* plasma, the active species in the gas phase and the growth surface can be controlled. As well as, the epitaxial film deposition process is dependent on various parameters such as precursor separation times, growth temperature, plasma and MO exposures, reactor pressure, and plasma power which controls the V/III ratio indirectly.

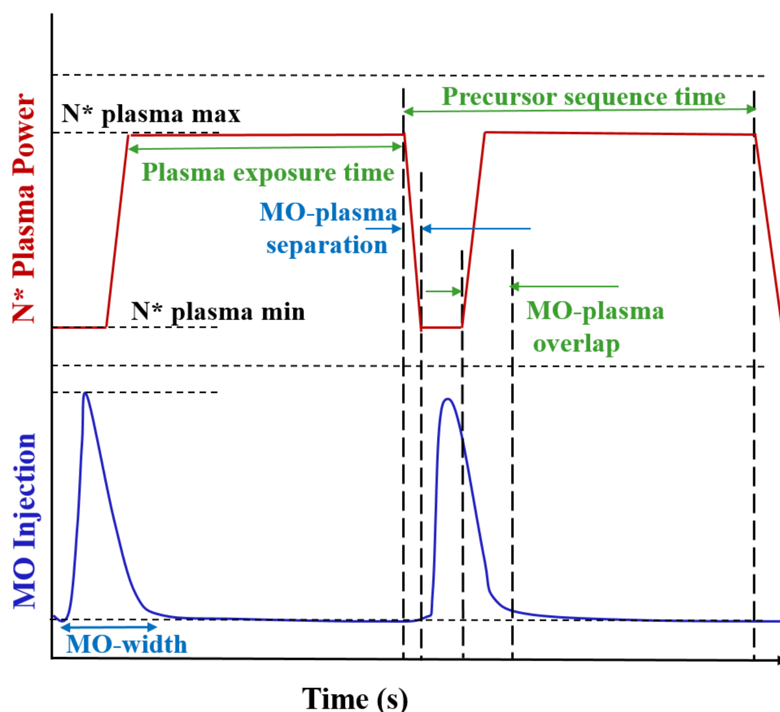

Figure 2.10 A schematic of a MO and N* plasma precursor injection modulation in MEPA-MOCVD system The epitaxial film deposition process is dependent on the various parameters such as precursor separation times, growth temperature, plasma and MO exposures, reactor pressure, and plasma power which controls the V/III ratio indirectly.

2.8 References

[1] M. A. Herman, W. Richter and H. Sitter, *Epitaxy : Physical Principles and technical Implementation*. (Springer-Verlag, New York, 2004).

[2] E. Trybus, G. Namkoong, W. Henderson, W. A. Doolittle, R. Liu, J. Mei, F. Ponce, M. Cheung, F. Chen, M. Furis and A. Cartwright, Journal of Crystal Growth **279** (3–4), 311-315 (2005).

[3] B. S. Zhang, M. Wu, X. M. Shen, J. Chen, J. J. Zhu, J. P. Liu, G. Feng, D. G. Zhao, Y. T. Wang and H. Yang, Journal of Crystal Growth **258** (1–2), 34-40 (2003).

[4] S.-T. Li, J.-X. Cao, G.-H. Fan, Y. Zhang, S.-W. Zheng and J. Su, Chinese Physics B **19** (10), 107206 (2010).

[5] T. Matsuoka, Superlattices and Microstructures **37** (1), 19-32 (2005).

[6] R. Lieten, Vrije Universiteit Brussel, 2008.

[7] F. Dwikusuma and T. F. Kuech, Journal of Applied Physics **94** (9), 5656-5664 (2003).

[8] N. N.M, Y. Z. zhen, L. Jiawei and X. Y. bou, Journal of Microwaves and Optoelectronics **2** (3) (2001).

[9] M. Rahman and N. Hasan, International Journal of Thin Films Science and Technology **5** (1), 45-49 (2016).

[10] T. Suntola and J. Antson, Patent No. 4058430 (November 15 1977).

[11] R. W. Johnson, A. Hultqvist and S. F. Bent, Materials Today **17** (5), 236-246 (2014).

[12] S. M. George, Chemical Reviews **110** (1), 111-131 (2010).

[13] X. Xu, Stanford University, School of Engineering *MOCVD growth of III-V & III-N nanostructures, thin films and heterostructures,* 07-05-2016, https://snf.stanford.edu/SNF/processes/mocvd-workshop/mocvd-workshop.../file

[14] D. W. Shaw, Journal of Crystal Growth **31**, 130-141 (1975).

[15] L. M. McGill, Dissertation, Massachusetts Institute of Technology, 2004.

[16] G. B. Stringfellow, *Organometallic Vapor-Phase Epitaxy: Theory and Practice*. (Academic Press, San Diego, CA, 1989).

[17] A. C. Jones and M. L. Hitchman, *Chemical Vapour Deposition: Precursors, Processes and Applications*. (Royal Society of Chemistry, 2009).

[18] H. Li, Journal of Semiconductors **32** (3), 033006 (2011).

[19] C. Tessarek, S. Figge, T. Aschenbrenner, S. Bley, A. Rosenauer, M. Seyfried, J. Kalden, K. Sebald, J. Gutowski and D. Hommel, Physical Review B **83** (11), 115316 (2011).

[20] I. h. Ho and G. B. Stringfellow, Applied Physics Letters **69** (18), 2701-2703 (1996).

[21] T. Kuykendall, P. Ulrich, S. Aloni and P. Yang, Nat Mater **6** (12), 951-956 (2007).

[22] M.-I. Richard, M. J. Highland, T. T. Fister, A. Munkholm, J. Mei, S. K. Streiffer, C. Thompson, P. H. Fuoss and G. B. Stephenson, Applied Physics Letters **96** (5), 051911 (2010).

[23] S. Y. Karpov, MRS Internet Journal of Nitride Semiconductor Research **3** (1998).

[24] N. Dietz, H. Born, M. Strassburg and V. Woods, MRS Online Proceedings Library Archive **798**, Y10.45 (16 pages) (2003).

[25] V. Woods and N. Dietz, Materials Science and Engineering: B **127** (2–3), 239-250 (2006).

[26] M. J. L. Bügler, Dissertation, Technische Universität Berlin, 2013.

[27] H. Yoshiji, K. Minoru and Y. Hiroshi, Japanese Journal of Applied Physics **25** (10A), L868 (1986).

[28] S. E. Hooper, C. T. Foxon, T. S. Cheng, N. J. Jeffs, G. B. Ren, D. E. Lacklison, J. W. Orton and G. Duggan:, in *Proc. MRS III–V Nitrides Symp.* (1997), pp. 325.

[29] K. S. A. Butcher, B. W. Kemp, I. B. Hristov, P. Terziyska, P. W. Binsted and D. Alexandrov, Japanese Journal of Applied Physics **51** (1S), 01AF02 (2012).

[30] K. S. A. Butcher, D. Alexandrov, P. Terziyska, V. Georgiev and D. Georgieva, physica status solidi (c) **9** (3-4), 1070-1073 (2012).

[31] E. Trybus, W. A. Doolittle, M. Moseley, W. Henderson, D. Billingsley, G. Namkoong and D. C. Look, physica status solidi (c) **6** (S2), S788-S791 (2009).

[32] T. Yamaguchi, D. Muto, T. Araki, N. Maeda and Y. Nanishi, physica status solidi (c) **6** (S2), S360-S363 (2009).

[33] D. Seidlitz, M. K. I. Senevirathna, Y. Abate, A. Hoffmann and N. Dietz, presented at the Fourteenth International Conference on Solid State Lighting and LED-based Illumination Systems, San Diego, CA, **Proc. SPIE 9571** (2015).

3 CHAPTER 3: CHARACTERIZATION TECHNIQUES

Characterization of group III-N semiconductor materials can be performed during the growth (in-situ) or after the growth (ex-situ). Different kinds of characterization tools are used to study the fundamental properties of the material, and the characterization techniques based on electromagnetic (EM) radiation (infrared to X-ray) are the most effective among these techniques. Most of characteristics of the semiconductors can be extracted through these EM radiation techniques. The phonons (by quantum vibration), the electronic band structure and the bandgap (absorb EM radiation), free electrons and holes (absorb EM radiation when they are moving), and defects and impurities (interact with EM radiation by their own lattice vibrations or by ionization process) of the crystal can be examined in the wavelengths from ultraviolet to the millimeter range [1]. Furthermore, EM radiation can be used to measure the dimensions and explore the interfaces of semiconductor microstructures. Hence, EM radiation is useful in examination of the structure and properties of a semiconductor. Among many characterization techniques, the optical techniques are more manifest, because they are fast, usually non-destructive, and required little sample preparation. These techniques explore the change in intensity, energy, phase, direction, or polarization of light after interaction of the material [2].

This chapter will discuss the Atomic Force Microscopy (AFM) in briefly, which is a non-optical technique, and four optical characterization methods: X-Ray diffraction (XRD), Photoluminescence spectroscopy, Raman spectroscopy, and Fourier Transform Infrared (FTIR) spectroscopy.

3.1 Atomic Force Microscopy (AFM)

Atomic force microscopy (AFM) measures the forces between a sharp tip (diameter ~20 nm) which connects on to a flexible cantilever, and the sample surface, and gives a three-dimensional topography d of the surface. Figure 3.1 illustrates the basic component of a typical AFM system.

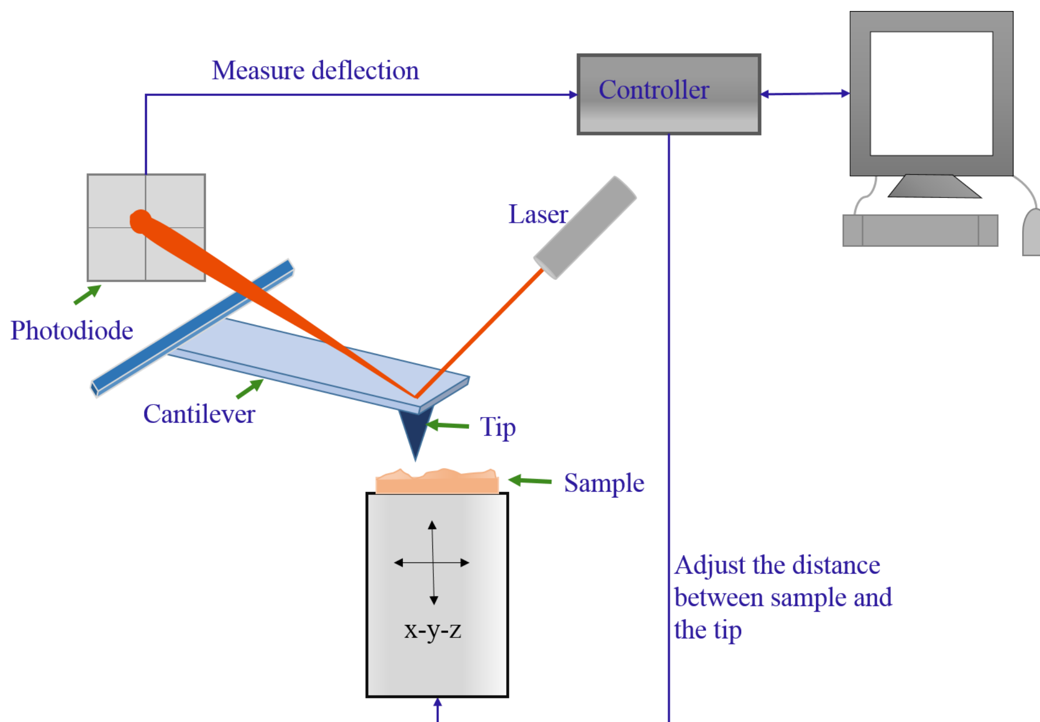

Figure 3.1 A schematic of a typical AFM.

Usually, AFM does not measure the forces between the tip and sample surface directly. They calculate by the Hook's law,

$$F = -kx \qquad 3.1$$

This force (F) depends on the stiffness [the spring constant (k)] and cantilever deflection (distance between the tip and the sample surface). Usually, in AFM, the beam bounce method (an optical lever technique) is used to measure the cantilever deflection. Here, a semiconductor laser diode beam is focused onto the back of the cantilever. Then, it is reflected onto a position sensitive photodiode detector, which measures the bending of the cantilever during the tip is raster-scanning across the sample. A map of the topography and other properties of the surface are generated using the change in force (small forces cause less deflections) as a function of position.

In AFM, there are three essential components which need to be controlled in order to achieve the near atomic resolution. (1) Cantilever with a sharp tip: The cantilever stiffness should be less than the effective spring constant holding atoms together (order of 1-10 nN/nm). The radius of curvature of the tip

should be smaller (less than 20-50 nm). (2) The scanner that controls the x-y-z position: A piezo-electric tube scanner is used to control the movement of the sample in the x, y, and z-directions or the tip. (3) The feedback control and loop: there are two principal modes that AFM can operate, which are the with the feedback control and the without the feedback control. With the feedback control mode: This operation mode is also called as constant force mode. In this mode, moving the sample up and down, the piezo will adjust the tip-separation to maintain a constant force. Without the feedback control mode: the microscope is operating in the deflection mode, and this mode is useful for imaging very flat samples at high resolution.

There are many ways to adjust the contrast of the image, and the three general modes are (1) contact mode, (2) non-contact mode, and (3) tapping mode. The three modes regimes in the forces-distance graph are shown in Fig. 3.2. In the contact mode, the tip is in intimate contact with the surface and the force on the tip is repulsive. The force between the tip and the sample is kept constant by maintaining the constant cantilever deflection. This mode is useful when a rough sample is scanning. In the non-contact mode, the tip does not contact with the sample. The tip is oscillated slightly above the surface at its resonant frequency and a constant oscillation amplitude is maintained during the scanning. The tapping mode is operating somewhere in between contact and non-contact modes [3]. In this study, non-contact mode is used.

In order to process (such as filtering, background subtraction), display (changes the view of image), analyze (quantitative information of the sample, such as roughness), and report the sample image, a computer software is used. The RMS (root-mean-squared) surface roughness can be calculated using following Eq.3.2 [4].

$$R_q = \sqrt{\frac{1}{N}\sum_{i}^{N}\left(Z_i - Z_{ave}\right)^2}; \qquad \text{where,} \quad Z_{ave} = \sum_{i}^{N} Z_i / N \tag{3.2}$$

Here, Z_i, N, and Z_m are the height at the i th row or column of the surface scan, number of rows and columns of the scanned area, and average height, respectively.

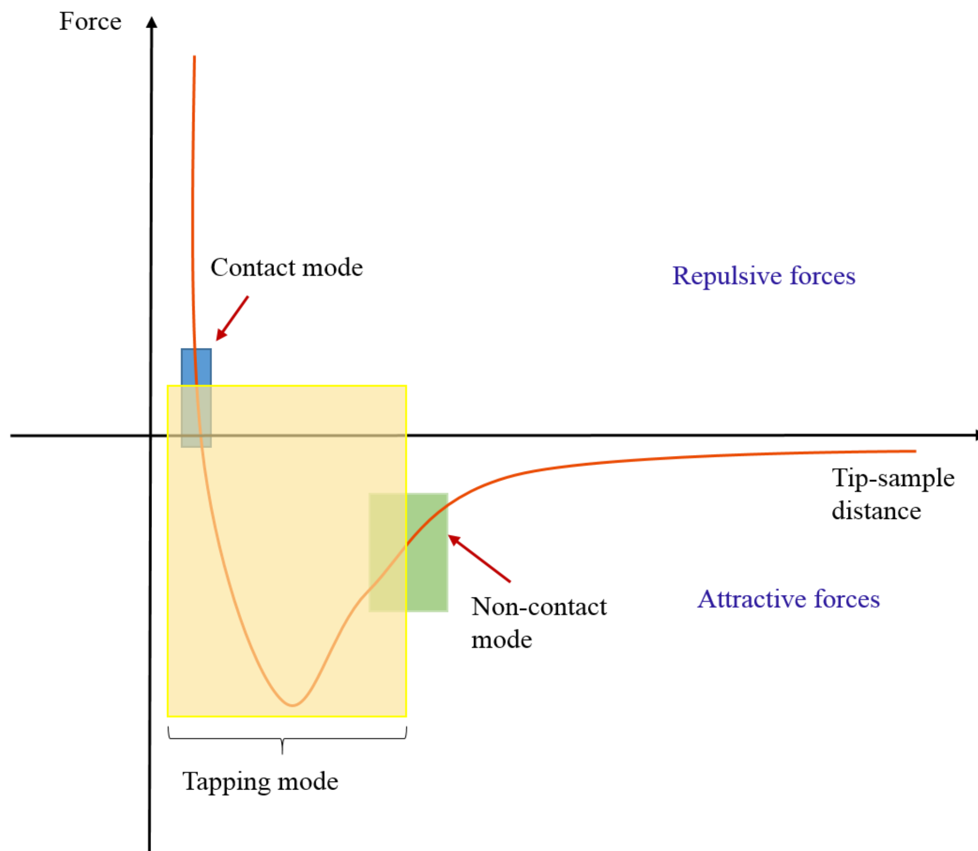

Figure 3.2 The typical force-distance curve and different modes and regimes of the tip-surface interaction in an AFM.

3.2 X-Ray Diffraction (XRD)

In one way or another, the optical or electronic properties of the semiconductor depend on its structural properties. There are many structural forms for the semiconductors materials and which are required a wide range of experimental techniques to analyze them. Structural properties can be basically divided into two: the macroscopic and the microscopic. Then, the structural parameters of materials can be categorized into those subdivisions as in Table 3.1 [5].

X-ray diffraction is a powerful tool for structural analysis. Which kind of information can be determined from it, is dependent on the sample itself. If the sample contains many crystallites, strains, phases, orientations, etc., separating of them is not quite an easy task. However, some properties can be

obtained rather accurately while others can be obtained by extending the range of experiments. The structural information of the sample may be limited to some average parameters, and its variations because the structural probe measures an average of a region or analyze an unrepresentative region of an inhomogeneous sample [5]. For highly inhomogeneous structural types, some long-range order, orientation distribution and their variations will be averaged by the X-ray diffraction. This averaging can be done in several ways, within a coherently diffracting volume and the X-ray beam dimensions on the samples. X-ray analysis techniques depend on the material, the property of interest, the flexibility of the diffractometer, the X-ray wavelength, etc., and the understanding of these are important when making a reliable analysis of the sample [5]. Figures 3.3 and 3.4 show a typical macroscopic and microscopic properties of a layered structure [5]. The probe is defined not only two dimensionally but also some depth into the sample. Therefore, the probe brings in all the information of the sample as shown to create a signal.

Table 3.1 Various structural parameters used in defining materials.

Type	General property	**Specific property**
Macroscopic	Shape	Layer thickness Lateral dimensions
	Form	Amorphous Polycrystalline Single Crystal
	Composition	Structural Phase Elements present Phase extent
	Orientation	General preferred texture Layer tilt
	Distortion	Layer strain tensor Lattice relaxation Warping
	Homogeneity	Between analyzed regions
	Interfaces	Interface spreading
	Density	Porosity Coverage
Microscopic	Shape	Average crystallite size Crystallite size distribution
	Composition	Local chemistry
	Orientation	Crystallite tilt distribution
	Distortion	Crystallite inter-strain distribution Crystallite intra-strain distribution Dislocation strain fields Point defects Cracks Strain from precipitates
	Interface	Roughness laterally
	Homogeneity	Distribution within region of sample studied

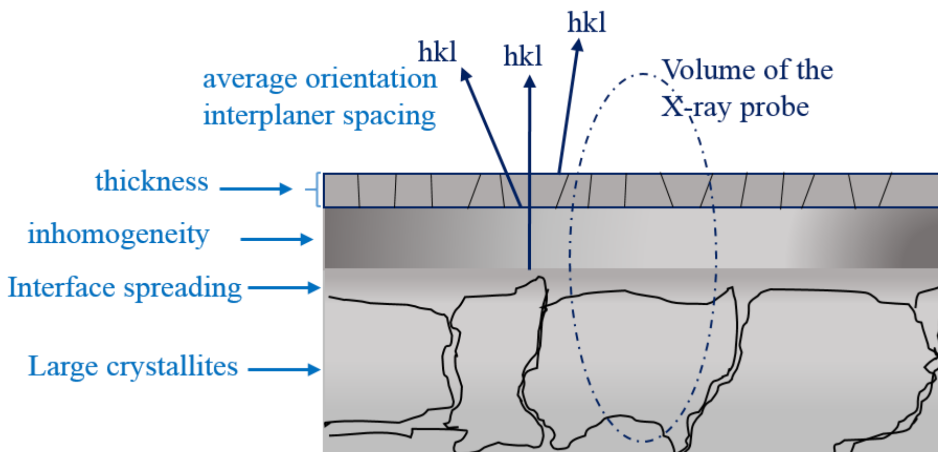

Figure 3.3 The main macroscopic parameters that characterize a layered structure.

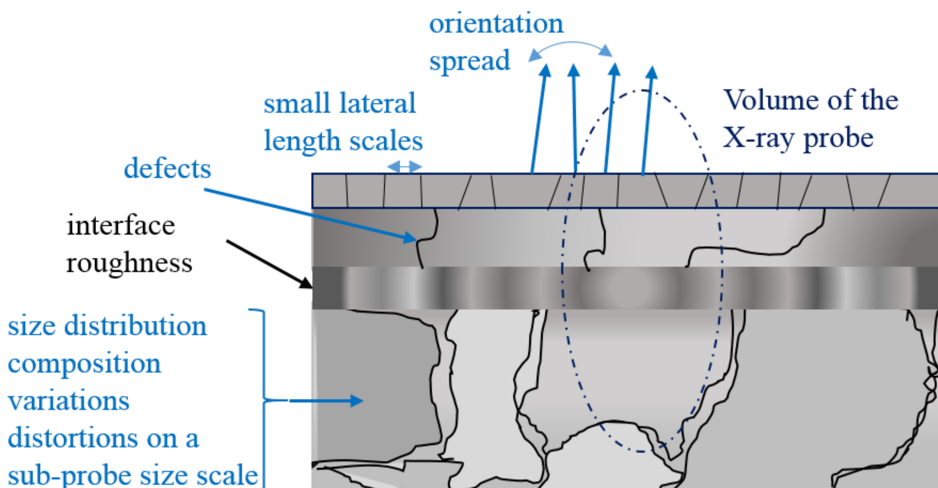

Figure 3.4 The main microscopic parameters that characterize a layered structure.

The interaction of the X-ray photon with the sample can occur in many different ways and that can depend on the energy of the photon and the nature of the sample. Hence, the X-ray photons are electromagnetic and it has the same nature as light, however shorter wavelength and the electric field vector interacts with the sample most strongly. However, the magnetic interactions are only seen in special conditions and which is very small.

X-rays are generated by colliding high speed electrons with a metal target (typically Cu) [6]. Generally, monochromatic x-rays are chosen for XRD. As these x-rays collide with the crystal at a certain angle of incident, intense reflected x-rays are produced by constructive interference. In order to occur constructive interference, the path difference AB (as shown in Fig. 3.5) is equal to an integer multiple of the wavelength. When the constructive interference occurs, the angle between the incident beam and line parallel to the surface and the angle between the diffracted (scattered) x-ray to a parallel line to the surface are equal; therefore the path difference can be calculated as a function of the lattice spacing and the angle [7]. This phenome is known as the Bragg's law, which is expressed by the Eq. 3.3. The conditions required for Bragg's diffraction are depicted in Fig. 3.5 [8].

$$n\lambda = 2d_{hkl}\sin\theta \qquad 3.3$$

where, n, λ, d_{hkl}, and θ are the order of reflection (an integer), incident x-ray wavelength, the interplanar spacing of the crystal, and angle of incidence, respectively. h, k, l are the Miller indices.

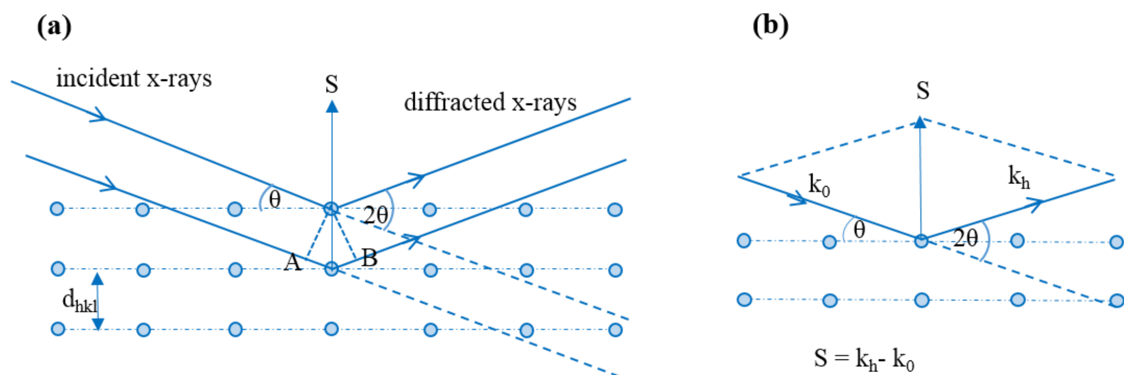

Figure 3.5 Schematic representation of x-ray diffraction; (a) conditions required for Bragg's diffraction to be occurred and (b) an illustration showing the relationship of the incident (k_0), diffracted (k_h), and scattering (S) vectors with respect the crystal.

The angle 2θ (diffracted angle) between the incident x-rays and the detector, is measured experimentally. The crystal behaves as a 3D diffraction grating. When the sample or the detector (or both) moves, a 3D array of diffraction maxima is generated. Each set of crystal planes generates a diffraction

spot. The positions and the shapes of the diffraction spots are inversely related to the spacing between the crystal planes and the size of the crystallites. The crystal planes and the diffraction spots are related to the real space and the reciprocal space, respectively and the latter form a 3D reciprocal lattice [8]. The diffraction process can also be demonstrated with respect to the reciprocal lattice as shown in Fig. 3.5 (b). The direction of the S vector depends on the angle ω. This is often illustrated by constructing of Ewald sphere. The reciprocal lattice can be investigated using the scattering vector (the probe) and magnitude of the S vector dependence on the angle 2θ [8].

By rotating the detector and the sample in a diffractometer, reciprocal space can be found. Typically, a diffractometer includes an x-ray source and a detector with incident and/or diffracted beam conditioners. Mostly, for the III-nitrides analysis, high resolution (HR) diffractometers are required [8]. Figures 3.6 (a) and (b) illustrate the example geometries used in the HR diffraction and the sample reference frame with axes of rotation in the set up. HR diffractometer is equipped with a primary monochromator to filter out unwanted wavelength, reduce $\Delta\lambda$ (the wavelength spread of the radiation), and reduce δ (the incident beam divergence).

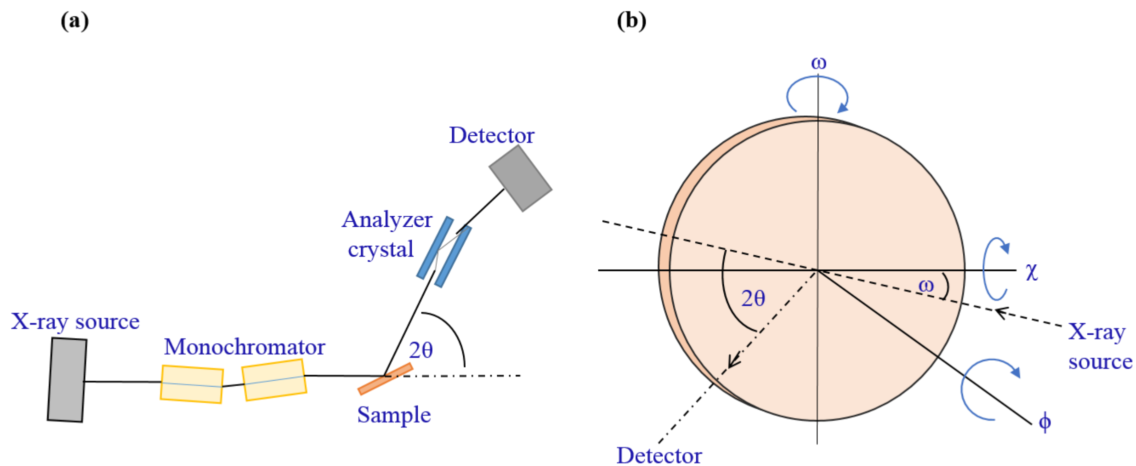

Figure 3.6 (a) The example geometries for the HR diffraction and (b) Sample reference frame with axes of rotation.
The ϕ axis projects out of the plane of the page. ω and χ axes are in the plane of the page [8].

HRXRD has two instrumental configurations; double axis and triple axis. In the double axis configuration, the detector is opened and all Bragg angles (2θ) are measured simultaneously [9]. In the triple axis configuration, there is a slit or analyzer crystal before the detector to define the 2θ direction. This configuration will provide a good 2θ resolution, even though it gives a lower intensity [8].

There are several scan types available according to the sample axes rotation. Figure 3.6 (b) shows the sample axes of rotation in a typical ‘four circle’ diffractometer and Table 3.2 summarizes the available scan type on HR diffractometers. Each of these scan types are used to in extracting the different type of sample information. The type “ω-scans” is used to measure the quality of the films by scanning the diffraction spots in arc. The broadening is used to detect the dislocations and the wafer curvature. The $\omega - 2\theta$ scans type uses for lattice parameter determination.

The lattice parameter c can be calculated for the hexagonal systems, by measuring the two high-angle symmetric reflections (d_{0006} and d_{0004}), directly using the Eq. 3.4 [8].

$$\frac{1}{d_{hkl}^2} = \frac{4}{3}\frac{h^2 + k^2 + hk}{a^2} + \frac{l^2}{c^2} \qquad 3.4$$

From high-angle asymmetric reflections measurements (usually, $d_{10\text{-}15}$, $d_{20\text{-}25}$, or $d_{20\text{-}24}$) and the previously calculated lattice parameter value “c”, the lattice parameter “a” can be determined. Note that this is just a quick method for determination of lattice parameters.

There are several x-ray techniques that can be used to learn about sample information. Table 3.3 are presented the x-ray techniques and the type of the sample information that can be extracted from the certain technique. This shows that the HRXRD coupled scan or RSM (reciprocal space map) is the best technique that can be used to analyze the thickness, composition, lattice strain/relaxation, and orientation of the nearly perfect and the textured epitaxial films. Here, coupled scan is a plot of scattered X-ray intensity versus 2θ, however, ω changes the way that is related to 2θ [9].

Table 3.2 Available scan type on HR diffractometers.
ω is the angle between incident rays and sample surface. $\omega - 2\theta$ is the angle between the incident and diffracted rays [8].

Scan type	Description
$2\theta - \omega$	The x-ray source or the sample is rotating by ω while detector is rotating by 2θ keeping the angular ratio as 1:2. The x-axis unit is 2θ . In reciprocal space, S moves outwards from the origin and the length of S changes, direction of S stays the same and depends on the offset. If no offset and $\omega = \theta$, which is a symmetrical scan ($\theta - 2\theta$) which is vertical in reciprocal space. Standard type for powder diffraction.
$\omega - 2\theta$	Like $2\theta - \omega$ scan, however, x-axis is ω Standard for HR and reflectivity work.
2θ	Detector is moving while the sample and the source is at stationary. Direction and length of S change. S traces an arc along the circumference of the Ewald sphere. Both direction and the length of S change.
ω-scan	The sample is rotating about the ω axis and the detector is at stationary. In reciprocal space, S traces an arc centered on the origin. The length of S remain the same, direction of the S changes.
Q-scan	Software can use to scan ω and 2θ in non-integer ratios, scanning S along a given direction in reciprocal space. It can collect reciprocal space maps of any preferred shape.
ϕ	Rotate the sample about the ϕ axis, generally in the plane of the sample. The length of the S remains the same and sample moves, bringing the reciprocal lattice spot through S, thus, the direction of the S changes with respect to the sample.
χ	Same as ϕ scans, except that sample rotation about the χ axis (plane of the sample rote with respect to the incident).

Table 3.3 The x-ray techniques and the type of the sample information that can be extracted from the certain technique.
The abbreviation are used as followings: XPR- X-ray Reflectivity, HRXRD- High Resolution XRD using coupled scan or RSM (reciprocal space maps), RC- Rocking Curve, XRPD- Bragg-Brentano powder diffraction, GIXD- grazing incidence XRD, IP-GIXD- in-plane grazing incidence XRD, PF- pole figure, Psi-sin^{2}psi using parallel beam [9].

	Thickness	Composition	Lattice strain/Relaxation	Defects	Orientation	Residual stress	Crystallite size
Perfect epitaxy	XPR, HRXRD	HRXRD, RC	Assume 100%	Assume none	HRXRD	-	-
Nearly perfect epitaxy	XPR, HRXRD	HRXRD, RC	HRXRD	RC	HRXRD	-	-
Textured epitaxial	XPR, HRXRD	HRXRD	HRXRD, IP-GIXD	RC	HRXRD	-	-
Strongly textured polycrystalline	XPR	XRPD, IP-GIXD	IP-GIXD	XRPD, IP-GIXD	IP-GIXD, PF	IP-GIXD	XRPD, IP-GIXD
Textured polycrystalline	XPR	XRPD, GIXD or IP-GIXD	-	XRPD, GIXD or IP-GIXD	PF	Psi	XRPD, GIXD
Polycrystalline	XPR	XRPD, GIXD	-	XRPD, GIXD	PF	Psi	XRPD, GIXD
Amorphous	XPR	-	-	-	-	-	-

3.3 Photoluminescence Spectroscopy (PL)

When electromagnetic radiation interact with the semiconductor, the energy of the photon will be absorbed by the electron. The electron will transfer onto a higher energy level (if available) where the energy difference equal to the photon energy. If the energy of the incident photon is greater or equal to the bandgap of the semiconductor, the photon can excite an electron from the energy state in valence band (VB) into the higher energy states in the conduction band (CB) through the process known as bandgap

excitation. Then, this electron, occupying in a higher energy state, will transit or return into an empty lower energy state generating radiation (recombination). In the case of radiative emission, the energy is emitted as electromagnetic radiation (photons) and the process is called as photoluminescence. The energy is emitted as heat (phonons) for the case of non-radiative recombination. In many ways, the radiative emission of the photons is opposite to the absorption of the photons. Additionally, according to the conservation laws of energy and momentum, the fundamental absorption of valence to conduction band is analog to the radiation recombination (band to band) of the electron and hole. Like in the rate of absorption, for the radiative emissions, according to the Fermi's Golden rule, the rate of the emission is the product of densities of the final states (empty lower states) and the densities of initial states (higher energy states) [10]. However, there are some distinction between them. They are: recombination process is a non-equilibrium process. As well as, absorption is expressed by Beers' law (the mean free path for photon decay), while emission is defined by the rate of photon generation for unit volume. Furthermore, all the electronic states in the semiconductor contribute in absorption yielding broad spectral features. However, radiative emission occur when recombining electrons and holes with well-defined energies. Consequently, PL spectrum is narrower than an absorption spectrum. Therefore, PL produce sharp peaks and gives an accurate values for bandgap and impurity energies than absorption. In PL, a laser is used as the excitation sources. The use of other excitation method, e.g. electric current, electron beam, etc. make different emission processes (e.g. electroluminescence, cathodoluminescence, etc.).

There are several possible recombination process in radiative recombination in a semiconductor and they are illustrated in Fig. 3.7.

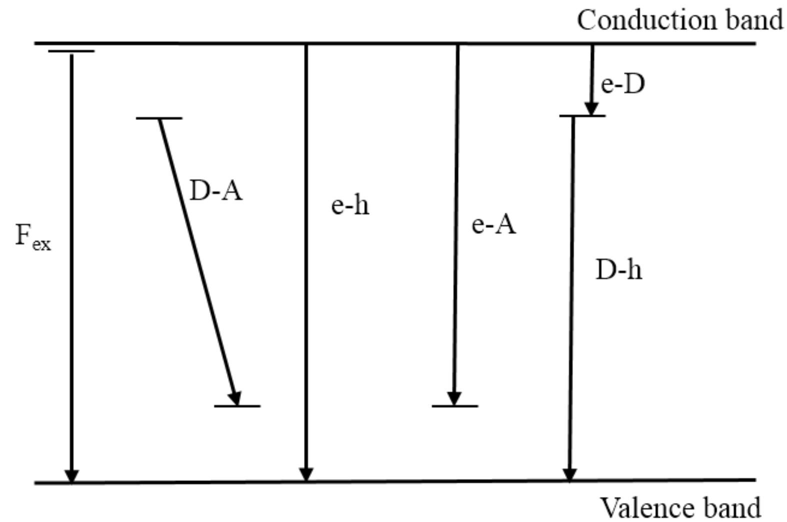

Figure 3.7 Possible recombination process in a semiconductor in real space.
Here, e and h represent the electron and hole carries, respectively, while D and A represent the donor and acceptor impurity levels [11].

The processes shown in Fig. 3.7 are, **(i) Band-to-band** (e-h): The radiative recombination of electron-hole pairs that occurs between the conduction band and the valence band.

(ii) Free excitons (F_{ex}): If the semiconductor material is intrinsic (very pure), an electron and a hole bound each other by the Coulomb attraction and form a quasi-particle called an exciton. Afterwards, a photon will be emitted as the exciton collapses radioactively producing a very narrow spectrum. Excitons can move through the lattice as a whole with zero net charge and no current. The energy of the emitted photon ($h\upsilon$) can be expressed in terms of energy gap of direct gap semiconductor (E_g) and the binding energy of the exciton (E_{ex}), as following Eq. 3.5 [1].

$$h\upsilon = E_g - E_{ex} \tag{3.5}$$

The binding energy of the exciton is a few millielectron volts and which is slightly below the excited state energy. In PL, behavior of the exciton is the indication of the sample quality.

If the semiconductor is extrinsic, free excitons can attract with donors, acceptor, or neutral impurities by Coulomb force and form bound excitons. However, the energy of the emitted photons are lower

than those of the free excitons, due to the higher binding energy. Each type of exciton generates a distinctive PL peak.

(iii) Free-to bound (e-A, D-h, e-D): New states can occur within the forbidden gap (between conduction band and the valence band) due to the presence of doping (n or p) or lattice defects. Hence, the transitions between the impurity states and one of the energy states (conduction or valence) can be occurred. Although these transition are less compared to band-band transition, they still appear intensely in PL spectrum.

(iv) Donor to acceptor (D-A): This transition occur between donor and acceptor levels.

The broadening of the line FWHM (the full width half maximum) of a given PL peak is known the linewidth of the emission peak. There are three reasons for broadening of a PL linewidth. They are, Heisenberg broadening, thermal (homogeneous) broadening, and inhomogeneous broadening [12].

3.3.1 Experimental setup for PL Spectroscopy

The designed PL measurement system in our lab is shown in Fig. 3.8.

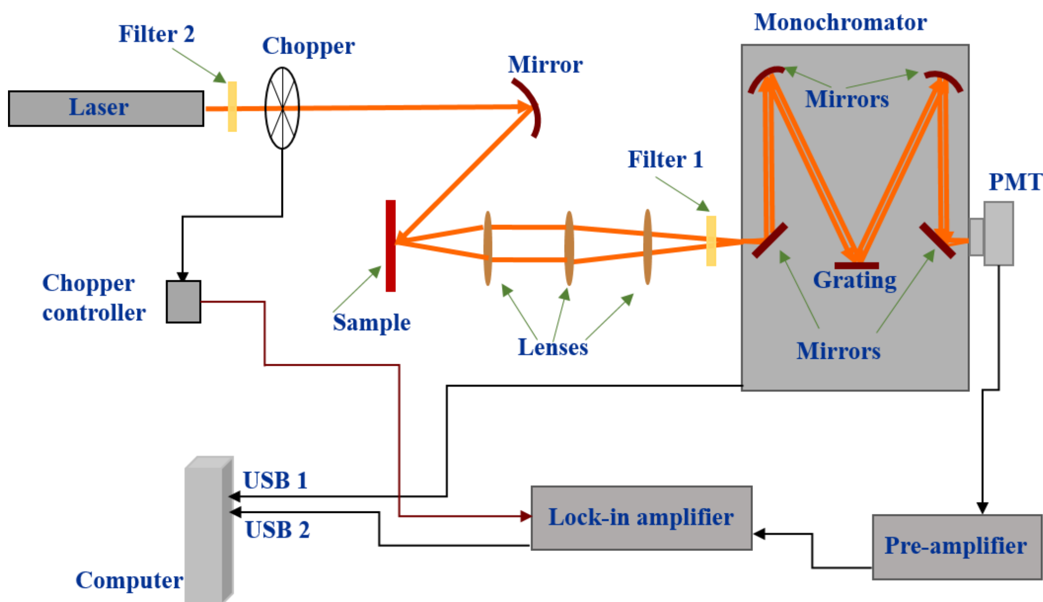

Figure 3.8 Designed experimental setup for PL measurements by the author.

The main components of the system are laser excitation source, monochromator, detector, and computer data acquisition system. The wavelength of the excitation source should be anywhere within the absorption spectrum of the material to sufficiently optically excite the sample and produce an emission spectrum. A laser, with narrow spectral linewidth, is selected due to several advantageous. Due to its coherent nature, it has a concentrated optical power within a narrow beam, high photon flux density and high rate of optical excitation [13]. Usually, the energy of the laser is greater than the fundamental bandgap of the semiconductor, and the average spot size is between 1 and 100 μm. In order to block the laser plasma emission and to transmit only the laser line (only the excitation wavelength) for exciting the material, filter 2 is used. The collected PL emission signal is directed into a monochromator and then into a photodetector. The filter 1, before the monochromator entrance, is used to avoid the laser line and to allow all other emissions to pass through it.

A mechanical chopper (with 6/5 slot windows and 4-400 Hz modulation frequency) is inserted in the excitation beam path to modulate optical excitation of the material. Periodic slots of chopper blade can interrupt the continuous wavelength, consequently, modulate a periodic excitation intensity, PL emission, and photodetector current. A lock-in amplifier is used to gain high signal-to-noise ratio (SNR), by filtering background noise (room lighting) from the photodetector current.

The monochromator (DK480) is employed with three grating: UV, Visible, and IR. The grating and the slits (entrance and exit) are controlled by LabView software. As the photodetector, a photomultiplier tube (PMT) is employed for visible and near visible measurements while the InGaAs detector is used for near infrared applications. In both devices, an electric field is created by an external bias voltage. In this electric field, the excess photogenerated carriers wipe out from the region of absorption to an external circuit. Then, the resulting total current will be measured by a voltage drop across a series resistor. The photodetector current is collected by the lock-in-amplifier. If the photodetector current is so small, a pre-amplifier can be utilized before the lock-in-amplifier to amplify the signal. Then, the lock-in-amplifier

can send a high SNR signal to a computer trough a USB/data acquisition to produce the PL intensity versus wavelength graph. In order to do this, all electrical system must communicate with the computer and LabView software is used for this. See the appendix.

3.4 Raman Spectroscopy

Raman scattering (inelastic scattering) is a versatile and powerful method for studying a wide variety of samples in different physical states; e.g. solids, liquids or vapors, in hot or cold states, in bulk or as surface layers. Raman spectroscopy allows examining the samples in aqueous solutions, inside glass/quartz containers, and without any sample preparations. Thus, the technique is used in many applications where microscopic, chemical analysis, imaging, and non-destructive method is needed.

Light is described as an electromagnetic wave or as a particle “beam” containing single energy quanta; therefore, carry both momentum and energy. Thus, photons can contribute in inelastic scattering by exchanging momentum and energy between them and the scattering medium [14]. Inelastic light scattering was theoretically anticipated by A. Smekal in 1923 [15] and this effect was first discovered experimentally in liquids by Sir C. V. Raman and K. S. Krishnan in 1928 [16]. The effect, inelastic scattering of light by molecular and crystal vibrations, was named as Raman effect.

When an incident photon with the frequency of ω_i interact/collide with a material, the photon can be scattered either at the original frequency (elastic scattering) or some shifted frequency (inelastic scattering). The first process is called Raleigh scattering (no exchange energy), and the second process is called Raman scattering. The frequency of the molecule can be an internal frequency equivalent to vibrational, rotational, or electronic transition inside the molecule. However, vibrational Raman effect is the most important. There are two types of Raman scattering processes. If the radiation scattering shifted to the lower frequency side (to the red) from the exciting line, the process is called Stokes scattering in which the molecule or the atom absorbs energy. If the light scattering is to the higher frequency side (to the blue), which is called anti-Stokes scattering, in which the molecule or the atom loses the energy.

Raman effect occurs based on three single processes: (1) the material absorbs an incoming photon (frequency ω_i and wave vector k_i), and then, the photon excites absorbing material from its initial state to a virtual state (intermediate state). (2) Generates (Stokes process) or annihilates (anti-Stokes process) an elementary excitation (frequency ω_p and wave vector q). In solids, excitations can be phonons, plasmons, magnons, etc. and the phonons (lattice vibrations) are the elementary excitations in a regular periodic structure. (3) Creates a scattered photon (frequency ω_s and wave vector k_s) through the recombination [14, 17].

Figure 3.9 illustrates the Rayleigh, Stokes, and anti-Stokes scattering processes in Raman scattering.

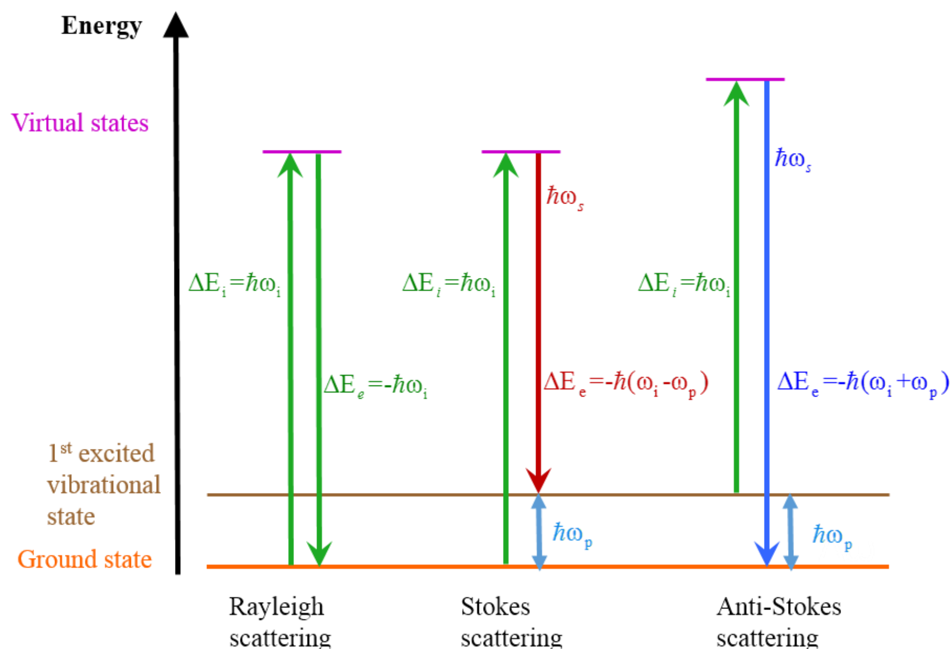

Figure 3.9 Jablonski diagram for Rayleigh and Raman (Stokes and anti-Stokes) scattering. Incident photon is characterized by its energy ($h\omega_i$) and wave vector (k_i). ω_p and q are the frequency and wave vector of the phonon, respectively. The scattered light is characterized by its energy ($h\omega_s$), wave vector (k_s), and its corresponding intensity, which are defined by the properties of the material. Raman measurements, usually, focus the Stokes scattering. The figure is after Ref. [17]

3.4.1 Kinematical limitation in Raman Scattering

For first-order Raman scattering (only one phonon process), the energy and momentum conservations yield,

$$\hbar\omega_s = \hbar\omega_i \pm \hbar\omega_p \quad 3.6$$

$$k_s = k_i \pm q \quad 3.7$$

Here, the signs '+' and '-' refer to anti-Stokes and Stokes scattering, respectively. The magnitude of the incident wave vector is, $|k_i| = \frac{\omega_i n(\omega_i)}{c} = \frac{2\pi n(\lambda)}{\lambda}$, where n and c are refractive index and speed of light, respectively. The magnitude of the scattered wave vector is, $|k_s| = \frac{\omega_s n(\omega_s)}{c} = \frac{2\pi n(\lambda)}{\lambda}$. In order to consider the conservation laws (energy and momentum), let's consider an ideal crystal with translational symmetry. The conditions for the momentum conservation are valid only for the samples that have large enough scattering. Typically, light scattering experiments perform with the incident and scattered photons in the visible frequency $\omega_{i,s}/2\pi \approx 10^{14}\text{-}10^{15}\text{Hz}$. The excitation frequency lay in the far- to near-infrared range $\omega_p/2\pi \approx 3\times10^{11}\text{-}10^{14}\text{Hz}$ (10-3000 cm^{-1}) [18]. Usually, the energy transfer is smaller than the energy of the incoming photons, which means, $\omega_p \ll \omega_i$ and $|k_i| \approx |k_s|$. Therefore, the conditions for wave vector can be approximated and written as, $|q| \approx 2|k_i|\sin(\theta/2)$, where θ is the angle between the directions of the incident and the scattered photon. The maximum excitation wave vector is $|q_{max}| = 2|k_i| = \frac{2n\omega_i}{c}$ and for typically probed Raman scattering experiments in typical solids, this is in the range of $0 < |q_{max}| < 3\times10^{-3}$ Å^{-1}, which is smaller than the size of the Brillouin zone boundary, $|k_{ZB}| \approx \frac{2\pi}{a} \approx 1$ Å^{-1} ('a'- lattice constant of the crystal) [13]. Hence, substantially, this conclude that Raman experiment can probe only excitations very close to the Brillouin zone center ($|q| \approx 0$). This makes a limitation comparison with other tech-

niques used in studying solid state excitations, for instance, neutron scattering. Nevertheless, the limitation can avoid in special situations, for examples, excitations of two-particle (two phonons, two magnetons, etc.), and in amorphous and discorded materials that have lost the wave vector conservation.

3.4.2 Raman Scattering Selection Rules

It is easiest to explain Raman scattering selection rule in a semiclassical way. Considering infinite medium and assuming the medium is isotropic, one can represent the electric susceptibility by a scalar. Consider an incoming electromagnetic field describes as follows [19],

$$E(r,t) = E(k_i, \omega_i)\cos(k_i \cdot r - \omega_i t) \quad 3.8$$

This external electric field interacts with the solids and leads to a local polarization, which can be written as,

$$P(r,t) = P(k_i, \omega_i)\cos(k_i \cdot r - \omega_i t) \quad 3.9$$

Here, $$P(k_i, \omega_i) = \chi(k_i, \omega_i, Q)E(k_i, \omega_i) \quad 3.10$$

where, χ is the electric susceptibility, the system's response to the electromagnetic field. At a finite temperature, χ can fluctuate due to thermally excited atomic vibrations, which refer to phonons in a crystalline semiconductors. Q is the atomic displacement, which is associated with a phonon and can be described as following,

$$Q(r,t) = Q(q, \omega_p)\cos(q \cdot r - \omega_p t) \quad 3.11$$

Supposing that the characteristic electronic frequencies which determine the electric susceptibility are greater than ω_p, therefore, the electric susceptibility changes as a function of the atomic displacement. Then, χ can be written as a Taylor series in *Q,* because, usually, the amplitude of these vibrations are smaller than to the lattice constant of the crystal.

$$\chi(k_i, \omega_i, Q) = \chi_0(k_i, \omega_i) + \left(\partial\chi / \partial Q\right)_0 Q(r,t) + ... \quad 3.12$$

where, χ_0 is the electric susceptibility without fluctuations. In above Eq. 3.12, χ has divided into two: a static and a dynamic Q-dependent part. Relating this for polarization of the solids, the first term corresponds to P_0, a static polarization which is oscillating with incident field. The second term represent the polarization induced by the lattice displacement. Therefore, material polarization is given [19],

$$P(r,t,Q) = P_0(r,t) + P_{ind}(r,t,Q) \quad 3.13$$

Then, Eq. 3.12 can be written as,

$$\begin{aligned} &P(r,t,Q) = \chi(k_i,\omega_i,Q)E(k_i,\omega_i)\cos(k_i.r-\omega_i t) = \\ &\chi_0(k_i,\omega_i)E(k_i,\omega_i)\cos(k_i\cdot r-\omega_i t) + \left(\partial\chi/\partial Q\right)_0 Qr,t)E(k_i,\omega_i)\cos(k_i\cdot r-\omega_i t) \end{aligned} \quad 3.14$$

From Eq. 3.13, 3.11, and 3.14,

$$P_{ind}(r,t,Q) = \left(\partial\chi/\partial Q\right)_0 Q(q,\omega_p)\cos(q\cdot r-\omega_p t)E(k_i,\omega_i)\cos(k_i\cdot r-\omega_i t) \quad 3.15$$

$$\begin{aligned} &P_{ind}(r,t,Q) = \chi_0(k_i,\omega_i)E(k_i,\omega_i)\cos(k_i\cdot r-\omega_i t) \\ &= \frac{1}{2}\left(\partial\chi/\partial Q\right)_0 Q(q,\omega_p)E(k_i,\omega_i)\{\cos[(k_i+q)\cdot r-(\omega_i+\omega_p)t]+\cos[(k_i-q)\cdot r-(\omega_i-\omega_p)t]\} \end{aligned}$$

3.16

The first term in Eq. 3.16 corresponds to the elastic scattering (Raleigh) while the second term presents the Raman scattering process. Raman scattering term consists two waves with shifted frequencies and wave vectors, resulted from the incident radiation. Stokes scattering wave has the wave vector $(k_i - q)$ and frequency $(\omega_i - q)$ while those for the anti-Stokes wave are $(k_i + q)$ and $(\omega_i + q)$, respectively. It is noted that only first-order Raman scattering has been considered in Eq. 3.16. The occupation number of a phonon state rises and energy of incident light transfer to the solid in Stokes scattering. In anti-Stokes scattering process, the occupation number of a phonon state drops and the energy of the phonon transfer to the incident light. The probabilities of these two processes are determined by the original occupation number of the phonon state. Stokes and anti-Stokes lines can find symmetrically around the Rayleigh line. Therefore, scanning of the anti-scattering region can be used to verify a peak in the Raman spectrum. The Stokes scattering can overcomes the anti-Stokes scattering at the room temperature. Because anti-Stokes

scattering will vanish at low temperature. Furthermore, there is no any contribution of PL, stray light or any artifacts from the substrate to the anti-Stokes spectrum.

The term, $\left(\partial\chi/\partial Q\right)_0 Q(q,\omega_0)$ in the Eq. 3.16 is related to the crystal structure and which is known as the Raman tensor ($\Re$). If the unit vectors of incident and scattered polarizations are e_i and e_s, the Raman intensity is proportional to [19],

$$I_s \propto \left|e_i \cdot \left(\partial\chi/\partial Q\right)_0 Q(\omega_p) \cdot e_s\right|^2 \qquad 3.17$$

In Eq. 3.18, it is approximated that q to be zero for one-phonon scattering and χ to be complex. Here, it is clear that scattered intensity is proportional to the Q (vibrational amplitude) squared, which means, if atomic vibration is absent, there is no Stokes scattering. This is a consequence of classical treatment [20].

If the unit vector of Q is, $\hat{Q} = Q/\left|Q\right|$, which is parallel to the phonon displacement, the modified Raman tensor ($\Re$) is,

$$\Re = \left(\partial\chi/\partial Q\right)_0 \hat{Q}(\omega_p) \qquad 3.18$$

Then, scattered intensity is,

$$I_s \propto \left|e_i \cdot \Re \cdot e_s\right|^2 \qquad 3.19$$

$\Re$ is a second-rank tensor including complex components. If one neglects the difference in frequency of incident and scattered light, it is a symmetric second-rank tensor since χ is a symmetric tensor. Both Raman tensor and the corresponding phonon have the same symmetry. Equation 3.19 determines under which experimental conditions regarding the incident and scattered polarization can observe a Raman-active phonon. A phonon to be Raman-active, $\left(\partial\chi/\partial Q\right)_0$ should be non-zero.

In order to analyze the Raman spectra of a material, Raman-active modes and their symmetries should be identified first. This can be carried out by three steps procedure. (1) Identify the crystal structure (the space group) and atoms location in the unit cell, precisely. (2) Determine the irreducible representations of the zone-center phonons. (3) Identify the scattering tensors for irreducible representations

and determine the Raman-active modes [21]. The first and second steps are valid for finding the IR active phonon modes too. Therefore, the following subsection discusses the Raman and IR active phonon modes of the hexagonal structure.

3.4.3 Raman and IR Allowed Phonons for Hexagonal Structure

The space group for the hexagonal structure is C_{6v}^{4} , which includes the elements that represent the translations, reflections and rotation operations. In order to find the symmetry of the Raman and IR active phonons, the irreducible representations of a vector in the structure should be known. If the space group is identified, one can find the corresponding character table in the literature. In a character table, a complete set of possible symmetry operations in a point group is listed as a matrix. The character table, which is derived from Group Theory, for C_{6v} point group symmetry, is given in Table 3.4 [22].

Table 3.4 Character table and the symmetry operation for C_{6v} point group symmetry.

C_{6v}		E	$2C_6(z)$	$2C_3(z)$	$C_2(z)$	$3\sigma_v$	$3\sigma_d$	Linear functions, rotations	Quadratic functions	Cubic functions
A_1	Γ_1	+1	+1	+1	+1	+1	+1	z	x^2+y^2, z^2	z^3, $z(x^2+y^2)$
A_2	Γ_2	+1	+1	+1	+1	-1	-1	R_z	-	-
B_1	Γ_3	+1	-1	+1	-1	+1	-1	-	-	$x(x^2-3y^2)$
B_2	Γ_4	+1	-1	+1	-1	-1	+1	-	-	$y(3x^2-y^2)$
E_1	Γ_5	+2	+1	-1	-2	0	0	(x, y) (R_x, R_z)	(xz, yz)	(xz^2, yz^2) [$x(x^2+y^2)$, $y(x^2+y^2)$]
E_2	Γ_6	+2	-1	-1	+2	0	0	-	(x^2-y^2, xy)	[xyz, $z(x^2-y^2)$]

In the character table, left upper corner Schoenflies symbol is for the point group. The Mulliken symbols under the first columns are given by the irreducible representations. 'A' indicates the symmetry

(singly degenerated or one dimensional) with regard to rotation of the principle axis. ‘B’ means the anti-symmetric (singly degenerated or one dimensional) with respect to rotation about principle axis. Symbol ‘E’ means that the representation is doubly degenerated or two dimensional. The subscript ‘1’ and ‘2’ indicate the symmetric and anti-symmetric, respectively to C_2 perpendicular to the principle axis, if C_2 perpendicular does not exit, then to σ_v.

Next columns represent the symmetry operations (conjugacy classes). E is the identity operation. C_n (n-fold rotation) means a rotation by $2\pi/n$ around an axis of symmetry. Wurtzite structure contains two six-fold ($2C_6$) symmetry axes parallel to the [0001] direction: $2\pi/6$ rotation and $10\pi/6$ rotation, two three-fold ($3C_3$) rotations around the [0001] direction: $2\pi/3$ and $4\pi/3$, and one two-fold (C_2) rotation around the [0001] direction by π. Additionally, there are six mirror planes three ($3\sigma_v$) of them are passing opposite vertices of the hexagon making $\pi/3$ each other, and other three ($3\sigma_d$) are passing through faces of hexagon making $\pi/3$ each other [23, 24].

Numbers in each row represent the character of the irreducible representations of the group. For instance, E in second column indicates the degeneracy of the row (A=B=1 and E=2).

The other three remaining columns are the basic functions, which represent the spectroscopically active elements, corresponding to each the representations. The symbols x, y and z indicate the Cartesian coordinates while R_x, R_y, and R_z represent the rotations about these axes. The basic functions have the same symmetry as the atomic orbitals. Therefore, p_x, p_y, and p_z orbitals have the same symmetry as x, y, and z. Their dipole moment component can be expressed as $\mu_x = -ex$, $\mu_y = -ey$ and $\mu_z = -ez$. The selection rule for IR spectroscopy is $(\partial\mu / \partial Q)_0 \neq 0$, which means that vibration must change the dipole moment of the molecule/phonon, a phonon to be an IR active. Since the atomic displacement and x, y, and z behave similarly, IR active modes transform as x, y or z. Hence, according to the Table 3.4, A_1 and E_1 are IR active.

As *p* orbitals and *d* orbitals (d_{xy}, d_{xz}, d_{yz}, d_{x2-y2}, and d_{z2}) are associated with xy, xz, yz, x^2-y^2 and z^2. As mentioned previously, a complex polarizability tensor (susceptibility) must be changed for a phonon mode to be a Raman active. Since the polarizability operator has the same symmetry of binary and quadratic basic functions of x, y, and z, the phonon modes transform these functions, hence are Raman active. According to the Table 3.4, A_1, E_1, and E_2 phonon modes are Raman active. The last column, cubic functions, are linked to the *f* orbitals and are not interested in this work.

In the wurtzite structure, there are four atoms in the basis for unit cell. The displacement of each atom is in the directions of Cartesian coordinates, x, y and z. Thus, possible phonon modes are 3×4=12. Therefore, there are nine optical modes (3×4-3) and three acoustical phonon modes in the long-wavelength limit for wurtzite materials. These optical phonon modes must show with the ratio of 2:1 transverse to longitudinal optical phonon modes [25]. Table 3.5 summarizes the number of the different long-wavelength phonon modes with N atoms unit cell [25].

Table 3.5 The number of phonon modes accompanied with a unit cell with N atoms in the basis.

Modes	Number of modes
Longitudinal acoustic (LA)	1
Transverse acoustic (TA)	2
Total # of acoustic modes	3
Longitudinal optical (LO)	N-1
Transverse optical (TO)	2N-2
Total # of optical modes	3N-3
Total # of modes	3N

In order to find the irreducible representation of phonon modes for the wurtzite structure, one can first construct the table for reducible representation of symmetry operations in wurtzite structure, and then reconstruct the irreducible representations of phonons. The irreducible representation of phonon modes at the zone center are,

$$\Gamma_{\text{irreducible}} = \Gamma_{\text{Acoustic}} + \Gamma_{\text{Optical}} = 2A_1 + 2B_1 + 2E_1 + 2E_2 \quad (3.20)$$

According to the character table, the B_1 phonon modes is neither Raman nor IR active. Thus, Raman active optical phonon modes are,

$$\Gamma_{Optical} = A_1 + E_1 + 2E_2 \ . \tag{3.21}$$

Wurtzite structures are uniaxial crystals, and the optical axis is coincided with the z-axis. Since these crystals are anisotropic, the frequency of the polar phonons polarized along c-axis (z-axis) is altered those from the polarized in the (x, y)-plane. A_1 and E_1 polar phonons split into longitudinal acoustic and longitudinal optical (LA, LO), as well as into transverse acoustic and transverse optical (TA, TO). The energies of the acoustical modes disappear at the Brillouin zone center, and that is not for optical modes. The optical branches of A_1 (z-polarized) and E_1 (polarized in the x, y plane) are both IR and Raman active. According to their frequencies, non-polar E_2 and B_1 phonons labeled as high and low. In brief, referring to the Eq. 3.20, there are three acoustical modes (one A_1LA, two E_1TA), and nine optical modes (one A_1LO, two E_1TO, one B_1low, one B_1high, two E_2low, and two E_2high).

Even though, 12 phonon modes should appear in the above representation (Eq. 3.20) as described, only eight phonon modes appear. The reason is, energy of the two E_1TA are same. As well as, energy of the each set, two E_1TO, two E_2low, and two E_2high phonon modes have the same energy.

The optical phonon modes for wurtzite structure are illustrated in Fig. 3.10. The atomic displacements of the A_1 and B_1 phonon modes are along the c-axis, while those for E_1 and E_2 are perpendicular to the c-axis.

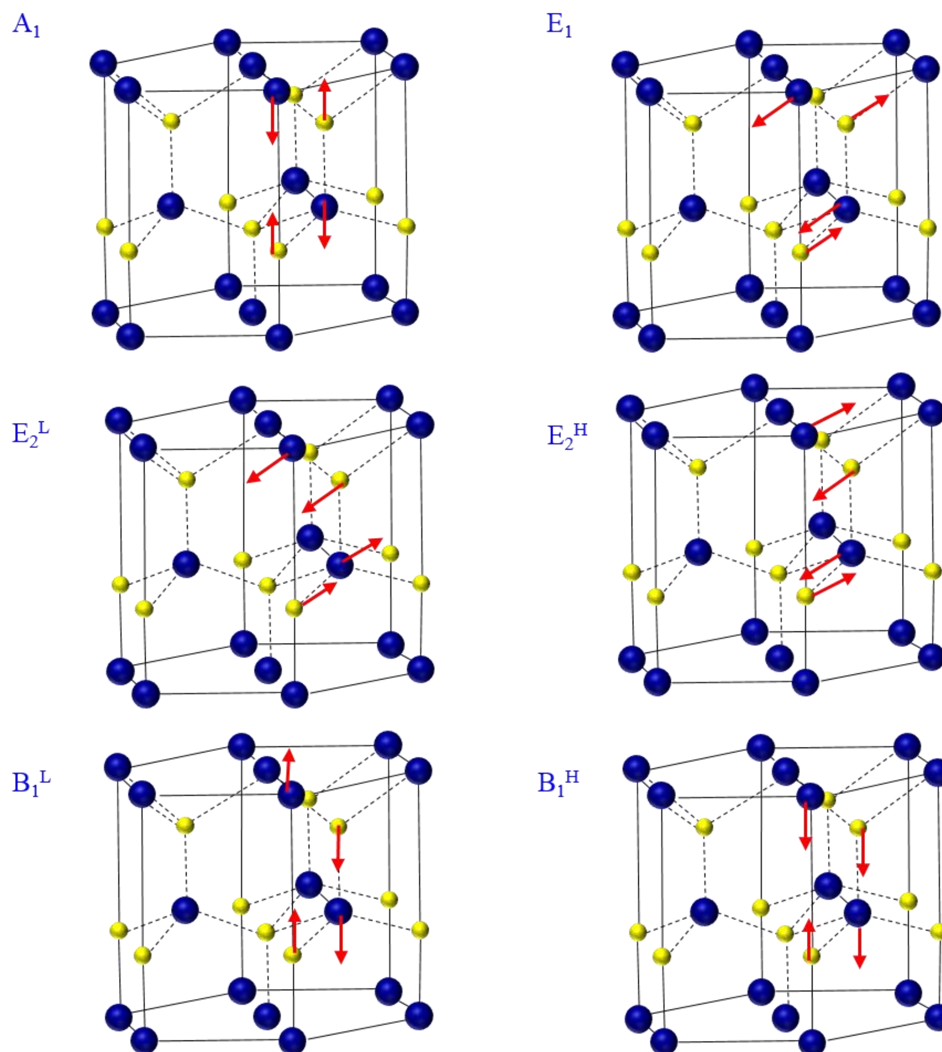

Figure 3.10 Optical phonon modes of wurtzite structure. In our case, the blue (big) and yellow (small) sphere represent the group III and nitride atoms, respectively.

3.4.4 Experimental Setup

Figure 3.11 illustrates a simple schematic view of the home built Raman setup. In general, the Raman signal is a very weak signal because only a very small fraction of the total scattered photons are Raman scattered (~10^{-8}). Thus, a laser is used as the excitation source. Higher power of the laser can increase the Raman scattering intensity, however this should be chosen without any damage to the sample. The wavelength (can be between UV-visible to near-IR range) of the laser depends on the application.

The laser light is focused onto the sample through a beamsplitter and confocal optics. Then, the scattered light from the sample is redirected onto the focal lens and passed through the beamsplitter. This is designed to configure the backscattering geometry. This beam is focused onto a mirror. The reflected light from the mirror is focused onto the McPherson double subtractive monochromator. The interference filter (Rayleigh rejection filter) is employed to filter only the Raman scattering light. A higher resolution spectrum can be generated using a grating with more lines per mm (in this case, grating with is 1800/mm). The signal from the grating is collected by the liquid nitrogen cooled CCD (or photomultiplier tube). The detector will measure the photocurrent from each wavelength section. The CCD detector is measured the photocurrent into electric current. LabView software is used to evaluate and save the measured data.

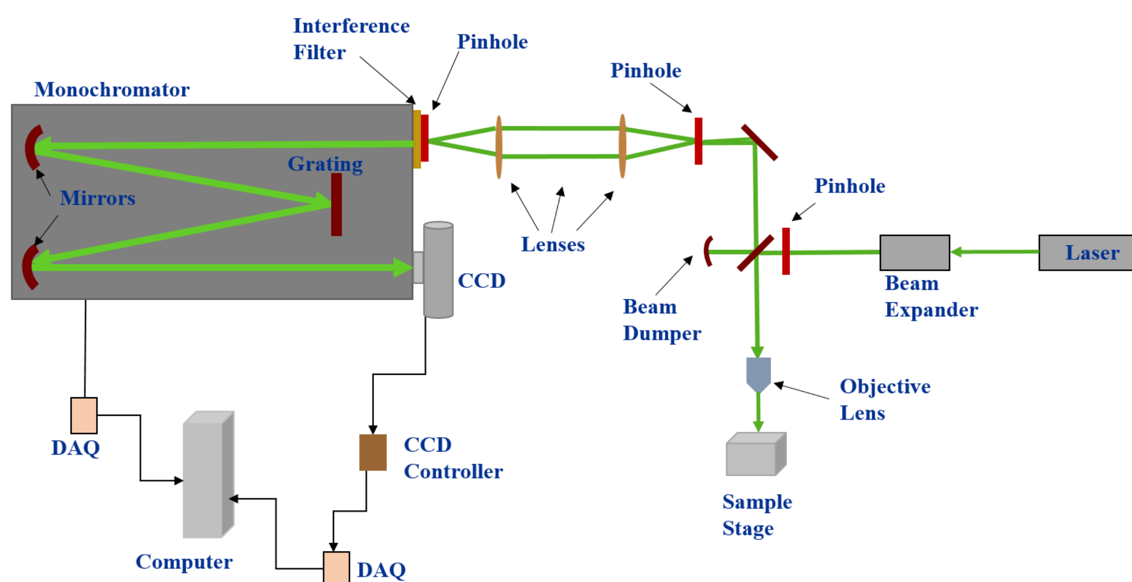

Figure 3.11 Designed experiment setup for the Raman measurements by the author.

3.4.5 Raman Scattering Geometry

For the wurtzite structure, the Raman tensor of the A_1 phonon mode has only the diagonal components and for the E_1 phonon mode, Raman tensor has only off-diagonal components. However, for the E_2 phonon mode, it has both components [26]. Thus, in order to observe the A_1 mode, the incident and

scattered light should have parallel polarization (back scattering geometry). The E_1 mode can be observed in crossed polarization (non- back scattering geometry). Raman active phonon modes of the hexagonal structure and their observing scattering geometry are summarized in Appendix A.1.

The both A_1LO and E_2 phonon modes can be observed by the $z(x, x)\bar{z}$ back scattering geometry. The symbols, outside the bracket left to right indicate the direction of the incident and scattered light, respectively. The symbols, inside the bracket left to right show the direction of the incident and scattered polarization, respectively. Here, the z- direction is along the c-axis and x- and y- directions are perpendicular to the c-axis.

3.5 Infrared (IR) Spectroscopy

Usually, the two analytical techniques, Infrared and Raman spectroscopy, are employed vibrational transitions techniques. In general, Infrared spectroscopy is the measure of the change in absorption, or transmission intensity as a function of wavelength (IR absorption and transmission spectroscopy). When a molecule or a crystal lattice absorb electromagnetic radiation, it can excite higher energy levels. This occurs in three process: (i) rotational transitions occur when the molecular or crystal lattice is excited by microwave or infrared radiation, (ii) vibrational transitions occur when it is excited by infrared or visible radiation, (iii) electronic transition occur when UV light involving. Absorption occurs, when the IR radiation energy matches with a specific molecular or lattice vibration energy. The vibration transitions occur between different vibrational states. As mentioned in Section 3.4.3, the dipole moment of the molecule or lattice should change during the vibration, for the molecule to be IR active.

The IR wavelength of the electromagnetic radiation is range from 0.8 μm (12 500 cm^{-1}) to 1000 μm (10 cm^{-1}). In the electromagnetic spectrum, infrared radiation region can be mainly divided in to three regions as near-IR (NIR), mid-IR (MIR), and far-IR (FIR). The NIR region 12 500-4000 cm^{-1} (0.8-2.5 μm) can excite overtone or harmonic vibrations. The MIR region is covered approximately 4000-400 cm^{-1} (2.5-25 μm), can use to study fundamental vibrations and associated rotational-vibrational structure. The FIR region, 400-10 cm^{-1} (25-1000 μm) excites lattice vibrations, and can use for rotational spectroscopy

[27]. One of the advantageous of IR spectroscopy is, it can be used for any samples in any states, liquids, solutions, gaseous, films, powders, etc. IR reflection spectroscopy was designed by associating the IR spectroscopy and the reflection theories.

3.5.1 Fourier Transform Infrared (FTIR) Spectroscopy

Dispersive IR spectrometers were commercially available since 1940s. The dispersive element was a prism in these instruments. In the 1950s, diffractive grating based IR spectrometers were available. In 1969, first MIR-FTIR spectrometer became commercially available with the resolution greater than 2 cm^{-1}. This employs an interferometer and exploits the Fourier Transform mathematical method. Based on the FTIR's interferometer, there are two fundamental advantages in FTIR spectrometer compared to dispersive instruments. One is known as Fellgett (multiplex) advantage. In the FTIR spectrometer, at any given time, all the wavelength are measured, while one wavelength is measured at a time in dispersive spectrometer. This causes a higher signal-to-noise ratio. Consequently, FTIR spectrometer can produce a faster spectrum. The second one is the Jaquinot (throughput) advantage. FTIR spectrometer can achieve spectral higher resolution without using narrow slits. Additional advantages are, FTIR spectrometer is self-calibrated and FTIR spectrometer cover the larger spectral range than dispersive spectrometers. As well as, spectrum is reproducible [27].

The basic components of the FTIR instruments can be different from one to another based on their primary applications. There are many designs for interferometer such as Michelson interferometer, Fabry-Perot interferometer, and lamellar grating interferometer. The resolving power is lower in Fabry-Perot interferometer. Michelson interferometer is the most commonly used one for infrared spectra measurements. Figure 3.12 shows the schematic of the basic components of FTIR spectrometer. IR radiation from the source reaches to the optics and passes through the interferometer onto the sample. The detector is focused the reflected or transmitted beam from the sample, depending on the analysis method required.

Then, this analogue signal from the detector is converted to a digital signal by the analogue-to-digital converters and the data send to a computer where the Fourier Transform take place. The final IR spectrum and data will be stored and presented in the computer.

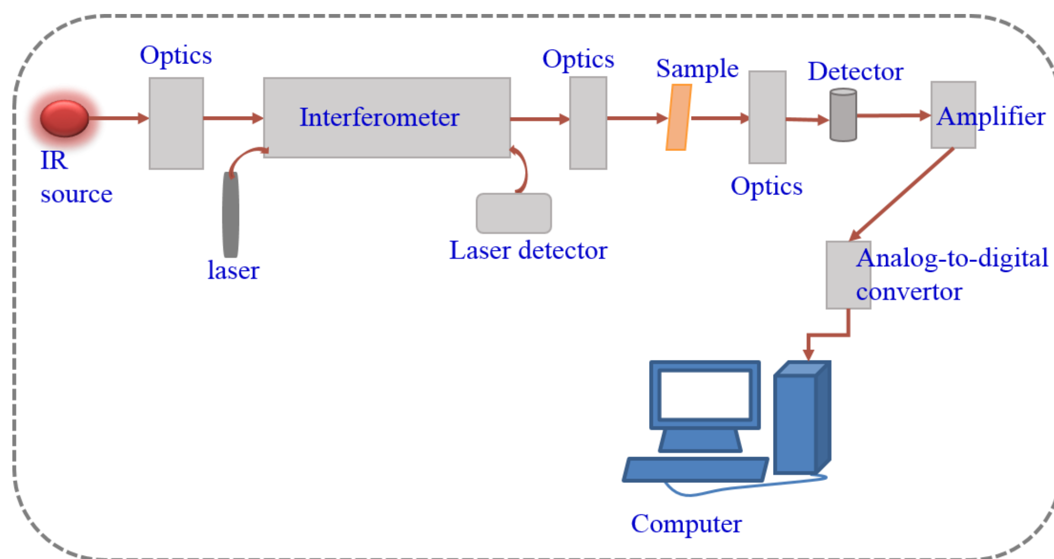

Figure 3.12 A schematic of the basic component of an FTIR spectrometer.
The figure is after Ref. [27].

Figure 3.13 illustrates a simple schematic of a Michelson interferometer. In both cases reflection and transmission, the sample is located between the beamsplitter (BS) and the detector. BS divides the incoming beam from the source into two parts (the source spectrum is $S(v)$). One beam can be partially reflected onto the fixed mirror and the other beam can be transmitted to the moving mirror which moves a very short distance away from the BS. Then, the two partial beams are reflected off from the mirrors interfere at the BS. The two partial waves acquire different phase shifts with respect to each other for different positions of the moving mirror. The laser beam is used for measuring the direction and the position of the moving mirror. The detector output is stored as a function of the mirror position x/2. The optical path difference of the two beams is x and the interference pattern $I(x)$, which results of this, is called the interferogram [13]. Then, this is Fourier Transformed to obtain the spectrum by the computer. The spectrum S is given by

$$S(v)=\int_{-\infty}^{+\infty} I(x)e^{+i2\pi vx}dx = F^{-1}[I(x)]\,. \qquad 3.22$$

$$I(x)=\int_{-\infty}^{+\infty} S(v)e^{-i2\pi vx}dv = F[S(v)]\,. \qquad 3.23$$

The first integral is the inverse Fourier Transform and the second one is the Fourier Transform [13].

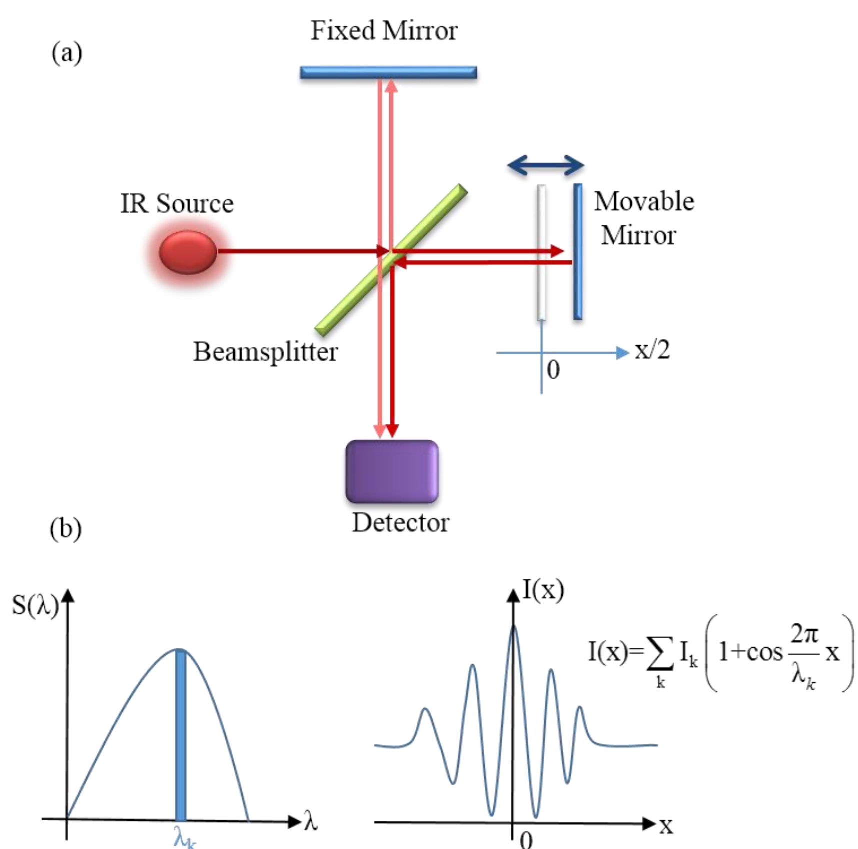

Figure 3.13 (a) Schematic of simplest form of the Michelson interferometer. At x=0, path difference between two beams is zero. (b) The source and interferogram I(x) plot is given.

FTIR spectrometers usually use the Globar source as the IR source for MIR region. For the far-IR and near-IR region mercury discharge lamp and tungsten-halogen lamp are used, respectively. Deuterium triglycine sulfate (DTGS) or mercury cadmium telluride (MCT) detectors are used for the MIR region.

These two detectors are also employed for the near-IR region. In the far-IR region, Triglycine sulfate (TGS) or liquid helium cooled silicon or germanium bolometers can be used. As the BS, KBr, mylar, and quartz are usually used for the MIR, far-IR, and near-IR regions, respectively.

In the IR region, some studies such as analysis of anisotropic structure and electronic states of the materials requires the polarization dependent studies. Wire grid polarizers (includes a grid of parallel conducting wires) are often used as the linear polarizers. For the MIR and near-IR range, a wire grid designed on substrate (KRS-5 and quartz) is applied. Free standing wire grid polarizers are employed in the far-IR range.

3.5.2 FTIR Reflection Spectroscopy Measurements

The sample compartments of the commercial FTIR spectrometer are usually designed for transmission/absorption measurements. For the reflection measurements, optical accessory must be inserted into the sample chamber or one can direct the IR beam into an external sample chamber with already has the built optics. One can buy the optical accessory for the reflection from manufacturer or the user can build it. There are two main reflection configurations, near-normal incidence and grazing angle incidence as shown in Fig. 3.14, that use in obtaining the optical constants of materials.

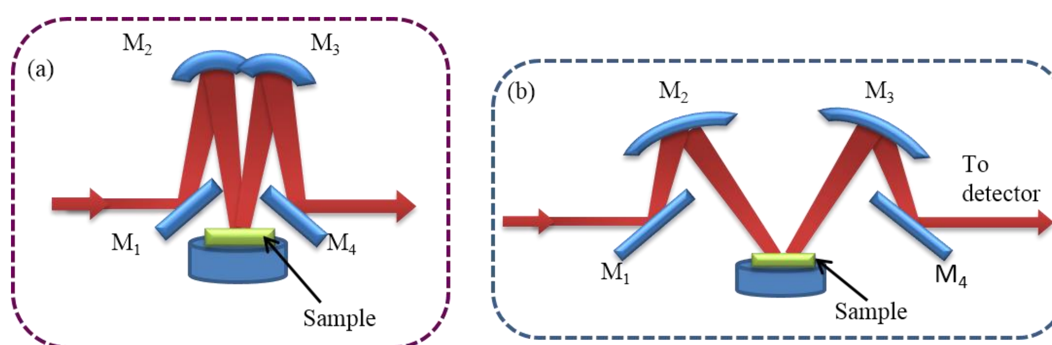

Figure 3.14 Reflection at (a) near-normal incidence and (b) grazing angle incidence.

3.6 References

[1] S. Perkowitz, *Optical Characterization of Semiconductors: Infrared, Raman, and Photoluminescnce Spectroscopy*. (Academic Press, San Diego, 1993).

[2] J. A. N. T. Soares, in *Practical Materials Characterization*, edited by M. Sardela (Springer, New York, 2014).

[3] *Basics of Atomic Force Microscope (AFM),* December 4, 2016, http://experimentationlab.berkeley.edu/sites/default/files/AFMImages/Lecture_10_AFM.pdf

[4] V. Dimitrova, D. Manova and E. Valcheva, Materials Science and Engineering: B **68** (1), 1-4 (1999).

[5] P. F. Fewster, *X-Ray Scattering From Semiconductors*. (Imperial College Press, London, 2000).

[6] B. D. Cullity and S. R. Stock, *Elements of X-Ray Diffraction*, 3rd ed. (Prentice Hall, Englewood Cliff, NJ, 2001).

[7] D. Henry, N. Eby, J. Goodge and D. Mogk, *X-ray reflection in accordance with Bragg's Law,* 08-02-2016, http://serc.carleton.edu/research_education/geochemsheets/BraggsLaw.html

[8] M. Moram and M. Vickers, Reports on progress in physics **72** (3), 036502 (2009).

[9] S. A. Speakman, MIT Center for Materials Science and Engineering, *Introduction to High Resolution X-Ray Diffraction of Epitaxial Thin Films,* 08-03-2016, http://prism.mit.edu/xray

[10] G. D. Gilliland, Materials Science and Engineering: R: Reports **18** (3), 99-399 (1997).

[11] P. K. Basu, *Theory of Optical Processess in Semiconductors: Bulk and Microstructures*. (Oxford, New York, 1997).

[12] S. saini, in *Optical Techniques for Solid-State Materials Characterization*, edited by R. P. Prasankumar and A. J. Taylor (CRC Press, New York, 2012).

[13] R. P. Prasankumar and A. J. Taylor, *Optical Techniques for Solid-State Materials Characterization*. (CRC Press Taylor & Francis Group, 2012).

[14] M. Opel and F. Venturi, European Pharmaceutical Review **7** (3), 76 (2002).

[15] A. Smekal, Naturwissenschaften **11** (43), 873-875 (1923).

[16] C. V. Raman and K. S. Krishnan, Nature **121**, 501-502 (1928).

[17] *Raman scattering,* December 4, 2016, https://en.wikipedia.org/wiki/Raman_scattering

[18] W. Hayes and R. Loudon, *Scattering of Light by Crystals*. (Dover Publications, Inc., Mineola, New York, 1978).

[19] *Raman Scattering in Solids,* September 2, 2016, http://www.physik.fu-berlin.de/studium/praktika-forward/fpa_dipl-ws2009/docs/Ma7_Raman.pdf

[20] P. Y. Yu and M. Cardona, *Fundamentals of Semiconductors: Physics and Materials Properties*. (Springer-Verlag Berlin Heidelberg, 2010).

[21] W. H. Weber and R. Merlin, *Raman Scattering in Materials Sceience*. (Spinger, New York, 2000).

[22] J. R. L. Flurry, *Symmetry Groups: Theory and Chemical Applications*. (Prentice-Hall, Inc, New Jersey, 1980).

[23] B. Gil, *Physics of wurtzite Nitrides and Oxides: Passport to Devices*. (Springer, Switzerland, 2014).

[24] P. Atkins and R. Friedman, *Molecular Quantum Mechanics*, fifth ed. (Oxford University Press, New York, 2005).

[25] M. A. Stroscio and M. Dutta, *Phonons in Nanostructures*. (Cambridge University Press, Cambridge, 2001).

[26] R. Loudon, Advances in Physics **13** (52), 423-482 (1964).

[27] K. P. Möllmann and M. Vollmer, European Journal of Physics **34** (6), S123 (2013).

4 CHAPTER 4: ANALYSIS OF GROUP III-NITRIDES PROPERTIES USING MULTILAYER STACK MODELLING OF FTIR REFLECTANCE SPECTRA

This chapter describes the analytical method used in the analysis of FTIR reflectance spectra in this study. FTIR reflectance (or transmittance) spectrum of a semiconductor contains various types of physical properties of that semiconductor. These parameters are dependent on the growth conditions/method, certain properties of the individual semiconductor, and external parameters (e.g. pressure, temperature). The extraction of these parameters employing the FTIR spectroscopy will be dependent on the wavelength regions and the type of the measurements (transmission or reflection). When employing the FTIR reflectance (or transmittance) spectroscopy, it measures the total reflectance (or transmittance) in the multilayer stacked structures. Therefore, in order to extract the material properties of the each layer in the material stack, a separation of reflection (or transmission) over each layer is required. Therefore, in order to extract the reflection/transmission details of each layer, one should choose a mathematical model that best describes, all the parameters of the materials. Reflection or transmission of the each layer in the multilayer stack is related to dielectric function, layer thickness, surface roughness, interface roughness, and band structure. Thus, modeling of the dielectric function also plays and important role in the modeling of the reflectance/transmittance spectrum. Therefore, the multilayer stack model, which calculates the total reflectance of the whole layer stack by adding the reflection or transmission at each interface, is more suitable for the analysis process. This chapter explains how the modeled reflectance spectrum of the isotropic materials and anisotropic materials are being included in the fitting procedure and how to use this process to obtain the associated parameters of the semiconductors.

4.1 Electromagnetic Wave and Maxwell's Equations

An electromagnetic wave is a transverse wave and it contains an electric field vector and a magnetic field vector. They are mutually perpendicular to each other and perpendicular to the direction of

propagation. The magnitudes of the two field vectors are a function of a position and time. The both electric field vector and magnetic field vector are dependent each other. The conditions/requirements of the electric field vector determine the magnetic field vector.

The properties of the electromagnetic waves and the interactions of the electromagnetic waves with matter can be described classically by Maxwell's equations and the constitutive equations which are given as follows [1]:

Gauss's law $$\vec{\nabla} \cdot \vec{D} = \rho \quad (4.1)$$

Gauss's law of magnetism $$\vec{\nabla} \cdot \vec{B} = 0 \quad (4.2)$$

Faraday's law of induction $$\vec{\nabla} \times \vec{E} = -\frac{\partial \vec{B}}{\partial t} \quad (4.3)$$

Ampere's circuit law $$\vec{\nabla} \times \vec{H} = \vec{J} + \frac{\partial \vec{D}}{\partial t} \quad (4.4)$$

Constitutive equations,

$$\vec{D} = \varepsilon \vec{E} \quad (4.5)$$

$$\vec{B} = \mu \vec{H} \quad (4.6)$$

$$\vec{J} = \sigma \vec{E} \quad (4.7)$$

Where, $\vec{E}$ -electric field, $\vec{B}$ -magnetic field, $\vec{D}$ -displacement field, $\vec{H}$ -magnetizing field, ρ -charge density, $\vec{J}$ -current density, ε -permittivity (dielectric tensor), and μ -permeability.

From the above equations, the plane electromagnetic wave can be given as,

$$\vec{E} = \vec{E}_0 \sin(\vec{k} \cdot \vec{r} - \omega t) \quad (4.8)$$

Where, $\vec{E_0}$ is the amplitude of the electric field and $\vec{k} = k_x \hat{x} + k_y \hat{y} + k_x \hat{z}$ is the wave vector, which describes the propagation direction. $\vec{r}$, ω, and t are position vector, angular frequency, and time, respectively.

4.2 Electromagnetic Waves at Dielectric Interfaces

Consider two dielectric media (k and k+1) with their dielectric functions ε_k and ε_{k+1}, respectively. Figure 4.1 shows a plane electromagnetic wave incident at an angle φ_i on two media.

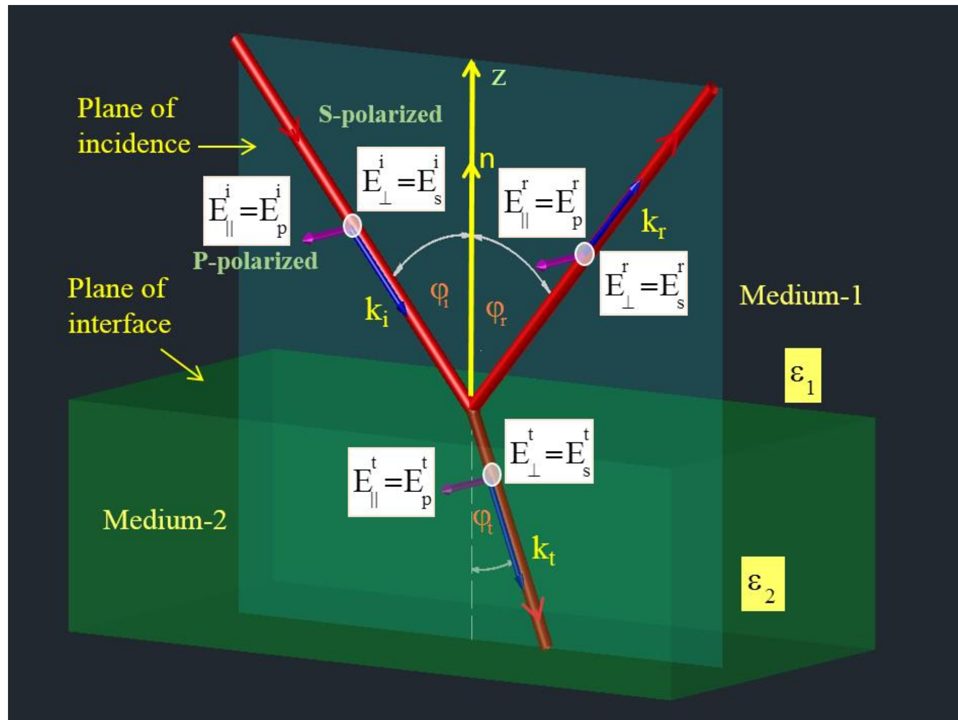

Figure 4.1 An electromagnetic wave incident on an interface between two dielectric media. Where, $\vec{k}_i$, $\vec{k}_t$, and $\vec{k}_r$ are the wave vectors of incident, transmitted, and reflected waves, respectively.

4.2.1 S- and P- Polarization

Light is considered as an electromagnetic wave, and the electric field of it fluctuates perpendicular to the direction of propagation. When the direction of the electric filed of the light oscillates arbitrarily in time, it is said, the light is un-polarized. When the electric field of light is oriented in a well-defined direction, it is referred to as polarized light. According to the orientation of the electric field of the wave, there are three types of polarizations. If the electric field vector of the electromagnetic wave is pointed in fixed direction, however, the magnitude of it varies periodically, it is called linear polarization. A plane electromagnetic wave is linearly polarized. The second is circular polarization, in which the electric field

vector contains two linear components. These are perpendicular to each other and have the same magnitude. The phase difference of those two is 90º. After the two waves combined, the electric field of the resultant wave moves in a circle around the direction of propagation (clockwise or counterclockwise). When the phase difference of the two waves is anything other than 90º and amplitude of the two waves is not equal, the resulting electric field describes an ellipse, and this is called elliptical polarization.

In reflection and transmission, the two types of linear polarization states, s- and p- polarization, which are orthogonal to each other, and are important. When the electromagnetic wave propagate through the medium 1 to the medium 2, it will be partially transmitted and partially reflected at the interface as shown in Fig. 4.1. If the electric field vector is polarized perpendicular to the plane of incidence, it is called as s-polarization ($\vec{E}_s$). The electric field vector is parallel to the plane of incidence in p-polarization ($\vec{E}_p$). The plane of the incidence is characterized by the wave vector of the incoming wave ($\vec{k}_i$) and the normal vector ($\vec{n}$), see Fig. 4.1.

4.2.2 Boundary Conditions at Interfaces

Boundary conditions for the electromagnetic field in between two different types of media can be derived from Maxwell's equations. The boundary conditions at the interface between two media identified as 1 and 2 can be given as following equations [1].

$$\vec{n}\cdot(\vec{D}_2-\vec{D}_1)=\rho=0 \quad 4.9$$

$$\vec{n}\cdot(\vec{B}_2-\vec{B}_1)=0 \quad 4.10$$

$$\vec{n}\times(\vec{E}_2-\vec{E}_1)=0 \quad 4.11$$

$$\vec{n}\times(\vec{H}_2-\vec{H}_1)=\vec{j}=0 \quad 4.12$$

The free charge on the surface (ρ) and the free surface current density ($\vec{j}$) are equal to zero with no charges or current. These equations let to specify the following relationships.

$$\vec{D}_{n,2}=\vec{D}_{n,1} \quad \text{and} \quad \vec{B}_{n,2}=\vec{B}_{n,1} \quad 4.13$$

$$\vec{E}_{t,2} = \vec{E}_{t,1} \quad \text{and} \quad \vec{H}_{t,2} = \vec{H}_{t,1} \qquad 4.14$$

Where, subscripts n and t represent the normal and tangential components, respectively. This summarize to be the normal components of $\vec{D}$ and $\vec{B}$ as well as tangential components of $\vec{E}$ and $\vec{H}$ are continuous at the interface.

4.3 Wave propagation in Isotropic and Anisotropic media

4.3.1 Reflection and Transmission Coefficients at a Single Interface

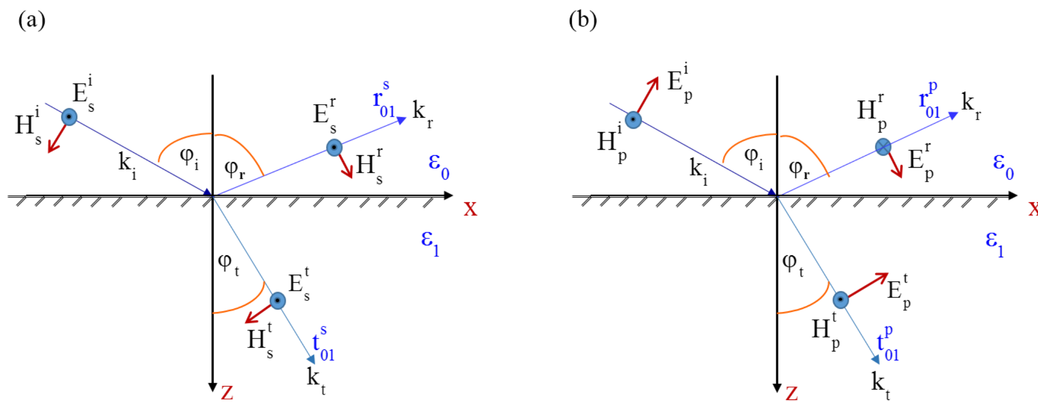

Figure 4.2 Schematic representation showing the transmission and reflection of an electromagnetic wave at interface. (a) s-polarization and (b) p-polarization.
Dot in a circle represent the field is out of the page and cross in a circle means field is into the page.

Again consider, a plane electromagnetic wave incident on the interface (x-y plane) between two media, a medium 0 (ambient) with dielectric function ε_0 and a medium 1 (substrate) with dielectric function ε_1 (see Fig. 4.2). The amplitudes of the s-polarized electric filed for incident, transmitted, and reflected wave are denoted as E_s^i, E_s^t, and E_s^r ,respectively. Those are for p-polarized wave are denoted as E_p^i , E_p^t, and E_p^r ,respectively. H_s^i, H_s^t, H_s^r, H_p^i, H_p^t, and H_p^r represent the corresponding magnetic field quantities. The p-wave can be further separated into two components as parallel (x-direction) to the surface and perpendicular (z-direction) to the surface. However, magnetic field has a component only in the

y-direction. For the s-wave, electric filed has a component only in the y-direction, while magnetic field has two components both x- and z-directions.

According to the boundary conditions, the sum of the tangential electric field components above the interface must be equal to those for below the interface. Same conditions apply for the magnetic field components. Thus, boundary conditions can be written as following form [2],

$$E_x^i + E_x^r = E_x^t \qquad 4.15$$

$$E_y^i + E_y^r = E_y^t \qquad 4.16$$

$$H_x^i + H_x^r = H_x^t \qquad 4.17$$

$$H_y^i + H_y^r = H_y^t \qquad 4.18$$

In literature, there is a difference in the sign used for the reflected field of p-polarization. Some book has considered the magnetic field of the reflected wave out of the page. This changes the sign of the equation for p-polarization reflection coefficient. In this work, it has been considered the magnetic field of the reflected wave into the page to satisfy the $\vec{E} \times \mu\vec{H} \propto \vec{k}_r$.

Considering the tangential electric filed components of s- and p-waves at the interface, Eq. 4.15 and 4.16 become.

$$(E_p^i + E_p^r)\cos\varphi_i = E_p^t \cos\varphi_t \qquad 4.19$$

$$E_s^i + E_s^r = E_s^t \qquad 4.20$$

Similarly for the magnetic field, Eq. 4.17 and 4.18 give the following form

$$(H_s^i - H_s^r)\cos\varphi_i = H_s^t \cos\varphi_t \qquad 4.21$$

$$H_p^i - H_p^r = H_p^t \qquad 4.22$$

Since $H = \sqrt{\varepsilon_0 / \mu\mu_0}.n.E$, (μ is taken as unity for both media, n is the refractive index of the medium and $n = \sqrt{\varepsilon}$) Eq. 4.21 and 4.22 can be written in terms of electric field.

$$\sqrt{\varepsilon_0}(-E_s^i + E_s^r)\cos\varphi_i = -\sqrt{\varepsilon_1}E_s^t \cos\varphi_t \qquad 4.23$$

$$\sqrt{\varepsilon_0}E_p^i - \sqrt{\varepsilon_0}E_p^r = \sqrt{\varepsilon_1}E_p^t \qquad 4.24$$

The reflection coefficients for the electric field are given as,

$$r_{01}^s = \frac{E_s^r}{E_s^i} \quad \text{and} \quad r_{01}^p = \frac{E_p^r}{E_p^i} \qquad 4.25$$

The transmission coefficients are

$$t_{01}^s = \frac{E_s^t}{E_s^i} \quad \text{and} \quad t_{01}^p = \frac{E_p^t}{E_p^i} \qquad 4.26$$

From Eq. 4.19, 4.20, 4.23, 4.24, 4.25, and 4.26,

$$r_{01}^s = \frac{\sqrt{\varepsilon_0}\cos\varphi_i - \sqrt{\varepsilon_1}\cos\varphi_t}{\sqrt{\varepsilon_0}\cos\varphi_i + \sqrt{\varepsilon_1}\cos\varphi_t} \qquad 4.27$$

$$r_{01}^p = \frac{\sqrt{\varepsilon_0}\cos\varphi_t - \sqrt{\varepsilon_1}\cos\varphi_i}{\sqrt{\varepsilon_1}\cos\varphi_i + \sqrt{\varepsilon_0}\cos\varphi_t} \qquad 4.28$$

$$t_{01}^s = \frac{2\sqrt{\varepsilon_0}\cos\varphi_i}{\sqrt{\varepsilon_0}\cos\varphi_i + \sqrt{\varepsilon_1}\cos\varphi_t} \qquad 4.29$$

$$t_{01}^p = \frac{2\sqrt{\varepsilon_0}\cos\varphi_i}{\sqrt{\varepsilon_1}\cos\varphi_i + \sqrt{\varepsilon_0}\cos\varphi_t} \qquad 4.30$$

These coefficients are known as Fresnel coefficients. Using Snell's law: $n_0 \sin\varphi_i = n_1 \sin\varphi_t$, and $\cos^2\varphi_t + \sin^2\varphi_t = 1$, the Eq. 4.27, 4.28, 4.29, and 4.30 can be re-written as follows,

$$r_{01}^s = \frac{\sqrt{\varepsilon_0}\cos\varphi_i - \sqrt{\varepsilon_1 - \varepsilon_0\sin^2\varphi_i}}{\sqrt{\varepsilon_0}\cos\varphi_i + \sqrt{\varepsilon_1 - \varepsilon_0\sin^2\varphi_i}} \qquad 4.31$$

$$r_{01}^p = \frac{\sqrt{\varepsilon_0}\sqrt{\varepsilon_1 - \varepsilon_0\sin^2\varphi_i} - \varepsilon_1\cos\varphi_i}{\varepsilon_1\cos\varphi_i + \sqrt{\varepsilon_0}\sqrt{\varepsilon_1 - \varepsilon_0\sin^2\varphi_i}} \qquad 4.32$$

$$t_{01}^s = \frac{2\sqrt{\varepsilon_0}\cos\varphi_i}{\sqrt{\varepsilon_0}\cos\varphi_i + \sqrt{\varepsilon_1 - \varepsilon_0\sin^2\varphi_i}} \qquad 4.33$$

$$t_{01}^{p} = \frac{2\sqrt{\varepsilon_0}\sqrt{\varepsilon_1}\cos\varphi_i}{\varepsilon_1\cos\varphi_i + \sqrt{\varepsilon_0}\sqrt{\varepsilon_1 - \varepsilon_0\sin^2\varphi_i}} \quad 4.34$$

From the Poynting vector, $S = \frac{c}{4\pi} n|E|^2$, reflectance and transmittance for s and p polarized are given [3],

$$R^{s} = \frac{(E_s^r)^2}{(E_s^i)^2} = (r_{01}^{s})^2 \quad 4.35$$

$$R^{p} = \frac{(E_p^r)^2}{(E_p^i)^2} = (r_{01}^{p})^2 \quad 4.36$$

$$T^{s} = \frac{n_1}{n_0}\frac{(E_p^t)^2}{(E_p^i)^2} = \frac{n_1}{n_0}(t_{01}^{s})^2 \quad 4.37$$

$$T^{p} = \frac{n_1}{n_0}\frac{(E_p^t)^2}{(E_p^i)^2} = \frac{n_1}{n_0}(t_{01}^{p})^2 \quad 4.38$$

At normal incidence $\varphi_i = 0$, in an isotropic medium, s- and p-component of the reflectance as well as those of transmittance coefficients are equal.

$$R^{s} = R^{p} = \left(\frac{\sqrt{\varepsilon_0} - \sqrt{\varepsilon_1}}{\sqrt{\varepsilon_0} + \sqrt{\varepsilon_1}}\right)^2 \quad 4.39$$

$$T^{s} = T^{p} = \frac{4\sqrt{\varepsilon_0}\sqrt{\varepsilon_1}}{\left(\sqrt{\varepsilon_0} + \sqrt{\varepsilon_1}\right)^2} \quad 4.40$$

For an absorbing medium, the dielectric function of that medium is complex, while it is real for a transparent medium for above equations.

4.3.2 Modelling Reflectance and Transmittance for Isotropic three layer Structures

Consider a three layer stacked structure (ambient/film/substrate) as shown in Fig. 4.3. The dielectric function of the ambient, film and substrate are ε_0, ε_1, and ε_2, respectively. Assume that the light incident on homogeneous, isotropic film (the film thickness is d_1) on semi-infinite substrate. Each time, when the beam incident on an interface, the beam is divided into the reflected and the transmitted beams and

amplitude of these beams are shown in Fig. 4.3 [3]. The complex phase factor between the first and the second partial wave is $e^{-2i\phi}$ and phase shift is $\phi = \frac{2\pi d_1\sqrt{\varepsilon_1 - \varepsilon_0 \sin^2\varphi_0}}{\lambda}$, where λ and φ_0 are the wave-length of the light beam and the angle of incidence, respectively.

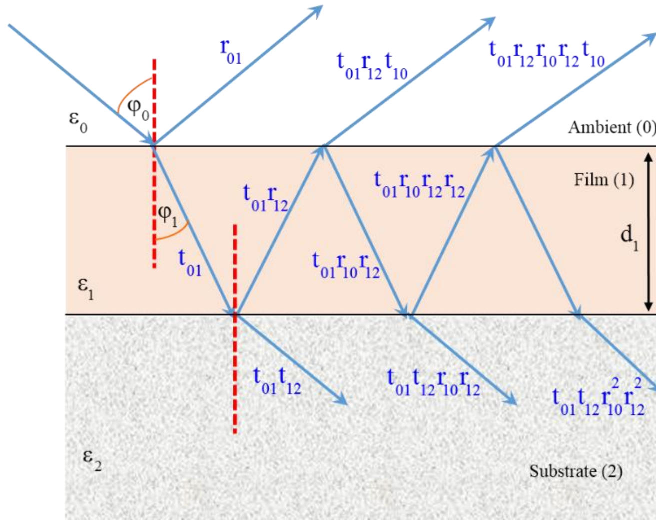

Figure 4.3 Schematic showing the partial waves of a single film on substrate.

Here the total reflection amplitude is given by [3]

$$rr = r_{01} + t_{01}r_{12}t_{10}e^{-2i\phi} + t_{01}r_{12}r_{10}r_{12}t_{10}e^{-4i\phi} + t_{01}r_{12}r_{10}r_{12}r_{10}r_{12}t_{10}e^{-6i\phi} + ... \quad 4.41$$

This equation can be further rearranged.

$$rr = r_{01} + t_{01}t_{10}r_{12}e^{-2i\phi}[1 + (r_{10}r_{12}e^{-2i\phi})^1 + (r_{10}r_{12}e^{-2i\phi})^2 + ...] \quad 4.42$$

$$rr = r_{01} + \frac{t_{01}t_{10}r_{12}e^{-2i\phi}}{1 - r_{10}r_{12}e^{-2i\phi}} \quad 4.43$$

For non-absorbing media this can be written in terms of reflection coefficients r_{01} and r_{12} since $r_{10} = -r_{01}$ and $t_{10}t_{01} = 1 - r_{01}^2$.

$$rr = \frac{r_{10} + r_{12}e^{-2i\phi}}{1 + r_{01}r_{12}e^{-2i\phi}} \quad 4.44$$

Similarly, the total transmission amplitude can be expressed as,

$$tt = t_{01}t_{12}e^{-i\phi} - t_{01}t_{12}r_{10}r_{12}e^{-3i\phi} + t_{01}t_{12}r_{01}r_{12}r_{01}r_{12}e^{-5i\phi} + ... \quad 4.45$$

$$tt = \frac{t_{01}t_{12}e^{-i\phi}}{1 + r_{01}r_{12}e^{-2i\phi}} \quad 4.46$$

The total reflectance (reflectivity) and transmittance (transmitivity) of three layer stack for s- and p-polarized are given by [3]

$$R^s = \sqrt{\varepsilon_0}rr.rr^* = \left(\frac{r_{01}^s + r_{12}^s e^{-2i\phi^s}}{1 + r_{01}^s r_{12}^s e^{-2i\phi^s}}\right)\left(\frac{r_{01}^s + r_{12}^s e^{-2i\phi^s}}{1 + r_{01}^s r_{12}^s e^{-2i\phi^s}}\right)^* = \frac{r_{01}^{s\,2} + 2r_{01}^s r_{12}^s \cos 2\phi^s + r_{12}^{s\,2}}{1 + 2r_{01}^s r_{12}^s \cos 2\phi^s + r_{01}^{s\,2} r_{12}^{s\,2}} \quad 4.47$$

$$R^p = \sqrt{\varepsilon_0}rr^p.rr^{p*} = \left(\frac{r_{01}^p + r_{12}^p e^{-2i\phi^p}}{1 + r_{01}^p r_{12}^p e^{-2i\phi^p}}\right)\left(\frac{r_{01}^p + r_{12}^p e^{-2i\phi^p}}{1 + r_{01}^p r_{12}^p e^{-2i\phi^p}}\right)^* = \frac{r_{01}^{p2} + 2r_{01}^p r_{12}^p \cos 2\phi^p + r_{12}^{p2}}{1 + 2r_{01}^p r_{12}^p \cos 2\phi^p + r_{01}^{p2} r_{12}^{p2}} \quad 4.48$$

$$T^s = \frac{\sqrt{\varepsilon_2}}{\sqrt{\varepsilon_0}}tt^s(tt^s)^* = \frac{\sqrt{\varepsilon_2}}{\sqrt{\varepsilon_0}}\left(\frac{t_{01}^s t_{12}^s e^{-i\phi^s}}{1 + r_{01}^s r_{12}^s e^{-2i\phi^s}}\right)\left(\frac{t_{01}^s t_{12}^s e^{-i\phi^s}}{1 + r_{01}^s r_{12}^s e^{-2i\phi^s}}\right)^*$$
$$= \sqrt{\varepsilon_2}.\frac{t_{01}^{s\,2} t_{12}^{s\,2}}{(1 + 2r_{01}^s r_{12}^s \cos 2\phi^s + r_{01}^{s\,2} r_{12}^{s\,2})} \quad 4.49$$

$$T^p = \frac{\sqrt{\varepsilon_2}}{\sqrt{\varepsilon_0}}tt^p(tt^p)^* = \frac{\sqrt{\varepsilon_2}}{\sqrt{\varepsilon_0}}\left(\frac{t_{01}^p t_{12}^p e^{-i\phi^p}}{1 + r_{01}^p r_{12}^p e^{-2i\phi^p}}\right)\left(\frac{t_{01}^p t_{12}^p e^{-i\phi^p}}{1 + r_{01}^p r_{12}^p e^{-2i\phi^p}}\right)^*$$
$$= \sqrt{\varepsilon_2}.\frac{t_{01}^{p\,2} t_{12}^{p\,2}}{(1 + 2r_{01}^p r_{12}^p \cos 2\phi^p + r_{01}^{p2} r_{12}^{p2})} \quad 4.50$$

where, ε_0 =1 for the ambient. The reflection and transmission coefficient can be written as follows

$$r_{01}^s = \frac{\sqrt{\varepsilon_0}\cos\varphi_0 - \sqrt{\varepsilon_1 - \varepsilon_0 \sin^2\varphi_0}}{\sqrt{\varepsilon_0}\cos\varphi_0 + \sqrt{\varepsilon_1 - \varepsilon_0 \sin^2\varphi_0}}, \qquad r_{12}^s = \frac{\sqrt{\varepsilon_1 - \varepsilon_0 \sin^2\varphi_0} - \sqrt{\varepsilon_2 - \varepsilon_0 \sin^2\varphi_0}}{\sqrt{\varepsilon_1 - \varepsilon_0 \sin^2\varphi_0} + \sqrt{\varepsilon_2 - \varepsilon_0 \sin^2\varphi_0}} \quad 4.51$$

$$r_{01}^p = \frac{\sqrt{\varepsilon_0}\sqrt{\varepsilon_1 - \varepsilon_0 \sin^2\varphi_0} - \varepsilon_1\cos\varphi_0}{\varepsilon_1\cos\varphi_0 + \sqrt{\varepsilon_0}\sqrt{\varepsilon_1 - \varepsilon_0 \sin^2\varphi_0}}, \quad r_{12}^p = \frac{\sqrt{\varepsilon_1}\sqrt{\varepsilon_2 - \varepsilon_0 \sin^2\varphi_0} - \varepsilon_2\sqrt{\varepsilon_1 - \varepsilon_0 \sin^2\varphi_0}}{\varepsilon_2\sqrt{\varepsilon_1 - \varepsilon_0 \sin^2\varphi_0} + \sqrt{\varepsilon_1}\sqrt{\varepsilon_2 - \varepsilon_0 \sin^2\varphi_0}} \quad 4.52$$

$$t_{01}^s = \frac{2\sqrt{\varepsilon_0}\cos\varphi_0}{\sqrt{\varepsilon_0}\cos\varphi_0 + \sqrt{\varepsilon_1 - \varepsilon_0 \sin^2\varphi_0}}, \qquad t_{12}^s = \frac{2\sqrt{\varepsilon_1 - \varepsilon_0 \sin^2\varphi_0}}{\sqrt{\varepsilon_1 - \varepsilon_0 \sin^2\varphi_0} + \sqrt{\varepsilon_2 - \varepsilon_0 \sin^2\varphi_0}} \quad 4.53$$

$$t_{01}^{p}=\frac{2\sqrt{\varepsilon_0}\sqrt{\varepsilon_1}\cos\varphi_i}{\varepsilon_1\cos\varphi_i+\sqrt{\varepsilon_0}\sqrt{\varepsilon_1-\varepsilon_0\sin^2\varphi_i}},\qquad t_{12}^{p}=\frac{2\sqrt{\varepsilon_1}\sqrt{\varepsilon_2}\sqrt{\varepsilon_1-\varepsilon_0\sin^2\varphi_0}}{\varepsilon_2\sqrt{\varepsilon_1-\varepsilon_0\sin^2\varphi_i}+\varepsilon_1\sqrt{\varepsilon_2-\varepsilon_0\sin^2\varphi_i}} \qquad 4.54$$

This summation method is not elegant for the calculating total reflection and transmission of a layer structure having more layers. There are several transfer matrix methods that have been developed for computing electromagnetic field in a system with multilayers. The 2×2 transfer method is the most convenient method that have been developed by Abeles used for light propagation in isotropic media. This method can be found in many text book. Following section reviews and describes this method for computing reflectance and transmittance of a multilayer structure [3, 4].

4.3.3 Modelling Isotropic Multilayer Structures

Figure 4.4 shows a schematic of a multilayer structure and reflection contribution from ambient to the substrate through k-films. The numbering of the media starts from ‘0’ (ambient), ‘1’ (film_1) to ‘k+1’ (substrate). Thicknesses of the each layer denote as d_1, d_2, …, $d_{(k+1)}$ and the dielectric function of corresponding layers are given as ε_0, ε_1,.., ε_{k+1}. The reflection coefficients of each interface are represented as r_{01}, r_{12},…, $r_{k(k+1)}$ (also known as Fresnel’s coefficients) for the isotropic homogeneous multilayer stack. The right going s- and p-polarized e-filed vectors are denoted as E_s^i and E_p^i, and their left going vector are symbolized as E_s^r and E_p^r (refer Fig. 4.4).

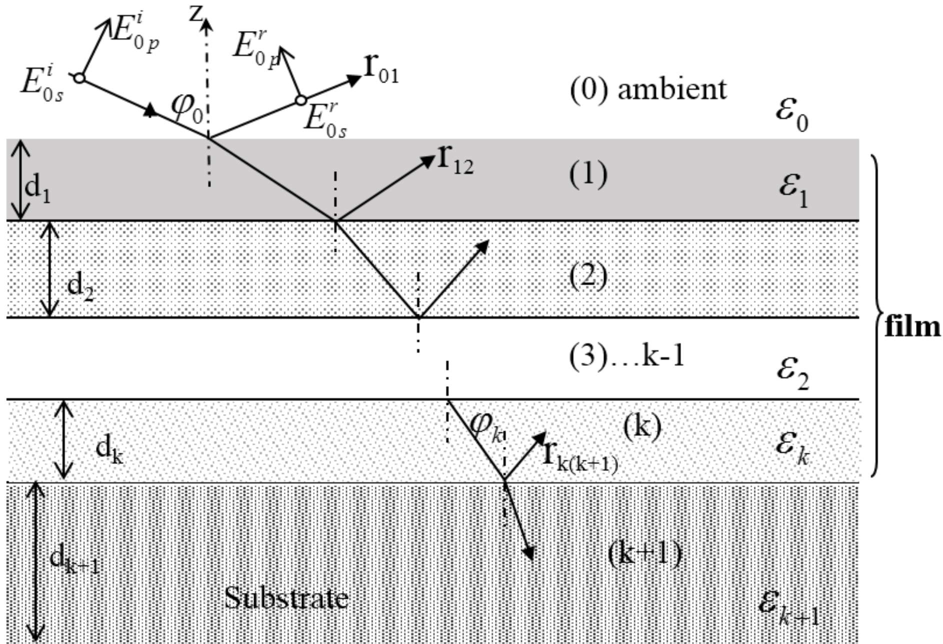

Figure 4.4 Schematic showing a multilayer stack (ambient/film_1 to film_k/substrate) and their reflection contributions.

Now, consider the mth film (film_m) laying somewhere between the film_3 and film_k-1 and suppose the film thickness is d_m, and e-fields are E_s^i E_p^i E_s^r , and E_p^r . See Fig. 4.5.

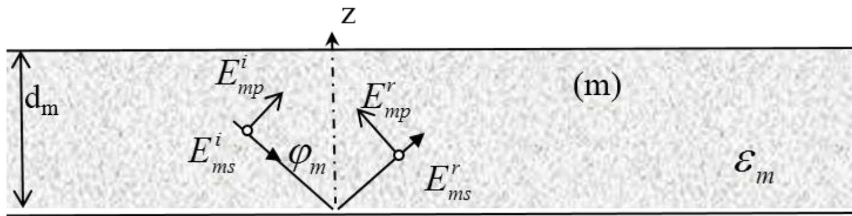

Figure 4.5 Schematic for illustration of mth layer showing the e-field components.

For the mth layer, the x and y components of the E and H can be written as [3]

$$E_{mx} = (E^i_{m,p} e^{-i\chi_m z} + E^r_{m,p} e^{i\chi_m z}) \cos\varphi_m \tag{4.55}$$

$$E_{my} = E^i_{m,s} e^{-i\chi_m z} + E^r_{m,s} e^{i\chi_m z} \tag{4.56}$$

$$H_{mx} = (-E^i_{m,s} e^{-i\chi_m z} + E^r_{m,s} e^{i\chi_m z}) \sqrt{\varepsilon_m} \cos\varphi_m \tag{4.57}$$

$$H_{my} = (E^{i}_{m,p} e^{-i\chi_m z} - E^{r}_{m,p} e^{i\chi_m z})\sqrt{\varepsilon_m} \quad 4.58$$

where $\chi_m = \dfrac{2\pi\sqrt{\varepsilon_m}\cos\varphi_m}{\lambda}$.

(m-1)th and mth layer are separated taking $c_m = \sum_{i=1}^{m-1} d_i$

$$(E^{i}_{m-1,p} e^{-i\chi_{m-1}c_m} + E^{r}_{m-1,p} e^{i\chi_{m-1}c_m})\cos\varphi_{m-1} = (E^{i}_{m,p} e^{-i\chi_m c_m} + E^{r}_{m,p} e^{i\chi_m c_m})\cos\varphi_m \quad 4.59$$

$$\sqrt{\varepsilon_{m-1}}(E^{i}_{m-1,p} e^{-i\chi_{m-1}c_m} - E^{r}_{m-1,p} e^{i\chi_{m-1}c_m}) = \sqrt{\varepsilon_m}(E^{i}_{m,p} e^{-i\chi_m c_m} - E^{r}_{m,p} e^{i\chi_m c_m}) \quad 4.60$$

$$E^{i}_{m-1,s} e^{-i\chi_{m-1}c_m} + E^{r}_{m-1,s} e^{i\chi_{m-1}c_m} = E^{i}_{m,s} e^{-i\chi_m c_m} + E^{r}_{m,s} e^{i\chi_m c_m} \quad 4.61$$

$$(-E^{i}_{m-1,s} e^{-i\chi_m c_m} + E^{r}_{m-1,s} e^{i\chi_{m-1}c_m})\sqrt{\varepsilon_{m-1}}\cos\varphi_{m-1} = (-E^{i}_{m,s} e^{-i\chi_m c_m} + E^{r}_{m,s} e^{i\chi_m c_m})\sqrt{\varepsilon_m}\cos\varphi_m \quad 4.62$$

Eq. 4.59-4.62 can be written in terms of Fresnel coefficients [3].

$$E^{i}_{m-1,p} e^{-i\chi_{m-1}c_m} = (E^{i}_{m,p} e^{-i\chi_m c_m} + r^{p}_{m} E^{r}_{m,p} e^{i\chi_m c_m}) / t^{p}_{m} \quad 4.63$$

$$E^{r}_{m-1,p} e^{i\chi_{m-1}c_m} = (r^{p}_{m} E^{i}_{m,p} e^{-i\chi_m c_m} + E^{r}_{m,p} e^{i\chi_m c_m}) / t^{p}_{m} \quad 4.64$$

$$E^{i}_{m-1,s} e^{-i\chi_{m-1}c_m} = (E^{i}_{m,s} e^{-i\chi_m c_m} + r^{p}_{m} E^{r}_{m,s} e^{i\chi_m c_m}) / t^{s}_{m} \quad 4.65$$

$$E^{r}_{m-1,s} e^{i\chi_{m-1}c_m} = (r^{p}_{m} E^{i}_{m,s} e^{-i\chi_m c_m} + E^{r}_{m,s} e^{i\chi_m c_m}) / t^{s}_{m} \quad 4.66$$

These equations can be simplified by substituting phase shift $\phi = \chi_m c_m = \dfrac{2\pi d_m\sqrt{\varepsilon_m}\cos\varphi_m}{\lambda}$

$$E^{i}_{m-1,p} = (E^{i}_{m,p} e^{i\phi^{p}_{m-1}} + r^{p}_{m} E^{r}_{m,p} e^{i\phi^{p}_{m-1}}) / t^{p}_{m} \quad 4.67$$

$$E^{r}_{m-1,p} = (r^{p}_{m} E^{i}_{m,p} e^{-i\phi^{p}_{m-1}} + E^{r}_{m,p} e^{-i\phi^{p}_{m-1}}) / t^{p}_{m} \quad 4.68$$

$$E^{i}_{m-1,s} = (E^{i}_{m,s} e^{i\phi^{s}_{m-1}} + r^{s}_{m} E^{r}_{m,s} e^{i\phi^{s}_{m-1}}) / t^{s}_{m} \quad 4.69$$

$$E^{r}_{m-1,s} = (r^{s}_{m} E^{i}_{m,s} e^{-i\phi^{s}_{m-1}} + E^{r}_{m,s} e^{-i\phi^{s}_{m-1}}) / t^{s}_{m} \quad 4.70$$

Matrix form of these equations are,

$$\begin{pmatrix} E^i_{m-1,p} \\ E^r_{m-1,p} \end{pmatrix} = \frac{1}{t^p_m} \begin{pmatrix} e^{i\phi^p_{m-1}} & r^p_m e^{i\phi^p_{m-1}} \\ r^p_m e^{-i\phi^p_{m-1}} & e^{-i\phi^p_{m-1}} \end{pmatrix} \begin{pmatrix} E^i_{m,p} \\ E^r_{m,p} \end{pmatrix} \quad 4.71$$

$$\begin{pmatrix} E^i_{m-1,s} \\ E^r_{m-1,s} \end{pmatrix} = \frac{1}{t^s_m} \begin{pmatrix} e^{i\phi^s_{m-1}} & r^s_m e^{i\phi^s_{m-1}} \\ r^s_m e^{-i\phi^s_{m-1}} & e^{-i\phi^s_{m-1}} \end{pmatrix} \begin{pmatrix} E^i_{m,s} \\ E^r_{m,s} \end{pmatrix} \quad 4.72$$

The linear correlation between the right going and the left going e-filed vectors for s- and p-polarization at the k - k+1 interface can be written as followings.

$$\begin{pmatrix} E^i_{k,s} \\ E^r_{k,s} \end{pmatrix} = \frac{1}{t^s_{k+1}} e^{i\phi^s_{m-1}} \begin{pmatrix} 1 & r^s_{k(k+1)} \\ r^s_{k(k+1)} e^{-2i\phi^s_{k-1}} & e^{-2i\phi^s_{k-1}} \end{pmatrix} \begin{pmatrix} E^i_{k+1,s} \\ E^r_{k+1,s} \end{pmatrix} \quad 4.73$$

$$\begin{pmatrix} E^i_{k,p} \\ E^r_{k,p} \end{pmatrix} = \frac{1}{t^p_{k+1}} e^{i\phi^p_{m-1}} \begin{pmatrix} 1 & r^p_{k(k+1)} \\ r^p_{k(k+1)} e^{-2i\phi^p_{k-1}} & e^{-2i\phi^p_{k-1}} \end{pmatrix} \begin{pmatrix} E^i_{k+1,p} \\ E^r_{k+1,p} \end{pmatrix} \quad 4.74$$

In the Eq. 4.73 and 4.74, the 2×2 transfer matrix are denoted as $M_{k+1,s}$ and $M_{k+1,p}$ for the simplicity.

$$\begin{pmatrix} E^i_{k,s} \\ E^r_{k,s} \end{pmatrix} = \frac{1}{t^s_{k+1}} \left(M_{k+1,s} \right) \begin{pmatrix} E^i_{k+1,s} \\ E^r_{k+1,s} \end{pmatrix} \quad 4.75$$

$$\begin{pmatrix} E^i_{k,p} \\ E^r_{k,p} \end{pmatrix} = \frac{1}{t^p_{k+1}} \left(M_{k+1,p} \right) \begin{pmatrix} E^i_{k+1,p} \\ E^r_{k+1,p} \end{pmatrix} \quad 4.76$$

In order to determine the total reflectance and the phase change in the multilayer stack for both the s- and p-polarization, the amplitude of the successive beams of reflected and transmitted rays through each interfaces need to be added up as shown in Eq. 4.75 and 4.76.

$$\begin{pmatrix} E^i_{0,s} \\ E^r_{0,s} \end{pmatrix} = \frac{\left(M_{1,s} \right)\left(M_{2,s} \right)....\left(M_{k+1,s} \right)}{t^s_1 t^s_2 .....t^s_{k+1}} \begin{pmatrix} E^i_{k+1,s} \\ E^r_{k+1,s} \end{pmatrix} \quad 4.77$$

$$\begin{pmatrix} E^i_{0,p} \\ E^r_{0,p} \end{pmatrix} = \frac{\left(M_{1,p} \right)\left(M_{2,p} \right)....\left(M_{k+1,p} \right)}{t^p_1 t^p_2 .....t^p_{k+1}} \begin{pmatrix} E^i_{k+1,p} \\ E^r_{k+1,p} \end{pmatrix} \quad 4.78$$

The matrix M for the s- and p-polarization can be given by form of Eq. 4.77 and 4.78.

$$M_s = \begin{pmatrix} M_{11} & M_{12} \\ M_{21} & M_{22} \end{pmatrix}_s = \left(M_{1,s}\right)\left(M_{2,s}\right)....\left(M_{k+1,s}\right)$$
$$= \begin{pmatrix} 1 & r_{21}^s \\ r_{01}^s & 1 \end{pmatrix} \begin{pmatrix} 1 & r_{12}^s \\ r_{12}^s e^{-2\phi_1^s} & e^{-2\phi_1^s} \end{pmatrix} \times ... \times \begin{pmatrix} 1 & r_{(k-1)k}^s \\ r_{(k-1)k}^s e^{-2\phi_k^s} & e^{-2\phi_k^s} \end{pmatrix} \quad 4.79$$

$$M_p = \begin{pmatrix} M_{11} & M_{12} \\ M_{21} & M_{22} \end{pmatrix}_p = \left(M_{1,s}\right)\left(M_{2,p}\right)....\left(M_{k+1,p}\right)$$
$$= \begin{pmatrix} 1 & r_{21}^p \\ r_{01}^p & 1 \end{pmatrix} \begin{pmatrix} 1 & r_{12}^p \\ r_{12}^p e^{-2\phi_1^p} & e^{-2\phi_1^p} \end{pmatrix} \times ... \times \begin{pmatrix} 1 & r_{(k-1)k}^p \\ r_{(k-1)k}^p e^{-2\phi_k^p} & e^{-2\phi_k^p} \end{pmatrix} \quad 4.80$$

Considering no back reflection from the exit medium ($E_{k+1,s}^r = 0$ and $E_{k+1,s}^r = 0$), in our case sapphire substrate, the Eq. 4.77 and 4.78 can be written as following form (Eq. 4.81 and 4.82).

$$\begin{pmatrix} E_{0,s}^i \\ E_{0,s}^r \end{pmatrix} = \frac{\left(M_{1,s}\right)\left(M_{2,s}\right)....\left(M_{k+1,s}\right)}{t_1^s t_2^s .....t_{k+1}^s} \begin{pmatrix} E_{k+1,s}^i \\ 0 \end{pmatrix} \quad 4.81$$

$$\begin{pmatrix} E_{0,p}^i \\ E_{0,p}^r \end{pmatrix} = \frac{\left(M_{1,p}\right)\left(M_{2,p}\right)....\left(M_{k+1,p}\right)}{t_1^p t_2^p .....t_{k+1}^p} \begin{pmatrix} E_{k+1,p}^i \\ 0 \end{pmatrix} \quad 4.82$$

Then, solving Eq. 4.81 and 4.82, the total reflection and transmission for s- and p-polarization (rr^s , rr^p , tt^s , and tt^p) of the multilayer structure can determined by the Eq. 4.83 - 4.86 [3].

$$rr^s = \frac{E_{0,s}^r}{E_{0,s}^i} = \frac{M_{21,s}}{M_{11,s}} \quad 4.83$$

$$rr^p = \frac{E_{0,p}^r}{E_{0,p}^i} = \frac{M_{21,p}}{M_{11,p}} \quad 4.84$$

$$tt^s = \frac{E_{k+1,s}^r}{E_{0,s}^i} = \frac{t_1^s t_2^s .....t_{k+1}^s}{M_{11,s}} \quad 4.85$$

$$tt^p = \frac{E_{k+1,p}^r}{E_{0,p}^i} = \frac{t_1^p t_2^p .....t_{k+1}^p}{M_{11,p}} \quad 4.86$$

The total complex reflectance and transmittance for each polarization components can be written as [3],

$$R^{s} = rr^{s} \cdot (rr^{s})^{*} = \left(\frac{M_{21,s}}{M_{11,s}}\right) \cdot \left(\frac{M_{21,s}}{M_{11,s}}\right)^{*} \tag{4.87}$$

$$R^{p} = rr^{p} \cdot (rr^{p})^{*} = \left(\frac{M_{21,p}}{M_{11,p}}\right) \cdot \left(\frac{M_{21,p}}{M_{11,p}}\right)^{*} \tag{4.88}$$

$$T^{s} = \frac{\sqrt{\varepsilon_{k+1}}}{\sqrt{\varepsilon_{0}}} tt^{s} \cdot (tt^{s})^{*} = \left(\frac{t_{1}^{s} t_{2}^{s} .....t_{k+1}^{s}}{M_{11,s}}\right) \cdot \left(\frac{t_{1}^{s} t_{2}^{s} .....t_{k+1}^{s}}{M_{11,s}}\right)^{*} \tag{4.89}$$

$$T^{p} = \frac{\sqrt{\varepsilon_{k+1}}}{\sqrt{\varepsilon_{0}}} tt^{p} \cdot (tt^{p})^{*} = \left(\frac{t_{1}^{p} t_{2}^{p} .....t_{k+1}^{p}}{M_{11,p}}\right) \cdot \left(\frac{t_{1}^{p} t_{2}^{p} .....t_{k+1}^{p}}{M_{11,p}}\right)^{*} \tag{4.90}$$

For the general interface, s- and p- reflection and transmission coefficients are given by,

$$r_{k(k+1)}^{s} = \frac{\sqrt{\varepsilon_{k} - \varepsilon_{0} \sin^{2} \varphi_{0}} - \sqrt{\varepsilon_{k+1} - \varepsilon_{0} \sin^{2} \varphi_{0}}}{\sqrt{\varepsilon_{k} - \varepsilon_{0} \sin^{2} \varphi_{0}} + \sqrt{\varepsilon_{k+1} - \varepsilon_{0} \sin^{2} \varphi_{0}}}, \tag{4.91}$$

$$r_{k(k+1)}^{p} = \frac{\sqrt{\varepsilon_{k}} \sqrt{\varepsilon_{k+1} - \varepsilon_{0} \sin^{2} \varphi_{0}} - \varepsilon_{k+1} \sqrt{\varepsilon_{k} - \varepsilon_{0} \sin^{2} \varphi_{0}}}{\varepsilon_{k+1} \sqrt{\varepsilon_{k} - \varepsilon_{0} \sin^{2} \varphi_{0}} + \sqrt{\varepsilon_{k}} \sqrt{\varepsilon_{k+1} - \varepsilon_{0} \sin^{2} \varphi_{0}}} \tag{4.92}$$

for the normal incidence $r_{k(k+1)}^{s} = \dfrac{\sqrt{\varepsilon_{k}} - \sqrt{\varepsilon_{k+1}}}{\sqrt{\varepsilon_{k}} + \sqrt{\varepsilon_{k+1}}}$, $r_{k(k+1)}^{p} = \dfrac{\sqrt{\varepsilon_{k}} - \sqrt{\varepsilon_{k+1}}}{\sqrt{\varepsilon_{k}} + \sqrt{\varepsilon_{k+1}}}$ 4.93

$$t_{k(k+1)}^{s} = \frac{2\sqrt{\varepsilon_{k} - \varepsilon_{0} \sin^{2} \varphi_{0}}}{\sqrt{\varepsilon_{k} - \varepsilon_{0} \sin^{2} \varphi_{0}} + \sqrt{\varepsilon_{k+1} - \varepsilon_{0} \sin^{2} \varphi_{0}}} \tag{4.94}$$

$$t_{12}^{p} = \frac{2\sqrt{\varepsilon_{k}} \sqrt{\varepsilon_{k+1}} \sqrt{\varepsilon_{k} - \varepsilon_{0} \sin^{2} \varphi_{0}}}{\varepsilon_{k+1} \sqrt{\varepsilon_{k} - \varepsilon_{0} \sin^{2} \varphi_{0}} + \varepsilon_{k} \sqrt{\varepsilon_{k+1} - \varepsilon_{0} \sin^{2} \varphi_{0}}} \tag{4.95}$$

for the normal incidence $t_{k(k+1)}^{s} = \dfrac{2\sqrt{\varepsilon_{k}}}{\sqrt{\varepsilon_{k}} + \sqrt{\varepsilon_{k+1}}}$, $t_{12}^{p} = \dfrac{2\sqrt{\varepsilon_{k}}}{\sqrt{\varepsilon_{k+1}} + \sqrt{\varepsilon_{k}}}$ 4.96

The phase shift is $\phi = \frac{2\pi d_m \sqrt{\varepsilon_m - \sin^2 \varphi_0}}{\lambda}$. At the normal incidence, $R^s = R^p$ and $T^s = T^p$ as well as $\phi = \frac{2\pi d_m \sqrt{\varepsilon_m}}{\lambda}$.

4.3.4 Modeling Surface Roughness

The decrease of measured reflectivity compare to the calculated reflectivity below the band gap energy attributed to the surface roughness due to increasing light scattering with photon wavelength [5]. The reflectivity including the root mean squared (RMS) roughness (at the oblique incidence) is given by

$$R_{new} = R.\exp\left(-\frac{16\pi^2 n_{amb}^2 \delta^2}{\lambda^2} \right) \quad 4.97$$

where R_{new}, R, n_{amb}, λ, and δ represent the reflectivity with surface roughness, reflectivity without surface roughness, refractive index of the ambient, wavelength, and RMS roughness, respectively.

4.4 Reflectance of Anisotropic Multilayer Structure

Analysis of optical constants of arbitrary anisotropic multilayer semiconductor materials are restricted due to larger numbers of unknown parameters associated with the dielectric function formulas compared to the isotropic media. Since the electric-field vector parallel to the plane of incidence (p-polarized) and electric-filed vector perpendicular to the plane of incidence (s-polarized) are dependent of each other, a 4×4 matrices are required to calculate the total reflectance or transmittance of anisotropic multilayer structures [6].

However, recently, Katsidis et al. [7] has shown that 2×2 transfer matrix algebra, used for the isotropic media, can be adapted to calculate the optical response of anisotropic multilayer structures consisting of homogeneous biaxial or uniaxial films, the crystal c-axis aligned with z-axis of laboratory coordinates. The 4×4 matrix algebra has been substituted by two consecutive applications of the 2×2 transfer matrix algebra, to calculate the s- and p-polarized transmittance and reflectance of the anisotropic multilayer structures separately. In this section, as described in following, this method is adapted to calculate

the reflectance of anisotropic multilayer structures such as InN grown on different templates or substrates (GaN, AlN or sapphire).

4.4.1 Modelling Anisotropic Multilayer Structures

Since the measureable reflectance value from the FTIR is linear combination of R^s and R^p, and considering the un-polarized IR light source has half of s and half of p-polarized light, the total complex reflectance (R) for the anisotropic homogeneous multilayer structure can be written as following Eq. 4.98.

$$R = \frac{1}{2}(R^s + R^p) \tag{4.98}$$

Where, R^s and R^p are calculated using isotropic model discussed in 4.4.3. For the anisotropic materials, one can model the R with adding the surface roughness term as in section 4.4.2.

The dielectric tensor is diagonal for homogeneous anisotropic media and it is given by,

$$\varepsilon = \begin{bmatrix} \varepsilon_x & 0 & 0 \\ 0 & \varepsilon_y & 0 \\ 0 & 0 & \varepsilon_z \end{bmatrix} = \begin{bmatrix} \varepsilon_\perp & 0 & 0 \\ 0 & \varepsilon_\perp & 0 \\ 0 & 0 & \varepsilon_{\|} \end{bmatrix} \tag{4.99}$$

The dielectric function of a semiconductor will be discussed further in the Section 4.5.

At general interface *k*-(*k+1*), the Fresnel's reflection coefficients ($r^s_{k(k+1)}, r^p_{k(k+1)}$) and the phase shifts ($\phi^s_k, \phi^p_k$) for the s- and p-polarization of the propagating rays through the *k*-th layer written in terms of dielectric functions (ordinary and extraordinary) and the incidence angle (φ_0), can be given as the following equations. The Fresnel's reflection coefficients has been written in terms of refractive index [7].

$$r^s_{k(k+1)} = \frac{\sqrt{\varepsilon_{k\perp} - \varepsilon_0 \sin^2\varphi_0} - \sqrt{\varepsilon_{(k+1)\perp} - \varepsilon_0 \sin^2\varphi_0}}{\sqrt{\varepsilon_{k\perp} - \varepsilon_0 \sin^2\varphi_0} + \sqrt{\varepsilon_{(k+1)\perp} - \varepsilon_0 \sin^2\varphi_0}} \tag{4.100}$$

$$r^p_{k(k+1)} = \frac{\sqrt{\varepsilon_{(k+1)\perp}\varepsilon_{(k+1)\|}}\sqrt{\varepsilon_{k\|} - \varepsilon_0 \sin^2\varphi_0} - \sqrt{\varepsilon_{k\perp}\varepsilon_{(k+1)\|}}\sqrt{\varepsilon_{(k+1)\|} - \varepsilon_0 \sin^2\varphi_0}}{\sqrt{\varepsilon_{(k+1)\perp}\varepsilon_{(k+1)\|}}\sqrt{\varepsilon_{k\|} - \varepsilon_0 \sin^2\varphi_0} + \sqrt{\varepsilon_{k\perp}\varepsilon_{(k+1)\|}}\sqrt{\varepsilon_{(k+1)\|} - \varepsilon_0 \sin^2\varphi_0}} \tag{4.101}$$

Phase shift for the s- and p- polarized can be expressed by

$$\phi_k^s = \frac{2\pi d_k \sqrt{\varepsilon_{k,\perp} - \varepsilon_0 \sin^2 \varphi_0}}{\lambda} \quad 4.102$$

$$\phi_k^p = \frac{2\pi d_k \sqrt{\varepsilon_{k,\perp}} \sqrt{\varepsilon_{k,\|} - \varepsilon_0 \sin^2 \varphi_0}}{\lambda \sqrt{\varepsilon_{k,\|}}} \quad 4.103$$

Where, $\varepsilon_{k\perp}$ and $\varepsilon_{k+1\perp}$ are ordinary dielectric function of the k and k+1 layers, as well as $\varepsilon_{k\|}$, and $\varepsilon_{k+1\|}$ are the extraordinary dielectric functions of the k and k+1 layers. The ε_0, φ_0, and d_k denote as dielectric function of the ambient, the angle of incidence, and the thickness of the *k*-th layer respectively.

4.5 Model of Dielectric Function of Semiconductors

The dielectric function of a semiconductor is a linear superposition of the susceptibility contributions of various physical mechanisms: the lattice vibrations (lat), free carriers (fc) [mobile electrons and holes], bound valence electrons (VE), and impurities (imp), assuming there is no interaction of these process with each other. Thus, the complex dielectric function can be given as [8],

$$\varepsilon(\omega) = \varepsilon_1(\omega) + i\varepsilon_2(\omega) = 1 + \chi_{VE} + \chi_{lat}(\omega) + \chi_{fc}(\omega) + \chi_{imp}(\omega) + \ldots \quad 4.104$$

For the IR region, bound valence contribution is not dependent on frequency and therefore is a real value. Thus, $1 + \chi_{VE} = \varepsilon_\infty$, and ε_∞ is called high frequency dielectric constant. Therefore, Eq. 4.104 can be re-written as,

$$\varepsilon(\omega) = \varepsilon_1(\omega) + i\varepsilon_2(\omega) = \varepsilon_\infty + \chi_{lat}(\omega) + \chi_{fc}(\omega) + \chi_{imp}(\omega) + \ldots \quad 4.105$$

The classical Lorentz oscillator model is used to model the dielectric function of ionic crystals in the IR region. This model works well for un-doped and doped semiconductors, and insulators.

Suppose, the valence electrons are tightly bound to the atoms within the materials. When applying an electric field by vibrating (damped harmonic oscillators), the equation of motion can be given by [1]

$$m\frac{d^2\vec{r}}{dt^2} + m\gamma\frac{d\vec{r}}{dt} + m\omega_0^2\vec{r} = -e\vec{E}_{loc} \quad 4.106$$

where, m and $-e$ are the mass and charge of the electron. And, the γ , ω_0 , $\vec{r}$, and $\vec{E}_{loc}$ are the damping, the displacement, the resonant frequency, and the local electric field acting on the electron, respectively.

Assume that the local electric filed and macroscopic electric filed are equal and time dependence of $e^{i\omega t}$. Then, the solution to the Eq. 4.106 yields [1]

$$\vec{r} = \frac{1}{m}\frac{-e\cdot\vec{E}_{loc}}{(\omega_0^2-\omega^2-i\gamma\omega)} \qquad 4.107$$

Induced dipole moment μ is,

$$\vec{\mu}(\omega) = -e\cdot\vec{r} = \frac{e^2\cdot\vec{E}_{loc}}{m(\omega_0^2-\omega^2-i\gamma\omega)} \qquad 4.108$$

The polarizability can be expressed as

$$\alpha(\omega) = \frac{E(\omega)}{\mu(\omega)} = \frac{e^2}{m}\frac{1}{(\omega_0^2-\omega^2-i\gamma\omega)} \qquad 4.109$$

Then, the polarization per unit volume yields,

$$P(\omega) = N\cdot\alpha(\omega).E(\omega) = \varepsilon_0\cdot\chi(\omega)\cdot E(\omega) \qquad 4.110$$

The susceptibility can be expressed by

$$\chi(\omega) = \frac{N\cdot e^2}{\varepsilon_0\cdot m}\frac{1}{(\omega_0^2-\omega^2-i\gamma\omega)} \qquad 4.111$$

With the characteristic of resonant frequency ω_{TO} and damping constant γ , dielectric function can be written as

$$\varepsilon(\omega) = \varepsilon_\infty + \frac{S\omega_{TO}^2}{(\omega_{TO}^2-\omega^2-i\gamma\omega)} \qquad 4.112$$

where, S is the oscillator strength and it may relate with ionic charge , volume density, reduced mass as follows

$$S\omega_{TO}^2 = \frac{N\cdot e^2}{\varepsilon_0\cdot m} \qquad 4.113$$

For more than one oscillator

$$\varepsilon(\omega) = \varepsilon_\infty + \sum_j \frac{S_j \omega_{j,TO}^2}{(\omega_{j,TO}^2 - \omega^2 - i\gamma_j \omega)} \qquad 4.114$$

If the damping factor is neglected, the Eq.4.112 becomes

$$\varepsilon(\omega) = \varepsilon_\infty + \frac{S\omega_{TO}^2}{(\omega_{TO}^2 - \omega^2)} \qquad 4.115$$

Due to no excess charges in the medium, Gauss equation should be valid and condition $\varepsilon(k \cdot E)$ should be satisfied. For the longitudinal filed $k \parallel E$, it is $\varepsilon = 0$, and the frequency is expressed by

$$\omega_{LO}^2 = \omega_{TO}^2 + \frac{S\omega_{TO}^2}{\varepsilon_\infty} \qquad 4.116$$

Then the dielectric function can be given as

$$\varepsilon(\omega) = \varepsilon_\infty + \frac{\varepsilon_\infty(\omega_{LO}^2 - \omega_{TO}^2)}{(\omega_{TO}^2 - \omega^2)} \qquad 4.117$$

With a non-zero the damping constant, the dielectric function can be given as

$$\varepsilon(\omega) = \varepsilon_\infty \left[1 + \frac{\omega_{LO}^2 - \omega_{TO}^2}{(\omega_{TO}^2 - \omega^2 - i\gamma\omega)} \right] \qquad 4.118$$

All the phonon frequencies need to be satisfied the Lyddane-Sachs-Teller relation (Eq.4.119) [9, 10]

$$\frac{\varepsilon_s}{\varepsilon_\infty} = \prod \frac{\omega_{LO}^2}{\omega_{TO}^2} \qquad 4.119$$

where $\varepsilon_s = \varepsilon(\omega \to 0)$ and $\varepsilon_\infty = \varepsilon(\omega \to \infty)$

For the positive imaginary part of the dielectric function, following equation should be fulfilled.

$$\sum_j (\gamma_{LO_j} - \gamma_{TO_j}) > 0 \qquad 4.120$$

The free carrier contribution can be expressed by the Drude model which is given at $\omega_0 = 0$ in Eq. 4.111.

$$\chi(\omega) = -\frac{N \cdot e^2}{\varepsilon_0 \cdot m} \frac{1}{(\omega^2 + i\gamma\omega)} \quad 4.121$$

With the plasma frequency

$$\omega_p = \frac{N \cdot e^2}{\varepsilon_0 \cdot \varepsilon_\infty \cdot m^*} \quad 4.122$$

$$\chi(\omega) = -\varepsilon_\infty \frac{1}{(\omega^2 + i\gamma\omega)} \quad 4.123$$

Now the IR isotropic dielectric function with multi oscillators can be expressed in the following forms

$$\varepsilon(\omega) = \varepsilon_\infty [1 - \frac{\omega_p^2}{(\omega^2 + i\gamma_p\omega)}] + \sum_j \frac{S_j \omega_{j,TO}^2}{(\omega_{j,TO}^2 - \omega^2 - i\gamma_j\omega)} \quad 4.124$$

$$\varepsilon(\omega) = \varepsilon_\infty [1 + \frac{\omega_{LO}^2 - \omega_{TO}^2}{(\omega_{TO}^2 - \omega^2 - i\gamma\omega)} - \frac{\omega_p^2}{(\omega^2 + i\gamma_p\omega)}] \quad 4.125$$

Additionally, the impurities which relate to the lattice vibrations can be solved by considering them as oscillators.

For the anisotropic materials the dielectric function in parallel ($\varepsilon_\parallel$) and perpendicular ($\varepsilon_\perp$) direction to the crystal c-axis, in the IR region can be written as following,

$$\varepsilon_\parallel(\omega) = \varepsilon_{\infty,\parallel} [1 + \frac{\omega_{LO,\parallel}^2 - \omega_{TO,\parallel}^2}{(\omega_{TO,\parallel}^2 - \omega^2 - i\gamma_\parallel\omega)} - \frac{\omega_{p,\parallel}^2}{(\omega^2 + i\gamma_{p,\parallel}\omega)}] \quad 4.126$$

$$\varepsilon_\perp(\omega) = \varepsilon_{\infty,\perp} [1 + \frac{\omega_{LO,\perp}^2 - \omega_{TO,\perp}^2}{(\omega_{TO,\perp}^2 - \omega^2 - i\gamma_\perp\omega)} - \frac{\omega_{p,\perp}^2}{(\omega^2 + i\gamma_{p,\perp}\omega)}] \quad 4.127$$

From the plasma frequency ($\omega_{p,\parallel}, \omega_{p,\perp}$) and damping constant of the plasma ($\gamma_{p,\parallel}, \gamma_{p,\perp}$), the free carrier concentrations ($N_{c,\parallel}, N_{c,\perp}$) and mobility of the carries ($\mu_{c,\parallel}, \mu_{c,\perp}$) in the semiconductor can be determined using following equations.

$$N_{c,\parallel} = \frac{\omega_{p,\parallel}^2 m_{eff,\parallel} \varepsilon_0 \varepsilon_{\infty,\parallel}}{e^2} \quad 4.128$$

$$N_{c,\perp} = \frac{\omega_{p,\perp}^2 m_{eff,\perp} \varepsilon_0 \varepsilon_{\infty,\perp}}{e^2} \tag{4.129}$$

$$\mu_{c,\|} = \frac{e}{m_{eff,\|} \gamma_{p,\|}} \tag{4.130}$$

$$\mu_{c,\perp} = \frac{e}{m_{eff,\perp} \gamma_{p,\perp}} \tag{4.131}$$

where, $m_{eff,\|}$ and $m_{eff,\perp}$ are the effective electron (hole) mass in parallel and perpendicular directions. The ε_0, and e denote the vacuum permittivity and the electrical unit charge respectively. For the isotropic materials $\varepsilon_\| = \varepsilon_\perp$, therefore, $N_{c,\|} = N_{c,\perp}$ and $\mu_{c,\|} = \mu_{c,\perp}$

In this study, the infrared dielectric response of the sapphire is described using a factorized model with the contribution of l (four) polar-optical phonon modes [9]. In order to account for the optical anisotropy, dielectric function is discriminated as parallel ($\varepsilon_\|(\omega)$) and perpendicular ($\varepsilon_\perp(\omega)$) to the crystal c-axis direction.

$$\varepsilon_\|(\omega) = \varepsilon_{\infty,\|} \prod_{m=1}^{l} \frac{\omega_{LO,m,\|}^2 - \omega^2 - i\omega\gamma_{LO,m,\|}}{\omega_{LO,m,\|}^2 - \omega^2 - i\omega\gamma_{LO,m,\|}} \tag{4.132}$$

$$\varepsilon_\perp(\omega) = \varepsilon_{\infty,\perp} \prod_{m=1}^{l} \frac{\omega_{LO,m,\perp}^2 - \omega^2 - i\omega\gamma_{LO,m,\perp}}{\omega_{LO,m,\perp}^2 - \omega^2 - i\omega\gamma_{LO,m,\perp}} \tag{4.133}$$

4.6 Flow Chart of Fitting Program

Figure 4.6 illustrates a simple flow chart of the program (Matlab) developed for the analysis of the IR reflectance spectra, in order for extracting the physical properties of the material, using the mathematical model discussed in Section 4.3 and 4.4.

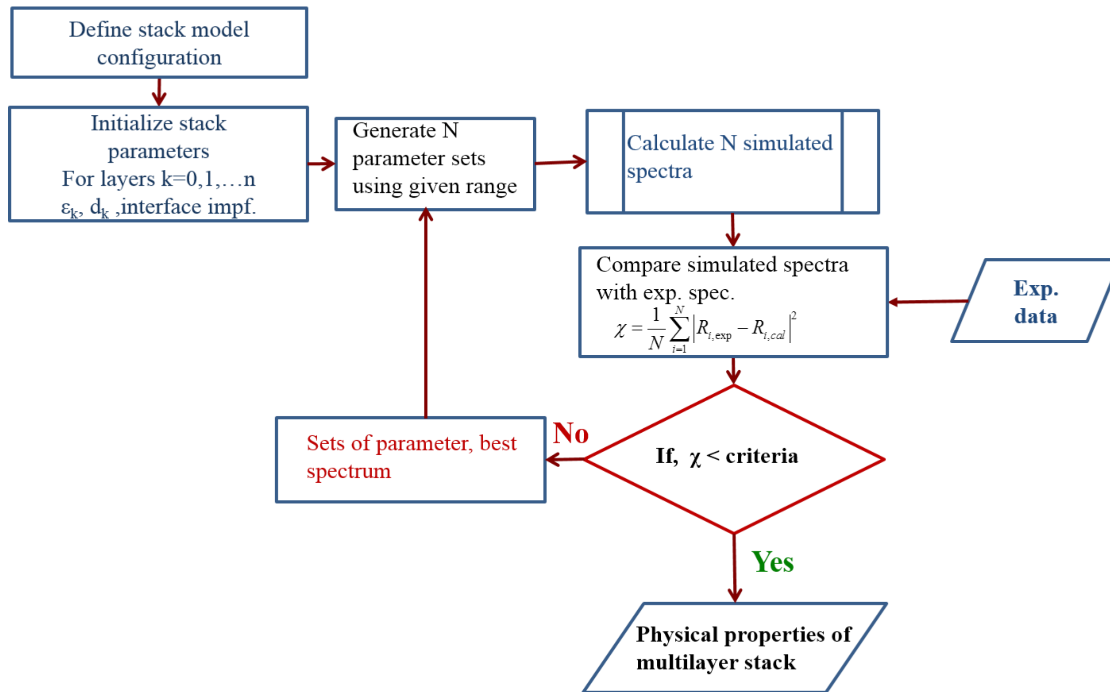

Figure 4.6 Flow chart of analysis reflectance spectra based on the Multilayer stack model and model of IR dielectric function.

❖ In the first step: layer stack configuration are modeled. In order to do this, the basic growth steps and the type of material that have grown need to be known. Fig. 4.7 shows an example for the layer stack configuration.

InN	d_{InN}	$\varepsilon_{InN}(\omega)$
GaN	d_{GaN}	$\varepsilon_{GaN}(\omega)$
Sapphire substrate	$d_{Sapph.}$	$\varepsilon_{sapph.}(\omega)$

Figure 4.7 Showing the layer configuration of InN on GaN/Sapphire.

❖ In the second step: initial layer parameters such as dielectric functions, layer thicknesses, and interface perfections of the each layer are defined. As the dielectric function, the user can select the one of the dielectric functions discussed above. Under this, a tolerance for the initial parameters of the dielectric function should be selected.

- In the next step, the program will generate an array of data based on the initial parameters and the tolerance, and compare it with the experimental data.
- If the calculated and the experimental data are not within the given criteria condition, the program will be looped to a new iteration cycle with new set of layer parameters based on its current cycle.

The MATLAB code is attached in Appendix B.

4.7 References

[1] R. P. Prasankumar and A. J. Taylor, *Optical Techniques for Solid-State Materials Characterization*. (CRC Press Taylor & Francis Group, 2012).

[2] H. G. Tompkins and W. A. McGahan, *Spectroscopic Ellipsometry and Reflectrometry*. (John Wiley & Sons, Inc., New York, 1999).

[3] O. S. Heavens, *Optical Properties of thin solid films*. (Dover Publications, Inc., New York, 1991).

[4] O. S. Heavens, Reports on Progress in Physics **23** (1), 1 (1960).

[5] S. Shokhovets, R. Goldhahn, G. Gobsch, T. S. Cheng, C. T. Foxon, G. D. Kipshidze and W. Richter, Journal of Applied Physics **86** (5), 2602-2610 (1999).

[6] M. Schubert, Physical Review B **53** (8), 4265-4274 (1996).

[7] C. C. Katsidis, A. O. Ajagunna and A. Georgakilas, Journal of Applied Physics **113** (7), 073502 (2013).

[8] G. Bauer and W. Richter, *Optical Characterization of Epitaxial Semiconductor Layers*. (Springer, New York, 1996).

[9] M. Schubert, T. E. Tiwald and C. M. Herzinger, Physical Review B **61** (12), 8187-8201 (2000).

[10] P. M. Amirtharaj and D. G. Seiler, in *Handbook of optics : Devices, Measurements, and Properties*, edited by M. Bass (Optical Society of America, 1995), Vol. II.

5 CHAPTER 5: INFLEUNCE OF SUBSTRATE POLARITY AND DOPING ON THE STRUCTURAL AND OPTOELECTRONIC PROPERITIES OF InN LAYERS GROWN BY HP-MOCVD

5.1 Introduction

In order to achieve the best quality devices (InN based), scientists have been devoted during last few decades on experimental investigations on the growth of InN thin films by various growth methods with different substrates. However, free carrier concentrations of those layers are still in the range of 10^{18}-10^{20} cm^{-3}, with an exception for the MBE growth films, it was achieved to the order 10^{17} cm^{-3}. As discussed in Section 1.2, several possible reasons have been suggested for the cause of the high background carrier concentration. However, it is still a mysterious. Recently, more researches have been focused on the development of InN films for plasmonic applications extending to the infrared (IR) and THz regimes due to its lower plasma frequency and its smaller real permittivity than those of the metals [1]. As an example, Qian et al. has been shown that aptness of InN films as plasma filters for GaSb and GaInAsSb photovoltaic cells in thermophotovoltaic systems with different carrier concentration, mobility, and film thickness [2]. Additionally, due to the high superficial electron concentration, the high sensitivity to charges in the environment, and the high chemical stability, InN has also been recently considered as material for biosensing. For instance, Naveed Alvi et al. has been suggested a development of an efficient InN QDs (quantum dots) based biosensor for medical diagnosis and shown it for the ability to detect real time changes in the concentration of cholesterol in the human body [3].

Based on these unique properties and its applications, the need of further studies of InN properties cannot be disregarded. Hence, studies of optical response in the IR regime is necessary since phonon modes (lattice vibrations), free carriers, and their coupling, etc. of InN are associated with the IR photon energies. Furthermore, these studies will also expose these physical properties of the commonly used substrates such as GaN, AlN, and sapphire used in the growth of InN films. Thus, especially, understanding of the IR optical anisotropy properties of InN play a significant role in devices designing due to the high

anisotropy in the wurtzite structure. Also, studies of the influence of the substrate properties on the InN films properties is crucial for the device fabrication because most physical properties of the materials such as point defect, strain, etc. originate from the substrate.

Y. Ishitani et al. found the dependence of the broadening of InN E_1(LO) phonon-plasmon coupled states with the electron concentration (from 8×10^{17} to 1×10^{19} cm^{-3}) and the crystal temperature by analyzing the S-polarized IR reflectance spectra [4]. As well as, by analyzing the IR reflectance spectra of InN down to 200 or 250 cm^{-1} including longitudinal phonon and plasmon coupling lower energy branch (LPP-) and higher energy branch (LPP+), Y. Ishitani et al. have extracted the electron concentration and mobility of inside region of the bulk nature by resolving the contribution of electron accumulation to the spectra [5]. One of the important properties of InN is the LO-plasmon coupling, and this has been studied using Raman spectra of InN [6] and IR reflectance spectra has been used to compare this features [5]. Moreover, the role of plasmon and LO-phonon damping on the IR spectra of InN films has also been studied [7]. Furthermore, A. Kasic et al. used IR spectroscopic ellipsometry to obtain the electron effective mass. These analysis results indicated the average electron effective mass of $0.14m_0$ for InN [8]. Later, Y.F. Chen et al. used IR reflectance measurements and obtained a smaller electron effective mass of $0.05m_0$ for InN films [9]. In addition to these studies, IR ellipsometry and IR reflectance analysis has been used to understand other properties of InN, such as the electron accumulation at nonpolar (112-0)-oriented and semi-polar (101-1)-oriented InN, hole properties of p-type InN films; surface, bulk, and interface electronic properties of nonpolar InN films [10-12]. Z. G. Qian et al. have reported the first detailed investigation of the free carrier concentration, carriers mobility, lattice vibration properties (phonon modes) [2]. A similar study has been conducted by K. Fukui et al. [13]. However, these studies have focused only isotropic properties of InN layers. Recently, C. C Katsidis et al. analyzed FTIR reflectance spectra of InN layers, taking into account a three-layer model and found the capability of separating the contribution of free carriers between the bulk, the surface and interface in InN films [14]. In this study, 2×2 matrix algebra based on a general transfer matrix method has been considered to interpret the optical response of arbitrary multilayers with homogeneous anisotropic layers from IR reflectance spectra.

The work presented in this chapter is a detailed study of free carrier concentrations, mobility of the carriers, high frequency dielectric constant, layer thicknesses and phonon modes of InN layers grown on different substrates, Ga-polar, N-polar, n- and p-type doped GaN, AlN, and sapphire by analyzing FTIR reflectance spectra (at normal and angle incidence un-polarized). Here, isotropic and anisotropic properties of InN layers were analyzed using Multilayer stack model and Model of IR dielectric function described in Chapter 4.

Furthermore, the structural properties of InN layers obtained from Raman spectroscopy analysis are presented. Additionally, surface morphology analysis of these layers by AFM are discussed.

5.2 Experimental

5.2.1 Growth of InN Films

All InN samples were grown on sapphire, AlN, Ga-polar GaN, N-polar GaN, p-type GaN, and n-type GaN templates by HP-MOCVD. Following steps are followed in the growth of all InN samples. First, template/substrate was thermally cleaned in N_2 flow at 875 °C. Next, in order to deposit low temperature InN layer, template/substrate was nitridized for two minutes, and then nucleated for 1 minute at 715 °C. After that, the temperature was gradually increased to the growth temperature, and the same time the V/III ratio was increased by decreasing trimethylindium (TMI) flow. The process, annealing the nucleation layer was done for 2 minutes. Next, V/III ratio was brought to ~8100 by increasing TMI flow gradually. Growth temperature for InN samples grown on sapphire and AlN/sapphire was kept at 875 °C, and it was kept at 840 °C for InN on GaN templates. The growth time and reactor pressure were 3 hours and 8 bar, respectively. Figure 5.1 illustrates a schematic for the temperature and precursor profiles for InN on sapphire or AlN growth.

Templates used in this analysis were grown at the MOCVD facility at North Carolina University. First, low temperature AlN buffer layer was grown on the sapphire substrate (commercially available). Then, the Ga- polar, N-polar GaN layer was directly deposited on top of the AlN buffer layer. The n-type, and p-type GaN layers were grown on top of the AlN buffer, followed by a thick i-GaN layer.

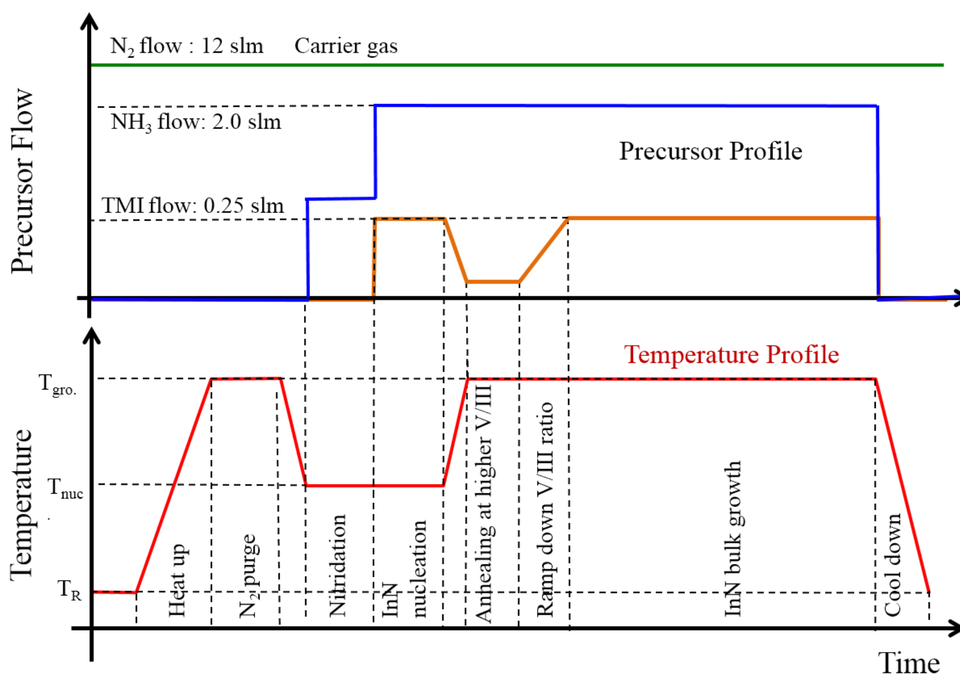

Figure 5.1 Schematic showing the temperature and precursor profiles of the InN growth.

5.2.1 Infrared Reflection Measurements

IR reflectance measurements were performed at room temperature using Perkin-Elmer 2000 FTIR spectrometer. IR spectra in the spectral range 450 cm^{-1}- 6500 cm^{-1} were taken by the MCT (HgCdTe) detector and KBr beamsplitter at near normal incidence (~8°) as well as for oblique incidence (25°) for un-polarized and polarized light. A TGS/POLY detector and 6-μm-thick Mylar beamsplitter were used for the measurements in the range of 300-600 cm^{-1}. In order to obtain the polarized light, a wire grid KRS-5 polarizer and polyethylene polarizer were employed in the MIR and FIR region, respectively. Gold and Aluminum mirrors were used for the reference spectra in the MIR and FIR regions, respectively.

5.2.2 Raman Measurements

The home-built Raman spectrometer with a McPhersom double subtractive monochromator and a liquid N_2 cooled charge-coupled (CCD) camera were used to record the Raman scattering. As the excitation source, a Diode-pumped solid-state (DPSS) laser light with an excitation energy of 2.33 eV (532 nm) was utilized. All the measurements were performed in back scattering geometry $z(x, x)\bar{z}$ along the c-plane at room temperature.

Raman measurements with the excitation of 488 nm were performed at Gediz University in Turkey.

5.3 Results and Discussion

5.3.1 Analysis of IR reflectance Spectra for Sapphire

The infrared optical properties of InN films and the substrates are explored by using reflectance spectra measured at near normal incidence and 25° un-polarized incident light. The normal incidence reflectance spectra were calculated based on the 2×2 transfer matrix method for multilayers and Lorentz-Drude model which represent the dielectric response for each layers assuming layers are isotropic. The 2×2 matrix method described in Section 4.3-4.6 was used to calculate the reflectance spectra and to obtain the best fit spectra for anisotropic media.

In order to analyze the FTIR reflectance spectra of the InN films, it is required the parameters for sapphire. Therefore, initially, the best fit parameter values of sapphire were obtained. Sapphire (α-Al_2O_3) has a rhombohedral structure and consists of a hexagonal closely packed (hcp) lattice of aluminum (Al) atoms with oxygen (O) atoms at octahedral sites [15]. The lattice structure of sapphire belongs to the space group D_{3d}^6. Group theory analysis shows that the irreducible representation for the optical modes at k = 0 of the first Brillouin zone is $\Gamma_{\mathrm{opt}} = 2A_{1g} + 2A_{1u} + 3A_{2g} + 2A_{2u} + 5E_g + 4E_u$. Among them, two A_{1g} modes and five E_g modes are only Raman active, while two A_{2u} modes and four E_u modes are only IR active. The two A_{1u} and three A_{2g} modes are neither Raman nor IR active [15].

The factorized model with contribution of l (four) polar-optical phonon modes (see Eq. 4.133 and 4.134) is well described the dielectric function of the sapphire [16]. For the convenience, the equations are recalled here as 5.1 and 5.2. In the anisotropic case (at 25° incident angle), the ordinary ($\varepsilon_{\perp}(\omega)$) and extraordinary ($\varepsilon_{\parallel}(\omega)$) dielectric functions are,

$$\varepsilon_{\parallel}(\omega) = \varepsilon_{\infty,\parallel} \prod_{m=1}^{l} \frac{\omega_{LO,m,\parallel}^2 - \omega^2 - i\omega\gamma_{LO,m,\parallel}}{\omega_{LO,m,\parallel}^2 - \omega^2 - i\omega\gamma_{LO,m,\parallel}} \quad 5.1$$

$$\varepsilon_{\perp}(\omega) = \varepsilon_{\infty,\perp} \prod_{m=1}^{l} \frac{\omega_{LO,m,\perp}^2 - \omega^2 - i\omega\gamma_{LO,m,\perp}}{\omega_{LO,m,\perp}^2 - \omega^2 - i\omega\gamma_{LO,m,\perp}} \quad 5.2$$

Here, $\omega_{LO,\parallel}$ and $\omega_{TO,\parallel}$ denote the frequencies of the LO and TO for sapphire A_u (which are parallel to c-axis) phonon modes. As well as, their broadening constants denote as $\gamma_{LO,\parallel}$ and $\gamma_{TO,\parallel}$. The $\omega_{LO,\perp}$ and $\omega_{TO,\perp}$ account for the frequencies of LO and TO for sapphire E_u (which are perpendicular to c-axis) phonon modes. Their broadening constants are $\gamma_{LO,\perp}$ and $\gamma_{TO,\perp}$ respectively. In the isotropic case (at normal incidence), $\varepsilon_{\perp}(\omega) = \varepsilon_{\parallel}(\omega)$.

The sapphire spectrum was fitted using the two layer model (ambient/Sapphire) and the above dielectric function as described in Chapter 4. Figure 5.2 (a) and (b) show the experimental and the best fitted reflectance spectra for sapphire at near normal incidence and at 25° un-polarized incident light, respectively. Simultaneously, Fig. 5.2 (c) and (d) illustrate the S-polarized and P-polarized experimental reflectance spectra of sapphire measured at 25° incident light. There is no apparent difference between the near normal and 25° s-polarized reflectance spectra, except for the dip around 895 cm^{-1}. Since the anisotropic materials are more sensitive to the incidence angle and the P-polarized light, It can be observed a clear difference between the near normal incidence and un-polarized or P-polarized reflectance spectra measured at 25° incident light around 500-515 cm^{-1}. Therefore, here the near normal incidence spectrum

and the 25° un-polarized spectrum for analysis of isotropic and anisotropic properties of materials, respectively. Furthermore, the best fit parameters are listed in Table 5.1, and they are very close to the reported values obtained from the IR-ellipsometry analysis [16].

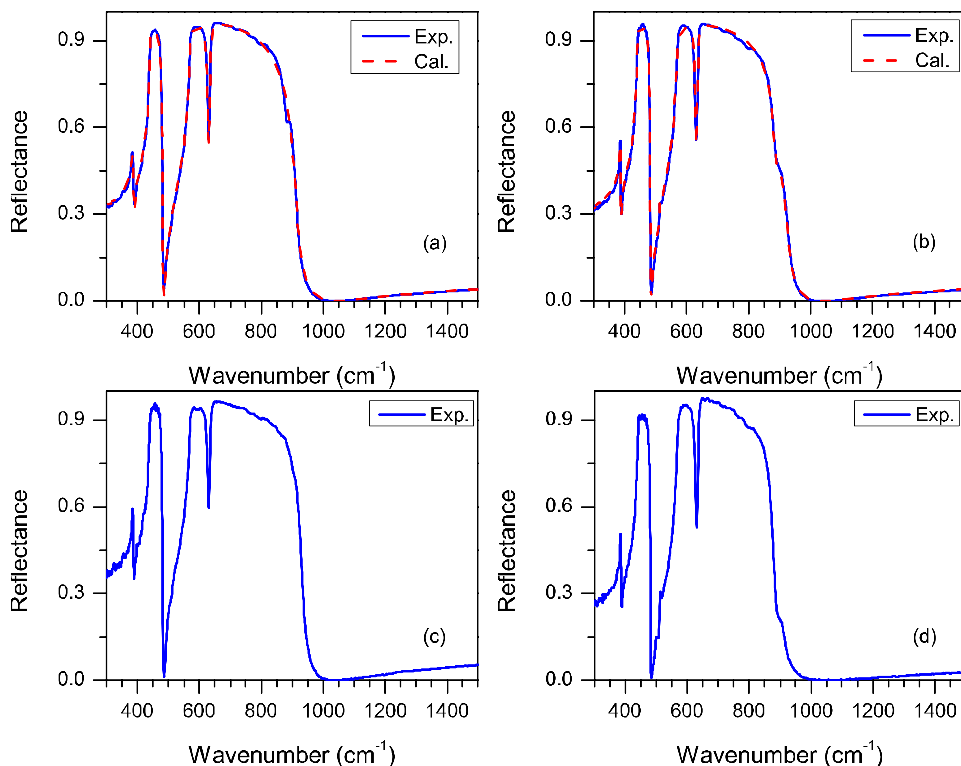

Figure 5.2 Experimental (solid) and the best fitted (dash) reflectance spectra for sapphire. (a) at near normal incidence, (b) for oblique incidence of 25° (un-polarized light), (c) S-polarized at 25° incidence, and (d) P-polarized at 25° incidence.

Table 5.1 The best parameters (isotropic and anisotropic) of sapphire.
The tolerance are given in the brackets. The thickness of the sapphire from the isotropic model and anisotropic model are 436180 nm and 439000 nm respectively.

	ε_∞	Oscillator	ω_{LO} (cm^{-1})	γ_{LO} (cm^{-1})	ω_{TO} (cm^{-1})	γ_{TO} (cm^{-1})
Normal Incidence (isotropic)	3.079 (±0.005)	1	388.2 (±0.1)	4.30 (±0.1)	385.63 (±0.1)	5.64 (±0.1)
		2	482.05 (±0.05)	2.77 (±0.10)	440.03 (±0.01)	3.77 (±0.01)
		3	629.33 (±0.05)	7.59 (±0.10)	569.80 (±0.10)	4.78 (±0.10)
		4	911.07 (±1.00)	25.91 (±1.00)	633.86 (±0.05)	6.43 (±0.10)
25°-Incidence (anisotropic)	3.083 (±0.005)	1	387.66 (±0.10)	2.96 (±0.10)	385.33 (±0.10)	3.76 (±0.10)
		2	481.5 (±0.05)	1.93 (±0.10)	439.55 (±0.10)	3.26 (±0.10)
		3	629.22 (±0.05)	6.67 (±0.10)	568.65 (±0.10)	6.23 (±0.10)
		4	906.25 (±1.00)	21.47 (±1.00)	633.31 (±0.10)	6.29 (±0.10)
	3.086 (±0.005)	1	510.82 (±0.10)	2.10 (±0.10)	397.10 (±0.10)	5.22 (±0.10)
		2	878.47 (±0.05)	20.96 (±1.00)	580.52 (±0.10)	2.63 (±0.10)

Figure 5.3 (a) and (b) illustrate the real and imaginary dielectric functions for sapphire at near normal and 25° un-polarized incidence. The dielectric functions perpendicular and parallel to the c-axis determined from the un-polarized reflectance spectrum are shown in dashed and short dashed lines, respectively. The imaginary dielectric function above 1000 cm^{-1} is almost zero, and this indicates that sapphire is optically transparent above 1000 cm^{-1}. The observed vibration modes in the imaginary dielectric function below 800 cm^{-1} is the TO phonon modes of sapphire. The real part of the dielectric function slightly increases with wavenumber above 700 cm^{-1}. In the range of 1800-6200 cm^{-1} (5.55-1.61μm), the

real part of the dielectric function is between 2.517 and 3.036 (refractive index is between 1.586 and 1.742), and this is closer to the reported values in the same wavelength range [17].

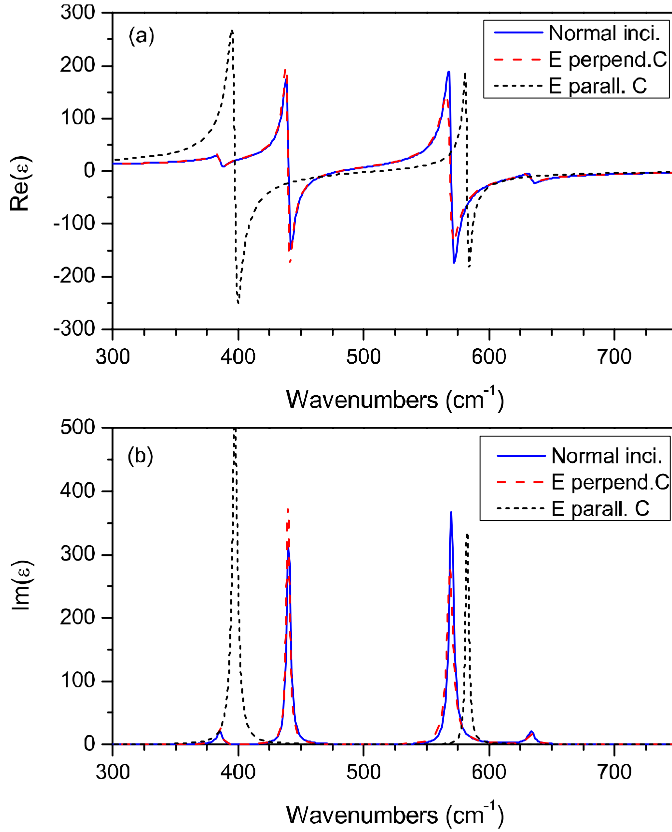

Figure 5.3 The real (a) and imaginary (b) dielectric function of sapphire at normal incidence (solid), at 25° incidence angle E-field perpendicular to the c-axis (dash), and at 25° incidence angle E-filed parallel to the c-axis (short-dash).

5.3.1 Analysis of IR reflectance Spectra for Templates

For the templates (AlN and GaN) and InN simulation, the following dielectric function in parallel and perpendicular direction to the crystal c-axis were used in the anisotropic analysis, and $\varepsilon_{\|}(\omega) = \varepsilon_{\perp}(\omega)$ is considered for isotropic analysis. However, Katssidis et al. [14] has used factorized model with and without the free carrier contribution term, for analysis of sapphire and InN (or GaN), respectively.

$$\varepsilon_{\|}(\omega) = \varepsilon_{\infty,\|}\left(1 + \frac{\omega_{LO,\|}^2 - \omega_{TO,\|}^2}{\omega_{TO,\|}^2 - \omega^2 - i\omega\gamma_{TO,\|}} - \frac{\omega_{p,\|}^2}{\omega^2 + i\omega\gamma_{p,\|}}\right) \quad 5.3$$

$$\varepsilon_{\perp}(\omega) = \varepsilon_{\infty,\perp}\left(1 + \frac{\omega_{LO,\perp}^2 - \omega_{TO,\perp}^2}{\omega_{TO,\perp}^2 - \omega^2 - i\omega\gamma_{TO,\perp}} - \frac{\omega_{p,\perp}^2}{\omega^2 + i\omega\gamma_{p,\perp}}\right) \qquad 5.4$$

The $\varepsilon_{\infty,\parallel}$ and $\varepsilon_{\infty,\perp}$ are denoted the high frequency dielectric constant in both directions: parallel and perpendicular to the c-axis. For the AlN, GaN, and InN, $\omega_{LO,\parallel}$, $\omega_{TO,\parallel}$, $\omega_{LO,\perp}$, and $\omega_{TO,\perp}$ are the A_1LO, A_1TO, E_1LO, and E_1TO phonon modes respectively. The $\gamma_{TO,\parallel}$ and $\gamma_{TO,\perp}$ account for the broadening constant of A_1TO and E_1TO phonon modes correspondingly. The $\omega_{p,\parallel}$ and $\omega_{p,\perp}$ represent the plasma frequency of the films in parallel and perpendicular directions to the c-axis while $\gamma_{p,\parallel}$ and $\gamma_{p,\perp}$ account for their corresponding damping constant.

Sapphire parameters were kept constant during the simulation of all templates and InN samples. A three layer model (air/AlN/sapphire) was used in AlN layer simulation and was obtained a ~30 nm AlN layer from the simulation. This value is consistent with the experimental value. Figure 5.4 (a) shows the measured reflectance spectra at normal and 25° (un-polarized) incidence light for AlN/sapphire. Even in such a thin layer, the E_1TO phonon mode (~674 cm^{-1}) of AlN can be observed in both spectra. However, the features of sapphire are more dominant to the reflectance spectra in other frequency ranges (see Fig. 5.4 (b), which depicts the measured reflectance spectra for the sapphire and AlN/sapphire for 25° un-polarized incidence light, and the inset shows the spectra further up to 6500 cm^{-1}). The attenuation of reflectance can be observed in the range between 675 cm^{-1} and 860 cm^{-1} in the spectrum of 25° incident angle compared that of normal incidence. The best fitted and experimental spectra at normal and 25° incident angle are presented in Fig.5. 4 (c) and (d), respectively. It is noted that the free carrier term (Drude term) is negligible in both cases since the sample is not intentionally doped. Table 5.2, 5.3, and 5.4 summarize the best fit parameter for AlN layers on sapphire obtained from the simulation.

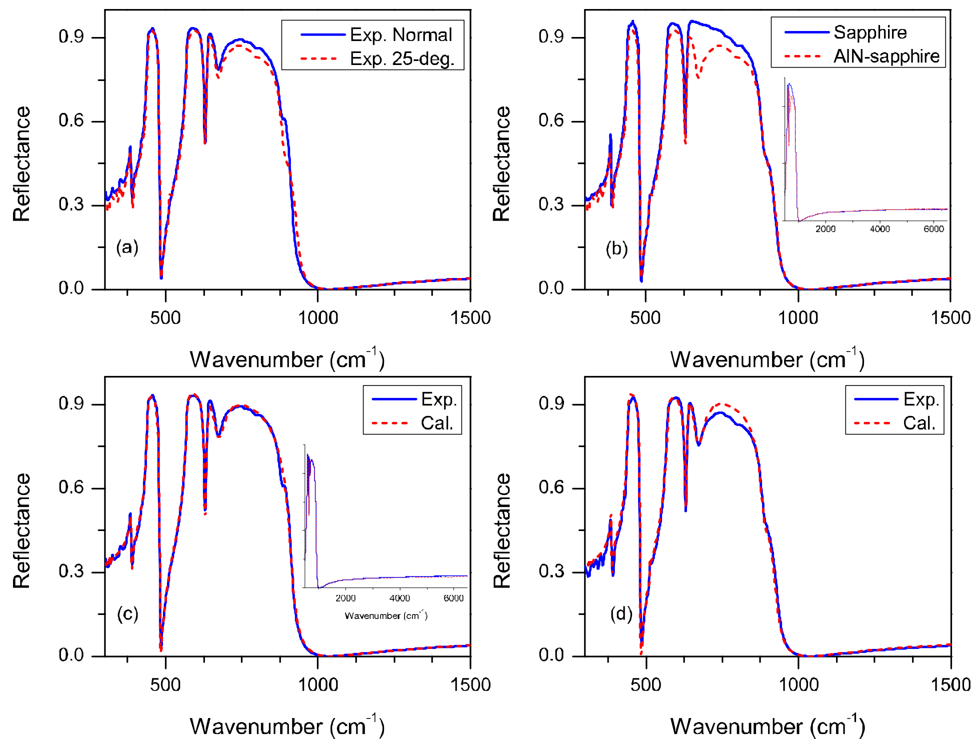

Figure 5.4 (a) Experimental spectra for AlN/Sapphire at near normal (solid) and 25° unpolarized incidence light (dash), (b) experimental spectra for sapphire (solid) and AlN/Sapphire at 25° unpolarized incidence, (c) and (d) experimental and best fitted spectra of sapphire at normal (solid) and 25° unpolarized incidence for AlN/Sapphire.

The real and imaginary part of the dielectric functions under the near normal incident and the 25° un-polarized incident light as function of wavenumber is depicted in Fig. 5.5 (a) and (b). The TO phonon frequency is located at the maximum value of the imaginary part of the dielectric function. The real part of the dielectric function is between 3.968 and 4.561 (refractive index is between 1.992 and 2.135), in the range of 1800-6200 cm^{-1} (5.51-1.61μm).

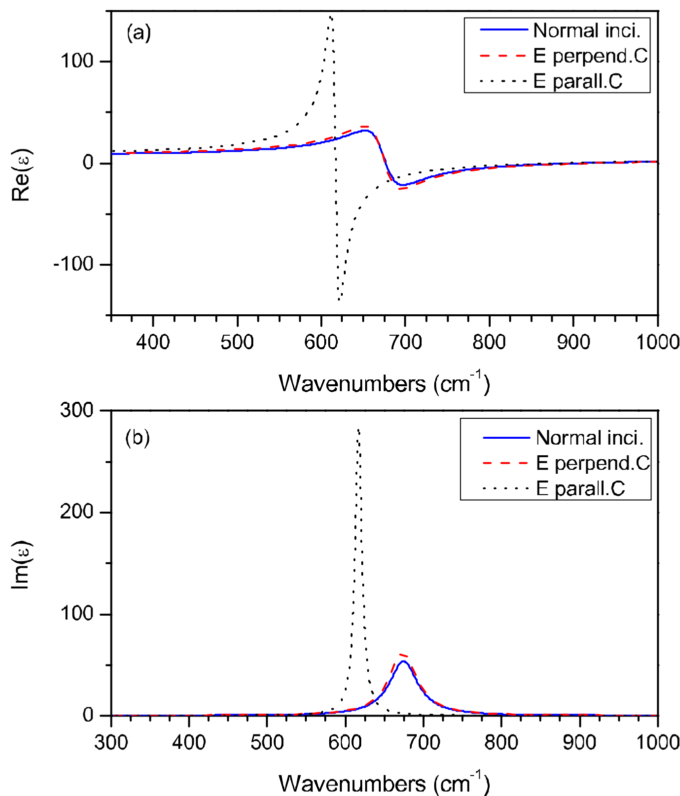

Figure 5.5 The real (a) and imaginary (b) dielectric function of AlN/sapphire at normal incidence (solid), at 25° incidence angle E filed perpendicular to the c-axis (dash), and at 25° incidence angle E filed parallel to the c-axis (short dashed).

For Ga-polar GaN simulation, a four layer model (air/Ga-polar GaN/AlN/sapphire) is used, and both the sapphire and AlN layer parameters were kept constant from above study. The experimental spectra for Ga-polar GaN, measured at near normal, 25° un-polarized, P-polarized, and S-polarized incident light are shown in Fig. 5.6 (a). In order to discriminate sapphire and AlN features from the GaN features in Ga-polar GaN/AlN/Sapphire reflectance spectra, the experimental reflectance spectra of sapphire (at normal and P-polarized incidence), AlN/Sapphire (at normal and 25° P-polarized incidence), Ga-polar GaN/AlN/Sapphire (at normal, 25° unpolarized, P-polarized, and S-polarized incidence light are over layered in Fig. 5.7. It is clear that the presence of a small dip at 630 cm^{-1} in both AlN and GaN spectra is coming from the sapphire substrate. The literature values for the phonon frequencies of A_1LO (in the range of 730-744 cm^{-1}) and E_1LO (738-746 cm^{-1}) of GaN show a large deviation because they are shifting with the thickness in addition to the measurement type [18]. The dip at the 735 cm^{-1} in GaN (near normal

incidence) spectrum is increasing with the angle of incidence and the polarized light. As well as, it is slightly shifted (737 cm^{-1}) with increasing incidence angle. The dip disappears in the S-polarized spectrum. Therefore, it is clear that the dip at the 735 cm^{-1} is due to the A_1LO phonon of GaN. When analyzing the near normal reflectance spectra of GaN, in the isotropic model, P-polarized component has ignored. However, even ~8°, the A_1LO phonon mode can be observed in the reflectance spectra of GaN. Therefore, this is not captured well on the best fit spectrum (see Fig. 5.6(b)). Figure 5.6 (c) shows the experimental and best fitted spectrum at 25° unpolarized incidence light for Ga polar-GaN/AlN/Sapphire and the fitting were carried out using the anisotropic model without free carrier term (since the sample was not intentionally doped). Figure 5.6 (d) depicts these two spectra from 300-6500 cm^{-1} which show the interference fringes (above 1500 cm^{-1}) above the reststrahlen region (above 1500 cm^{-1}). The experimental and theoretical spectra were well agreed with the model used.

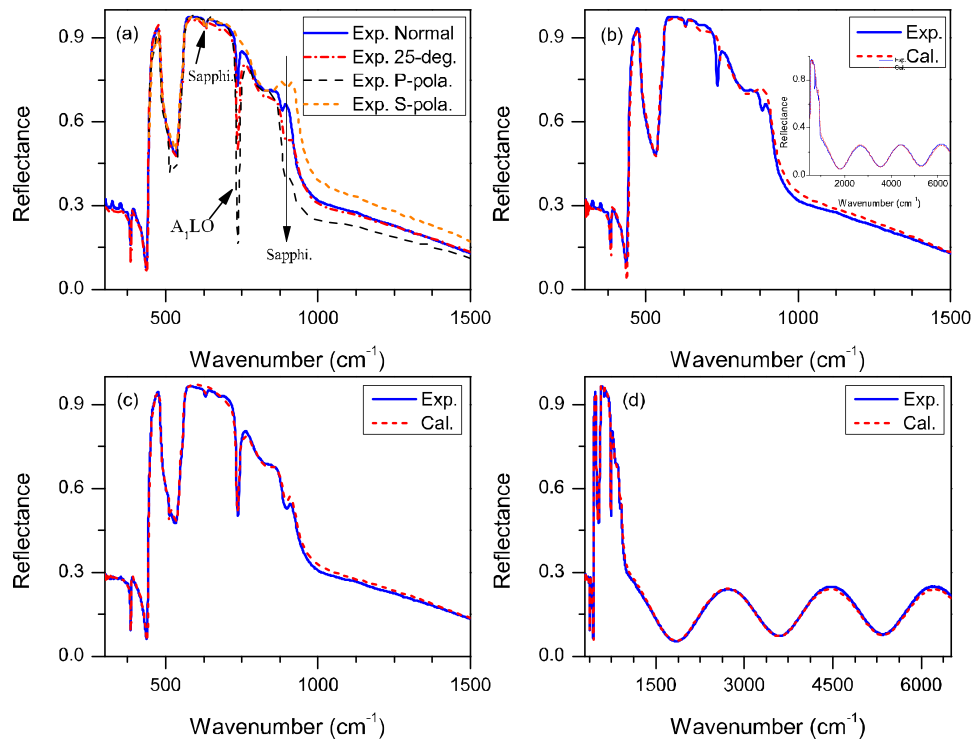

Figure 5.6 (a) Experimental spectra at normal incidence (solid), at 25° incidence for unpolarized (dash-dot), P-polarized (dash), and S-polarized (short-dash) light, (b) and (c) experimental and best fitted spectra at normal and 25°-unpolarized incidence light, respectively, and (d) experimental and best fitted spectra for 25°unpolarized incidence light, showing range of 300-6500 cm^{-1}, for Ga-polar GaN/AlN/Sapphire.

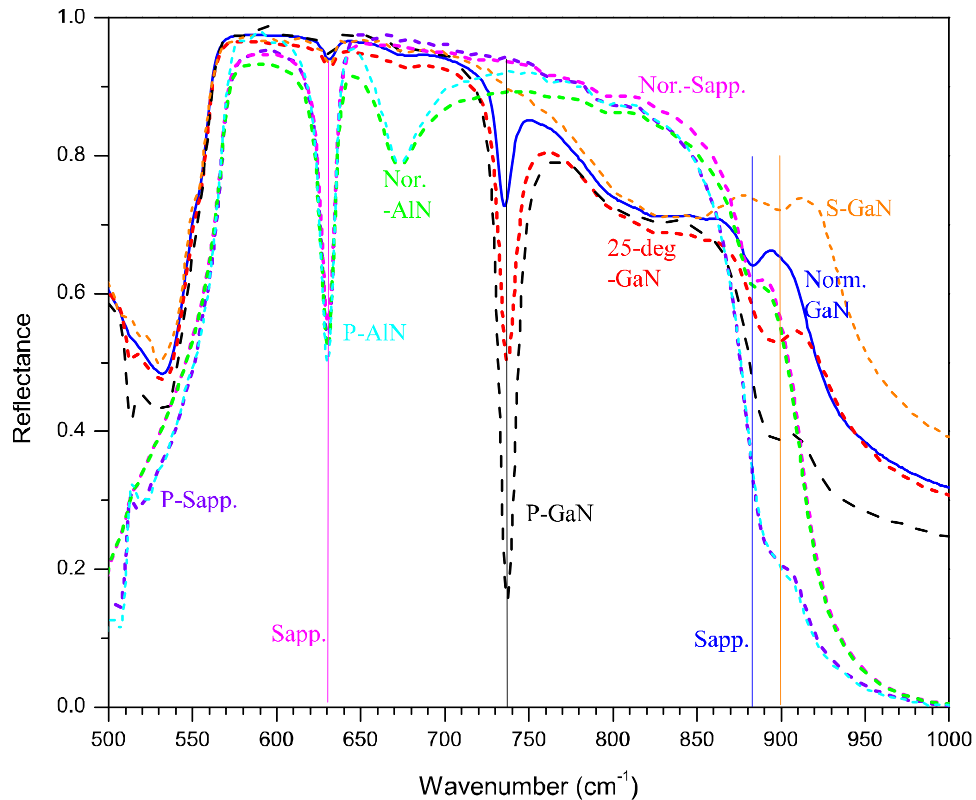

Figure 5.7 Experimental reflectance spectra for Sapphire, AlN/Sapphire, and Ga-polar GaN/AlN/Sapphire.
Nor., P, and S represent the normal incidence, P-polarized and S-polarized.

The best fit values from the IR reflectance analysis for are summarized Table 5.2, 5.3, and 5.4. GaN parameters reported by Kasic et al. by IR ellipsometry analysis were used as the initial GaN parameters for the simulation [19].

Figure 5.8 (a) and (b) depicts the real and imaginary part of the dielectric functions for near normal incident and 25° un-polarized incident light as a function of wavenumber. The real part of the dielectric function is between 4.878 and 5.279 (refractive index is between 2.208 and 2.297), in the range of 1800-6200 cm^{-1} (5.51-1.61μm). These values are in close agreement with the reported values [20].

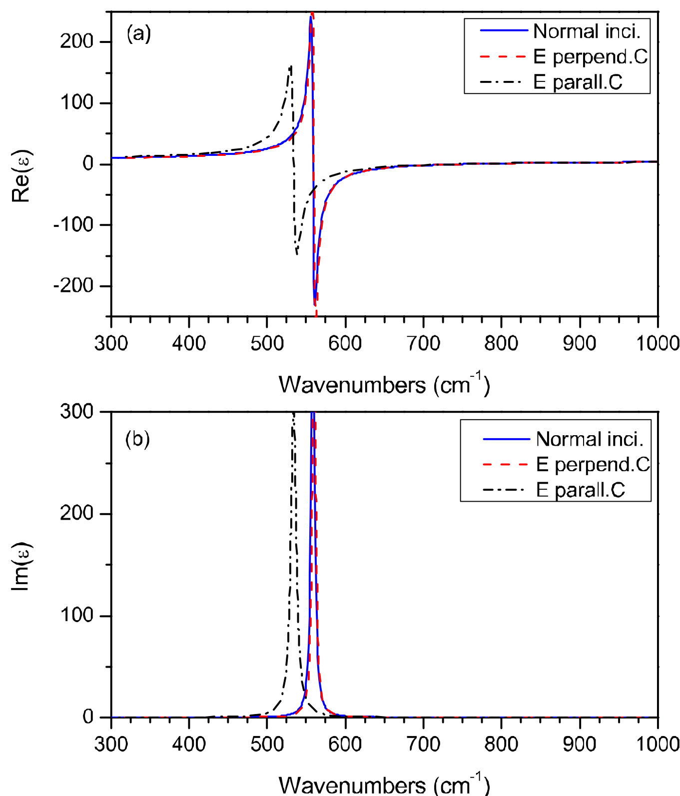

Figure 5.8 The real (a) and imaginary (b) dielectric function of Ga polar GaN/AlN/sapphire at normal incidence (solid), at 25° incidence angle E filed perpendicular to the c-axis (dash), and at 25° incidence angle E filed parallel to the c-axis (dash-dotted).

The experimental reflectance spectra at the near normal incidence at the 25° incidence unpolarized, the P-polarized, and the S-polarized for N-polar GaN/Sapphire template are shown in Fig. 5.9 (a). There is no much difference between the near normal and 25° (un-polarized) incidence reflectance spectra. A slight difference (in the region of 1750-2750 cm^{-1}) can be observed in S-polarized spectrum compared with these two spectra. It can be observed that S-polarized spectra is less damped compared to the other spectra. These results shows that N-polar GaN is dominated by the reflection of plasma. Conversely, the Ga polar GaN is dominated by the phonons [21].

Initially, a four layer stack model (air/N polar GaN/AlN/sapphire) was considered for the simulation and was not achieved a poor fitting. Thus, three layer stack model (air/N-polar GaN/Sapphire) as shown in Fig. 5.10 (a) was used. Figure 5.11 depicts the experimental spectrum and best fit spectrum [(a)] obtained from this simulation. The fitted spectra showed a significant deviation from the experimental

spectrum, especially, in the region > 2000 cm^{-1} (the interference region, where the interference creates a periodic pattern). This deviation might be due to an additional interface layer with a different dielectric function from the GaN layer and sapphire, formed in between the sapphire and GaN during the growth, and have not been considered for the simulation. Hence, an interface layer between sapphire and GaN [which is label as L2 in Fig. 5.10 (b)] is added to achieve the best fitting between experimental and calculated spectra. The best fitted spectrum achieved from the four layer model is shown in Fig. 5.11 (b). The interface layer modulated the interference fringes and provided a better fitting between the experimental and calculated spectra. In order to further improve the fitting quality, a surface layer is added in between ambient and GaN layer as shown in Fig. 5.10 (c). A further agreement between the experimental and calculated spectra was not achieved using five layer model [see Fig. 5.11 (c)]. Thus, four layer model was used in the 25° (un-polarized) incidence spectrum simulation. Figure 5.9 (b) and (c) depict the experimental and best fitted spectra at normal and 25° (un-polarized) incidence light.

The lower reflectivity in the experimental spectrum than the calculated spectrum [see Fig. 5.9 (b)] may be due to scattering by influence of surface roughness [22]. Thus, the total reflectance was corrected including surface roughness term δ (see Eq. 4.97). The Fig. 5.9 (d) shows the further improved best fitted spectrum after reflectivity correction and experimental spectrum for N-polar GaN/sapphire. The best fitted parameters are listed in Table 5.2, 5.3, and 5.2. The isotropic and anisotropic free carrier concentration and the mobility of the carriers of the N polar GaN layer were calculated using Eqs. 4.128-4.131. The effective mass values of $m^* = 0.2m_0$, $m_{||}^* = 0.228m_0$, and $m_{\perp}^* = 0.237m_0$ were used for these calculations [19].

Figure 5.12 (a) and (b) show the real and imaginary part of the dielectric functions for near normal incident and 25° un-polarized incident light as a function of wavenumber, respectively. It is clear that both the real part and imaginary part of the dielectric function of the layer 1 are different those from the layer 2 especially due to plasma damping in the first layer. In the range of 1800-6200 cm^{-1} (5.51-1.61μm),

the real part of the isotropic dielectric function for the layer 1 is between 2.479 and 4.602 (refractive index is between 1.574 and 2.145).

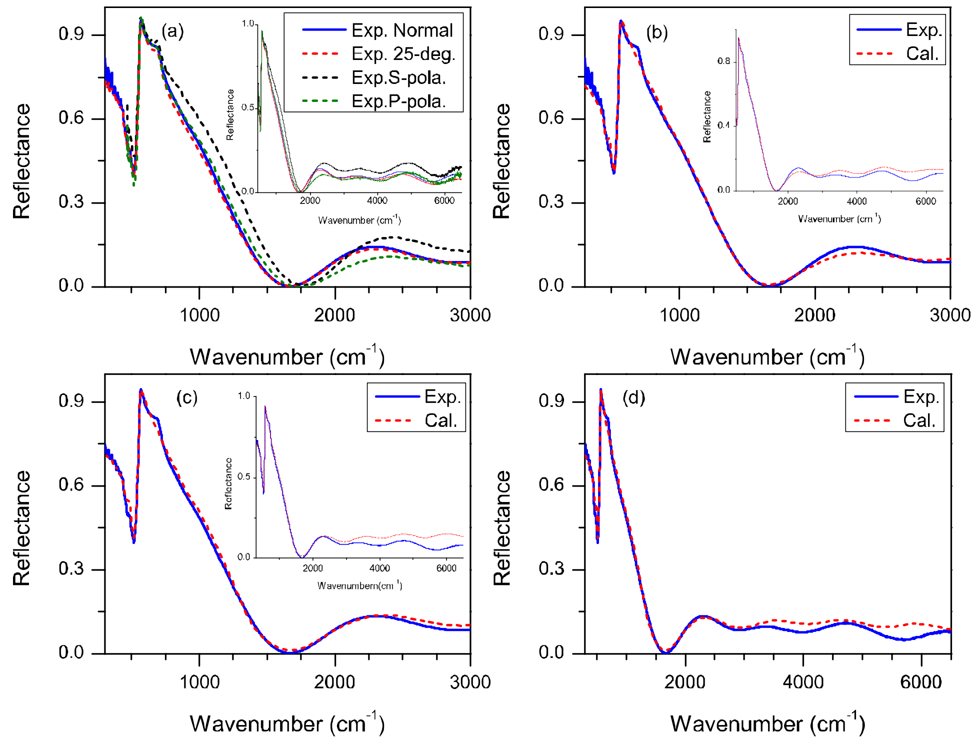

Figure 5.9 (a) Experimental spectra at normal incidence (solid), at 25° incidence for unpolarized, P-polarized, and S-polarized (dash), (b) and (c) experimental and best fitted spectra at normal and 25°-unpolarized incidence light, respectively, and (d) experimental and best fitted spectra with surface roughness for 25° unpolarized incidence light for N-polar GaN/Sapphire.

Figure 5.10 Model layer structures used in N-polar GaN/sapphire simulation.

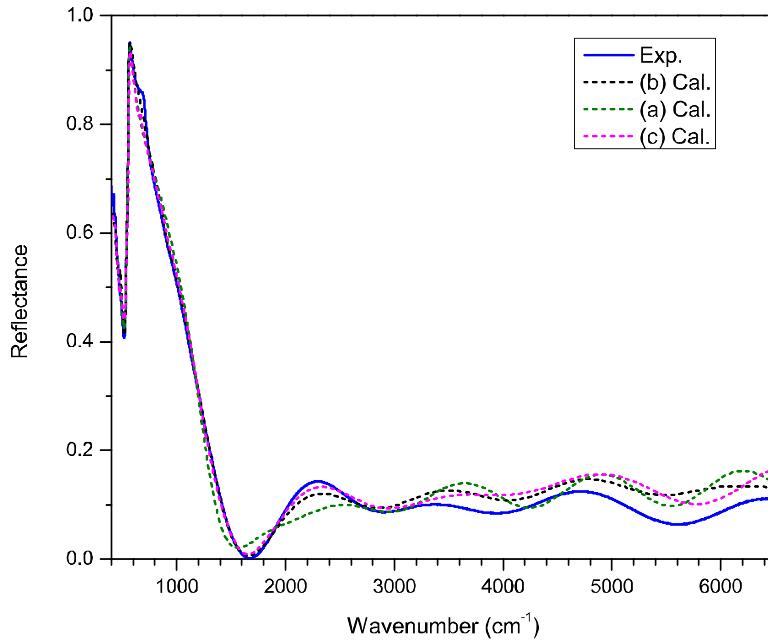

Figure 5.11 Experimental and best fitted spectra obtained using (a) three layer, (b) four layer, and (c) five layer models for N polar GaN/sapphire template.

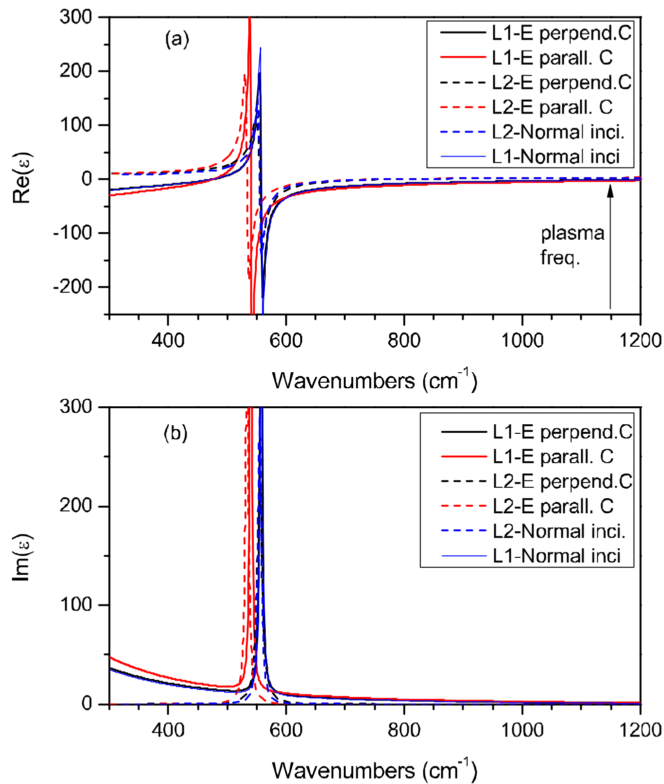

Figure 5.12 The real (a) and imaginary (b) dielectric function of N polar GaN layers (L1 and L2) at normal incidence, at 25° incidence angle E filed perpendicular to the c-axis, and at 25° incidence angle E filed parallel to the c-axis.

Figure 5.13 (a) shows the experimental spectra for the n-GaN/i-GaN/AlN/sapphire at near normal, 25° un-polarized, P-polarized, and S-polarized incident light. Except intensity changing in the region of 770-900 cm^{-1} and 350-420 cm^{-1}, the spectra are very similar to the Ga-polar GaN/AlN/sapphire. The changes of the intensity 350-420 cm^{-1} may be due to the free carrier absorption. As in the N polar GaN, two GaN layers (with and without free carriers) were found using five layer model. Further improved best fitted spectrum with surface roughness and experimental spectrum are exhibited Fig. 13 (d). For the calculations of free carrier concentration and mobility, effective mass values of $m^* = 0.2m_0$, $m_{\|}^* = 0.228m_0$, and $m_{\perp}^* = 0.237m_0$ were used. See Table 5.2, 5.3, and 5.3 for the obtained properties of n-GaN layers.

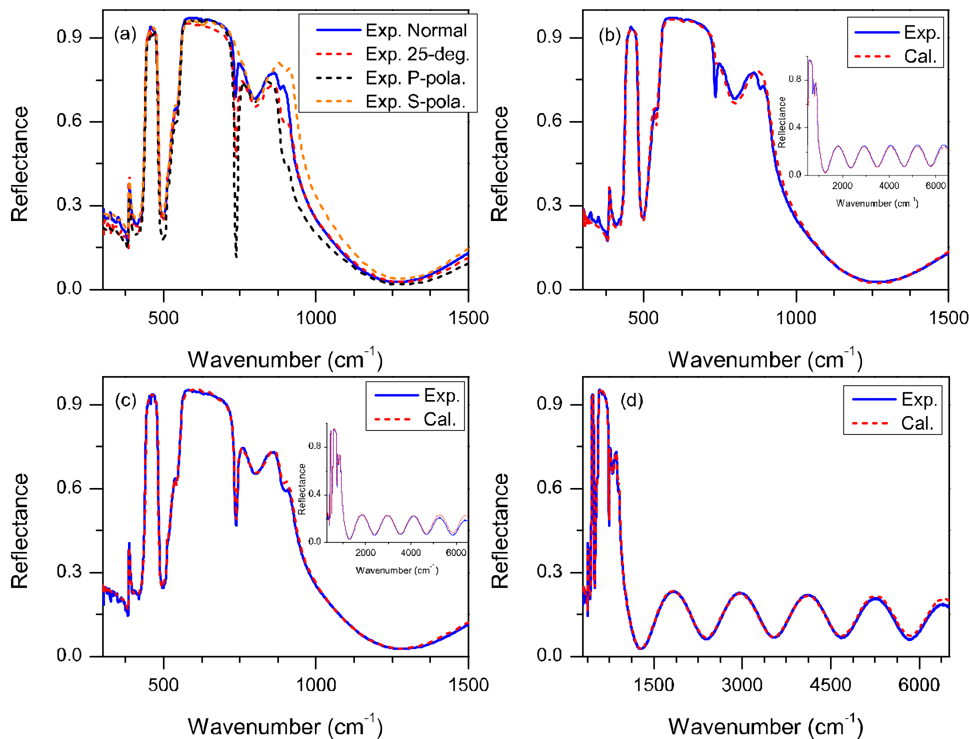

Figure 5.13 (a) Experimental spectra at normal incidence (solid), at 25° incidence for unpolarized, P-polarized, and S-polarized (dash), (b) and (c) experimental and best fitted spectra at normal and 25°-unpolarized incidence light, respectively, and (d) experimental and best fitted spectra with surface roughness for 25° unpolarized incidence light for n-GaN/i-GaN/AlN/Sapphire.

The real and imaginary part of the dielectric functions for near normal incident and 25° un-polarized incident light as a function of wavenumber, respectively are depicted in Fig. 5.14 (a) and (b). Since

the plasma frequency of the layer 1 is in the region below 150 cm^{-1}, there is no much influence on the dielectric function in the shown region. However, the both the real part and imaginary part of the dielectric functions of the layer 1 are different those from the layer 2 due to different phonon frequencies and their broadening. This may be due to the different strains in the layers. The real part of the isotropic dielectric function for layer 1 is between 4.751 and 5.192 (refractive index is between 2.179 and 2.278) in the frequency range of 1800-6200 cm^{-1} (5.51-1.61μm).

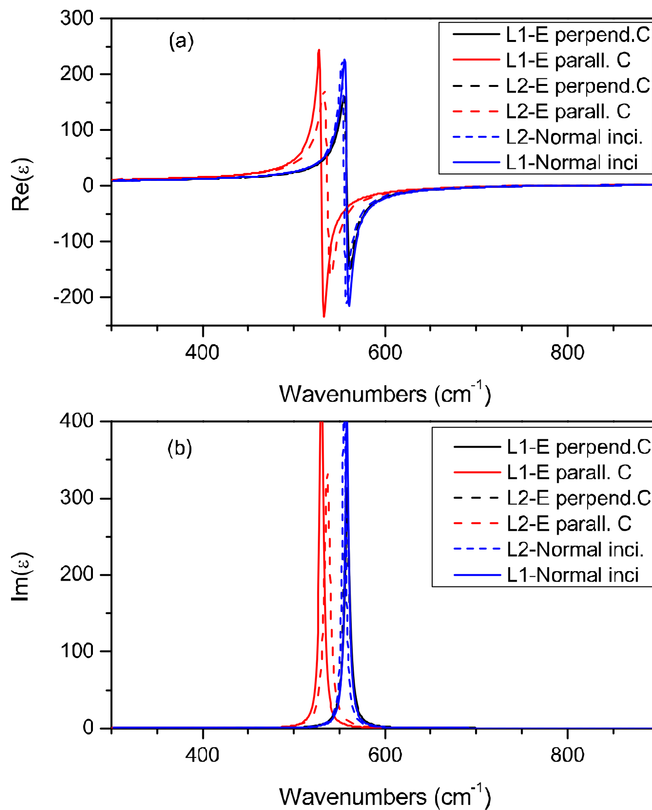

Figure 5.14 The real (a) and imaginary (b) dielectric function of n-GaN layers (L1 and L2) at normal incidence, at 25° incidence angle E filed perpendicular to the c-axis, and at 25° incidence angle E filed parallel to the c-axis.

The experimental spectra of the p-GaN/i-GaN/AlN/sapphire at near normal, 25° un-polarized, P-polarized, and S-polarized incident light are shown in Fig. 5.15. The sapphire features around 630 cm^{-1} were not observed in these spectra. As well as, the dip of the A_1LO phonon mode at the normal incidence is less compared to the Ga polar and n-type GaN because p-GaN layer is thicker than the Ga polar and n-

type GaN layers. However, the A_1LO phonon mode is sensitive to the angle of the incidence and P-polarized light.

Two GaN layers were found using five layer model. Fig. 5.15 (b) and (c) show the best fitted and experimental reflectance spectra for p-GaN/i-GaN/AlN/sapphire at normal and 25° (unpolarized) incidence light. The experimental spectrum and best fitted spectrum with surface roughness are depicted in Fig. 5.15 (d). The best fit properties of p-GaN layers are listed in Table 5.2, 5.3, and 5.4. The free carrier concentration and mobility of the carriers were calculated using effective mass values of $m^* = 1.4m_0$, $m_{\parallel}^* = 1.4m_0$, and $m_{\perp}^* = 1.4m_0$ [19].

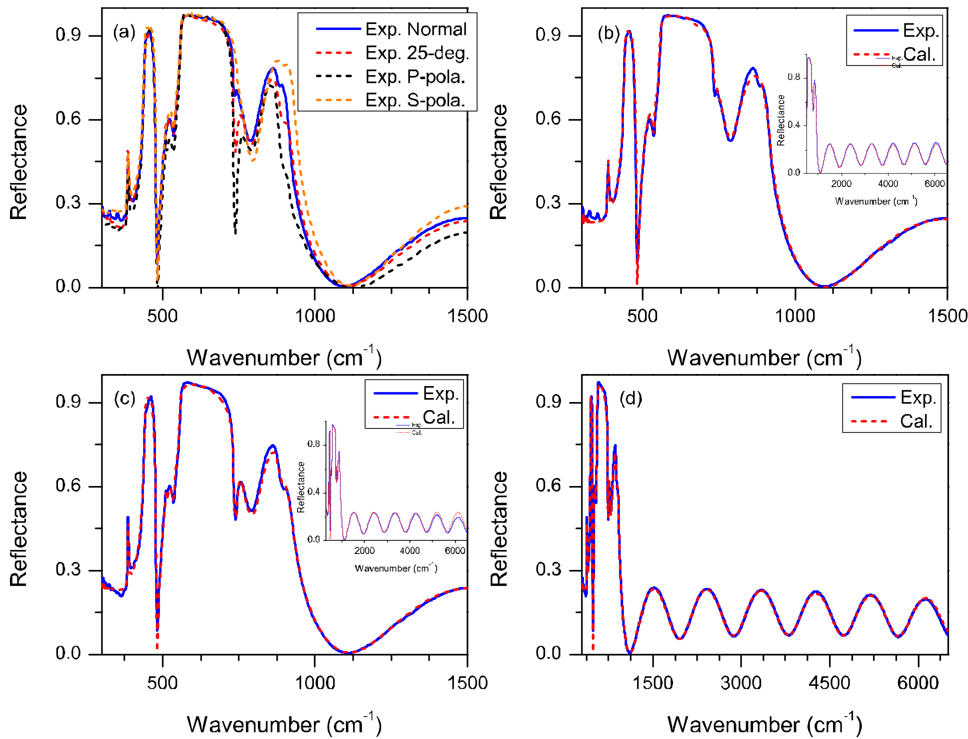

Figure 5.15 (a) Experimental spectra at normal incidence (solid), at 25° incidence for unpolarized, P-polarized, and S-polarized (dash), (b) and (c) experimental and best fitted spectra at normal and 25°-unpolarized incidence light, respectively, and (d) experimental and best fitted spectra with surface roughness for 25° unpolarized incidence light for p-GaN/i-GaN/AlN/Sapphire.

For p-GaN layers, the real and imaginary part of the dielectric functions at near normal incident and 25° un-polarized incident light as a function of wavenumber are shown in Fig. 5.14 (a) and (b). It is

observed that the dielectric function of the layer 1 is different from the layer 2. The real part of the isotropic dielectric function for layer 1 is between 4.715 and 5.144 (refractive index is between 2.171 and 2.268). In the frequency range of 1800-6200 cm^{-1} (5.51-1.61µm).

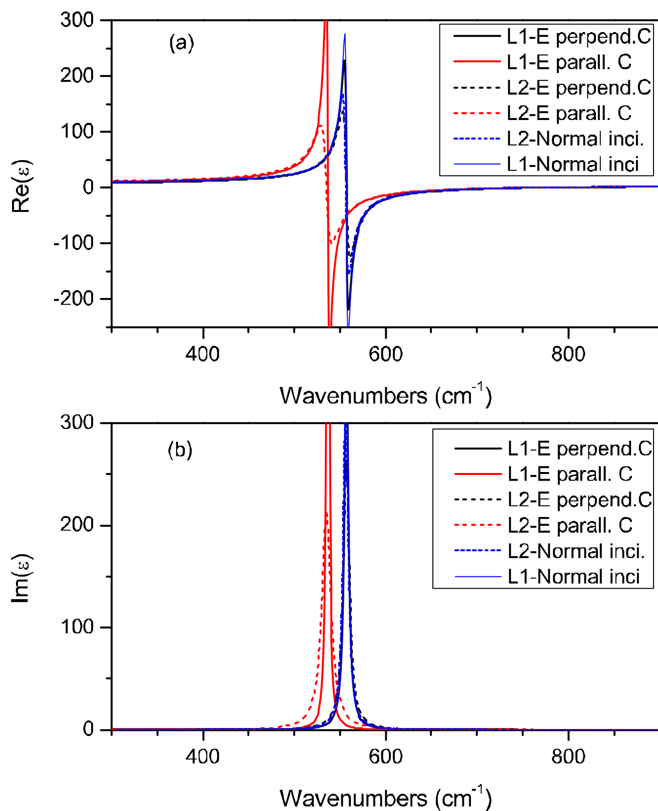

Figure 5.16 The real (a) and imaginary (b) dielectric function of p-GaN layers (L1 and L2) at normal incidence, at 25° incidence angle E filed perpendicular to the c-axis, and at 25° incidence angle E filed parallel to the c-axis.

Table 5.2 Best fitted isotropic and anisotropic high frequency dielectric constant, plasma frequencies, and their damping values for AlN and GaN layers.
The tolerance for the high frequency dielectric constant is (±0.01), and that is for plasma frequency and damping of the plasma is (±5.0).

Substrate		Normal Incidence			25° Incidence					
		ε_∞	ω_p (cm^{-1})	γ_p (cm^{-1})	$\varepsilon_{\infty,\perp}$	$\omega_{p,\perp}$ (cm^{-1})	$\gamma_{p,\perp}$ (cm^{-1})	$\varepsilon_{\infty,\parallel}$	$\omega_{p,\parallel}$ (cm^{-1})	$\gamma_{p,\parallel}$ (cm^{-1})
AlN/sapphire	L1	4.46	-	-	4.73	-	-	4.61	-	-
Ga-polar-GaN/AlN/sapphire	L1	5.32	-	-	5.15	-	-	5.31	-	-
N-polar-GaN/sapphire	L1	4.8	1152	347	5.05	1157	373	5.1	1305	345
	L2	4.26	-	-	4.79	-	-	4.8	-	-
n-type-GaN/AlN/sapphire	L1	5.23	150	86	5.04	55	40	5.31	111	100
	L2	5.14	-	-	4.93	-	-	5.35	-	-
p-type-GaN/AlN/sapphire	L1	5.18	130	130	5.1	186	170	5.24	101	100
	L2	5.31	-	-	5.13	-	-	5.33	-	-

Table 5.3 Best fit isotropic and anisotropic phonon frequencies, and their broadening values for AlN and GaN layers.
The tolerance for the phonon frequencies and their broadening is (±0.1).

Substrate		Normal Incidence			25° Incidence					
		ω_{LO} (cm^{-1})	ω_{TO} (cm^{-1})	γ_{TO} (cm^{-1})	$\omega_{LO,\perp}$ E_1LO (cm^{-1})	$\omega_{TO,\perp}$ E_1TO (cm^{-1})	$\gamma_{TO,\perp}$ (cm^{-1})	$\omega_{LO,\parallel}$ A_1LO (cm^{-1})	$\omega_{TO,\parallel}$ A_1TO (cm^{-1})	$\gamma_{TO,\parallel}$ (cm^{-1})
AlN/sap.	L1	907.1	675.0	45.1	917.7	674.0	44	882.3	616.8	10.4
Ga-polar-GaN/AlN/sap.	L1	742.5	558.7	4.8	741.8	560.0	4.0	734.2	533.7	8.0
N-polar-GaN/sapp.	L1	754.7	557.5	4.5	740.8	557.2	5.1	746.6	540.3	3.8
	L2	742.0	555.0	6.4	757.8	555.0	10.0	738.1	533.6	6.1
n-type-GaN/AlN/sap.	L1	747.6	558.0	5.2	745.3	558.4	7.0	728.8	530.4	5.2
	L2	734.1	555.0	4.8	742.5	557.7	6.7	735.7	536.7	7.5
p-type-GaN/AlN/sap.	L1	747.0	557.0	4.2	742.7	557.0	4.9	730.4	536.6	3.1
	L2	733.0	556.1	6.7	737.2	556.9	8.1	737.5	535.1	11.9

Table 5.4 Best fit isotropic and anisotropic layer thicknesses, free carrier concentration, mobility of the carriers, and surface roughness values for AlN and GaN layers.
The effective mass values used in the free carrier concentration and mobility of the carrier calculations are shown in the brackets.

Substrate		Normal Incidence			25° Incidence					
		d (nm)	N_c (×10^{19} cm^{-3})	μ_c (cm[2]V[-1]s[-1])	d (nm)	$N_{c,\perp}$ (×10^{19} cm^{-3})	$\mu_{c,\perp}$ (cm[2]V[-1]s[-1])	$N_{c,\parallel}$ (×10^{19} cm^{-3})	$\mu_{c,\parallel}$ (cm[2]V[-1]s[-1])	Surf. Rough. (nm)
AlN/sap.	L1	25	-	-	28	-	-	-	-	-
Ga-polar-GaN/AlN/sap.	L1	1227	-	-	1244	-	-	-	-	-
N-polar-GaN/sapp.	L1 L2	1200 576	1.4 -	130 -	1169 580	1.8 -	110 -	2.2 -	120 -	28
n-type-GaN/AlN/sap.	L1 L2	680 1129	0.030 -	470 -	620 1328	0.004 -	980 -	0.016 -	410 -	25
p-type-GaN/AlN/sap.	L1 L2	822 1508	0.136 -	51 -	740 1641	0.275 -	39 -	0.083 -	67 -	20

As a summary, both the isotropic and the anisotropic broadening of the E_1TO phonon modes for the AlN layer have a higher value compared to that of the GaN layers. Since the broadening of the E_1TO phonon mode is related to the crystalline quality of the layers, these results indicate that poor quality for AlN layer in these structures. It has been attributed the thicker interface layer as an effective optical transition layer due to the interface imperfections [23]. The phonon frequencies for un-doped Ga polar GaN layer have a close agreement with the reported values obtained from Raman analysis, except for the A_1TO (531 cm^{-1}) [24]. It is observed that phonon frequencies of N polar GaN, n-GaN, and p-GaN layers are shifted with respect to that of the Ga polar GaN layers. This may be due to the presence of stains and those been different in each layer [23]. Higher carrier concentration in N polar GaN layers compared to that of Ga polar GaN layers has been attributed to the presence of donors, likely the oxygen [21].

5.3.2 Analysis of IR reflectance Spectra for InN films

For the simulation of InN grown on the template described in previous two section, these obtained physical properties of templates were kept constant and used the values obtained in those studies.

Figure 5.17 (a) shows the experimental reflectance spectra of InN/sapphire, measured at near normal, 25° un-polarized, P-polarized, and S-polarized incident light. There was no significant difference between near normal incidence spectrum and the 25° (unpolarized) incidence spectrum. The S- and P-polarized spectra were slightly difference from these two spectra, especially, plasma damping. As well as, the intensity in the region of 2000-6500 cm^{-1} has increased in the S-polarized spectrum. Due to the free carrier absorption, it is difficult to discriminate the phonon mode of InN layers by experimentally.

The best fitted spectrum was achieved for four layer stack structure. Two InN layers with different dielectric function were found from the simulation. Figure 5.17 (a) and (b) show the experimental and best fitted spectra for InN/sapphire at normal and 25° (unpolarized) incidence light. The obtained isotropic and anisotropic optoelectronic properties of the InN layers from the fitting are listed in Table 5.5, 5.6, and 5.7. Thickness of the layer (L2) between the sapphire and the top InN layer is 283 nm and the thickness of the layer (L1) close to the ambient is 115 nm. According to our growth process, there can be two InN layers (a nucleation layer and a bulk layer). However, the thickness of the L2 is higher than the nucleation layer thickness. Therefore, the L2 layer can be attributed to a mixture of both nucleation and bulk layers. This layer has the higher carrier concentration and lower carrier mobility compared to that of L1 layer.

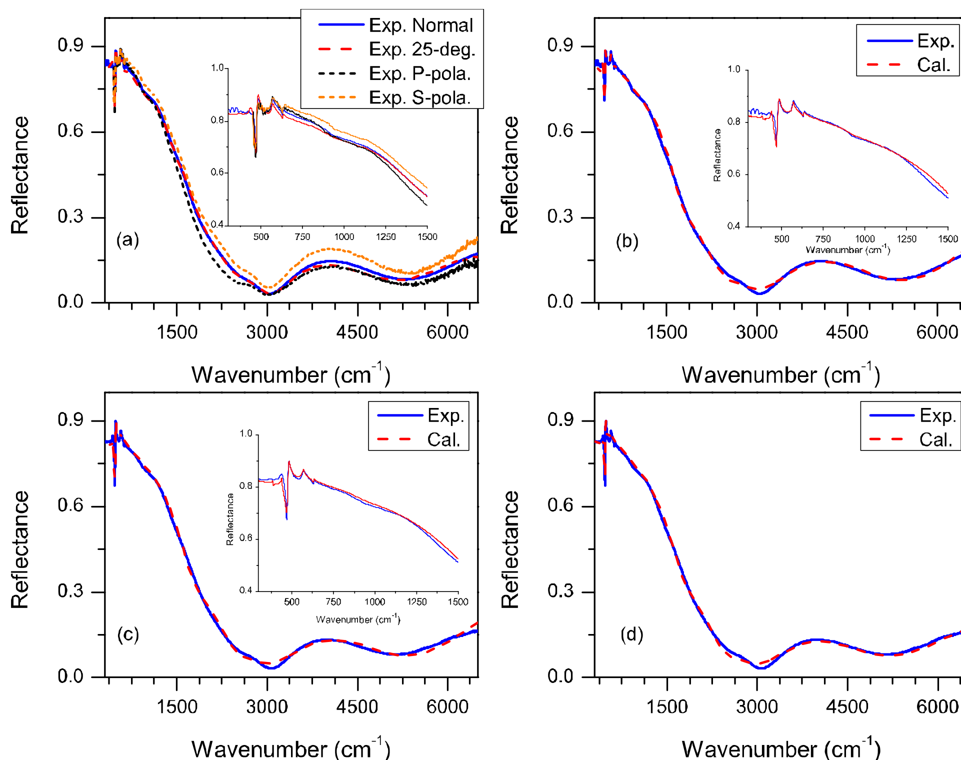

Figure 5.17 Experimental spectra at normal incidence, at 25° incidence for unpolarized, P-polarized, and S-polarized, (b) and (c) experimental (solid) and best fitted (dash) spectra at normal and 25°-unpolarized incidence light, respectively, and (d) experimental and best fitted spectra with surface roughness for 25° unpolarized incidence light for InN/Sapphire.
Insets show the region of 300-1500 cm^{-1}.

Figure 5.18 (a) and (b) show the real and imaginary part of the dielectric functions for InN layers grown on sapphire at the near normal incident and the 25° unpolarized incident light as a function of wavenumber, respectively. The damping behavior of the dielectric function is due to the plasma. In the range of 2800-6200 cm^{-1} (3.57-1.61μm), the real part of the isotropic dielectric function for the layer 1 is between 3.859 and 5.663 (refractive index is between 1.964 and 2.379).

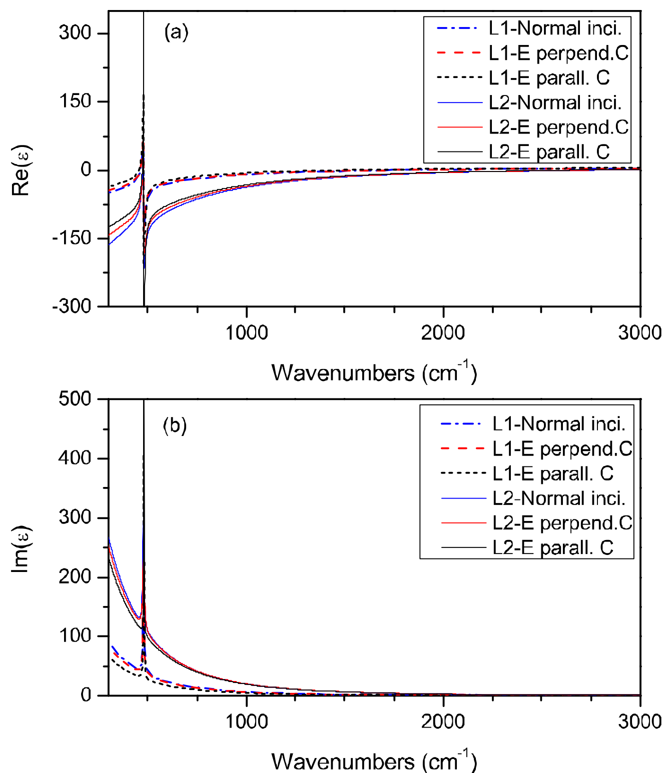

Figure 5.18 The real (a) and imaginary (b) dielectric function of InN layers (L1 and L2) grown on sapphire at normal incidence, at 25° incidence angle E filed perpendicular to the c-axis, and at 25° incidence angle E filed parallel to the c-axis.

The experimental reflectance spectra at the near normal and the 25° un-polarized incidence light for the InN/AlN/sapphire structure are given in Fig. 5.19 (a). It can be observed that the dip ~467 cm^{-1} has increased with the angle of incidence as well as, the spectrum for the 25° un-polarized incidence light has more damped in the region of 1000-2500 cm^{-1} than the spectrum at normal incidence due to different carrier absorptions. The best fitted spectra were found for six layered structure and Fig. 5.19 (b) and (c) are given the best fitted and experimental spectra at normal and 25° un-polarized incidence light, respectively. The best fitted spectra with surface roughness are shown in Fig. 5.19 (d). See Table 5.5, 5.6, and 5.7 for the obtained properties of InN layers on AlN/sapphire. Three InN layers were obtained from the simulation. The bulk layer (L2) has the higher carrier concentration and lower carrier mobility compared to the other two InN layers (L1 and L3). The top InN layer (L1) could be attributed to a layer that is dominated by voids.

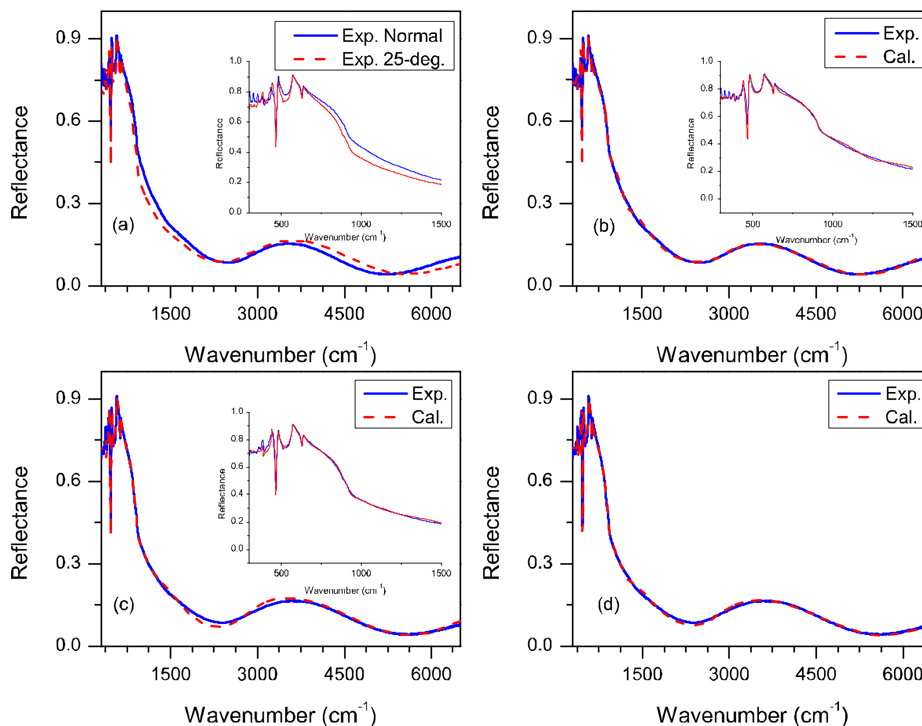

Figure 5.19 Experimental spectra at normal incidence (solid), at 25° (unpolarized) incidence (dash), (b) and (c) experimental (solid) and best fitted (dash) spectra at normal and 25°-unpolarized incidence light, respectively, and (d) experimental and best fitted spectra with surface roughness for 25° unpolarized incidence light for InN/AlN/Sapphire.

The real and imaginary part of the dielectric functions for three InN layers at 25° (un-polarized) incident light as a function of wavenumber, respectively are shown in Fig. 5.20 (a) and (b). The real part of the ordinary dielectric function (which is not shown here) for layer 1 is between 4.239 and 4.897 (refractive index is between 2.213 and 2.058) in the range of 2800-6200 cm^{-1} (3.57-1.61μm).

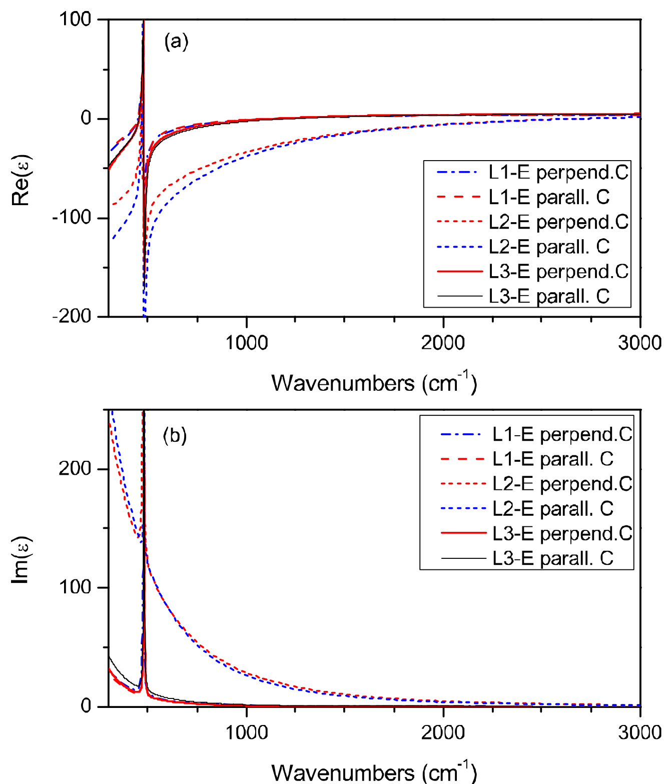

Figure 5.20 The real (a) and imaginary (b) dielectric function of InN layers (L1, L2 and L3) grown on AlN/sapphire at normal incidence, at 25° incidence angle E filed perpendicular to the c-axis, and at 25° incidence angle E filed parallel to the c-axis.

Figure. 5.21 (a) shows the experimental reflectance spectra at the near normal and the 25° un-polarized incidence light for the InN/Ga polar GaN/AlN/sapphire structure. Three InN layers were found on Ga polar GaN/AlN/sapphire using seven layer stack model and the anisotropic model for 25° un-polarized incidence light. However, from analysis of spectrum at normal incidence using isotropic model, only two InN layers on Ga polar GaN/AlN/sapphire were found. Anisotropic model allowed separate surface InN layer (10 nm) with lower carrier concentration. Figure 5.21 (b) and (c) show the best fitted spectra and experimental spectra at normal and 25° un-polarized incidence light, respectively. A well agreement between the calculated and experimental spectra was found for the 25° un-polarized incidence light without surface roughness term. Therefore, there is no RMS data for this layer from IR reflectance analysis. Table 5.5, 5.6, and 5.7 summarize the properties obtained for InN layers on Ga polar GaN/AlN/sapphire.

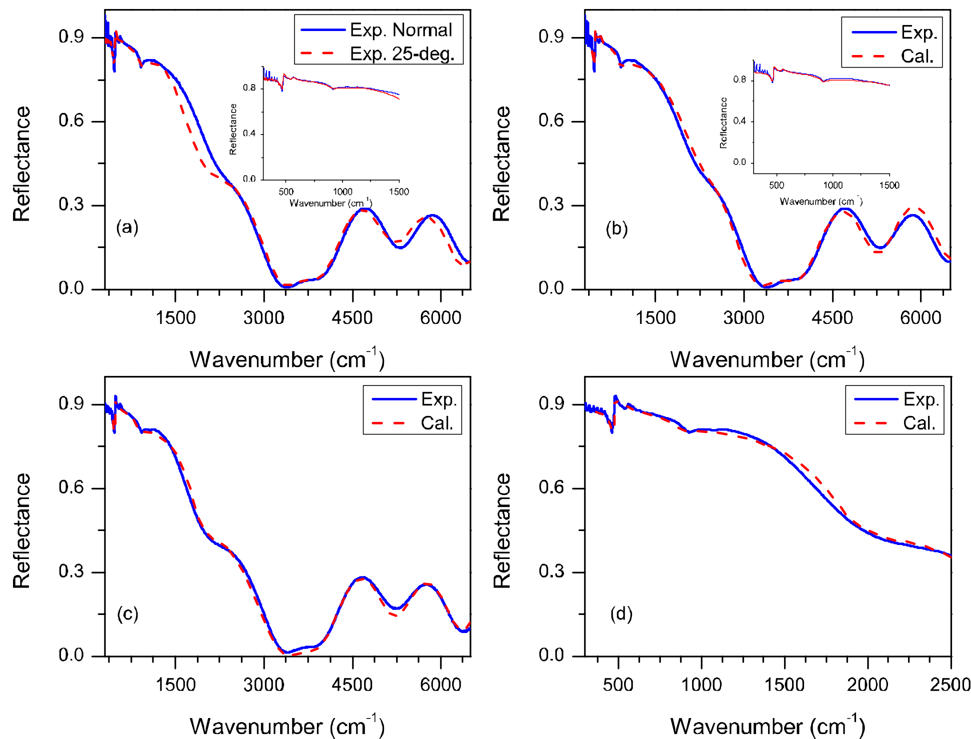

Figure 5.21 Experimental spectra at normal incidence (solid), at 25° (unpolarized) incidence (dash), (b) and (c) experimental (solid) and best fitted (dash) spectra at normal and 25°-unpolarized incidence light, respectively, and (d) experimental and best fitted spectra for 25° unpolarized incidence light, in the range of 300-2500 cm^{-1} for InN/Ga polar GaN/AlN/Sapphire.

For the three InN layers on Ga polar GaN layers, the real and imaginary part of the dielectric functions at the 25° un-polarized incident light as a function of wavenumber are shown in Fig. 5.22 (a) and (b). The damping of the dielectric function increases from L1 to L3 since plasma frequency increases from L1 to L2. The real part of the ordinary dielectric function for layer 1 is between 4.536 and 4.897 (refractive index is between 2.129 and 2.212) in the frequency range of 3500-6200 cm^{-1} (2.85-1.61μm).

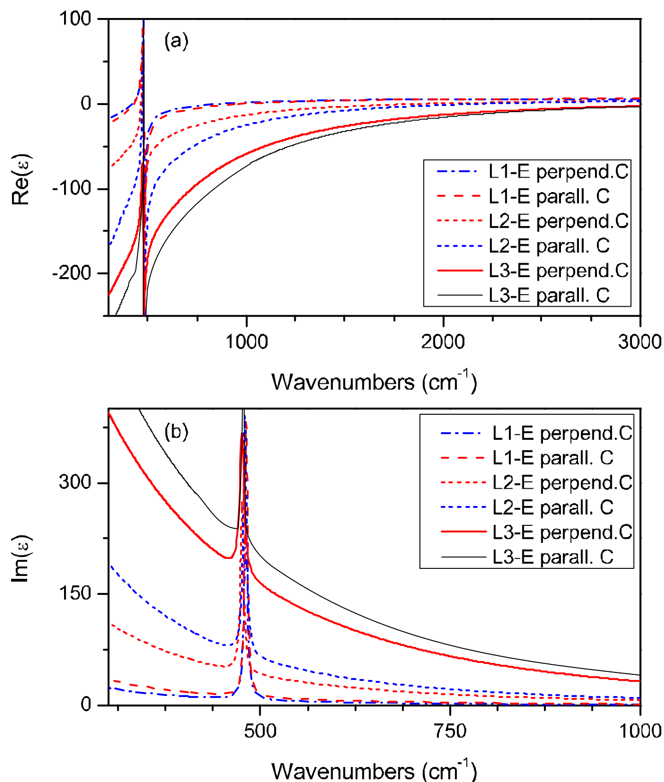

Figure 5.22 The real (a) and imaginary (b) dielectric function of InN layers (L1, L2 and L3) grown on Ga polar GaN/AlN/sapphire at normal incidence, at 25° incidence angle E filed perpendicular to the c-axis, and at 25° incidence angle E filed parallel to the c-axis.

The Figure 5.23 (a) shows the experimental spectra for the InN on N polar GaN/sapphire structure at the near normal, the 25° (un-polarized) incident light. There is a slight difference of plasma damping and interference fringes between these two spectra. Three InN layers were found by fitting normal incidence spectrum with calculated spectrum. Those two spectra are shown in Fig. 5.23 (b). However, only two InN layers were investigated on N polar GaN/sapphire for 25° (un-polarized) incident light using anisotropic model. It is supposed that the layer close to the N polar GaN (in anisotropic analysis) is a combination of nucleation layer and a layer with interface imperfection. Figure 5.23 (c) shows the best fitted and experimental reflectance spectra for 25° (un-polarized) incident light. Further improved best fitted spectrum with surface roughness, and experimental spectrum is depicted in Fig. 5.23 (d).

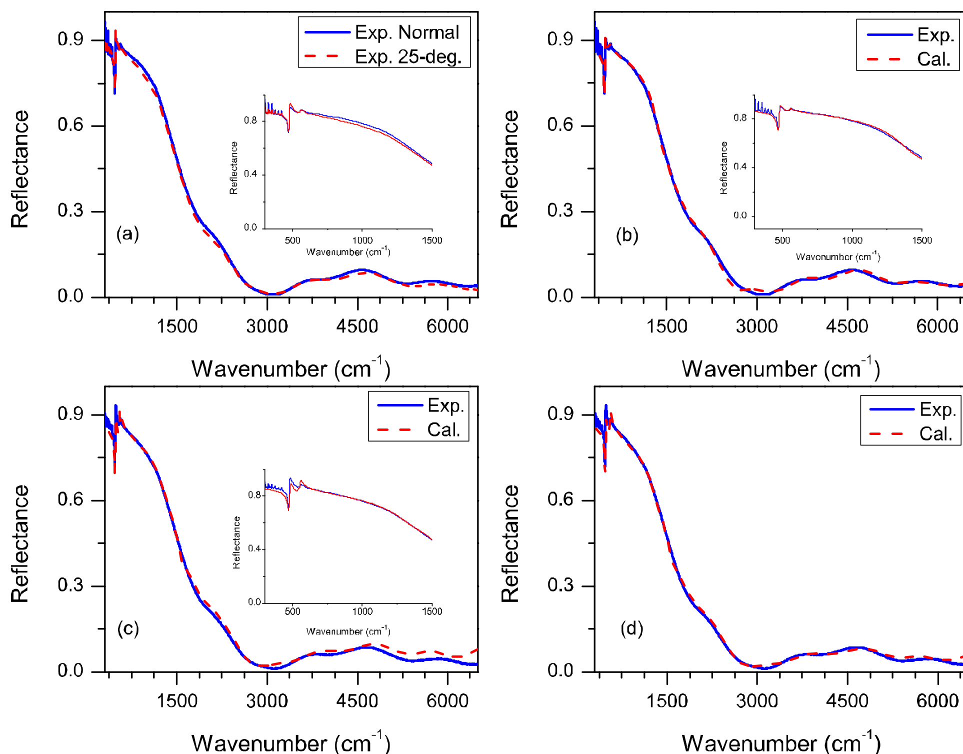

Figure 5.23 Experimental spectra at normal incidence (solid), at 25° (unpolarized) incidence (dash), (b) and (c) experimental (solid) and best fitted (dash) spectra at normal and 25°-unpolarized incidence light, respectively, and (d) experimental and best fitted spectra with surface roughness for 25° unpolarized incidence light for InN/N polar GaN/Sapphire.

The real and imaginary part of the dielectric functions of InN layers grown on N polar GaN/sapphire for 25° un-polarized incident light as a function of wavenumber are depicted in Fig. 5.24 (a) and (b). It can be observed that the dielectric function of the L2 is highly damped compared to all other InN layers grown on different template since this layer shows highest damping of plasma. In the range of 3000-6200 cm^{-1} (3.33-1.61μm), the real part of the ordinary dielectric function for layer 1 (L1) is between 3.519 and 4.485 (refractive index is between 1.875 and 2.117).

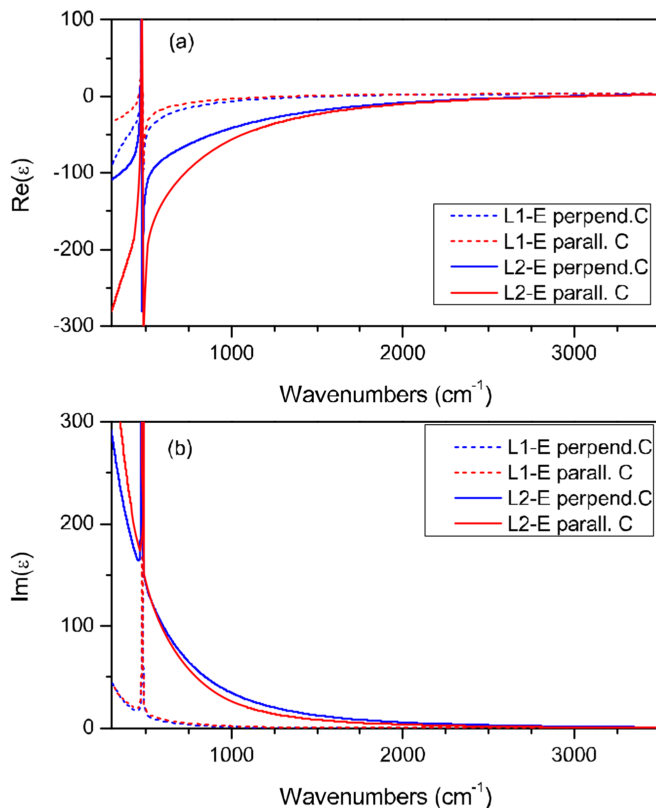

Figure 5.24 The real (a) and imaginary (b) dielectric function of InN layers (L1 and L2) grown on N polar GaN/sapphire at normal incidence, at 25° incidence angle E filed perpendicular to the c-axis, and at 25° incidence angle E filed parallel to the c-axis.

The experimental reflectance spectra for InN on n-GaN/AlN/sapphire at 25° un-polarized incident light are shown in Fig. 5.25 (a). It can be observed that the interference fringes in the reflectance spectrum for 25° un-polarized incident light are more damped than those in the near normal incidence reflectance spectrum. Two InN layers were investigated on n-GaN/AlN/sapphire by analyzing the normal incidence spectrum and three InN layers were found by analyzing the 25° un-polarized incident light reflectance spectrum. The anisotropic model allowed to separate an interface layer (24 nm) between two InN layers. Fig. 5.25 (b) and (c) shows the best fitted and experimental reflectance spectra for n-GaN/AlN/sapphire at normal and 25° (unpolarized) incidence light. Figure 5.25 (d) depict the experimental spectrum and best fitted spectrum with surface roughness (25 nm). It is clear that there is no much improvement of the fitting by considering the surface roughness. These results indicate that the reduction of the reflection of the

experimental spectrum at higher frequency compared with the calculated spectrum is not related to the surface roughness of the layer.

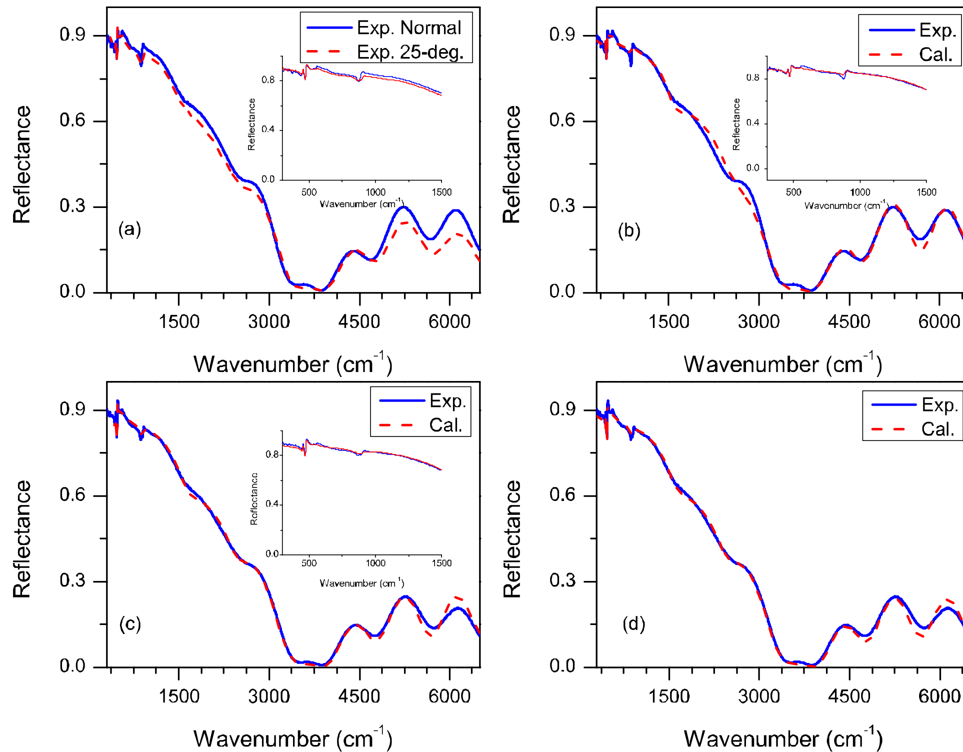

Figure 5.25 Experimental spectra at normal incidence (solid), at 25° (unpolarized) incidence (dash), (b) and (c) experimental (solid) and best fitted (dash) spectra at normal and 25°-unpolarized incidence light, respectively, and (d) experimental and best fitted spectra with surface roughness for 25° unpolarized incidence light for InN/n-GaN/AlN/Sapphire.

Figure. 5.26 (a) and (b) shows the real and imaginary part of the dielectric functions of three InN layers grown on N polar GaN/sapphire for 25° un-polarized incident light as a function of wavenumber. In the range of 3500-6200 cm^{-1} (2.85-1.61μm), the real part of the ordinary dielectric function for layer 1 (L1) is between 4.731 and 5.565 (refractive index is between 2.175 and 2.359).

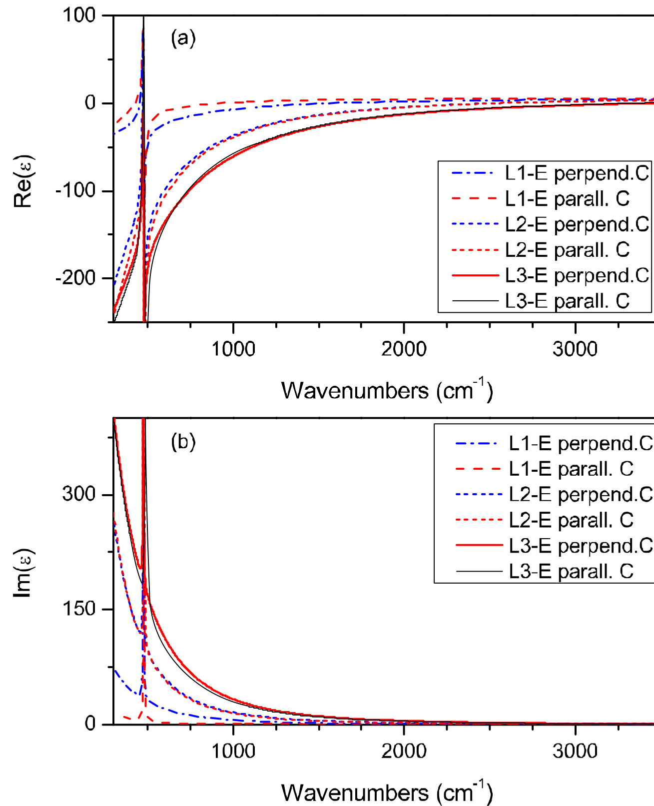

Figure 5.26 The real (a) and imaginary (b) dielectric function of InN layers (L1, L2 and L3) grown on n-GaN/AlN/sapphire at normal incidence, at 25° incidence angle E filed perpendicular to the c-axis, and at 25° incidence angle E filed parallel to the c-axis.

Figure 5.27 (a) depicts the experimental reflectance spectra for InN on p-GaN/AlN/sapphire at 25° un-polarized incident light. Two InN layers were investigated on n-GaN/AlN/sapphire by analyzing the normal incidence spectrum and the 25° un-polarized incident light reflectance spectrum. The best fitted and experimental reflectance spectra for p-GaN/AlN/sapphire at normal and 25° (unpolarized) incidence light are depicted in Fig. 5.27 (b) and (c). Figure 5.25 (d) shows the experimental spectrum and best fitted spectrum with surface roughness (40 nm). As in InN on n-GaN/AlN/sapphire, there is no much influence on the fitting by the surface roughness.

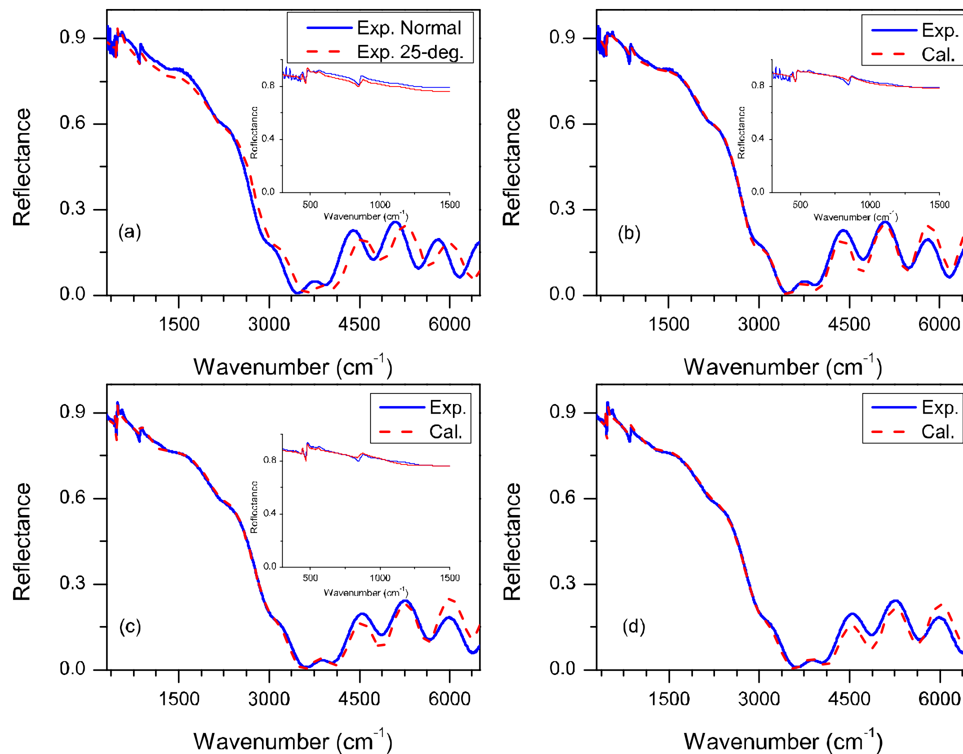

Figure 5.27 Experimental spectra at normal incidence (solid), at 25° (unpolarized) incidence (dash), (b) and (c) experimental (solid) and best fitted (dash) spectra at normal and 25°-unpolarized incidence light, respectively, and (d) experimental and best fitted spectra with surface roughness for 25° unpolarized incidence light for InN/p-GaN/AlN/Sapphire.

Figure. 5.26 (a) and (b) depict the real and imaginary part of the dielectric functions of InN layers grown on p-GaN/AlN/sapphire for 25° un-polarized incident light as function of wavenumber. In the range of 3500-6200 cm^{-1} (2.85-1.61μm), the real part of the ordinary dielectric function for layer 1 (L1) is between 6.326 and 6.784 (refractive index is between 2.515 and 2.604).

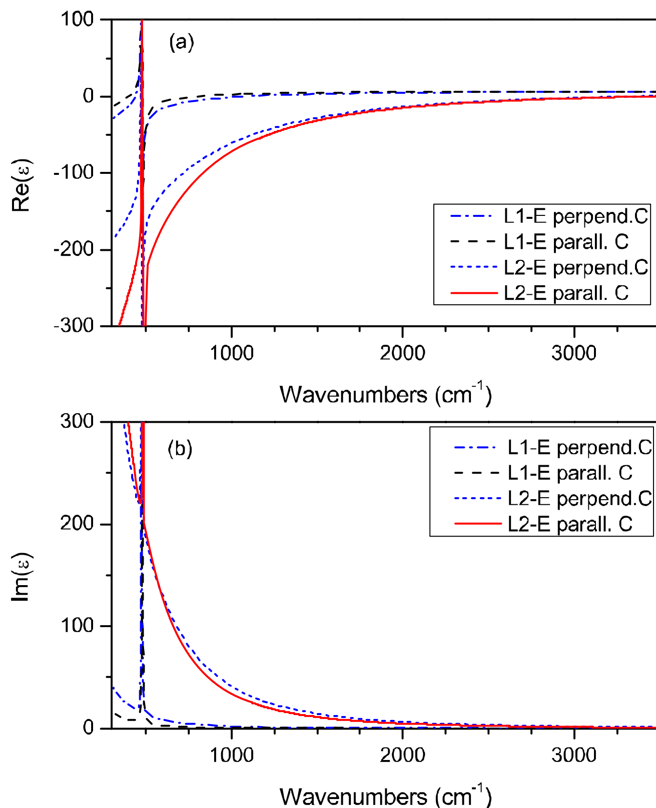

Figure 5.28 The real (a) and imaginary (b) dielectric function of InN layers (L1 and L2) grown on p-GaN/AlN/sapphire at normal incidence, at 25° incidence angle E filed perpendicular to the c-axis, and at 25° incidence angle E filed parallel to the c-axis.

Overall FTIR reflectance analysis results of InN layers in different templates indicate followings. A thicker InN layer can be achieved by using Ga polar GaN template. The lowest carrier concentration of 6.0×10^{18} cm^{-3} with mobility of 450 $cm^2V^{-1}s^{-1}$ (the InN layers close to the ambient were used for the comparison. However, the surface layer (10 nm) with carrier concentration 4.3×10^{18} cm^{-3} did not include for this comparison) was obtained for the sample grown on AlN template. The lowest carrier concentration of 7.1×10^{18} cm^{-3} with mobility of 660 $cm^2V^{-1}s^{-1}$ (the InN layers close to the templates were used for the comparison) was obtained for the InN grown on AlN template The highest mobility value of 740 $cm^2V^{-1}s^{-1}$ was achieved for the layer grown on n-GaN template. The InN layer close to the template has higher carrier concentration for the samples grown on sapphire, Ga polar, N polar, n-GaN, and p-GaN templates. However, the layer grown on AlN template behaves differently forming a film with lower carrier concentration on AlN first.

The reason for the variation seen (from 4.29 to 8.3) of the high frequency dielectric constant is discussed in Chapter 7.

Table 5.5 Best fitted isotropic and anisotropic high frequency dielectric constant, plasma frequencies, and their damping values for InN layers.
The tolerance for the high frequency dielectric constant is (±0.01), and that is for plasma frequency and damping of the plasma is (±5.0).

Sample		Normal Incidence			25° Incidence					
		ε_∞	ω_p (cm^{-1})	γ_p (cm^{-1})	$\varepsilon_{\infty,\perp}$	$\omega_{p,\perp}$ (cm^{-1})	$\gamma_{p,\perp}$ (cm^{-1})	$\varepsilon_{\infty,\parallel}$	$\omega_{p,\parallel}$ (cm^{-1})	$\gamma_{p,\parallel}$ (cm^{-1})
InN/sapphire	L1	6.14	1698	457	5.74	1695	462	6.2	1451	433
	L2	7.22	2702	460	7.12	2683	491	7.2	2590	511
InN/AlN/sapphire	L1	4.91	1190	260	5.07	1091	230	4.93	1052	208
	L2	7.71	2880	537	8.25	2723	705	8.3	2697	584
	L3	6.11	1215	424	6.12	1076	158	6.11	1158	223
InN/Ga-polar-GaN/AlN/sapphire	L1	6.2	890	198	6.78	800	244	7.38	916	282
	L2	7.02	3266	485	6.02	1850	380	7.6	2130	310
	L3	-	-	-	6.58	3500	500	8.3	3480	515
InN/N-polar-GaN/sapphire	L1	4.29	1392	337	4.78	1513	144	4.51	1317	300
	L2	7.97	2890	379	8.31	2970	711	8.28	3003	403
	L3	5.21	1490	120	-	-	-	-	-	-
InN/n-type-GaN/AlN/sapphire	L1	8.02	1553	388	5.97	1574	484	5.99	808	140
	L2	5.97	3525	508	7.95	2493	362	8.07	2497	323
	L3	-	-	-	7.21	3395	493	7.24	3304	455
InN/p-type-GaN/AlN/sapphire	L1	7.53	947	354	7.0	1042	300	6.99	690	203
	L2	6.88	3002	379	8.3	3356	170	8.24	3400	424

Table 5.6 Best fit isotropic and anisotropic phonon frequencies, and their broadening values for InN layers.
The tolerance for the phonon frequencies and their broadening is (±0.1).

Sample		Normal Incidence			25° Incidence					
		ω_{LO} (cm^{-1})	ω_{TO} (cm^{-1})	γ_{TO} (cm^{-1})	$\omega_{LO,\perp}$ E_1LO (cm^{-1})	$\omega_{TO,\perp}$ E_1TO (cm^{-1})	$\gamma_{TO,\perp}$ (cm^{-1})	$\omega_{LO,\parallel}$ A_1LO (cm^{-1})	$\omega_{TO,\parallel}$ A_1TO (cm^{-1})	$\gamma_{TO,\parallel}$ (cm^{-1})
InN/sap.	L1	568.0	479.1	7.2	568.1	477.8	5.5	579.8	479.8	3.5
	L2	570.6	477.4	7.0	569.0	478.6	8.7	580.2	480.3	1.6
InN/AlN/sap.	L1	567.1	478.2	5.1	567.9	477.1	8.4	579.6	480.4	4.3
	L2	571.4	479.1	4.7	567.4	475.9	8.9	581.8	479.9	1.0
	L3	570.9	479.2	4.2	568.5	480.5	4.3	581.1	480.9	4.5
InN/Ga-polar-GaN/AlN/sap.	L1	571.0	476.0	6.3	567.3	480.9	5.5	580.6	481.4	4.2
	L2	572.1	477.5	5.3	567.1	476.1	5.2	578.6	479.7	5.1
	L3	-	-	-	567.4	475.9	6.9	582.1	478.6	2.1
InN/N-polar-GaN/sapp.	L1	570.3	476.9	6.9	564.7	481.0	7.2	578.2	480.1	5.9
	L2	570.2	477.9	6.7	568.9	476.8	4.4	581.1	479.2	1.3
	L3	570.5	477.7	6.7	-	-	-	-	-	-
InN/n-type-GaN/AlN/sap.	L1	571.8	477.2	6.0	570.1	476.3	5.8	578.9	478.6	6.8
	L2	573.2	474.0	9.5	571.5	475.8	4.5	577.7	480.7	6.5
	L3	-	-	-	570.0	475.1	4.7	580.7	479.5	1.3
InN/p-type-GaN/AlN/sap.	L1	569.8	475.3	9.2	570.5	475.9	4.6	577.2	480.8	6.6
	L2	572.5	471.6	10.0	569.2	475.1	4.7	580.6	479.6	1.4

Table 5.7 Best fit isotropic and anisotropic layer thicknesses, free carrier concentration, mobility of the carriers, and surface roughness values for InN layers.
The effective mass values used in the free carrier concentration and mobility of the carrier calculations are shown in the brackets.

Substrate		Normal Incidence			25° Incidence					
		d (nm)	N_c (×10^18 cm^-3)	μ_c (cm^2V^-1s^-1)	d (nm)	$N_{c,\perp}$ (×10^18 cm^-3)	$\mu_{c,\perp}$ (cm^2V^-1s^-1)	$N_{c,\parallel}$ (×10^18 cm^-3)	$\mu_{c,\parallel}$ (cm^2V^-1s^-1)	Surf. Rough. (nm)
InN/sap.	L1	115	17.7	230	114	16.6	220	13.0	240	77
	L2	283	52.8	230	309	51.4	210	48.4	200	
InN/AlN/sap.	L1	162	6.9	400	187	6.0	450	5.4	500	40
	L2	59	64.1	190	62	61.4	150	60.5	180	
	L3	185	9.0	240	136	7.1	660	8.2	470	
InN/Ga-polar-GaN/AlN/sap.	L1	106	4.9	520	10	4.3	430	6.2	370	-
	L2	308	75.0	210	121	20.7	270	34.6	330	
	L3	-	-	-	391	81.0	210	100.0	200	
InN/N-polar-GaN/sapp.	L1	197	8.3	310	228	11.0	720	7.8	350	70
	L2	177	66.8	270	137	73.5	150	74.9	260	
	L3	157	11.0	860	-	-	-	-	-	
InN/n-type-GaN/AlN/sap.	L1	58	19.0	270	56	14.8	210	3.9	740	25
	L2	390	74.4	200	24	49.5	290	50.4	320	
	L3	-	-	-	376	83.3	210	79.3	230	
InN/p-type-GaN/AlN/sap.	L1	24	6.7	290	57	7.6	350	3.3	510	40
	L2	447	62.2	270	324	93.0	170	95.6	240	

5.3.1 AFM Analysis

AFM topography for the templates and InN films were obtained, in order to compare the surface morphology of the InN layers on different templates and compare the RMS surface roughness values obtained from the AFM with the values determined by FTIR reflectance analysis. Figures 5.29, 5.30, 5.31, 5.32, 5.33 present the 2D-, 3D-AFM surface topographies with the profile of the change in the height along the distance, and the corresponding s-SNOMs for (a) the templates and (b) InN films on templates.

Table 5.9 summarizes the RMS surface roughness values for the layers determined from the AFM analysis and FTIR analysis.

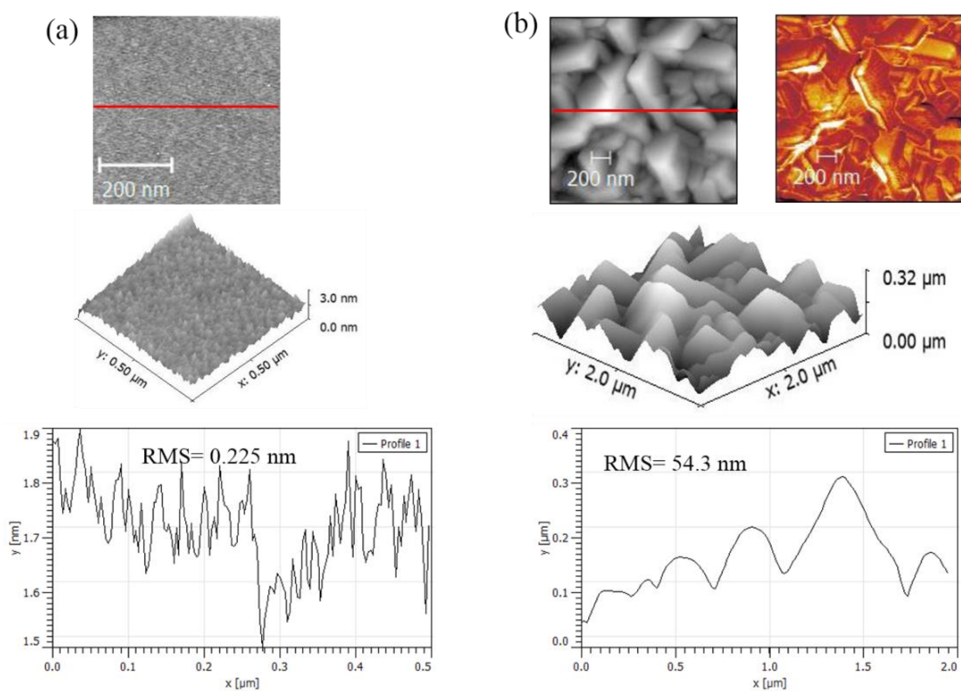

Figure 5.29 2D-AFM and 3D-AFM surface images with the profile of change in the height along distance, and corresponding s-SNOM images for (a) sapphire and (b) InN/sapphire.
The corresponding s-SNOM image for sapphire was not obtained.

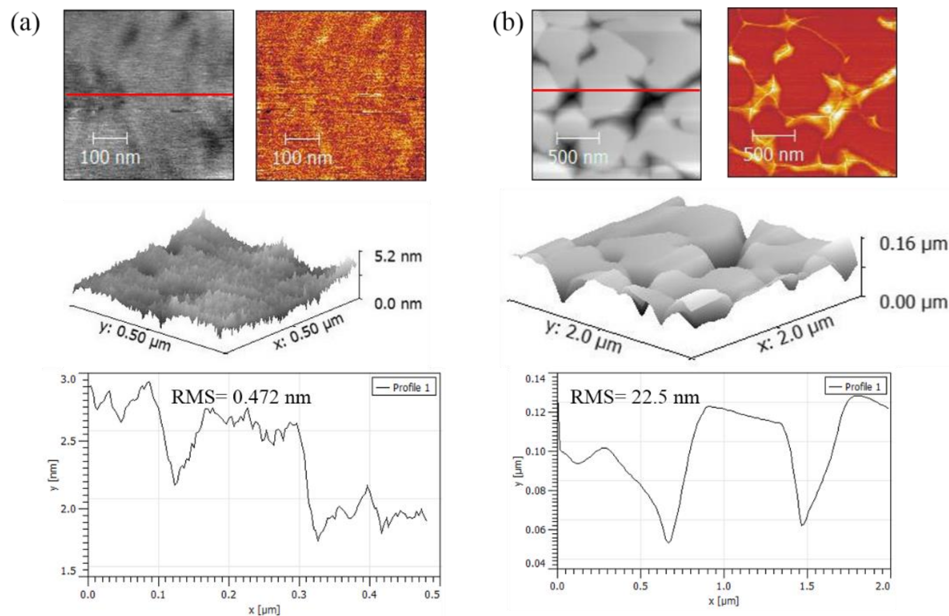

Figure 5.30 2D-AFM and 3D-AFM surface images with the profile of change in the height along distance, and corresponding s-SNOM images for (a) Ga polar GaN template and (b) InN on Ga polar GaN.

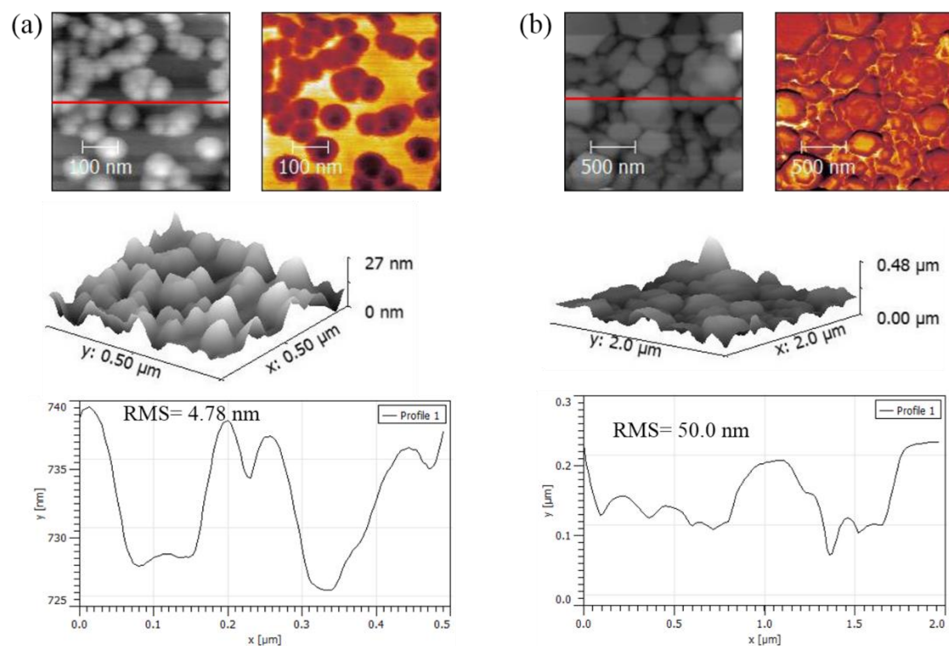

Figure 5.31 2D-AFM and 3D-AFM surface images with the profile of change in the height along distance, and corresponding s-SNOM images for (a) N polar GaN template and (b) InN on N polar GaN.

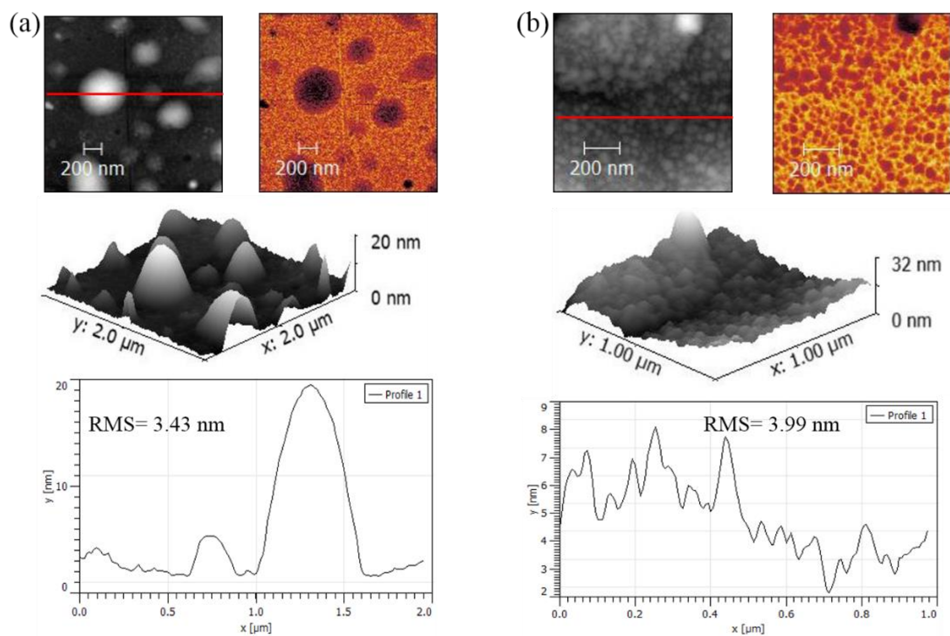

Figure 5.32 2D-AFM and 3D-AFM surface images with the profile of change in the height along distance, and corresponding s-SNOM images for (a) n-GaN template and (b) InN on n-GaN.

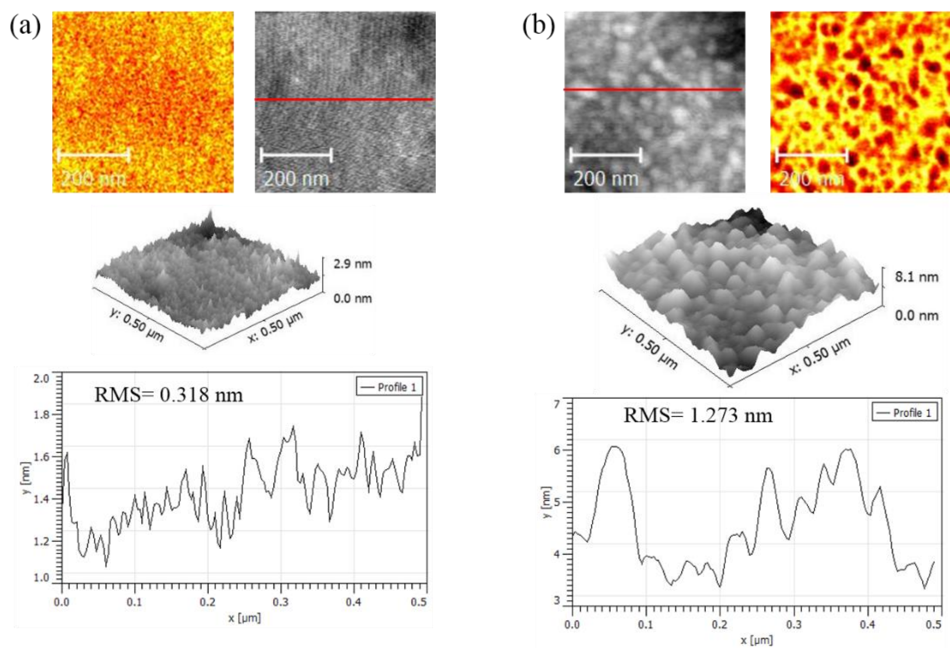

Figure 5.33 2D-AFM and 3D-AFM surface images with the profile of change in the height along distance, and corresponding s-SNOM images for (a) p-GaN template and (b) InN on p-GaN.

Table 5.8 The RMS surface roughness values obtained from AFM analysis and FTR analysis (in parentheses) for templates and InN films on corresponding templates.

Template	RMS values (nm)	Sample	RMS values (nm)
Sapphire	0.225	InN/sapphire	54.3 (77)
Ga polar GaN	0.472	InN/Ga polar GaN	22.5
N polar GaN	4.78 (30)	InN/N polar GaN	50.0 (70)
n-GaN	3.43 (25)	InN/n-GaN	3.99
p-GaN	0.318 (20)	InN/p-GaN	1.27

AFM topography and s-SNOM picture show that the InN film grown on sapphire has large tilted grains on the surface (see Fig. 5.29). This resulted in the highest RMS surface roughness in this sample compared to the other InN surfaces. It can be observed steps feature on the Ga polar surface. The InN film grown on this Ga polar surface has large grains on the surface. However, here, they are not tilted as observed for the InN films grown on sapphire. Non-uniform corn shape grains are observed on N polar GaN surface and this surface has a higher roughness compared to the other templates. Hexagonal shape crystalline grains in different sizes can be observed on the InN film grown on N polar GaN. Similarly, randomly distributed large corn shape grains randomly are observed on the n-GaN surface. The InN film on n-GaN has small grains on the surface. It is observed steps feature similar to the one observed on the Ga polar GaN surface. The smoothest InN surface was found on the InN film grown on p-GaN. However, it is noted that scanned area is different from the other samples.

The surface roughness values obtained from the IR reflectance spectra analysis are higher than that of the AFM surface roughness values. Further studies are needed to explain the reason.

5.3.2 Analysis of Raman Spectra

Figure 5.34 shows the Raman spectra for each templates with excitation wavelength of 532 nm (solid lines) and 488 nm (short-dashed lines), in back scattering geometry. The allowed six Raman phonon modes for sapphire with 532 nm (488 nm) excitation wavelength were observed at E_g 378.0 cm^{-1} (378.8 cm^{-1}), A_{1g} 416.0 cm^{-1} (417.0 cm^{-1}), E_g 429.0 cm^{-1} (430.0 cm^{-1}), E_g 446.6 cm^{-1} (448.6 cm^{-1}), E_g 576.7 cm^{-1} (576.1) cm^{-1}, E_g 749.7 cm^{-1}. Note that Raman spectrum with excitation wavelength of 488 nm for sapphire is measured only up to 700 cm^{-1}. Raman scattering intensities of all phonon modes except 749.9 cm^{-1} mode (since there is no measured data after 700 cm^{-1} for 488 nm excitation wavelength) are same. In the Raman spectrum of AlN/sapphire (Fig. 5.34 (b)), sapphire modes are stronger than AlN due to penetration depth into the sapphire for relatively thinner film (25 nm). A slight indication of A_1LO peak is observed at 888 cm^{-1} though and there is no prominent peak of E_2 high peak at 653 cm^{-1} observed.

Raman spectrum (excitation wavelength 532 nm) for Ga polar GaN film grown on AlN/sapphire is illustrated in the Fig. 5.34 (c). According to the Ref. [25], the peaks at 569.4 cm^{-1}, and 734.8 cm^{-1} can be attributed to the E_2 high, and A_1LO phonon modes of GaN, respectively. As mentioned in the Ref. [25], with Lorentzian fit for the range 700-800 cm^{-1}, E_1LO phonon mode of GaN can be found at 742 cm^{-1}. Fig. 5.34 (d) is depicted the Raman spectra of N-polar GaN grown on sapphire for the excitation wavelength of 532 nm and 488 nm. As well as, Raman spectra of n- and p-type doped GaN grown on i-GaN/AlN/sapphire are shown in the Fig. 5.34 (e), and (f) respectively. The Raman scattering from sapphire are absence in the Raman spectra for each samples measured with 488 nm excitation wavelength. For this case, the Raman scattering measured using micro-Raman system and which allowed to focus the Raman features from the samples (in this case GaN) and sapphire scattering became much weaker. In fact, the intensity of A_1LO phonon modes decreases for both n- and p-type samples. The absence of A_1LO peak in N-polar GaN grown sapphire in both cases, 532 nm and 488 nm excitation wavelength and coincidence of A_1LO with LPP modes and this was also observed from the FTIR reflectance spectrum.

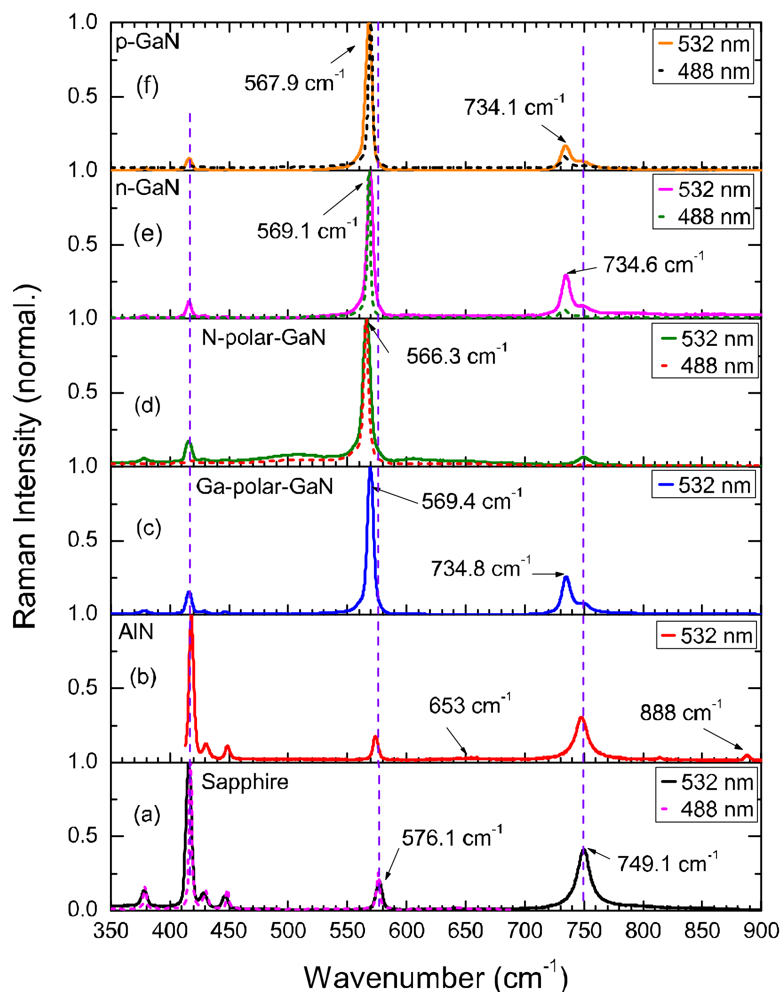

Figure 5.34 Raman spectra of sapphire (a), AlN/sapphire (b), Ga-polar GaN/AlN/sapphire (c), N-polar-GaN/sapphire (d), n-type GaN/i-GaN/AlN/sapphire (e), p-type GaN/i-GaN/AlN/sapphire (f). Solid line and short dashed lines are the Raman spectra for the excitation wavelength of 532 nm and 488 nm respectively. Dashed lines mark for the strongest sapphire-related Raman peaks.

Before arriving at conclusions about the InN samples, it is important to understand the quality of the templates or substrate since most of the dislocations can be originated from the substrate or template. Therefore, the Raman E_2 high and A_1LO phonon modes were analyzed in order to understand the structural and electronic properties. The sifting of the Raman E_2 high peak position from the ideal position is resulted by the stress or strain in semiconductors hence it can be used as a qualitative measure of those stress or strains. The stress is tensile as the E_2 high peak exhibit the red shift (decrease of Raman frequency) and the stress is compressive as the E_2 high peak has a blue shift (increase of Raman frequency).

Further, the full width half maximum (FWHM) of E_2 high peak is expounded the short range ordering of the crystalline structure. The narrow E_2 high FWHM is the better crystalline quality. The Raman E_2 high and A_1LO phonon modes FWHM maximum values and positions are listed in the Table 5.9.

Table 5.9 Raman E_2 high and A_1LO position and their FWHM values different templates. (532 nm of excitation wavelength).
Parentheses shows the values determined with 488 nm excitation wavelength.

Substrate	E_2 high (cm^{-1})		A_1 LO (cm^{-1})	
	FWHM	Peak Position	FWHM	Peak Position
sapphire	-	-	-	-
AlN/sapphire	-	-	-	888.0
Ga polar GaN/AlN/sapphire	5.3	569.4	7.4	734.8
N polar GaN/AlN/sapphire	6.7 (4.4)	566.3 (565.8)	-	-
n-GaN/AlN/sapphire	5.6 (2.7)	569.1 (568.1)	7.3 (5.6)	734.6 (733.3)
p-GaN/AlN/sapphire	5.6 (3.7)	567.9 (569.5)	7.8 (6.3)	734.1 (733.9)

For the Ga polar GaN and n-GaN templates, Raman E_2 high peak position has shown a blue shift of 1.4 cm^{-1} and 1.1 cm^{-1}, respectively, from the bulk value of 568 cm^{-1} [24]. Raman E_2 high peak position of the p-GaN is almost close to the bulk value. In contrast, N polar E_2 high peak position exhibits a red shift of 2.3 cm^{-1} indicating it has tensile stress. A slight shift of E_2 high modes with excitation wavelength is observed. Local crystalline order of the all GaN templates is almost same except N polar GaN template.

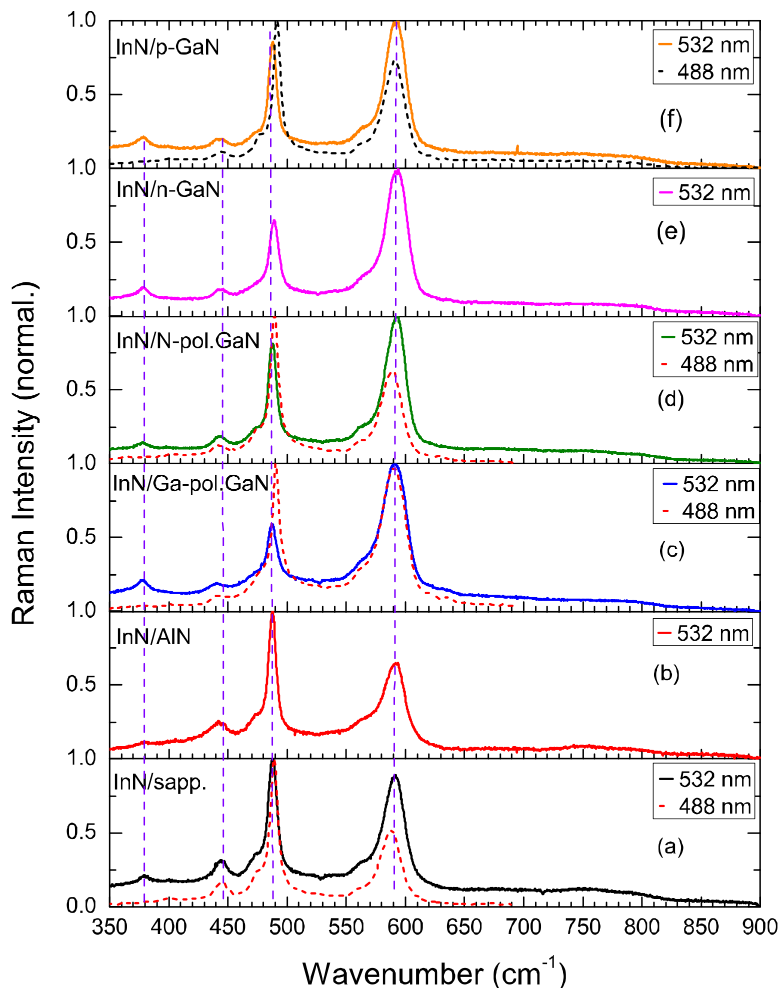

Figure 5.35 Raman spectra of InN films grown on sapphire (a), AlN/sapphire (b), Ga-polar GaN/AlN/sapphire (c), N-polar-GaN/sapphire (d), n-type GaN/AlN/sapphire (e), p-type GaN/AlN/sapphire (f).

The Raman spectra of InN layers on each template with the excitation wavelength of 532 nm (solid lines) and 488 nm (short-dashed lines), in back scattering geometry, are depicted in Fig. 5.35. It is indicated that Raman scattering intensity and the broadening of the phonon modes are dependent on the excitation energy. The sapphire phonon modes (~378.7 cm^{-1}) is absent in the Raman spectra with 488 nm excitation wavelength. A_1TO (445 cm^{-1}) phonon mode is not allowed in the scattering geometry used in this study. However, for all above InN layers, the A_1TO mode is detected. The E_2 high and A_1LO phonon modes of InN are observed ~487.5 cm^{-1} and ~590-593.2 cm^{-1} with 532 excitation wavelength. Table 5.10 summarizes the Raman E_2 high and A_1LO phonon modes FWHM maximum values and positions.

The intensity enhancement of the A_1LO phonon mode compare to the E_2 high, is related to the high carrier concentration [26]. Raman spectra of InN layers performed with the excitation wavelength of 532 nm indicate that this wavelength excites the properties of the InN layer close to the templates. When compare the intensity of A_1LO phonon mode with the intensity of E_2 high mode (with excitation wavelength of 532 nm), InN grown on AlN/sapphire has the lowest A_1LO phonon mode intensity. Thus, lowest carrier concentration. This confirms by the FTIR analysis results. See Table 5.7. The InN layer close to the AlN has the lowest carrier concentration comparison with the other samples.

The lowest Raman E_2 high FWHM values of 6.8 cm^{-1} (with the 532 nm excitation source) is observed the InN grown on AlN/sapphire. Therefore, the InN layer grown on AlN template shows the better local crystalline order. The broadening of the E_1TO phonon mode in IR reflectance spectra is related to the quality of the film [23]. From the FTIR analysis, lowest E_1TO broadening value of 4.3 cm^{-1} was also obtained for this sample. It is further confirmed that InN on AlN has the better crystalline InN layer.

Table 5.10 Raman E_2 high and A_1LO position and their FWHM values for InN layers grown on different templates (532 nm of excitation wavelength).
Parentheses shows the values determined with 488 nm excitation wavelength.

Sample	E_2 high (cm^{-1})		A_1 LO (cm^{-1})	
	FWHM	Peak Position	FWHM	Peak Position
InN/sapphire	8.9 (7.6)	487.8 (489.1)	17.5 (19.6)	591.4 (587.8)
InN/AlN/sapphire	6.8	487.7	17.1	591.9
InN/Ga polar GaN/AlN/sapphire	10.3 (7.9)	487.4 (490.5)	19.9 (21.7)	592.3 (590.7)
InN/N polar GaN/AlN/sapphire	8.3 (8.0)	487.6 (489.2)	17.4 (16.3)	592.7 (589.3)
InN/n-GaN/AlN/sapphire	8.2	489.1	19.3	593.2
InN/p-GaN/AlN/sapphire	7.9 (7.5)	487.8 (491.4)	19.6 (19.6)	592.0 (591.1)

5.4 Conclusion

FTIR reflectance spectra (measured at near normal incidence and 25° incident light) of InN samples grown on different substrate were analyzed using multilayer stack model based on the transfer matrix method and model IR dielectric function to determine the isotropic and anisotropic properties (film thickness, high frequency dielectric constant, phonon modes and broadening, plasma frequency, damping of the plasma, free carrier concentration, and mobility of the carriers) of the films. These results suggest that the films on the templates have more than one layer with different properties. Further studies are needed to explain these results. The lowest carrier concentration of 7.1×10^{18} cm^{-3} with the mobility of 660 $cm^2V^{-1}s^{-1}$ was found in the InN film grown on AlN template. The smoothest InN surface (RMS=1.273 nm) was observed the InN film on p-GaN template. InN grown AlN/sapphire shows the better local crystalline order. Further studies are carrying out to correlate the results.

5.5 References

[1] A. Shetty, K. J. Vinoy and S. B. Krupanidhi, presented at the COMSOL, Bangalore, India2012).

[2] Z. G. Qian, W. Z. Shen, H. Ogawa and Q. X. Guo, Journal of Applied Physics **92** (7), 3683-3687 (2002).

[3] N. ul Hassan Alvi, V. Gómez, P. Soto Rodriguez, P. Kumar, S. Zaman, M. Willander and R. Nötzel, Sensors **13** (10), 13917 (2013).

[4] Y. Ishitani, T. Ohira, X. Wang, S.-B. Che and A. Yoshikawa, Physical Review B **76** (4), 045206 (2007).

[5] Y. Ishitani, X. Wang, S.-B. Che and A. Yoshikawa, Journal of Applied Physics **103** (5), 053515 (2008).

[6] R. Cuscó, J. Ibáñez, E. Alarcón-Lladó, L. Artús, T. Yamaguchi and Y. Nanishi, Physical Review B **79** (15), 155210 (2009).

[7] J. S. Thakur, G. W. Auner, D. B. Haddad, R. Naik and V. M. Naik, Journal of Applied Physics **95** (9), 4795-4801 (2004).

[8] A. Kasic, M. Schubert, Y. Saito, Y. Nanishi and G. Wagner, Physical Review B **65** (11), 115206 (2002).

[9] S. P. Fu and Y. F. Chen, Applied Physics Letters **85** (9), 1523-1525 (2004).

[10] V. Darakchieva, M. Schubert, T. Hofmann, B. Monemar, C.-L. Hsiao, T.-W. Liu, L.-C. Chen, W. J. Schaff, Y. Takagi and Y. Nanishi, Applied Physics Letters **95** (20), 202103 (2009).

[11] M. Fujiwara, Y. Ishitani, X. Wang, S.-B. Che and A. Yoshikawa, Applied Physics Letters **93** (23), 231903 (2008).

[12] W. M. Linhart, T. D. Veal, P. D. C. King, G. Koblmüller, C. S. Gallinat, J. S. Speck and C. F. McConville, Applied Physics Letters **97** (11), 112103 (2010).

[13] K. Fukui, Y. Kugumiya, N. Nakagawa and A. Yamamoto, physica status solidi (c) **3** (6), 1874-1878 (2006).

[14] C. C. Katsidis, A. O. Ajagunna and A. Georgakilas, Journal of Applied Physics **113** (7), 073502 (2013).

[15] S. P. S. Porto and R. S. Krishnan, The Journal of Chemical Physics **47** (3), 1009-1012 (1967).

[16] M. Schubert, T. E. Tiwald and C. M. Herzinger, Physical Review B **61** (12), 8187-8201 (2000).

[17] I. H. Malitson, J. Opt. Soc. Am. **52** (12), 1377-1379 (1962).

[18] Z. G. Hu, A. B. Weerasekara, N. Dietz, A. G. U. Perera, M. Strassburg, M. H. Kane, A. Asghar and I. T. Ferguson, Physical Review B **75** (20), 205320 (2007).

[19] A. Kasic, M. Schubert, S. Einfeldt, D. Hommel and T. E. Tiwald, Physical Review B **62** (11), 7365-7377 (2000).

[20] *Optical constants of GaN (Gallium nitride),* December 5, 2016, http://refractiveindex.info/?shelf=main&book=GaN&page=Barker-o

[21] F. Tuomisto, T. Suski, H. Teisseyre, M. Krysko, M. Leszczynski, B. Lucznik, I. Grzegory, S. Porowski, D. Wasik, A. Witowski, W. Gebicki, P. Hageman and K. Saarinen, physica status solidi (b) **240** (2), 289-292 (2003).

[22] S. Shokhovets, R. Goldhahn, V. Cimalla, T. S. Cheng and C. T. Foxon, Journal of Applied Physics **84** (3), 1561-1566 (1998).

[23] Z. C. Feng, Y. T. Hou, S. J. Chua and M. F. Li, Surface and Interface Analysis **28** (1), 166-169 (1999).

[24] H. Harima, Journal of Physics: Condensed Matter **14** (38), R967 (2002).

[25] Z. C. Feng, M. Schurman, R. A. Stall, M. Pavlosky and A. Whitley, Appl. Opt. **36** (13), 2917-2922 (1997).

[26] J. S. Thakur, D. Haddad, V. M. Naik, R. Naik, G. W. Auner, H. Lu and W. J. Schaff, Physical Review B **71** (11), 115203 (2005).

6 CHAPTER 6: EFFECT OF REACTOR PRESSURE ON THE ELECTRICAL AND STRUCTURAL PROPERTIES OF InN EPILAYERS GROWN BY HP-MOCVD

6.1 Introduction

Indium nitride (InN) and indium-rich group III-nitride alloys are of renowned interest due to their potential in high-speed (THz-regime) device structures, for high-efficient energy conversion devices such as photovoltaic cells and various light emitting device structures [1]. Therefore, understanding and optimizing of the material properties as function of growth process conditions are of crucial importance for fabrication of InN and indium-rich group III-nitride epilayers and heterostructures [2].

As of today, the structural and optoelectronic properties of the binary InN vary widely depending on the growth process used. Under low-pressure MOCVD conditions, the integration of InN epilayers with other group III-nitrides is challenged due to the low dissociation temperature of InN [1] (~600 °C) relative to that of GaN [3] (~1000 °C), which leads to stoichiometric instabilities [4, 5] and a potential immiscibility for ternary InGaN alloys [6]. In 1970, MacChesney et al. [5] assessed the use of high pressure as a potential pathway to stabilize the group III-nitrides and their alloys at higher growth temperatures under thermodynamic equilibrium conditions. Though thin film growth processes can employ various degrees of non-equilibria to stabilize epilayers, the regime of super-atmospheric CVD is still mostly unexplored for the growth of III-nitride alloys. At low-pressure MOCVD, the growth of InN is limited to growth temperatures at or below 600 °C [7], requiring a high group-V/III precursor ratio due to the insufficient cracking of ammonia. In order to stabilize InN epilayers at higher growth temperatures that may allow for improved materials quality as well as the stabilization of indium-rich ternary InGaN heterostructures, we explore in this study the growth of InN by high-pressure chemical vapor deposition (HPCVD) at reactor pressures ranging from 2.5 bar and up to 20 bar. The details of the HPCVD rector system have been described previously [8-11] and in Section 2.6. For reactor pressures around 15 bar, the growth temperatures for InN are in the vicinity of 850 °C [12], with group V/III precursor ratio from 1000 to 5000 explored. The smaller V/III precursor ratio compared to low-pressure MOCVD is due to the improved

NH_3 decomposition kinetics at higher temperatures and gas densities. So far there are no studies that correlate the reactor pressure with the structural and electrical properties of InN epilayers grown by HPCVD which is the goal of this contribution. This study present results on the influence of the rector pressure on the structural and optoelectronic properties of epitaxial InN layers, noting however that the reactor pressure is only one of the many process parameters that affects the properties of the epilayers.

6.2 Experimental

The InN epilayers were grown on GaN/Sapphire (0001) templates using a custom-built HPCVD reactor system. Ammonia (NH_3) and trimethylindium (TMI) were used as group-V and group-III precursors. The group-V/III molar precursor ratio was kept at ~ 2500, while the reactor pressure was varied between 2.5 bar and 18.5 bar. The total flow (carrier gas and reactants) was adjusted to maintain a constant flow velocity in the reaction zone, above the growth surface. The growth temperatures were adjusted for each reactor pressure to obtain optimum crystallinity. The growth temperature increases linearly with reactor pressure from 750 °C to 865 °C [12]. The InN deposition process consists of the following steps (see Fig. 6.1 (a)): First, the substrate was heated to the growth temperature and exposed to a constant ammonia flow of 1200 sccm for 5 minutes. Afterwards, an InN nucleation layer was deposited with a group-V/III ratio of 2400 for 1 minute. This nucleation layer was annealed with a group-V/III flow ratio of 12000 for 1 min, which was immediately followed by the steady-state growth of the bulk InN epilayer grown with a group-V/III ratio of 2400. All these steps were done at the same temperature. The growth time for each samples was 90 minutes. In order to prevent the gas phase reactions in the reactor, TMI and NH_3 are injected into the carrier gas (N_2) alternately by pulsed injection. Figure 6.2 illustrates the pulsing sequence used for injection of precursors into the reactor. The pulse durations for TMI and NH_3 were 800 and 2000 ms, respectively. The s_1, pulse separation between TMI and NH_3 (s_2) was 1650 ms, while the pulse separation between NH_3 was 350 ms.

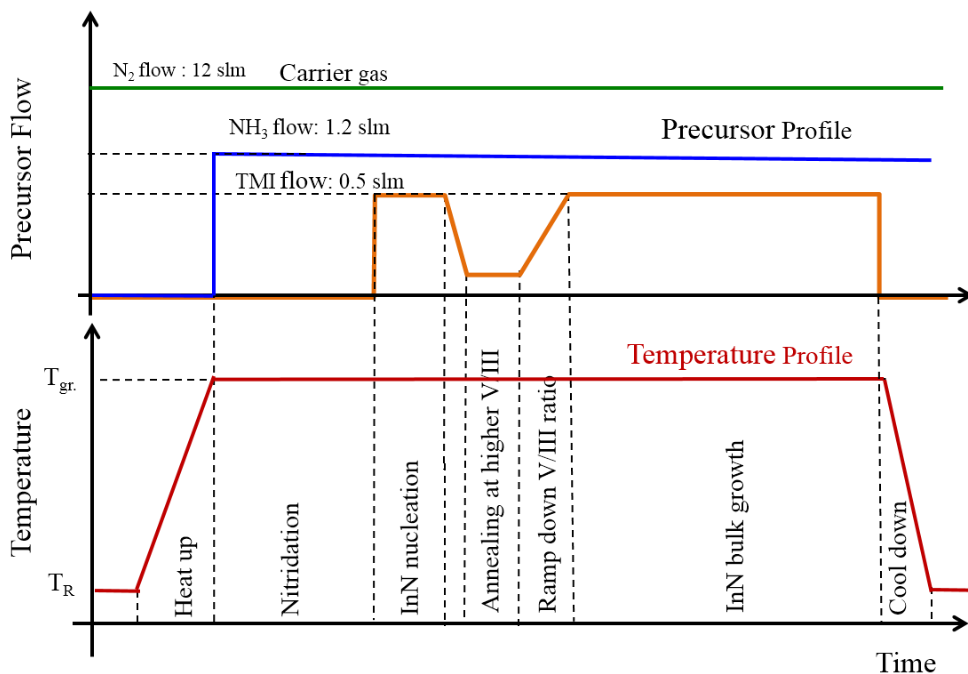

Figure 6.1 Schematic illustration of the temperature precursor profiles for the growth process.

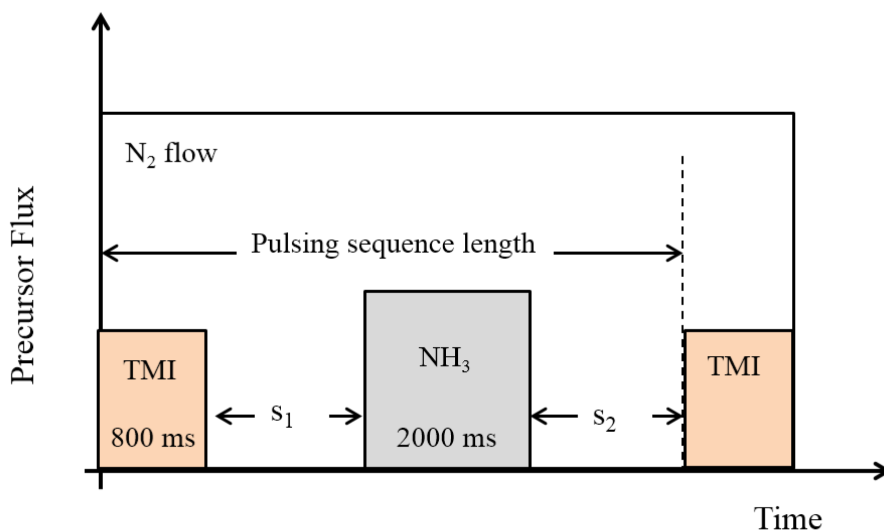

Figure 6.2 Schematic illustration for precursor pulse timing.

The grown InN epilayers were characterized by FTIR reflection measurements, Raman, and XRD measurements. The IR reflection measurements on the samples were performed in near normal incidence (~8°) configuration at room temperature using a Perkin-Elmer FTIR spectrophotometer, in the spectral

range of 450-7000 cm^{-1} with the MCT (HgCdTe) detector and KBr beam splitter. The structural properties of the InN epilayers have been analyzed by X'pert Pro MRD PANalytical high-resolution X-ray diffraction spectrometer performing both on-axis as well as off-axis and by a custom built Raman spectrometer (see Section 3.4.4) utilizing a McPherson McTripleLE spectrometer system equipped with a 40x-times microscope lens. The Raman spectra were taken at room temperature in un-polarized back scattering geometry along the (0001) crystalline plane with excitation energy of 2.33 eV (532 nm).

6.3 Results and Discussion

The FWHM values of the InN (0002) XRD (2θ-ω scan) Bragg reflex as a function of the reactor pressure are depicted in the Fig. 6.3. With increasing reactor pressure the FWHM values decrease but show a wide statistical variance. In order to extensively study the crystalline quality of the samples, the off-axis measurements were also performed using XRD 2θ-ω scans. The correlation between the FWHM values of off-axis InN (2-102) with the reactor pressure is depicted in Fig. 6.4. A similar trend as for the on-axis scan is observed indicating an improved in plane structural quality. The Raman analysis of FWHM values for the Raman E_2 (high) mode of the InN epilayers grown on GaN templates are exhibited in Fig. 6.5 as a function of reactor pressure. The Raman E_2(high) mode position and FWHM values are microscopic measurements for the local strain and for the local crystalline structure and ordering perfection respectively, while the position and the FWHM values of the InN (0002) XRD (2θ-ω scan) reflects the long range ordering and crystalline perfection in the InN epilayers. As shown in the Fig. 6.3, a sudden improvement of the FWHM value of the InN (0002) XRD (2θ-ω scan) is observed for the sample grown at 10 bar, a phenomenon not understood at present and not consistent with the sample grown at 12.5 bar.

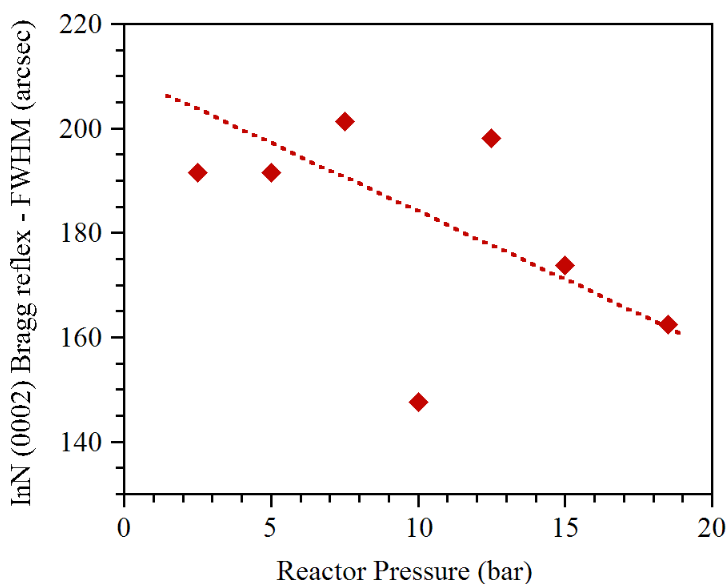

Figure 6.3 XRD FWHM (2θ –ω) scan in triple crystal geometry) of InN peak ((0002) Bragg reflex at about 31.33°) as function of the reactor pressure.

However, the overall tendency shows a systematic improvement of FWHM values with increasing reactor pressure and with this a better long range crystalline ordering in the InN epilayers. Tuna et al. [4] reported a similar behavior for InN epilayers grown on GaN/Sapphire templates by low-pressure MOCVD, in the pressure range of 200 mbar to 800 mbar. The InN sample grown at 18.5 bar with a group V/III precursor ratio of 2500 shows a good long range crystalline ordering with a XRD (2θ–ω scan) FWHM value of 162.5 arcsec. Since the InN epilayers were grown on GaN/Sapphire templates of different origins, we observe a large statistical variation in the crystalline quality of the InN epilayers, as depicted in Fig. 6.4. Nevertheless, the overall FWHM values for the off-axis Bragg reflexes decrease with the increase of reactor pressure, a similar trend as shown in on axis crystalline order (Fig.6.3). The InN epilayer grown at 5 bar shows the best crystalline quality, which is attributed to the high crystalline template quality with controlled Ga-polar surface [13], indicating a further potential to improve the quality through the use of better templates and through an improved nucleation procedure. The Raman results indicate a local optimum of the short-range crystalline ordering around 10 bar with an E_2 (high) FWHM value of 10.3 cm^{-1}.

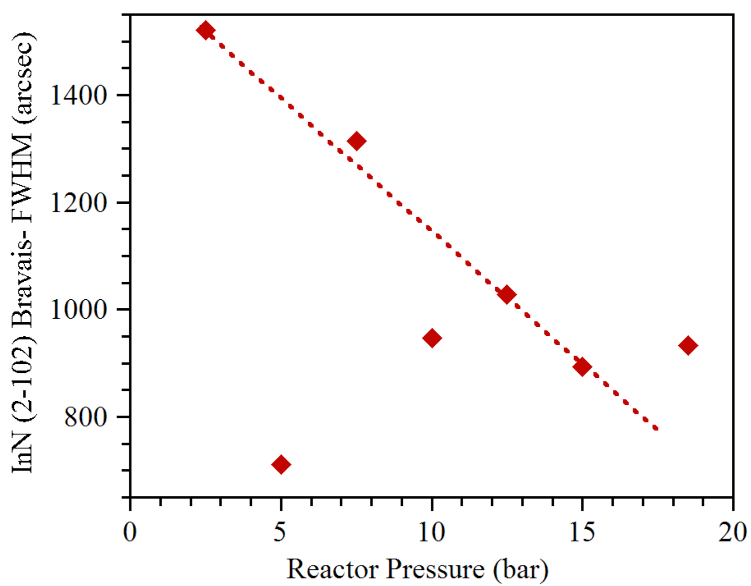

Figure 6.4 XRD FWHM (2θ-ω scan in triple crystal geometry) values of off-axis InN (2-102) of the InN epilayers as a function of reactor pressure.

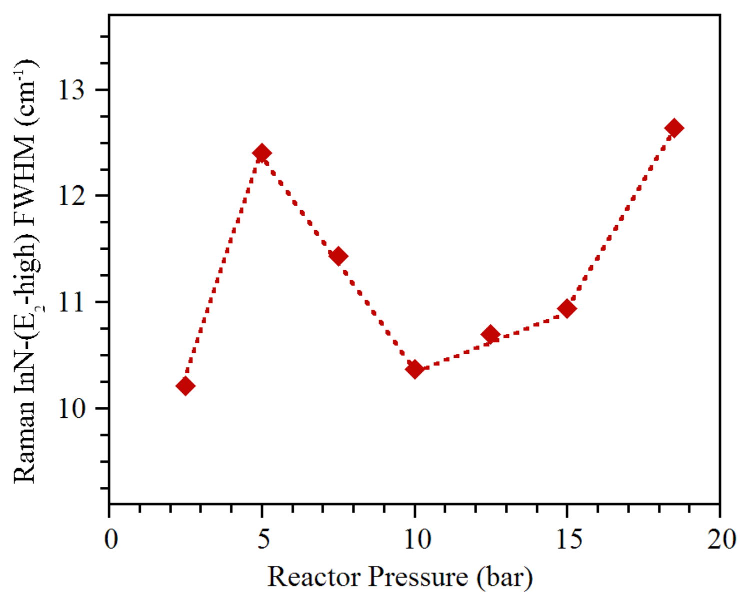

Figure 6.5 The FWHM of the Raman E_2 (high) of the InN epilayers grown on GaN templates vs. reactor pressure.

For higher reactor pressures, a slight degradation in the near-range crystalline ordering is observed, a phenomenon that might be related to higher point defect densities. To understand the discrepancies between near- and long-range crystalline ordering, further experiments in an extended process parameter field are needed.

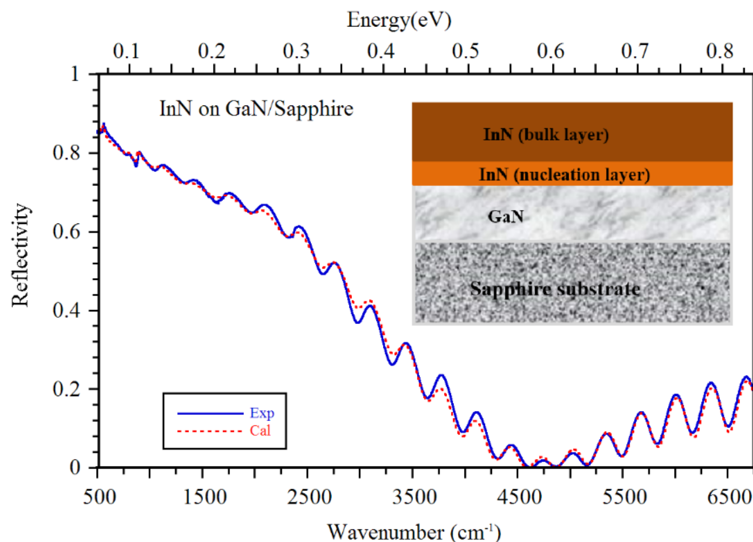

Figure 6.6 Experimental (solid line) and best fit (dotted line) IR reflectance spectra for an InN /GaN/ Sapphire film grown at 800°C and 10 bar reactor pressure.
Inset illustrates the layer structures were used for best fit.

In order to correlate and understand the relationships between the structural epilayer quality and the electrical properties as function of reactor pressure, infrared reflectance spectroscopy is utilized to analyze the InN samples. A typical FTIR reflectance spectrum for an InN-epilayer grown on a GaN/Sapphire template is shown in Fig. 6.6. The solid line depicts the experimental reflectance spectrum and the dotted line (color online) depicts the simulated IR reflectance spectrum for a multilayer stack, consisting of a Sapphire/GaN/InN layered structure as depicted in the inset of Fig. 6.6. The Multilayer stack model and Model of IR dielectric function for isotropic media as explained in Section 4.3, 4.5 and 4.6 allowed the determination of the high-frequency dielectric function (ε_∞), layer thickness, as well as the free carrier concentration and mobility of the free carriers for each layer in the stack by simulating the properties for each layer and fitting it to the experimental IR-reflectance spectrum. The dielectric function of the InN

and GaN layers can be modeled in the infrared region by the lattice vibrations contribution, the free carrier contribution, and the high frequency dielectric constant ε_∞ as follows.

$$\varepsilon(\omega) = \varepsilon_\infty \cdot \left(1 + \frac{\omega_{LO}^2 - \omega_{TO}^2}{\omega_{TO}^2 - \omega^2 - i\omega\gamma} - \frac{\omega_p^2}{\omega^2 + i\omega\gamma_p} \right) \quad 6.1$$

where, ε_∞ is the high frequency dielectric constant, ω_{TO}, ω_{LO}, and γ are the TO, LO phonon frequencies and broadening parameter of the phonons, respectively. ω_p and γ_p are the plasma frequency and the damping constant of plasma respectively. The theoretical IR reflection spectrum is calculated using Eq. 6.1 and the Multilayer stack model. A nonlinear fitting algorithm, utilizing a Levenberg-Marquardt approach [14], was used to obtain the best fit parameters for each layer. To improve the reliability of the parameter set for each layer, FTIR reflection spectra were taken for the Sapphire and GaN/Sapphire templates to first establish the GaN and the sapphire parameter sets. For the simulation of the grown InN epilayers, the established GaN/Sapphire template parameters were kept constant.

The simulation results show that a single InN layer on top of the GaN/Sapphire-template structure did not converge sufficiently well, thus a second InN layer was added to improve the simulation model. This additional InN layer is assumed to capture the different properties of InN in the interfacial region at the GaN/InN interface and is related to the nucleation conditions. The inset of Fig. 6.6 shows the multilayer stack for the samples considered in the analysis. The plasma frequency and damping constant was extracted from the simulation for each layer, the free carrier concentration and the mobility of the free carriers were calculated using Eq. 6.2 and Eq. 6.3.

$$N_c = \frac{{\omega_p}^2 m_{eff} \varepsilon_\infty \varepsilon_0}{q^2} \quad 6.2$$

$$\mu_c = \frac{e}{m_{eff} \gamma_p} \quad 6.3$$

where, N_c is the free carrier concentration, e is the electron charge, m_{eff} is the effective mass of the carriers, and μ is the free carrier mobility. The established best fit data for InN layer thickness, dielectric function, and electrical parameter for all samples grown between 2.5 and 18.5 bar reactor pressure are summarized in Table 6.1. Table 6.1 contains two rows for each sample with the established fit parameter for the 1st - bulk (top row) and the 2nd - nucleation (bottom row) simulated two-layered stack as schematically illustrated in the inset of Fig. 6.6.

Figure 6.7 and 6.8 show the computed free carrier concentrations for the InN bulk and nucleation layer as a function of reactor pressure, respectively. The free carrier concentration of the bulk layers vary from 1.5×10^{18} cm^{-3} to 7.8×10^{19} cm^{-3} and in the nucleation layers the free carrier concentration range from 6.6×10^{19} cm^{-3} to 1.5×10^{20} cm^{-3}. The lowest free carrier concentration of 1.5×10^{18} cm^{-3} was obtained for the InN bulk layer grown at 12.5 bar. These values for the bulk free carrier concentration is still higher compared to recent reported bulk free carrier concentrations of 5.6×10^{17} cm^{-3} in InN epilayers grown on GaN by plasma assisted molecular beam epitaxy (PA-MBE) [15]. Figure 6.8 depicts the variation of free carrier concentration in the nucleation layer as a function of the reactor pressure, indicating a slight reduction of free carrier concentration with the increasing reactor pressure. This result suggests that the reactor pressure does not significantly alter the nucleation process - and with it the free carrier concentration in the nucleation layer. Other process parameter such as the integration of a strain relaxation layer and/or optimized nuclei coalesce process have to be investigated to improve the properties of the nucleation layer.

A further possible source for the high free carrier concentration may be the presence of impurities such as hydrogen and carbon [16], which may be incorporated through an insufficient decomposition of the precursor sources. Yamamoto et al. [17] showed that the free carrier concentration of the bulk InN layer grown on sapphire by MBE decreases with increasing the growth temperature at two different reactor pressures, 0.1 bar and 1 bar.

Table 6.1 InN layer parameters obtained from the best fits of FTIR reflectance spectra for InN epilayers grown are various reactor pressures.
The free carrier concentration and mobilty were derived from the plasma frequency and the its damping constant, respectively. The effective mass for InN and GaN were taken constant as 0.09 m_0 and 0.2 m_0, respectively. The two rows for each sample contain the parameter for the modeled two-layered InN stack, representing the bulk (top raw) and the nucleation (bottom raw) layer of the deposited InN.

Sample	Pressure (bar)	Thickness d (nm)	ε_∞	Plasma freq. (cm^{-1})	Damping const. (cm^{-1})	Mobility ($cm^2V^{-1}s^{-1}$)	Free carri. conc. (cm^{-3})
a	2.5	452.1	5.61	3720.4	1180.2	87.9	7.78×10^{19}
		195.5	6.03	4808.5	224.1	460	1.39×10^{20}
b	5.0	72.9	5.95	1801.3	1093.3	95	1.94×10^{19}
		193.8	7.44	4452.9	1210.4	85.7	1.44×10^{20}
c	7.5	34.1	5.84	1048	1033.7	110	0.44×10^{18}
		325.7	6.59	3710.6	1046.8	99.1	9.11×10^{19}
d	10.0	33.1	6.63	1316.9	881.1	120	1.15×10^{19}
		275.8	6.57	3970	742.2	140	1.04×10^{20}
e	12.5	62.2	6.08	492.4	378.5	270	1.49×10^{19}
		189.3	6.54	4286.8	686.2	150	1.21×10^{20}
f	15.0	10	7.69	983.9	872.7	120	7.47×10^{18}
		307.4	5.29	3543.8	592.5	180	6.62×10^{19}
g	18.5	21.2	7.19	1608.3	1518	68.4	1.87×10^{19}
		248.5	6.15	3522.2	485.1	210	7.66×10^{19}

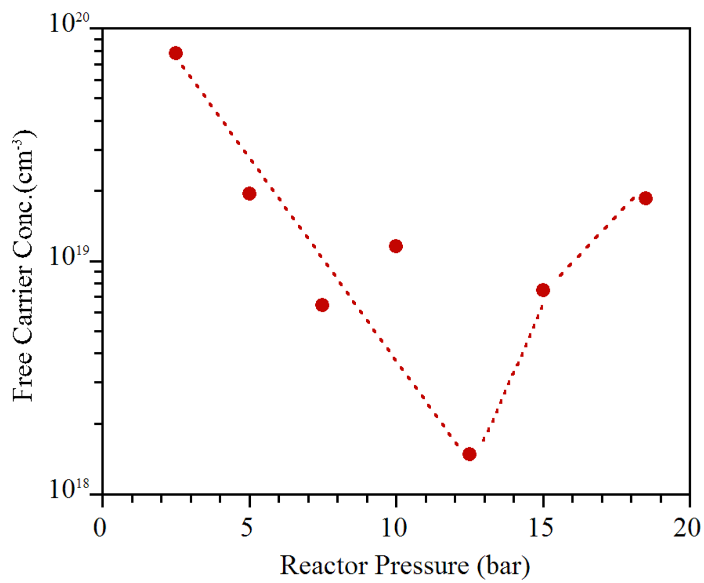

Figure 6.7 Dependence of free carrier concentration of InN- bulk layer on the reactor pressure.

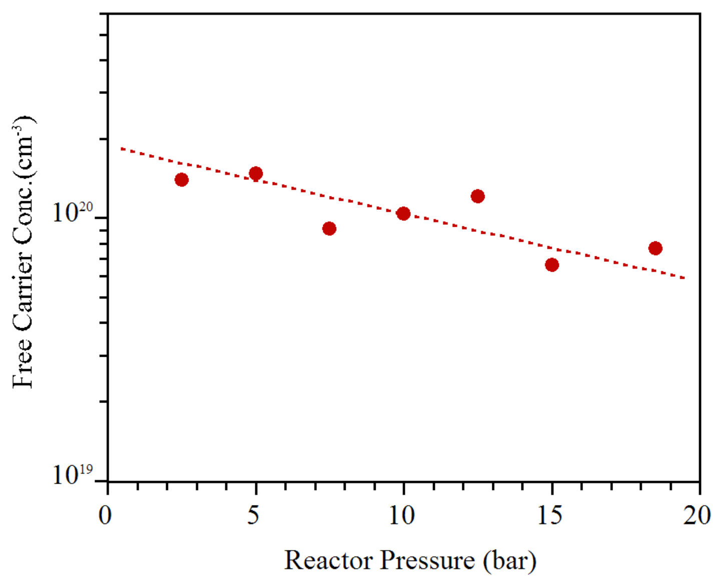

Figure 6.8 Dependence of free carrier concentration of InN- nucleation layer on the reactor pressure.

Yamamoto et al. [17] also showed that InN layers grown at atmospheric pressure had a lower free carrier concentration compared to InN layers grown at lower, sub-atmospheric pressures. This indicates that increasing the reactor pressure can decrease the free carrier concentration. The results from the investigated set of InN samples indicate that for reactor pressures above 12.5 bar, the free carrier concentration increases with increasing reactor pressure, even though the crystalline quality of the epilayers improves with reactor pressure as depicted in Fig. 6.3. However, the trend in the free carrier concentration behavior correlates with the Raman E_2 (high) FWHM values, indicating a possible link of point defect density with bulk free carrier concentration. Since the higher reactor pressure enables higher growth temperatures, the effective V/III precursor ratio changes due to the higher cracking efficiency of the ammonia precursor. In this series, the group V/III precursor ratio was kept constant and has not been adjusted for the change in growth temperature with reactor pressure, which may explain the increase in the bulk free carrier concentration in the samples grown at pressures above 12 bar.

The mobility values for the InN bulk layer as a function of reactor pressure is depicted in the Fig. 6.9. These values were calculated using the Eq. 6.3 with the effective mass taken constant as 0.09 m_0. The mobility shows a maximum for the InN bulk layer grown with a reactor pressure of 12.5 bar, and the highest mobility of the bulk layer is found to be 270 $cm^2V^{-1}s^{-1}$. It was also observed and inverse correlation between the mobility and the free carrier concentration, as the bulk free carrier concentration shows a minimum at this pressure. The similar correlation between the mobility and the free carrier concentration has been reported by Yamamoto et al. [17]. In addition, Lin et al. [18] reported that the InN sample grown on GaN/Sapphire template by MOCVD at 675 °C has the highest mobility (1300 $cm^2V^{-1}s^{-1}$) and lowest free carrier concentration (4.6×10^{18} cm^{-3}) with the increase of growth temperature.

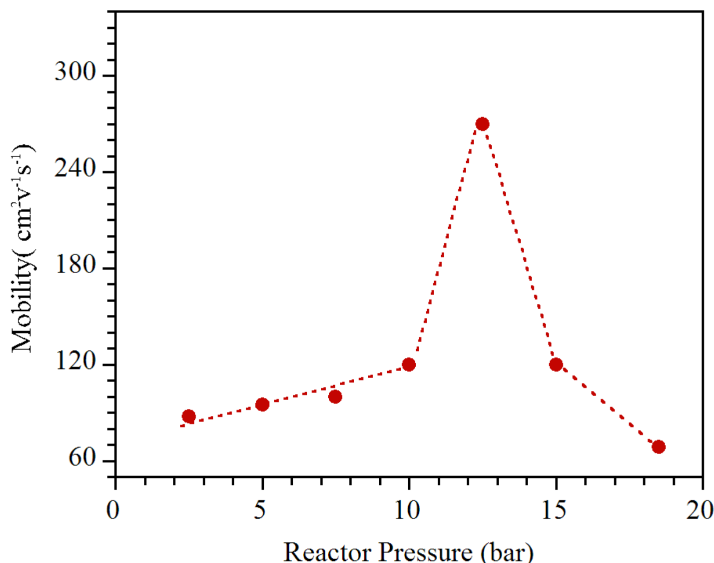

Figure 6.9 Mobility of the carriers of the InN bulk layer as function of reactor pressure.

These findings could indicate structural defects and non-intentional co-doping as sources for the high free carrier concentration, since they generate more carriers which act as scattering centers in the crystal reducing the carrier mobility. Therefore, we conclude that the free carrier mobility and free carrier concentration of the bulk InN layer can be further improved by adjusting the V/III precursor ratio and improving the nucleation of the InN by introducing an AlN buffer. This assumption is supported by Khan et al. [19] who reported a decrease in free carrier concentration and increased mobility for InN layer grown on AlN/Sapphire template with increasing V/III precursor ratio.

The InN layer thicknesses obtained from the reflectance spectra analysis were used to compute the growth rate as function of the reactor pressure. As depicted in Fig. 6.10, the growth rate decreases linearly with increasing reactor pressure as observed in the previous study [12]. Since the diffusion layer thickness decreases inversely proportional to the square root of the pressure, a similar behavior would be expected for the growth rate in the transport limited growth regime. The InN layer grown at 2.5 bar has a large processing error, since in our present reactor the flow channel height is fixed at 1 mm and cannot be adjusted for the variation in the diffusion layer thickness as function of the reactor pressure.

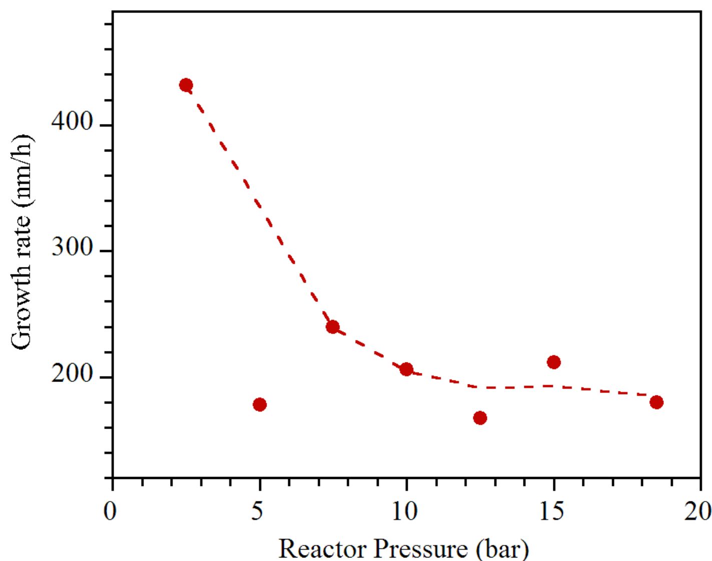

Figure 6.10 Growth rate as a function of reactor pressure.

6.4 Conclusion

The reactor pressure dependent structural and electronic properties of InN epilayers have been studied. The XRD results show that the structural quality of the InN epilayers improves with increasing reactor pressure. This tendency was confirmed by the Raman results, which showed that the near-field crystallinity improves as reactor pressure increase up to 12.5 bar. Above 12.5 bar the near-filed ordering decreases, which is likely due to the higher ammonia cracking efficiency requiring adjustment of the group V/III ratio. The lowest free carrier concentration and highest mobility were found for InN grown at 12.5 bar, with values of 1.5×10^{18} cm^{-3} and 270 $cm^2V^{-1}s^1$, respectively. Further investigation are in progress in order to study the influence of the group V/III precursor ratio at higher reactor pressure and to investigate the influence of nitrogen and indium precursor fragments at the growth surface on the electrical and structural properties of the InN epilayers.

6.5 References

[1] A. G. Bhuiyan, A. Hashimoto and A. Yamamoto, Journal of Applied Physics **94** (5), 2779-2808 (2003).

[2] D. Alexandrov, K. Scott A. Butcher and T. L. Tansley, Journal of Crystal Growth **288** (2), 261-267 (2006).

[3] D. D. Koleske, A. E. Wickenden, R. L. Henry, J. C. Culbertson and M. E. Twigg, Journal of Crystal Growth **223** (4), 466-483 (2001).

[4] Ö. Tuna, H. Behmenburg, C. Giesen, H. Kalisch, R. H. Jansen, G. P. Yablonskii and M. Heuken, physica status solidi (c) **8** (7-8), 2044-2046 (2011).

[5] J. B. MacChesney, P. M. Bridenbaugh and P. B. O'Connor, Materials Research Bulletin **5** (9), 783-791 (1970).

[6] G. B. Stringfellow, Journal of Crystal Growth **312** (6), 735-749 (2010).

[7] H. Lu, W. J. Schaff, J. Hwang, H. Wu, W. Yeo, A. Pharkya and L. F. Eastman, Applied Physics Letters **77** (16), 2548-2550 (2000).

[8] N. Dietz, in *III-Nitride Semiconductor Materials*, edited by Z. C. Feng (Imperial College Press, London, 2006), pp. 203-235.

[9] N. Dietz, H. Born, M. Strassburg and V. Woods, MRS Proceedings **798** (2011).

[10] M. Buegler, M. Alevli, R. Atalay, G. Durkaya, I. Senevirathna, M. Jamil, I. Ferguson and N. Dietz,**7422** (2009).

[11] V. Woods, H. Born, M. Strassburg and N. Dietz, Journal of Vacuum Science & Technology A **22** (4), 1596-1599 (2004).

[12] M. Buegler, S. Gamage, R. Atalay, J. Wang, M. K. I. Senevirathna, R. Kirste, T. Xu, M. Jamil, I. Ferguson, J. Tweedie, R. Collazo, A. Hoffmann, Z. Sitar and N. Dietz, physica status solidi (c) **8** (7-8), 2059-2062 (2011).

[13] N. Dietz, M. Alevli, R. Atalay, G. Durkaya, R. Collazo, J. Tweedie, S. Mita and Z. Sitar, Applied Physics Letters **92** (4), 041911 (2008).

[14] W. H. Press, S. A. Teukolsky, W. T. Vetterling and B. P. Flannerry, *The Art of Scientific Computing*. (Cambridge University Press, Cambrigde, MA, 1992).

[15] I. Gherasoiu, M. O'Steen, T. Bird, D. Gotthold, A. Chandolu, D. Y. Song, S. X. Xu, M. Holtz, S. A. Nikishin and W. J. Schaff, Journal of Vacuum Science & Technology A **26** (3), 399-405 (2008).

[16] V. Darakchieva, K. Lorenz, N. P. Barradas, E. Alves, B. Monemar, M. Schubert, N. Franco, C. L. Hsiao, L. C. Chen, W. J. Schaff, L. W. Tu, T. Yamaguchi and Y. Nanishi, Applied Physics Letters **96** (8), 081907 (2010).

[17] A. Yamamoto, Y. Murakami, K. Koide, M. Adachi and A. Hashimoto, physica status solidi (b) **228** (1), 5-8 (2001).

[18] J. C. Lin, Y. K. Su, S. J. Chang, W. H. Lan, W. R. Chen, Y. C. Cheng, W. J. Lin, Y. C. Tzeng, H. Y. Shin and C. M. Chang, Optical Materials **30** (4), 517-520 (2007).

[19] N. Khan, A. Sedhain, J. Li, J. Y. Lin and H. X. Jiang, Applied Physics Letters **92** (17), 172101 (2008).

7 CHAPTER 7: INITIAL GROWTH AND CHARACTERIZATION RESULTS OF InN-AlN-SAPPHIRE GROWN BY MIGRATION-ENHANCED PLASMA ASSISTED MOCVD

7.1 Introduction

Due to the narrow direct band gap of Indium nitride (InN), its small effective mass, high electron mobility and high drift velocity, indium-rich group III-nitride alloys are of high interest for photovoltaic-, electronic-, and optoelectronic device applications [1-4]. Furthermore, InN containing heterostructures might be utilized the performance of electronic devices such as sensors and terahertz emitters [5, 6]. However, the growth of high quality InN is a challenge, due to the high partial pressure of nitrogen at optimum growth temperatures above the growth surface. Ammonia, the main nitrogen source used in the traditional CVD/MOCVD growth of InN, decomposes at a temperature above 900 °C, which is greater than the decomposition temperature of InN. Additionally, the growth of multinary indium-rich group III-nitrides, is further challenged due to the differences in the partial pressures of the group III-N binaries, requiring the adjustment of the growth processing parameters for each target composition. In order to reduce the growth temperature gaps between the binaries and to control the growth surface chemistry, several advanced growth techniques are presently explored. For example, super-atmospheric pressure chemical vapor deposition (denoted as HPCVD) [7-10], atomic layer deposition (ALD), plasma-assisted ALD [11], and migration-enhanced, plasma-assisted metalorganic chemical vapor deposition (MEPA-MOCVD) [12-16], are explored to assess the control of the vastly different partial pressures and surface chemistries by thermodynamic and/or kinetic means. However, at present, the layers grown by the various growth methods exhibit variations in their measured physical properties (e.g. free carrier concentrations, optical band gap, structural quality, etc.), leading to widely speculative assumptions on the fundamental properties of InN and indium-rich alloys. In this contribution, we evaluate the layer properties of group III-N alloys grown by MEPA-MOCVD using plasma activated nitrogen species/ fragments as nitrogen precursors that are directed to the growth surface in the afterglow regime. The MEPA-MOCVD reactor system is equipped with a load lock system, metalorganic precursors (MO's) showerhead injection system, and a

MEAglow oxygen-free hollow cathode N_2 plasma source to generate energy-controlled active nitrogen species and the afterglow regime above the growth surface. The reactor pressure can be operated in the range of 1 mbar -10 mbar. The MO and plasma-activated nitrogen precursor species can be supplied temporal and spatially separated, which allows controlling the surface diffusion processes of adatoms at the growth surface. The plasma-activated nitrogen species are formed at much lower temperatures compared to conventionally used ammonia as the nitrogen precursor. At present, the vast growth parameter space in MEPA-MOCVD is hardly explored. In this study, we focus only on the crystalline quality of the InN epilayer grown on various AlN interlayers deposited at growth temperatures between 550 and 780 °C. As widely reported in the literature [17, 18], the AlN interlayer between sapphire (c-Al_2O_3) and a group III-nitride epilayer plays a critical role in the transition from a metal-oxygen surface chemistry to a metal-nitrogen chemistry, reducing dislocation and defect densities in the subsequent group III-N overgrowth process. However, lattice mismatch induced strain has to be still dealt with in the InN/AlN overgrowth process.

7.2 Experimental

Group III-N heterostructures were deposited on sapphire (0001) substrate using a customized MEPA-MOCVD reactor, which details are provided elsewhere [12, 15, 19]. A MEAglow plasma source is used to provide controlled nitrogen fragments in an afterglow regime towards the growth surface. As schematically illustrated in Fig. 2.10, a spatial and temporal controlled injection of MO's and plasma-activated nitrogen precursor injection scheme is used in this study. The deposition of InN and AlN epilayers were examined by varying, growth temperature, plasma power, and plasma exposure time. In order to study the influence of the AlN interlayer between the sapphire and the subsequent InN layer, the growth conditions for the InN layer were taken from a previous study [19] and kept constant with a reactor pressure of 3.3 Torr, a growth temperature of 775 °C, a pulsed plasma power of 400 W (14 s), followed by a TMI (Trimethylindium) pulse of 1 sec (9.6 µmol/min). The deposition conditions for the AlN buffer layers were varied as described in the result section.

The InN layers grown on top of the AlN buffer layers were characterized by AFM, FTIR reflection- and Raman spectroscopy. In order to analyze the local crystalline order, the Raman spectra of the samples were taken at room temperature in z (xx)-z back scattering geometry with excitation energy of 2.33 eV. Here, a customized Raman set up was utilized, based on a single 2m-monochromator and a liquid N_2-cooled multichannel CCD (Charge-Couple Detector). The surface morphology of the layers was analyzed by AFM.

The IR reflection measurements were performed at room temperature, at near normal incidence (~8°) configuration using a Perkin-Elmer 2000 FTIR spectrophotometer. A MCT (HgCdTe) detector and KBr beam splitter were used to cover the spectral range of 450 - 6500 cm^{-1}.

7.3 Results and Discussion

Initial growth of AlN buffer layers were carried out at a growth temperature of 775°C, a reactor pressure of 3.3 Torr, and a plasma power of 400 W, followed by a subsequent deposition of an InN epilayer. In the first series, the precursor trimethylaluminum (TMA) and plasma activated nitrogen (PAN) were introduced temporally spaced with a 1 sec TMA injection following a PAN exposure time that was varied from 4 s to 12 s.

The E_2(high) and A_1(LO) phonon modes for the wurtzite structure of the AlN, should be observed around 657 cm^{-1} and 890 cm^{-1} [20]. In our Raman spectra, these two modes were very weak, which might be due to the very low thickness of the AlN layer or the limited AlN crystallinity. Surface morphology studies of the layers were carried out by AFM. Figure 7.1 shows the AFM topography and corresponding island height-vs-position plots for sapphire (a) and the AlN layers grown with 4 s (b), 8 s (c), and 12 s (d) PAN exposure time, respectively. The corresponding surface RMS roughness in a 0.5×0.5 μm^2 area are 0.245 nm, 2.4 nm, 2.16 nm and 1.36 nm, respectively. The RMS surface roughness is calculated using the following equation:

$$R_q = \sqrt{\frac{1}{N}\sum_i^N \left(Z_i - Z_{ave}\right)^2}; \qquad \text{where,} \quad Z_{ave} = \sum_i^N Z_i / N \qquad 7.1$$

Here, Z_i , N, and Z_m are the height at the i th row or column of the surface scan, number of rows and columns of the scanned area, and average height, respectively.

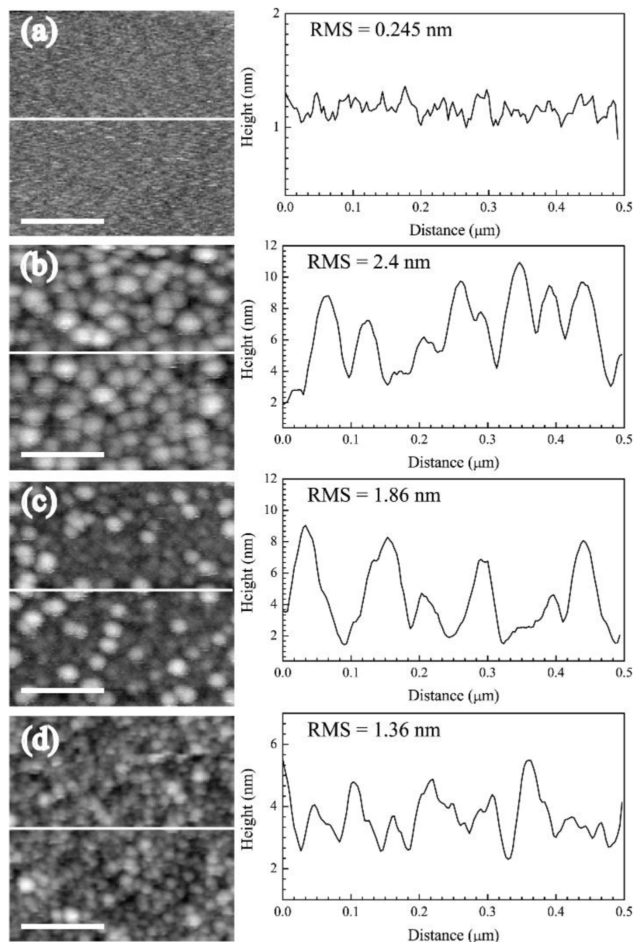

Figure 7.1 2D-AFM surface topography (scale bar = 200 nm) of sapphire (a) and AlN buffer layers grown with 4 s (b), 8 s (c), and 12 s (d) plasma exposure per pulse
On the right are the corresponding AFM height pro-files. The scan area is 0.5×0.5 μm^2.

The results show that a longer plasma pulse exposure time (12 s) leads to a smoother layer surface, with a smaller grain size, and a higher grain density compared to AlN nucleation layers grown at 4 s and 8 s. Increasing the plasma exposure time, increases the growth surface nitridation which can result in higher nuclei density. The efficiency of the nitridation procedure depends on the concentration of active nitrogen species at the growth surface and the amount of active nitrogen generated via the hollow cathode source (e.g. plasma power and N_2 flow).

In order to study the influence of the plasma power on plasma activated nitrogen species on the growth chemistry and the related surface morphology, a set of AlN samples were grown with a 12 s PAN exposure time and a variation of the plasma power from 300 W to 500 W. The AFM topography and corresponding height profiles of the AlN surfaces at 300 W, 400 W, and 500 W are depicted in the Fig. 7.2.

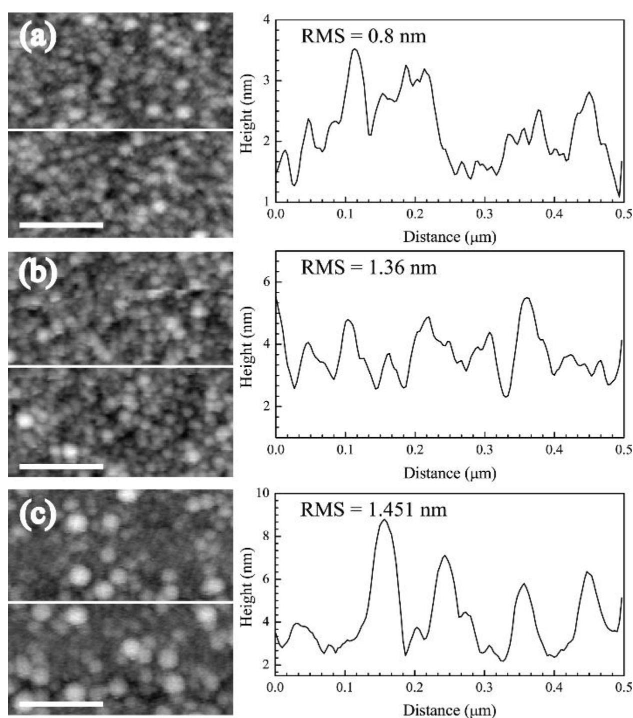

Figure 7.2 2D-AFM surface topography (scale bar = 200 nm) within a 0.5×0.5 μm^2 scan area and corresponding profile of change in the height along distance for AlN-NL grown at (a) 300 W, (b) 400 W, and (c) 500 W plasma power.
The RMS surface roughness values are 0.8 nm, 1.36 nm, and 1.451 nm, respectively.

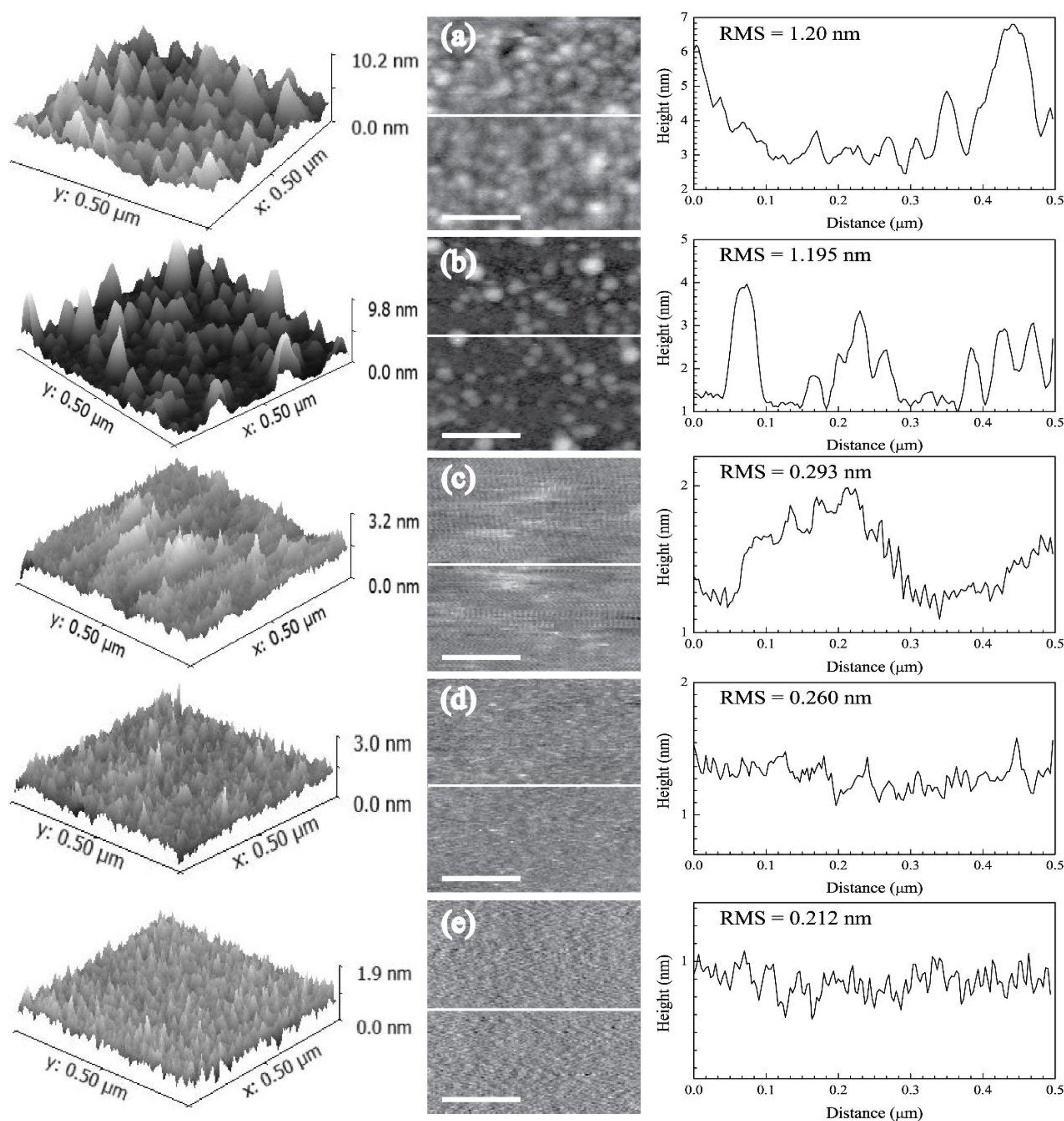

Figure 7.3 2D-AFM surface topography (scale bar = 200 nm) of (a) as- grown AlN-NL and annealing temperature of AlN -NL layers at (b) 800 °C, (c) 825 °C, (d) 850 °C and (e) 875 °C.
On the left and right are the corresponding AFM 3D topography and the height profiles. The scan area is $0.5\times0.5\ \mu m^2$.

The results show that the surface roughness increases with plasma power, which suggests that the energies of the PAN species are too high. An increase of hollow cathode plasma power changes not only the kinetic energies of the activated nitrogen species, but also the type of nitrogen species in the afterglow regime above the growth surface. Consequently, we can expect damage to the growth surface at higher plasma power, which may lead to a higher surface roughness. On the other hand, AFM topography shows

the highest grain size and lowest nuclei density for the sample grown at 500 W plasma power. Since a higher grain size of AlN buffer improves the crystalline quality of a subsequent overgrown GaN layers [21], the 500W plasma power was used in the growth of AlN buffer layer in further studies.

As discussed in the literature [21], the quality of an AlN layer may improve upon thermal annealing. Thus, we annealed the AlN-NLs grown at 775 °C for 60 minutes. The injection of plasma and MO were continuous during the growth. The annealing temperature was varied from 800 °C to 875 °C at 3 Torr N_2 pressure. Figure 7.3 depicts the AFM 2D-3D topography for as-grown AlN layer, and AlN layers annealed at various annealing temperatures with 800 °C, 825 °C 850 °C, 875 °C, respectively. The RMS surface roughness values versus annealing temperature are shown in Fig. 7.4.

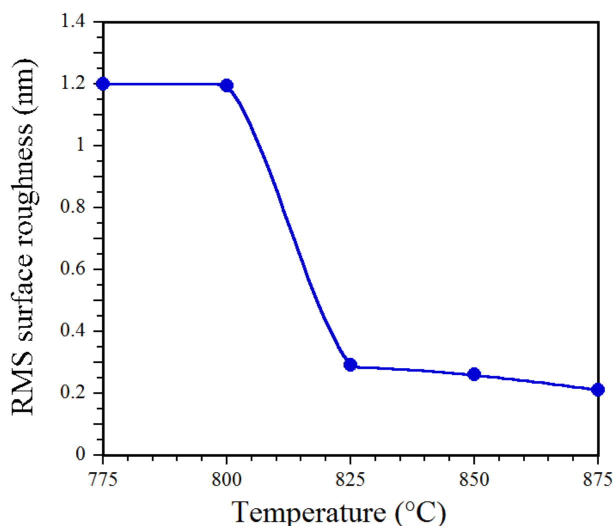

Figure 7.4 RMS surface roughness vs annealing temperature

These results show that the RMS surface roughness of the AlN layers improves with the annealing temperature of the deposited AlN layers. With increasing the annealing temperature, the RMS surface roughness values reduces from 1.2 nm to 0.212 nm indicating an atomically flat surface. To evaluate the influence of the annealed AlN layer on the crystalline quality, the Raman spectra were taken for the post-annealing AlN layers. As shown in Fig. 7.5 with increasing annealing temperature, the Raman A1(LO) phonon mode appears at 890 cm^{-1} for the AlN buffer layer annealed at 850 °C, indicating an improvement of the crystalline quality of the AlN layer.

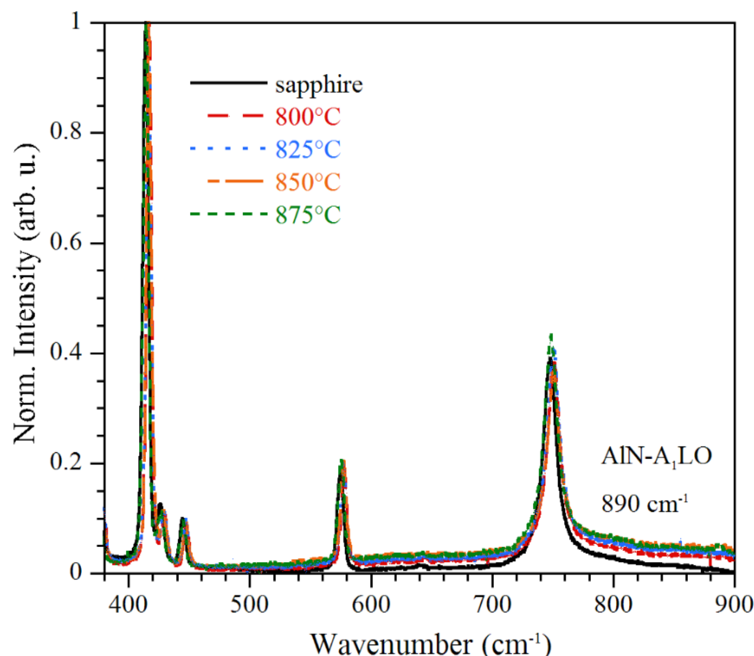

Figure 7.5 Raman spectra for the AlN buffer grown on sapphire by varying post-annealing temperature, (long-dashed)) 800 °C, (dotted) 825 °C, (dashed-long dashed) 850 °C, (dashed) 875 °C, and (solid) sapphire.

In the following step, we investigated the crystalline quality and surface morphology of InN layers as a function of the AlN/sapphire template. First, an InN sample was grown on sapphire. The second InN layer was grown on an AlN template which was not annealed. The third InN layer was grown on AlN layer which was subsequently annealed at 850 °C for 60 minutes. For all InN films, a mirror-like surface was observed. Figures 7.6, 7.7, and 7.8 depict (a) 2D-AFM and (b) 3D-AFM topographies for the various InN layers deposited.

The three samples investigated show that the InN islands density decreases if an AlN buffer is added and the AlN layer is annealed. At the same time, the lateral size of the islands increases. These results indicate that an annealed AlN buffer layer between sapphire and InN layers leads to an improved surface morphology of subsequent InN layer, with a RMS surface roughness value of 2.02 nm for the AlN layer annealed at 850 °C/sapphire.

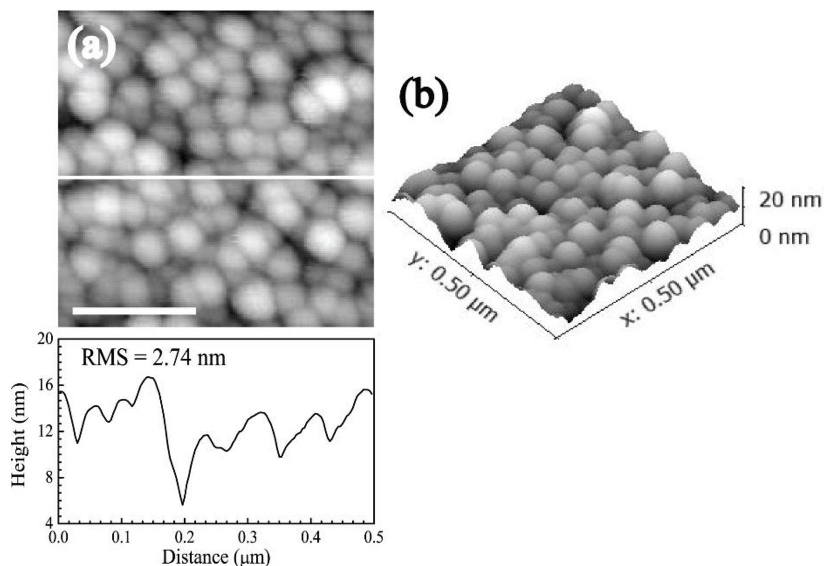

Figure 7.6 (a) 2D-AFM surface image (scale bar = 200 nm) with the corresponding profile of change in the height along position, (b) 3D-AFM surface topography for the InN/sapphire
The scan area is 0.5×0.5 μm^2.

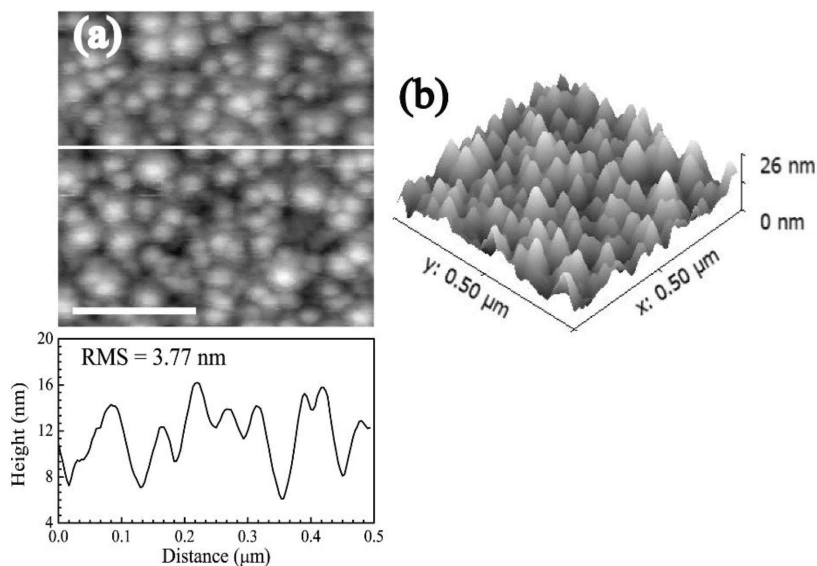

Figure 7.7 2D-AFM surface image (scale bar = 200 nm) with the profile of change in the height along distance, and (b) 3D-AFM surface topography for the InN/AlN/sapphire
The scan area is 0.5×0.5 μm^2.

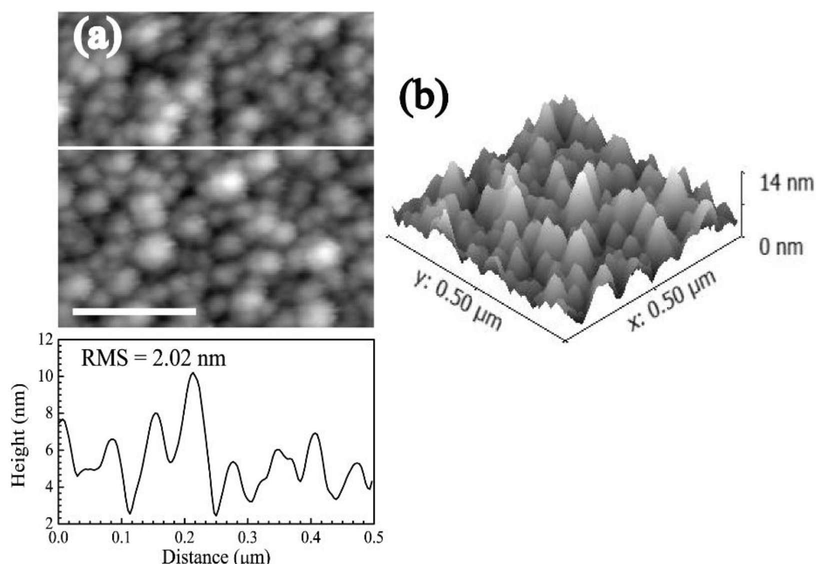

Figure 7.8 (a) 2D-AFM surface image (scale bar = 200 nm) with the profile of change in the height along distance, and (b) 3D-AFM surface topography for the InN/AlN-annealed at 850 °C/sapphire The scan area is 0.5×0.5 µm^2.

For the layers investigated by Raman spectroscopy, the InN epilayer grown directly on sapphire exhibit a pronounced Raman E_2 (high) mode, indicating a good local crystalline ordering of the InN epilayer. As depicted in Fig. 7.9, the Raman spectrum for the InN layer grown on top of AlN buffer layer (dashed line) shows an improved E_2(high) mode, which is further improved if the AlN layer is annealed (dashed line). The E_2 (high) and A_1(LO) phonon modes are observed at ~ 488 cm^{-1} and ~586 cm^{-1} respectively [22]. In addition to these two modes, the sapphire phonon modes at 749 cm^{-1} and 575 cm^{-1} are observed. These modes diminish for thicker InN epilayers. The broadening and strength of the A_1(LO) mode in the layers is attributed to the high free carrier concentration in the films [23], while the broadened E_2(high) mode relates to the local structural disorder (point and extended defects) in the InN layers. The FWHM values of the E_2 (high) mode of the three InN layers are 14.3 cm^{-1}, 12.2 cm^{-1}, and 11.5 cm^{-1}, respectively. We also observe a decrease of the Raman background scattering for the InN layers grown with AlN layers, which is related to structural defects and/or metallic inclusions. Further experiments are needed to improve the local crystallinity of the InN layers.

FTIR reflectance measurements were carried out to extract the free carrier concentration, mobility of the carriers, and high frequency dielectric function of the InN layers. Figure 7.10 summarizes the experimental FTIR reflectance spectra for InN/sapphire (dotted line), InN/AlN/sapphire (solid line), and InN grown on post-annealed (at 850 °C) AlN buffer/sapphire (dashed line).

To extract the layer properties, a multilayer stack model and a fit program are used. The dielectric function in the IR region is approximated using the Lorentz-Drude model [24] and effective high frequency dielectric function ε_∞, accounting for the lattice (phonon) contributions, free carrier contributions, and the contribution due to the inter-band transitions, respectively (see Eq. 7.2).

$$\varepsilon(\omega) = \varepsilon_\infty \cdot \left(1 + \frac{\omega_{LO}^2 - \omega_{TO}^2}{\omega_{TO}^2 - \omega^2 - i \cdot \omega \cdot \gamma_p} - \frac{\omega_p^2}{\omega^2 + i \cdot \omega \cdot \tau} \right) \tag{7.2}$$

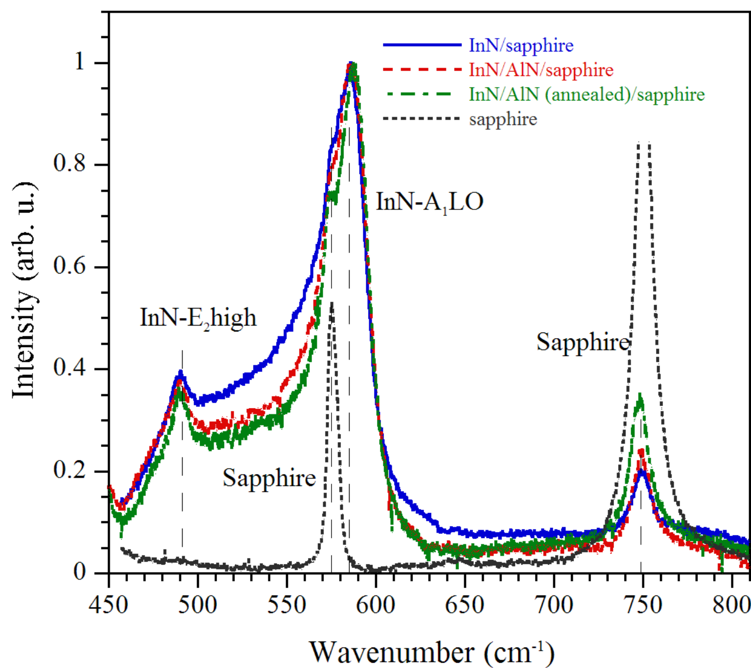

Figure 7.9 The Raman spectra for the InN/sapphire (solid), InN/AlN/sapphire (dashed), and InN grown on AlN annealed at 850°C /sapphire (dotted-dashed), and sapphire (dotted).

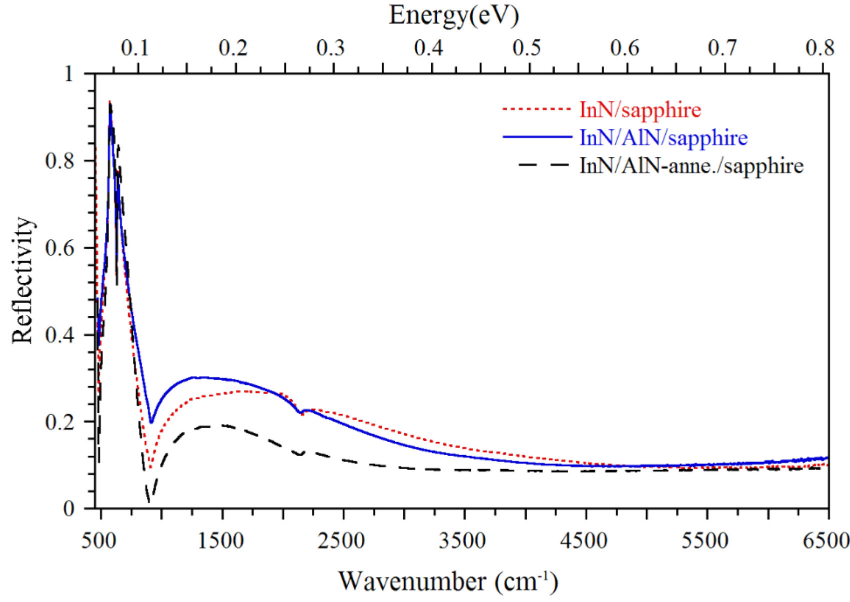

Figure 7.10 The experimental reflectance spectra for InN/sapphire (dotted line), InN/AlN/sapphire (solid line), and InN/AlN annealed at 850 °C/sapphire (dashed line)

Here, ω_{TO}, ω_{LO}, and γ_p are the TO, LO phonon frequencies and broadening parameter of the phonons. ω_p and τ are the plasma frequency and the damping constant of plasma. ε_∞ is the high frequency dielectric constant. The free carrier concentration and mobility of the carriers were calculated by using following Eq. 7.3 and Eq. 7.4.

$$n_c = \frac{{\omega_p}^2 m_{eff} \varepsilon_\infty \varepsilon_0}{q^2} \qquad 7.3$$

$$\mu = \frac{q}{m_{eff} \tau} \qquad 7.4$$

Here, n_c, q, m_{eff}, and μ are the free carrier concentration, the electron charge, the effective mass of the carriers and the free carrier mobility, respectively. Each layer in the multilayer stack is parameterized with layer thickness, effective dielectric function, and interfacial imperfection parameter, which allows establishing a model reflectance spectrum, which is fitted to the experimental spectrum [25]. A nonlinear fitting algorithm was used to determine the best fit parameter for the layers [24].

The experimental and calculated FTIR reflectance spectra for InN/AlN/sapphire are depicted in Fig. 7.11. The inset shows the modeled three-layer stack structure used to determine the parameter of the InN layer. The AlN interlayer was not resolvable in the model configuration. The other two samples were modeled in the manner. The extracted layer thickness, high frequency dielectric constant, free carrier concentration and the mobility of the free carries for each InN layers are summarized in Table 7.1. The free carrier concentration was confirmed by the Hall measurements.

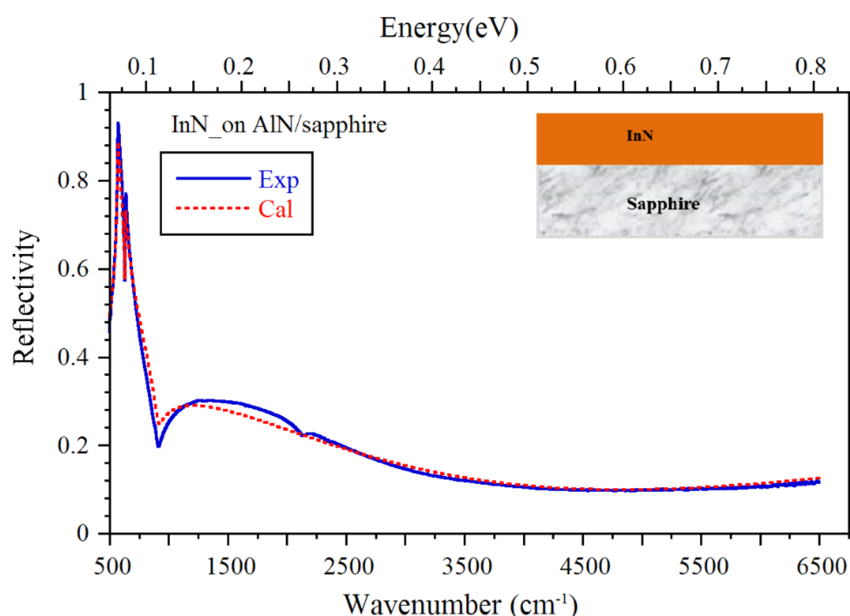

Figure 7.11 Experimental (solid line) and best fit (dashed line) IR reflectance spectra for InN/AlN/sapphire.
Inset shows the layer structure used for best fit.

Table 7.1 The best fit InN layer parameters, thickness (d), high frequency dielectric constant (ε_∞), free carrier concentration, and mobility obtained from the FTIR reflectance simulation.

Sample	Thickness (nm)	ε_∞	Free carrier conc. (cm^{-3})	Mobility ($cm^2V^{-1}s^{-1}$)
InN/sapphire	64	5.78	9.5×10^{19}	57
InN/AlN/sapphire	80	5.96	7.6×10^{19}	72
InN/AlN(annealed)/sapphire	54	5.81	5.6×10^{19}	85

These results show an improvement in free carrier concentration and mobility of the free carriers for InN films grown on AlN buffer and annealed at 850 °C. As discussed in the literature [26-28], the mobility and electron concentration depends on the InN layer thickness and has to be greater than 0.5 µm in order to achieve a mobility above 1000 $cm^2V^{-1}s^{-1}$ and an electron concentration below 10^{18} cm^{-3}. As indicated in Table 7.1, there is no significant influence of high frequency dielectric constant of the layers grown with without AlN buffer layer, which indicates that the optical density of the layers remains. Literature data report large variations for high frequency dielectric constant ε_∞, varying from 10.8 to 5.03 [29, 30], with a ε_∞ value reported as 8.4 for InN wurtzite structure [31-34]. Later studies used this value to calculate the free carrier concentration and mobility of InN layers [35-39]. Bernardini et al. [40, 41] calculated the high frequency constant InN as 8.49 using geometric quantum phase polarization theory and density-functional theory. Inushima et al. [42] obtained a ε_∞ value of 5.8 using Kramers–Konig analysis of reflectivity data for InN layer grown on sapphire by ALE (atomic layer epitaxy). Qian et al. [43] used a value of $\varepsilon_\infty = 5.8$ to obtain the mobility and free carrier concentration of InN layers grown on GaAs and the sapphire substrate using RF magnetron sputtering. Different values of ε_∞ = 5.03, 7.054, 7.27, and 8.1 have been obtained from different theoretical models [30] assuming InN wurtzite structure. Kasic et al. [44] utilized infrared spectroscopic ellipsometry data (IR-SE) data to determine a ε_∞ value of 6.7. Later studies [23, 45-55] of InN based on IR-SE, IR reflectivity data or Raman data used this value to calculate the free carrier concentration, mobility, effective mass, etc.. Ishitani et al. [56] determined a ε_∞ of 8.3 by IR reflectivity data measured at 296 K and 5 K temperature. In 2006, Fukuik et al. [57] obtained ε_∞ as 8.5 from the IR reflectivity data analysis for the InN grown on sapphire by OMVPE. Schley et al. [58] obtained ε_∞ as 7.84 and 7.76 by IR-SE data analysis for the In-face and N-face InN layers, grown by plasma-induced molecular beam epitaxy. In the previous studies [10], we obtained a ε_∞ value of 5.78 for InN grown on GaN/sapphire by HPCVD. This value is closer to the value reported by Inushima et al. [42]. In our other study, [24] we obtained ε_∞ values varying between 5.29 and 7.69 for different InN layers grown at different reactor pressure by HPCVD. Model simulations of IR-SE data by Himmerlich et al. [59] suggest that ε_∞ is strongly influenced by carbon doping concentration and may vary from 7.64 for undoped

InN layer (7.4×10^{17} cm^{-3}) to 7.28 for doped layer (3.5×10^{18} cm^{-3}) grown on GaN/sapphire by MBE. Zang et al. [29] determined ε_∞ for InN grown on sapphire by PR-MOVPE (pressurized-reactor metalorganic vapor phase epitaxy) at different growth temperature. The ε_∞ values obtained from IR reflectance analysis varied from 10.8, 6.0, and 6.3 for 500 °C, 600 °C, and 700 °C, respectively.

All these results indicate the large variation of the high frequency dielectric constant ε_∞ for InN layers grown with various growth techniques. This might be related to extended defects, voids in the bulk material, a shift in the effective band structure, or the calculation methods used to determine the dielectric constant. These uncertainties in ε_∞ makes it difficult to compare the obtained ε_∞ values for our InN layers with reported values. However, the obtained ε_∞ high frequency dielectric constants of InN layers from this study are close the value of 5.8 obtained by Inushima et al. [42].

7.4 Conclusion

We presented first results on the structural and optoelectronic properties of InN layers grown on AlN buffer layer/sapphire (0001) by Migration-Enhance Plasma Assisted Metal Organic Chemical Vapor Deposition (MEPA-MOCVD). The results indicate that an AlN buffer layer annealed at 850 °C, between the InN layer and sapphire improves the structural quality and optoelectronic properties of overgrown InN layers. Further improvements on the AlN buffer layer quality and InN growth processing parameters are needed to further improve the structural quality of the InN epilayers and their optoelectronic properties.

7.5 References

[1] T. Matsuoka, H. Okamoto, M. Nakao, H. Harima and E. Kurimoto, Applied Physics Letters **81** (7), 1246-1248 (2002).

[2] J. Wu, W. Walukiewicz, K. M. Yu, J. W. A. III, E. E. Haller, H. Lu, W. J. Schaff, Y. Saito and Y. Nanishi, Applied Physics Letters **80** (21), 3967-3969 (2002).

[3] A. G. Bhuiyan, A. Hashimoto and A. Yamamoto, Journal of Applied Physics **94** (5), 2779-2808 (2003).

[4] J. Wu, W. Walukiewicz, K. M. Yu, W. Shan, J. W. A. III, E. E. Haller, H. Lu, W. J. Schaff, W. K. Metzger and S. Kurtz, Journal of Applied Physics **94** (10), 6477-6482 (2003).

[5] H. Lu, W. J. Schaff and L. F. Eastman, Journal of Applied Physics **96** (6), 3577-3579 (2004).

[6] E. Starikov, P. Shiktorov, V. Gružinskis, L. Reggiani, L. Varani, J. C. Vaissière and J. H. Zhao, Physica B: Condensed Matter **314** (1–4), 171-175 (2002).

[7] V. Woods, H. Born, M. Strassburg and N. Dietz, Journal of Vacuum Science & Technology A **22** (4), 1596-1599 (2004).

[8] N. Dietz, M. Alevli, V. Woods, M. Strassburg, H. Kang and I. T. Ferguson, physica status solidi (b) **242** (15), 2985-2994 (2005).

[9] V. Woods and N. Dietz, Materials Science and Engineering: B **127** (2–3), 239-250 (2006).

[10] M. Buegler, S. Gamage, R. Atalay, J. Wang, M. K. I. Senevirathna, R. Kirste, T. Xu, M. Jamil, I. Ferguson, J. Tweedie, R. Collazo, A. Hoffmann, Z. Sitar and N. Dietz, physica status solidi (c) **8** (7-8), 2059-2062 (2011).

[11] A. Haider, S. Kizir, C. Ozgit-Akgun, E. Goldenberg, S. A. Leghari, A. K. Okyay and N. Biyikli, Journal of Materials Chemistry C **3** (37), 9620-9630 (2015).

[12] K. S. A. Butcher, D. Alexandrov, P. Terziyska, V. Georgiev and D. Georgieva, physica status solidi (c) **9** (3-4), 1070-1073 (2012).

[13] P. W. Binsted, K. S. A. Butcher, D. Alexandrov, P. Terziyska, D. Georgieva, R. Gergova and V. Georgiev, MRS Proceedings **1396** (2012).

[14] K. S. A. Butcher, D. Alexandrov, P. Terziyska, V. Georgiev, D. Georgieva and P. W. Binsted, physica status solidi (a) **209** (1), 41-44 (2012).

[15] K. S. A. Butcher, B. W. Kemp, I. B. Hristov, P. Terziyska, P. W. Binsted and D. Alexandrov, Japanese Journal of Applied Physics **51** (1S), 01AF02 (2012).

[16] G. Togtema, V. Georgiev, D. Georgieva, R. Gergova, K. S. A. Butcher and D. Alexandrov, Solid-State Electronics **103**, 44-48 (2015).

[17] D. G. Zhao, D. S. Jiang, L. L. Wu, L. C. Le, L. Li, P. Chen, Z. S. Liu, J. J. Zhu, H. Wang, S. M. Zhang and H. Yang, Journal of Alloys and Compounds **544**, 94-98 (2012).

[18] H. Lu, W. J. Schaff, J. Hwang, H. Wu, G. Koley and L. F. Eastman, Applied Physics Letters **79** (10), 1489-1491 (2001).

[19] D. Seidlitz, M. K. I. Senevirathna, Y. Abate, A. Hoffmann and N. Dietz, presented at the Fourteenth International Conference on Solid State Lighting and LED-based Illumination Systems, San Diego, CA, **Proc. SPIE 9571** (2015).

[20] V. Y. Davydov, Y. E. Kitaev, I. N. Goncharuk, A. N. Smirnov, J. Graul, O. Semchinova, D. Uffmann, M. B. Smirnov, A. P. Mirgorodsky and R. A. Evarestov, Physical Review B **58** (19), 12899-12907 (1998).

[21] D. G. Zhao, J. J. Zhu, Z. S. Liu, S. M. Zhang, H. Yang and D. S. Jiang, Applied Physics Letters **85** (9), 1499-1501 (2004).

[22] H. Harima, Journal of Physics: Condensed Matter **14** (38), R967 (2002).

[23] J. S. Thakur, D. Haddad, V. M. Naik, R. Naik, G. W. Auner, H. Lu and W. J. Schaff, Physical Review B **71** (11), 115203 (2005).

[24] M. K. Indika Senevirathna, S. Gamage, R. Atalay, A. R. Acharya, A. G. Unil Perera, N. Dietz, M. Buegler, A. Hoffmann, L. Su, A. Melton and I. Ferguson, Journal of Vacuum Science & Technology A **30** (3), 031511 (2012).

[25] N. Dietz, Materials Science and Engineering: B **87** (1), 1-22 (2001).

[26] W. Xinqiang, L. Shitao, M. Nan, F. Li, C. Guang, X. Fujun, T. Ning, H. Sen, J. C. Kevin, Z. Shengqiang and S. Bo, Applied Physics Express **5** (1), 015502 (2012).

[27] S. Junichi, A. Tsutomu, F. Tatsuya, M. Elison, P. Tomás and N. Yasushi, Japanese Journal of Applied Physics **52** (8S), 08JD06 (2013).

[28] S. Ruffenach, M. Moret, O. Briot and B. Gil, physica status solidi (a) **207** (1), 9-18 (2010).

[29] Y. Zhang, T. Kimura, K. Prasertusk, T. Iwabuchi, S. Kumar, Y. Liu, R. Katayama and T. Matsuoka, Thin Solid Films **536**, 152-155 (2013).

[30] in *Group IV Elements, IV-IV and III-V Compounds. Part a - Lattice Properties*, edited by O. Madelung, U. Rössler and M. Schulz (Springer Berlin Heidelberg, Berlin, Heidelberg, 2001), pp. 1-3.

[31] H. Morkoç, S. Strite, G. B. Gao, M. E. Lin, B. Sverdlov and M. Burns, Journal of Applied Physics **76** (3), 1363-1398 (1994).

[32] S. N. Mohammad and H. Morkoç, Progress in Quantum Electronics **20** (5–6), 361-525 (1996).

[33] S. K. O'Leary, B. E. Foutz, M. S. Shur, U. V. Bhapkar and L. F. Eastman, Journal of Applied Physics **83** (2), 826-829 (1998).

[34] S. Yu, K. W. Kim, L. Bergman, M. Dutta, M. A. Stroscio and J. M. Zavada, Physical Review B **58** (23), 15283-15287 (1998).

[35] T. L. Tansley and R. J. Egan, Physical Review B **45** (19), 10942-10950 (1992).

[36] V. W. L. Chin, T. L. Tansley and T. Osotchan, Journal of Applied Physics **75** (11), 7365-7372 (1994).

[37] J. S. Dyck, K. Kim, S. Limpijumnong, W. R. L. Lambrecht, K. Kash and J. C. Angus, Solid State Communications **114** (7), 355-360 (2000).

[38] Z. G. Qian, W. Z. Shen, H. Ogawa and Q. X. Guo, Journal of Applied Physics **92** (7), 3683-3687 (2002).

[39] V. Y. Davydov, V. V. Emtsev, I. N. Goncharuk, A. N. Smirnov, V. D. Petrikov, V. V. Mamutin, V. A. Vekshin, S. V. Ivanov, M. B. Smirnov and T. Inushima, Applied Physics Letters **75** (21), 3297-3299 (1999).

[40] F. Bernardini, V. Fiorentini and D. Vanderbilt, Physical Review Letters **79** (20), 3958-3961 (1997).

[41] F. Bernardini and V. Fiorentini, Physical Review B **58** (23), 15292-15295 (1998).

[42] T. Inushima, T. Shiraishi and V. Y. Davydov, Solid State Communications **110** (9), 491-495 (1999).

[43] Z. G. Qian, G. Yu, W. Z. Shen, H. Ogawa and Q. X. Guo, Physica B: Condensed Matter **318** (2–3), 180-187 (2002).

[44] A. Kasic, M. Schubert, Y. Saito, Y. Nanishi and G. Wagner, Physical Review B **65** (11), 115206 (2002).

[45] J. Wu, W. Walukiewicz, W. Shan, K. M. Yu, J. W. Ager, E. E. Haller, H. Lu and W. J. Schaff, Physical Review B **66** (20), 201403 (2002).

[46] V. Darakchieva, P. P. Paskov, E. Valcheva, T. Paskova, M. Schubert, C. Bundesmann, H. Lu, W. J. Schaff and B. Monemar, Superlattices and Microstructures **36** (4–6), 573-580 (2004).

[47] A. Kasic, E. Valcheva, B. Monemar, H. Lu and W. J. Schaff, Physical Review B **70** (11), 115217 (2004).

[48] B. R. Nag, Journal of Crystal Growth **269** (1), 35-40 (2004).

[49] J. S. Thakur, G. W. Auner, D. B. Haddad, R. Naik and V. M. Naik, Journal of Applied Physics **95** (9), 4795-4801 (2004).

[50] T. Inushima, K. Fukui, H. Lu and W. J. Schaff, Applied Physics Letters **92** (17), 171905 (2008).

[51] R. Cuscó, J. Ibáñez, E. Alarcón-Lladó, L. Artús, T. Yamaguchi and Y. Nanishi, Physical Review B **79** (15), 155210 (2009).

[52] J. G. Kim, Y. Kamei, N. Hasuike, H. Harima, K. Kisoda, K. Sasamoto and A. Yamamoto, physica status solidi (c) **7** (7-8), 1887-1889 (2010).

[53] J. S. Thakur, A. Dixit, Y. V. Danylyuk, C. Sudakar, V. M. Naik, W. J. Schaff and R. Naik, Applied Physics Letters **96** (18), 181904 (2010).

[54] E. Tiras, M. Tanisli, N. Balkan, S. Ardali, E. Iliopoulos and A. Georgakilas, physica status solidi (b) **249** (6), 1235-1240 (2012).

[55] S. P. Fu and Y. F. Chen, Applied Physics Letters **85** (9), 1523-1525 (2004).

[56] Y. Ishitani, K. Xu, W. Terashima, N. Hashimoto, M. Yoshitani, T. Hata and A. Yoshikawa, physica status solidi (c) **0** (7), 2838-2841 (2003).

[57] K. Fukui, Y. Kugumiya, N. Nakagawa and A. Yamamoto, physica status solidi (c) **3** (6), 1874-1878 (2006).

[58] P. Schley, R. Goldhahn, G. Gobsch, M. Feneberg, K. Thonke, X. Wang and A. Yoshikawa, physica status solidi (b) **246** (6), 1177-1180 (2009).

[59] M. Himmerlich, A. Knübel, R. Aidam, L. Kirste, A. Eisenhardt, S. Krischok, J. Pezoldt, P. Schley, E. Sakalauskas, R. Goldhahn, R. Félix, J. M. Mánuel, F. M. Morales, D. Carvalho, T. Ben, R. García and G. Koblmüller, Journal of Applied Physics **113** (3), 033501 (2013).

8 CHAPTER 8: SUMMARY

In this work, the optoelectronic and structural properties of group III-N (InN and AlN) layers grown by high pressure metal organic chemical vapor deposition (HP-MOCVD) and migration-enhanced plasma-assisted metal organic chemical vapor deposition (MEPA-MOCVD) have been studied by Fourier Transform Infrared (FTIR) spectroscopy, Raman Spectroscopy, and X-ray diffraction (XRD)

FTIR reflectance spectrum of a semiconductor contains various types of physical properties that depend on the experimental conditions/type, wavelength range, certain properties of the individual semiconductor, and external parameters (e.g. pressure, temperature). When studying a multilayer structure, in order to extract the properties of the each layer, through the reflectance spectra, it requires a method to separate the reflection of each layer from the total spectrum. The multilayer stack model, which calculates the total reflectance of the whole layer stack by adding the reflectance or transmission at each interface was used to archive this task. The choice of the model is important as it should include most of the properties of the materials, such as dielectric function, layer thickness, surface roughness, interface roughness, and the band structure. Thus, modeling of the dielectric function also plays a major role in the modeling of the reflectance spectrum. The dielectric function in the IR region can be modeled as described in Section 4.5.

The effect of the substrates/templates (Sapphire, AlN, Ga-polar GaN, N-polar GaN, n-GaN, and p-GaN) on the free carrier concentration, carrier mobility of the InN layers grown on HP-MOCVD were investigated by FTIR reflectance spectra analysis. The FTIR reflectance spectra analysis prevailed, on identifying an intermediate InN layers with different optoelectronic properties in these sample, in addition to the bulk layer on the substrate/template, there were intermediate InN layers with different properties in these samples The lowest carrier concentration of 7.1×10^{18} cm^{-3} with the mobility of 660 cm^{2}V^{-1}s^{-1} was found in the InN film grown on AlN template, by FTIR reflectance spectra analysis. Additionally, the Raman E_2 high analysis indicates the best local ordering in the same InN film. The AFM study revealed the

smoothest InN surface (RMS=1.273 nm) on the InN film grown on the p-GaN template. Further studies are carrying out to correlate the results.

The influence of reactor pressures (2.5–18.5 bar) on the long-range crystalline order, in-plane structural quality, local crystalline order, free carrier concentration, and carrier mobility of the InN epilayers deposited on GaN/sapphire by HP-MOCVD has been investigated using these techniques. The XRD 2θ-ω scans InN (2-102) off-axis and InN (0002) on-axis studies showed the structural quality improvement with increasing reactor pressure. This tendency was confirmed by the Raman results. The near-field crystallinity improves as reactor pressure increase up to 12.5 bar. Above 12.5 bar reactor pressure the near-filed ordering of the InN films has decreased, which is likely due to the higher ammonia cracking efficiency requiring adjustment of the group V/III ratio. Additionally, a low free carrier concentration and the highest mobility with values of 1.5×10^{18} cm^{-3} and 270 $cm^2V^{-1}s^1$, respectively were found for the InN film grown at 12.5 bar.

The effect of the AlN buffer layer on the free carrier concentration, carrier mobility, local crystalline ordering, and surface morphology of InN layers grown by Migration-Enhanced Plasma Assisted MOCVD was also studied. Here, the AlN nucleation layer was varied to assess the physical properties of the InN layers. This study was focused on optimizing of the AlN nucleation layer (e.g. temporal precursor exposure, nitrogen plasma exposure, plasma power, and annealing temperature) and studying its effect on the InN layer properties. The results indicated that the annealing of the AlN buffer layer at 850 °C improves the structural quality and optoelectronic properties of overgrown the InN layers. Further improvements on the AlN buffer layer quality and InN growth processing parameters are needed to further improve the structural quality of the InN epilayers and their optoelectronic properties.

APPENDICES

Appendix A

Appendix A.1 Geometry configuration and Raman active modes for wurtzite structure

Geometry Configuration	Raman active phonon mode
$x(y, y)\bar{x}$	A_1 (TO), E_2
$x(z, z)\bar{x}$	A_1 (TO)
$x(z, y)\bar{x}$	E_1 (TO)
$x(y, z)y$	E_1 (TO), E_1 (LO)
$x(y, y)z$	E_2
$z(x, y)\bar{z}$	E_2
$z(x, x)\bar{z}$	A_1 (LO), E_2

Appendix A.2 The Operating Window for PL

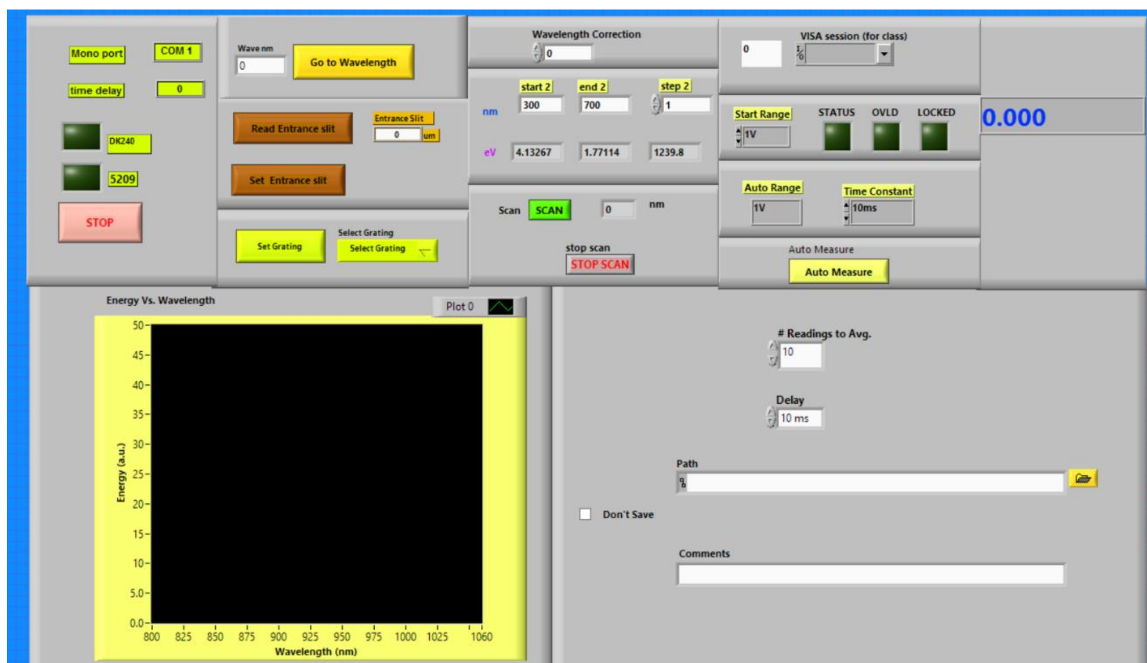

Appendix B

Appendix B.1 MATLAB code for the simulation program

```
%================================== Main program for multilayer reflection
calculations ==========================
%==================================                         ©NALD
==========================

%
% ---------------------------------------------------------------------------
------------------------------------------------------------------

clear all

clc;

IR_Refl_Header;

%  stepwidth width
stepwidth    = 1.0;

 %  Numbers of layers - in addition to ambient and substrate!!!
Nblay        = 2;

%  Material id# for each layer
Eps_lay       =[22, 9];

%  Dielectric function of ambient
eps_amb      = 1;

 %  Dielectric function of last infinite medium
eps_sub      = 1;

 %  Thickness for each layer
thi_lay       = [1790, 461230.16];

%  Thickness variation for each layer
thicknvar     = [10,  00];

%  Interface perfection / loss for each layer
InterfPerf    = [0.90,   0.89764];

%  Interface perfection variation range
InterfPerfvar =  [0.01,  0.0];

% limits for x-axis range in simulation

xlowlimit = 450;
xuplimit = 6500;

% Parthilay:  initial thickness array - which are the parent parameter!!
```

```
Parthilay     = thi_lay;
% ParInterfPerf:  initial Interface perfections parameter
%  always with respect to layer k/k+1
ParInterfPerf = InterfPerf;

% enter here the number of childrens generated through each fit iteration cy-
cle
itnumb       = 450;
% best least-square fit value between experiment and simmulation data
bestfitres   = 100;
% stop if best least-square fit value is below bestfitvalue
bestfitvalue = 0.000001;
% The pointer to the parent or child with the sofar best set of fitting pa-
rameters
parent       =   1;

% close all windows and open new windows for display
set_displaywin;
if (~set_IR_Refl_ProgPath())
   error('error setting the pathes - check!!!! ');
   break;
else
    disp(' path for read-in\write data file location and fitting parameter
files correct found and set! ');
    disp(progfilepath);
    disp(datafilepath);
    disp(IRfitParamPath);
end

 % read in experimental data array
 [xarrayhlp, Experim, start,stop,NbStep]= read_experiment_dat(xlowlimit,
xuplimit);
 if (NbStep==0)
    error('error reading in experimental data');
    break;
 end

 hp1         = 1;
 hp2         = NbStep;
 xaxisarray  = zeros(NbStep,3);
 % 4 = experimental x-axis defines the remaining x-axis array
 xaxisarray(1:NbStep,1:3) = init_xaxis(4, start, stepwidth, NbStep, xarrayhlp
);
 figure(fig_h1); plot(xarrayhlp,Experim);

%---------------------------------------%
% EspMLarr = [1:NbStep] [ Nblay + 2  ]  [ itnumber + 1 ] dielectric function
array
EspMLarr      = zeros(NbStep,(Nblay + 2), (itnumb +1) );
ParEspMLarr   = zeros(NbStep,(Nblay + 2));
DeltPar       = zeros(NbStep,1);
Trans         = zeros(NbStep,1);
Refl          = zeros(NbStep,1);
Refl2         = zeros(NbStep,1);

% Eps - Parameter field for a single layer
```

```
SingStack      = zeros(9, 4);
% Cildren parameter set generaterd from Parent set of Eps - Parameter fields

IterLayEps     = zeros(itnumb, Nblay+2, 9, 4);
DeltChild      = zeros(NbStep,1);

%---------------------------------------------------%
% get all dielectric function values

% get the initial simmulation parameter sets for the parent
%       ParEspMLarr(NbStep,(Nblay + 2)):  eps-values for all layers
%       Parthilay :thickness values for each layer
% calculate all the dielectric functions and their variations
    for m = 0:1:Nblay,
        if (m ==0)
             SingStack(1:9,1:4)            = Dielectfct_ML_init(eps_amb);
             [ParEspMLarr(1:NbStep,1), ParMLStack_eps(1,1:9,1:4)] = Dielect-
fct_ML_Lorentz(eps_amb,SingStack,xaxisarray(1:NbStep,3), NbStep, 1);
        else
            SingStack(1:9,1:4)            = Dielectfct_ML_init(Eps_lay(m));
            [ParEspMLarr(1:NbStep,(m+1)), ParMLStack_eps(m+1,1:9,1:4)] = Die-
lectfct_ML_Lorentz(Eps_lay(m),SingStack,xaxisarray(1:NbStep,3),NbStep, 1);

        end
    end % end for m - layers ......
    %-- add susbtrate layer
    SingStack(1:9,1:4)                        = Dielectfct_ML_init(eps_sub);
    [ParEspMLarr(1:NbStep,Nblay+2), ParMLStack_eps(Nblay+2,1:9,1:4)] = Die-
lectfct_ML_Lorentz(eps_sub,SingStack,xaxisarray(1:NbStep,3),NbStep, 1);
    %
    %--  ParMLStack_eps:    contains the original parameter set for varying
the dielectric functions
    %--  ParEspMLarr:       is an array with the dielectric functions as
function of wave#

    % Parthilay:      initial thickness array - which are the parent parame-
ter!!
    Parthilay     = thi_lay;
    % ParInterfPerf:   initial Interface perfections parameter
    ParInterfPerf = InterfPerf;
    Refl  = CalMLRef02(xaxisarray, NbStep, Nblay,
ParEspMLarr(1:NbStep,1:(Nblay+2)), Parthilay, ParInterfPerf);

    %-- calculate difference spectra and chi^2
    DeltPar(1:NbStep) = Refl(1:NbStep) - Experim(1:NbStep);
    sumhlp =0;
    for j=1:1:NbStep,
        sumhlp = sumhlp + DeltPar(j)^2;
    end
    SumDeltPar = sumhlp / (NbStep+1);


bestfitres = SumDeltPar;
parent = 0;
```

```
strhlp = sprintf('bestfitres for Parent parameter set: %-8.5f', bestfitres);
disp(strhlp);
echo off; stopflg = 0;
% ----------------------------------------------------------------------------
-------------------------------------------------------------------
% --------------------------------------------     here starts the main loop
for the fitting      ---------------------------------------------
while (bestfitres > bestfitvalue)
    % 1.)  calculate the dielectric functions and generate a set of childrens
from the parent parameter set


% calculate the dielectric functions for all layers (parent) and generate a
set childrens (defined by itnumb)

        for m = 0:1:Nblay,                                                  %
calculate all the dielectric functions and their variations
            if (m==0)
                 SingStack(1:9,1:4)      = ParMLStack_eps(1,1:9,1:4);
                 [EspMLarr(1:NbStep, 1,1:itnumb), IterLayEps(1:itnumb,
1,1:9,1:4) ] = Dielectfct_ML_Lorentz(eps_amb,  SingStack, xaxisar-
ray(1:NbStep,3), NbStep, itnumb);

            else
                 SingStack(1:9,1:4)        = ParMLStack_eps(m+1,1:9,1:4);
                 hlpeps                        = Eps_lay(m);
                 [EspMLarr(1:NbStep,m+1,1:itnumb), IterLayEps(1:itnumb,
m+1,1:9,1:4)] = Dielectfct_ML_Lorentz(hlpeps,SingStack,xaxisar-
ray(1:NbStep,3),NbStep,itnumb);

            end % end if m .....
        end % end for m = ...
        SingStack(1:9,1:4)                = ParMLStack_eps(Nblay+2,1:9,1:4);
        [EspMLarr(1:NbStep,Nblay+2,1:itnumb), IterLayEps(1:itnumb,
Nblay+2,1:9,1:4)] = Dielectfct_ML_Lorentz(eps_sub,SingStack,xaxisar-
ray(1:NbStep,3),NbStep,itnumb);
        % end of calculate the dielectric functions for all layers ......
        %
        %
        sumdelt = zeros(1,itnumb);
        for k=1:itnumb,             % k=1; is the parameter set is initially
defined
           if (k>1)   % vary the layer thicknesses / Interface perfection  by
generating a new set from the original defined parameter
                for m = 1:Nblay,
                    thi_lay(m)    = Parthilay(m)     + thicknvar(m)     *
rand*(-1)^(round(rand(1)*10));  % vary layer thicknesses
                    InterfPerf(m) = ParInterfPerf(m) + InterfPerfvar(m) *
rand*(-1)^(round(rand(1)*10));  % vary Interface perfection
                    if (InterfPerf(m) > 1)
                        InterfPerf(m) = 1.0;
                    end
                    if (InterfPerf(m) < 0.05)
                        InterfPerf(m) = 0.05;
                    end
```

```
                end % end for - vary the thickness / Interface perfection for
each layer!
            end % end if

            if (k==1)
             figure(fig_h1);
             xarr = xaxisarray(hp1:hp2,3);   yarr1 = real(EspMLarr(hp1:hp2,2,
k));  yarr2 = imag(EspMLarr(hp1:hp2,2, k));
             plot(xarr,yarr1, xarr,yarr2), title(' Dielectric functions -
Layer 1) '); xlabel('wavenumber (cm-1)');
            end


            Refl = CalMLRef02(xaxisarray, NbStep, Nblay, Es-
pMLarr(1:NbStep,1:(Nblay+2), k), thi_lay, InterfPerf);
            DeltChild(1:NbStep) = Refl(1:NbStep) - Experim(1:NbStep);
            sumhlp =0;
            for j=1:1:NbStep,
                sumhlp = sumhlp + DeltChild(j)^2;
            end
            sumdelt(k) = sumhlp / (NbStep+1);
            if (sumdelt(k) <  bestfitres)
                bestfitres = sumdelt(k);
                % k is better than original parent and becomes new parent!!
                parent        = k;
                % save thickness area of potential new Parent value
                Parthilay     = thi_lay;
                % save InterfPerf to ParInterfPerf
                ParInterfPerf = InterfPerf;


                figure(fig_h2); xarr = xaxisarray(hp1:hp2,3);
                plot(xarr,Refl,xarrayhlp,Experim), title(' Reflectance of
original parent parameter '); xlabel('wavenumber (cm-1)');  ylabel('reflec-
tance (a.u.)'),
                figure(fig_h3); plot(xarr,DeltChild), title(' Difference: Exp
- Simul) '); xlabel('wavenumber (cm-1)');

                 strhlp = sprintf('bestfitres for child # %3d = %-8.5f', k,
bestfitres); disp(strhlp);

%                  strhlp = sprintf('Thicknesses: Lay#(%2d)=%-8.5f;
Lay#(%2d)=%-8.5f; Lay#(%2d)=%-8.5f \n', ...
%                                 Eps_lay(1), Parthilay(1),Eps_lay(2), Par-
thilay(2),Eps_lay(3), Parthilay(3)); disp(strhlp);
%                   strhlp = sprintf('Thicknesses: Lay#(%2d)=%-8.5f;
Lay#(%2d)=%-8.5f; Lay#(%2d)=%-8.5f \n', ...
%                                 Eps_lay(1), Parthilay(1),Eps_lay(2), Par-
thilay(2)); disp(strhlp);

                  strhlp = sprintf('Thicknesses: Lay#(%2d)=%-8.5f;
Lay#(%2d)=%-8.5f; Lay#(%2d)=%-8.5f \n', ...
                                Eps_lay(1), Parthilay(1)); disp(strhlp);
%
```

```
%                    strhlp = sprintf('Interface Perfection: Lay#(%2d)=%-
8.5f; Lay#(%2d)=%-8.5f; Lay#(%2d)=%-8.5f \n', ...
%                                Eps_lay(1), ParInterfPerf(1), Eps_lay(2),
ParInterfPerf(2), Eps_lay(3), ParInterfPerf(3)); disp(strhlp);

%
                 strhlp = sprintf('Interface Perfection: Lay#(%2d)=%-8.5f;
Lay#(%2d)=%-8.5f; Lay#(%2d)=%-8.5f \n', ...
                               Eps_lay(1), ParInterfPerf(1) ); disp(strhlp);
%
                 strhlp = sprintf('Parameter Layer1 '); disp(strhlp);
                 strhlp = sprintf(' %-10.4f   %-10.4f %-10.4f %-10.4f\n', It-
erLayEps(parent,2,1:9,1:4)); disp(strhlp);

                 strhlp = sprintf('Parameter Layer2 '); disp(strhlp);
                 strhlp = sprintf(' %-10.4f   %-10.4f %-10.4f %-10.4f\n', It-
erLayEps(parent,3,1:9,1:4)); disp(strhlp);

%                  strhlp = sprintf('Parameter Layer3 '); disp(strhlp);
%                  strhlp = sprintf(' %-10.4f   %-10.4f %-10.4f %-10.4f\n',
IterLayEps(parent,4,1:9,1:4)); disp(strhlp);
           end

           figure(gcf);
           if ((strcmpi(get(gcf,'CurrentKey'),'q')) && ~stopflg)
               echo on;
               disp('q has been pressed - fit will stop after iteration loop
is completed');
               stopflg = 1;
               bestfitres = 0;
               echo off;
           end

        end % for loop

    %--  Now check whether any of the children parameter set generated a bet-
ter fit result

    if (parent > 0)
         %  eps-parameter of child k will become the parent parameter
           ParMLStack_eps(1:Nblay+2,1:9,1:4) = IterLayEps(parent,
1:Nblay+2,1:9,1:4);
           ParEspMLarr(1:NbStep,1:(Nblay+2)) = EspMLarr(1:NbStep,1:(Nblay+2),
parent);
           parent = 0;
    end

end % -------------------------------     End  while (bestfitres ..... main
loop for the fitting      ---------------------------------------------
% -----------------------------------------------------------------------------
-----------------------------------------------------------------
% echo on;
% Save data:   the best fitting result should be in ParEspMLarr
% 1st - write the parameter established:
%
```

```
    action = 0; retval = Write_IR_MLStackFitParam(action);
    if ~retval
        error(' Error writing Fit parameter to file!');
    end


    close(fig_h3); close(fig_h2);
    %  next recalculate the reflectance spectra with the best fitting result
    %

    Refl = CalMLRef02(xaxisarray, NbStep, Nblay,
ParEspMLarr(1:NbStep,1:(Nblay+2)), Parthilay, ParInterfPerf);
    figure(fig_h1); xarr = xaxisarray(hp1:hp2,3);
    plot(xarr, Refl, xarr, Experim), title(' Experimental and Simulated Re-
flectance Spectra'); xlabel('wavenumber (cm-1)');  ylabel('reflectance
(a.u.)');
    %
    % write the data to a file
    %
    retval = Write_BestFitSimData(NbStep, xaxisarray(1:NbStep,3), Ex-
perim(1:NbStep), Refl(1:NbStep));
    if ~retval
        error(' Error writing Best Simulation fit data file!');
    end
%
% End of Main Program
% ---------------------------------------------------------------------------
-----------------------------------------------------------------
% ---------------------------------------------------------------------------
-----------------------------------------------------------------
   function Refl = CalMLRef02(xaxis, Numbstep, Numblay, Epsarr, thi-
lay,IntPerf)

% This function calculates the reflectance of a multilayer stack in normal
incidence configuration
%
% Input parameter:
%           xaxis:     Array for x-axis:  xaxis(:,1)= nm; xaxis(:,2)= eV;
xaxis(:,3) = cm-1
%           Numbstep:  number of Steps
%           Numblay:   Number of layers in stack (in addition to to ambient
and substrate!!!
%           epsamb:    medium # for ambient
%           epsubs:    medium # for susbtrate
%           Epslay:    Array of medium #'s for each layer
%           thilay:    Array of layer thicknesses for each layer given in nm
%           IntPerf:   Array of interface perfection parameters for k/k+1
layer interfaces


% global  fig_h1 fig_h2 fig_h3       % Window handles

im      = sqrt(-1);                %  definition of imaginary part
pi      = 3.141593;
```

```
Refl     = zeros(Numbstep,1);
 %ReflN    = zeros(Numbstep,1);
phase    = zeros(Numblay+1);
delta = 0.0;

% ------------------------------------------------------------------------
for k = 1:Numbstep,


 if (Numblay > 0)
        for m = 1:Numblay,
            phshlp = (2 * pi * thilay(m) * sqrt(Epsarr(k,m+1))) / xaxis(k,1);
% phase will need xaxis in nm!!
            phase(m) = phshlp;
        end % end for m = ...

 end % endif (Numblay > 0)


    % Calculate Matrix:   M0 = ambient - Layer_1 and  M_subs = Layer_N - Sub-
strate
    for m = 0:1:Numblay,
        rnk = (sqrt(Epsarr(k,m+1))-sqrt(Epsarr(k,m+2)))/(sqrt(Ep-
sarr(k,m+2))+sqrt(Epsarr(k,m+1)));
        if (m == 0)
           Matr   = [1  rnk;    rnk   1];
        else
            if ((IntPerf(m) > 0) && (IntPerf(m) < 1.0)) rnk = rnk *
IntPerf(m); end
            Matr = Matr * [            1                                 rnk;
                            rnk * exp(complex(0,-2)*phase(m))    exp(com-
plex(0,-2)*phase(m))];
        end % endif
    end % end for m = ...

    Refl(k) = calc_reflect(Matr);


end  % End for-loop: compute normal incidence reflectance of multi-layer
stack


% -----------------------------------------------------------------------------
-
end % function


% -----------------------------------------------------------------------------
--------------------------------------------
% -----------------------------------------------------------------------------
--------------------------------------------
% -----------------------------------------------------------------------------
--------------------------------------------
%                 Help functions multilayer stack calculations
```

```
%%
function [reflect] = calc_reflect(Rmatr)  % calculated the total reflectivity
of the multilayer stack
                                          % matr is a complex 2x2 matrix
   reflect =  (real(Rmatr(2,1)/Rmatr(1,1)))^2 +
(imag(Rmatr(2,1)/Rmatr(1,1)))^2;
   if (reflect > 1) reflect=1.0; elseif (reflect < 0) reflect = 0.0; end

end % end calc_reflect
```